DETECTION OF FUGITIVE EMISSIONS FROM VALVE STEMS – DC RESISTANCE RESPONSE AND GAS ADSORPTION OVER TIN DIOXIDE MIXED WITH ALUMINA

by

James Elliott MacKay

B.Sc., Dalhousie University, 1990

B.Eng., Memorial University of Newfoundland, 1994

A THESIS SUBMITTED IN PARTIAL FULFILLMENT OF
THE REQUIREMENTS FOR THE DEGREE OF
MASTER OF APPLIED SCIENCE

in

THE FACULTY OF GRADUATE STUDIES

(DEPARTMENT OF CHEMICAL AND BIOLOGICAL ENGINEERING)

We accept this thesis as conforming
to the required standard

The University Of British Columbia

April, 2004

Library Authorization

In presenting this thesis in partial fulfillment of the requirements for an advanced degree at the University of British Columbia, I agree that the Library shall make it freely available for reference and study. I further agree that permission for extensive copying of this thesis for scholarly purposes may be granted by the head of my department or by his or her representatives. It is understood that copying or publication of this thesis for financial gain shall not be allowed without my written permission.

JAMES E MACKAY — Name of Author *(please print)*

20/04/2004 — Date (dd/mm/yyyy)

Title of Thesis: DETECTION OF FUGITIVE EMISSIONS FROM VALVE STEMS - DC RESISTANCE RESPONSE AND GAS ADSORPTION OVER TIN DIOXIDE MIXED WITH ALUMINA

Degree: MASc. Year: 2004

Department of CHEMICAL AND BIOLOGICAL ENGINEERING
The University of British Columbia
Vancouver, BC Canada

ABSTRACT

Stringent fugitive emission limits for process equipment including valves, as proposed by European regulatory bodies for example, require significant improvements in valve sealing technology and maintenance techniques and will create a need for monitoring and containment of very small leakage rates to reduce ambient air concentrations (to 1 ppm). Conceptually, the potential of a combined adsorbent / metal oxide sensor bed provides a novel solution to this problem and is studied to determine the feasibility of achieving the dual purposes of containment and monitoring at levels typical of default valve leakage rates, $E = 6.56 \times 10^{-7}$ *kg/hr/source*.

Simultaneous adsorption breakthrough and electrical resistance measurements (dc) were obtained in a quartz reactor utilizing 2 co-centric tantalum electrodes. A loosely packed sensor bed consisting of 22.5 cc of a mechanical mixture of up to 40 %vol. Al_2O_3 (adsorbent) in SnO_2 (metal oxide sensor) was studied. 1 to 10 %vol. propylene in He was passed through the bed alternately with He and air gas cycles, and the adsorption breakthrough and electrical resistance monitored at temperatures of 50 – 150 °C. Results showed that the adsorption uptake was linearly proportional to the %vol. mixture of Al_2O_3 in the sensor bed, indicating that Al_2O_3 was responsible for the adsorption in the bed and that SnO_2 was essentially acting as a non-porous media limited to relatively low levels of surface adsorption responsible for very large changes in the bed electrical resistance. The change in electrical resistance between the oxidized state of the bed and the reduced state of the bed was used as the sensor bed's measured variable for the present system. Equilibrium adsorption uptake of 10 %vol. C_3H_6 in He over 100% Al_2O_3 at 50 °C and 12 kPa was 0.12 mmol of C_3H_6 per g of Al_2O_3. The uptake dropped significantly to 0.03 mmol/g at 100 °C with $-\Delta H_{ads}$ = 29.2 kJ/mol (calculated from the vant Hoff equation). Maximum sensor bed sensitivity of 5.29 (the ratio of the bed resistance in air to the bed resistance after reduction by C_3H_6) was recorded for sensor bed composition consisting of 40

%vol. Al_2O_3 in SnO_2 at 150 °C but sensitivity dropped to 1.67 at 50 °C. The contrast between the temperature relationship of adsorption and that of electrical sensitivity indicates a significant challenge for the dual purpose sensor bed. That is, elevated operating temperatures favour fast sensor response and sensitivity but are unfavourable for adsorption uptake and the time between adsorbent regeneration (sensor life). Practical perspectives dictate that strong adsorbents should be utilized for light hydrocarbon or VOC recovery at elevated temperatures, in the 150 – 200 °C range, and metal oxide sensing materials prepared to improve sensitivity and selectivity for target gases in this same temperature range or lower, should be explored in combination to optimize sensor performance. Literature suggests that this is potentially viable, using additives such as Pt and Pd in sensor bed preparation and potentially using newly developed bed geometry such as wire mesh honeycomb (WMH) designs to further enhance this novel sensor concept.

The electrical resistance in the sensor bed is modeled as a function of adsorption breakthrough using the axially dispersed plug flow model of Levenspiel and Bischoff (1963). The model was a good fit at 150 °C, but the modeled electrical resistance response was much faster than the observed response at lower temperatures indicating that kinetic effects were dominant at lower temperatures. A simple first order reaction mechanism in $[O_2^-]$ was proposed in which an empirical reaction rate fitting parameter, a, was used to obtain a good fit between the model and the experimental data for all conditions between 50 to 150 °C. An activation energy, E_a = 42.4 kJ/mol, was determined. A modified plug flow model (inclusive of dispersive and mass transfer effects) was compared to the axially dispersed plug flow model for adsorption and was not found to be of any additional benefit.

It is concluded that the sensor bed concept is viable for containment and sensing of the default valve emission rate over a period of at least 1 year, but that further research and development is required to optimize materials, preparation and operating temperature.

TABLE OF CONTENTS

LIST OF TABLES

LIST OF FIGURES

NOMENCLATURE

a	fitting parameter $a = k_a P_R$ (s^{-1})
A	cross section area of bed (cm^2)
A_0	pre-exponential factor for the Arhennius equation for the activation energy (kJ/mol)
B	Langmuir constant (kPa^{-1})
c	concentration (%vol., ppmv)
c_g	concentration of reducing gas in air
c_0	inlet concentration
d_p	weighted root mean average particle size (cm)
D_L	axial dispersion coefficient (cm^2/s)
D_m , D_{12}	molecular diffusivity, molecular diffusivity of a binary gas mixture (cm^2/s)
D'	effective diffusivity (cm^2/s)
D^o	diffusivity in the ambient (cm^2/s)
D_p	macroporous diffusivity (cm^2/s)
D_c	inter-crystalline (microporous) diffusivity (cm^2/s)
E	fugitive emission flow rate (kg/hr/source)
E_a	activation energy (kJ/mol)
E, E_c, E_f	electron energy level, conduction band energy level fermi energy (where the Fermi probability is ½) (eV)
F	gas flow rate (sccm)
G, G_a, G_R	conductance, conductance in oxidized state, conductance in reduced state (ohm^{-1}),
G	Gibbs energy (kJ/mol)
G_0, $G_{0,d}$	initial conductance (related to contact area, charge mobility, and other factors) (ohm^{-1})
h	Planck's constant, $h = 6.62 \times 10^{-34}$ Js
I	intercept
i	index for sensor bed parallel resistive layer
j	index for time
k, k_a	reaction rate constant (s^{-1})
k_b	Boltzmann's constant, $k_b = 1.3807 \times 10^{-23}$ J/K
k_{eff}	effective mass transfer coefficient, reaction rate constant (s^{-1})
k_f	external fluid film mass transfer coefficient (cm/s)
k_F	Freundlich Isotherm constant of proportionality (mmol/g)
K	Henry's constant ($cc_{adsorbate}/cc_{adsorbent}$)
K	proportionality constant
K_{eq}	equilibrium constant (dimensionless)
K_0	pre-exponential factor in the Arhennius equation for heat of adsorption
L	length (cm)

$LMTR$	lumped mass transfer resistance (s)
M_1, M_2	molecular weight of species 1 and 2 in a binary gas mixture (g/mol)
n	fractional power of the Freundlich Isotherm (dimensionless)
n	power of the Bruggeman equation (dimensionless)
n_b	density of electrons in the bulk (cm^{-3})
n_s	density of electrons on the surface of an n-type semiconductor (cm^{-3})
N_c	effective density of states near the edge of the conduction band ($\sim 10^{19}$ cm^{-3})
N_D	density of donors in the bulk (cm^{-3})
N_i	net density of ions in the space charge region (cm^{-3})
N_s	density of charged surface states (cm^{-3})
N_T	total density of oxygen ion and electrons on the surface (cm^{-3})
$[O_2^-]$	density of oxygen ion on the metal oxide surface (cm^{-3})
P	pressure (kPa, kPag)
P_R	partial pressure of reducing gas (kPa)
q	charge of an electron, $q = 1.602 \times 10^{-19}$ *C (coulomb)*
q	local adsorbate concentration (mmol/g)
$\overline{q}$	average adsorbate concentration over a grain (mmol/g)
q^*	equilibrium adsorbate concentration (mmol/g)
q_m	concentration at saturation (assumed to be a monolayer) (mmol/g)
R	universal gas constant, $R = 0.0083144\ kJ\ mol^{-1}\ K^{-1}$
R	electrical resistance (Ω)
R_a	resistance in air (Ω)
R_g	resistance in reducing gas (Ω)
R_L	load resistance (Ω)
$R_{O,i}$	layer resistance: oxidized component of parallel layer (Ω)
$R_{O,0}$	initial bed resistance at $t = 0$ (Ω)
$R_{R,i}$	layer resistance: reduced component of parallel layer (Ω)
$R_{R,f}$	final bed resistance at $t = t_f$ (Ω)
R_S	sensor resistance (Ω)
r_c	grain (crystal) radius (cm)
Re_p	modified Reynolds number (dimensionless)
R_p	particle radius (cm)
S	slope
S	site for adsorption
S_1, S_2, S_3, S_4	sensitivity according to the key of Table 4.6 (dimensionless)
S, S_N, S_A	sensitivity, absolute sensitivity, normalized sensitivity (dimensionless)
S_{ads}, S_{gas}	entropy adsorbed phase, gas phase ($kJmol^{-1}K^{-1}$)
t , $\bar{t}$	time, mean residence time (s)
t	thickness (cm)

T	temperature (K unless otherwise stated)
u_n	mobility of the carriers
u	superficial velocity (cm/s)
v	interstitial velocity (cm/s)
v	photon light frequency (Hz)
V_c	operating voltage of the circuitry (Volts)
V_{out}	output voltage (Volts)
V_s	potential of the energy gap depletion region (eV)
V_E	volume of empty space in the bed (cm^3)
V_T	total bed volume (cm^3)
W	width (cm)
z	distance down the length of a packed column (cm)

α	constant for integration
β	proportionality constant
$-\Delta H_{ads}$	heat of adsorption (kJ/mol)
ε_b	bed voidage
ε_{inert}	%vol. fraction of inert material (non-conducting) in bed including gas space
ε, ε_0	dielectric constant of the semiconductor, permittivity of free space respectively
ε_p	particle porosity (dimensionless)
ε_{12}	force constant for intermolecular forces (Lennard-Jones expression for intermolecular forces)
f	Fermi probability
μ_f	gas viscosity ($gcm^{-1}s^{-1}$)
μ, μ_{corr}	mean residence time, corrected mean residence time (s)
ρ_g	gas density (g/cc)
σ	effective conductivity ($ohm^{-1}cm^{-1}$)
σ_0	bulk conductivity ($ohm^{-1}cm^{-1}$)
σ^2	variance (s^2)
σ_{12}	variance (s^2)
τ, τ'	dimensionless time parameter (plug flow model)
Ω_D	collision integral (Lennard-Jones expression for intermolecular forces)
ξ, ξ'	dimensionless bed length parameter (plug flow model)

ACKNOWLEDGEMENTS

I would like to thank Fred Cahill, for sponsoring this project, and giving me leave of absence from GJ Cahill, and NSERC for providing the additional financial support necessary to carry it out. Des McGrath of Cahill Instrumentation deserves credit for initially suggesting that a project of this nature could be investigated and would be interesting both personally and strategically for the company.

I would also like to thank Dr. Kevin Smith, my supervisor, for giving me the opportunity to carry out this project and whose guidance and feedback has been instrumental in making it a success. I am sure I have tried his patience in his push to make a chemical engineer out of me.

Lesley, my wife, has given me her wonderful support, and our three children, Victoria, Meg, and David, have been both patient and fabulously distracting throughout this endeavour.

Lastly I would like to express love and gratitude to my mother and father, Ethel and G. David MacKay for always providing me with support in all of my endeavours. It is ironic that my father, a professor of chemical engineering, is not here now to discuss my own research experiences. I thank him for the inspiration that his memory continues to provide.

Chapter 1 - Introduction

1.1 Background

Fugitive emissions are leaks that occur from process equipment such as valves, pumps, compressors, and flanges. The United States Environmental Protection Agency (EPA) indicates that fugitive emissions account for over 250,000,000 lbs (over 125,000 metric tonnes) of lost product per year in the United States alone (refer to Table 1.1).

Table 1.1: US Air Emissions (lbs/year) from all reported industrial sources including Fugitive Emissions where levels exceed 5 million pounds per year to the atmosphere (source: US EPA 1997)

Chemical (only > 5 million lbs/yr shown)	**Fugitive Air**	**Total Air Emissions**
Ammonia	33,230,000	151,066,000
Certain glycol ethers	8,670,000	36,116,000
Chlorodifluoromethane	5,090,000	8,660,000
Dichloromethane	11,166,000	35,804,000
Ethylene	10,378,000	25,550,000
Methanol	21,309,000	185,947,000
Methyl ethyl ketone	15,487,000	38,458,000
N-hexane	19,531,000	56,501,000
Propylene	7,889,000	13,584,000
Styrene	13,012,000	57,818,000
Toluene	30,989,000	90,590,000
Trichloroethylene	5,826,000	10,550,000
Xylene (mixed isomers)	15,306,000	66,938,000
Total (all EPA Listed Chemicals)	**277,500,000**	**2,036,500,000**

In the United States and Europe estimates of the percentage of fugitive emissions that come from valve stems have been reported in the range 60% to > 85% (Sear, 1997; Allen and Rosselot, 1994). Although the leak rate from individual valves may be small, the large number of valves compared to other types of process equipment, as well as the dynamic nature of valve stems, means that the cumulative impact of valve stem leakage is significant. In Figure 1.1, Allen and Rosselot (1994) compare the emission estimates by equipment type for a typical refinery complex, including valves, pumps, relief valves, flanges, etc. As can be seen from the figure, most of the emissions (77%) occur from valves which comprise only 23% of the components.

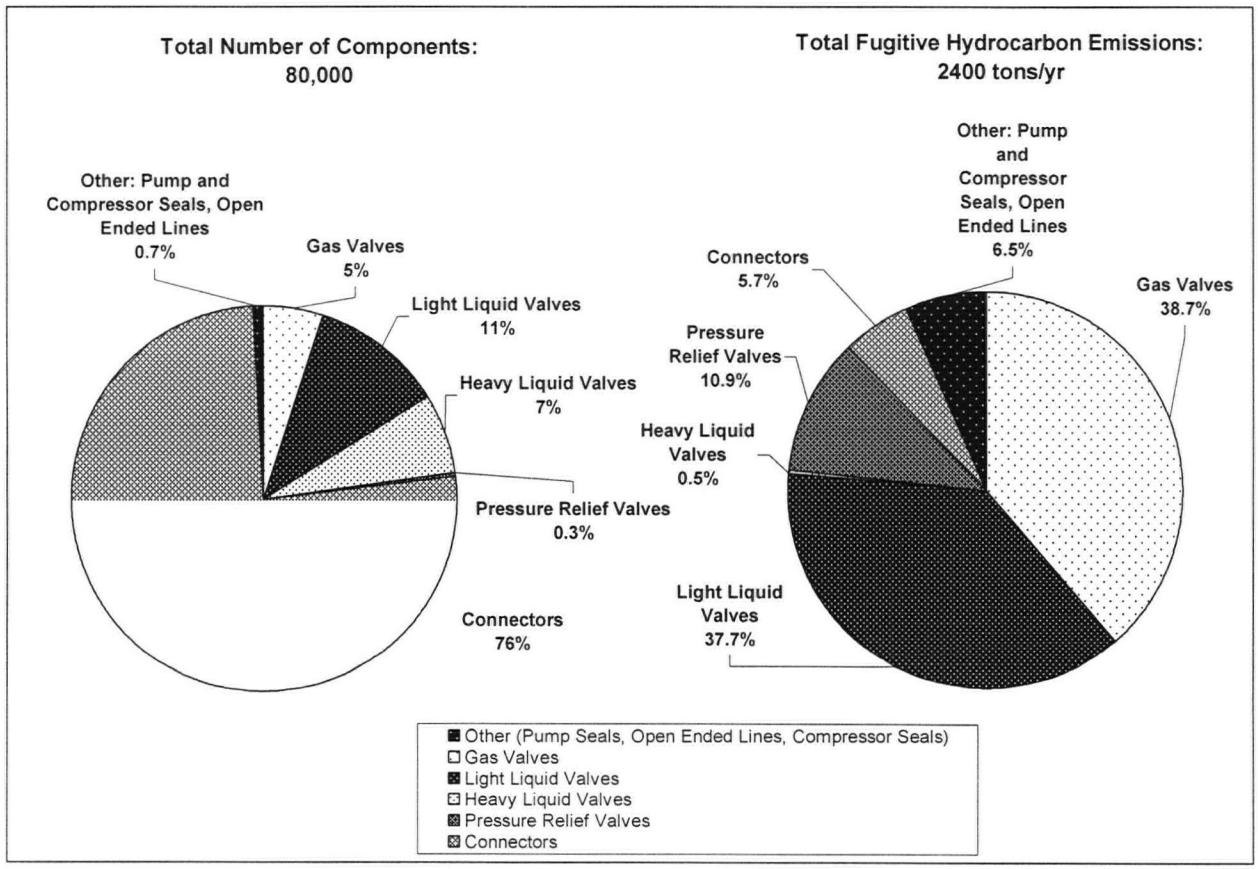

Figure 1.1: Typical medium capacity refinery fugitive emission source distribution and fugitive emission distribution (adapted from Allen and Rosselot, 1994).

Regulatory bodies such as Environment Canada, the US EPA and European regulatory agencies recognize that leaks from process equipment contribute to the release of toxic, carcinogenic and

other harmful chemicals to the environment. Regulatory requirements have evolved in Canada, the US and Europe to require that certain industries such as petroleum refining and chemical processing report chemical releases to the environment. The US EPA reports the Toxic Release Inventory (TRI), which indicates the cumulative annual release of toxic chemicals by all reporting plants throughout the country. Various methods of determining the chemical emissions are utilized and are carried out as part of Leak Detection and Repair (LDAR) programs. LDAR programs are used to manage fugitive emissions from valves and other process equipment and to provide a database of information for monitoring and reporting purposes. These programs require monitoring and reporting of leaks and the subsequent repair of any leaking equipment according to jurisdictional regulation.

1.1.1 Classification of Pollutants

Of all valve fugitive emissions, volatile organic compounds (VOC's) and hydrocarbons (HC's) are generally of the greatest concern. However, pollutants released from a process into the environment are classified into three groupings that correspond to the major categories of the US EPA. They are:

- Criteria Air Pollutants
- Toxic Chemicals
- Hazardous Chemicals

The US EPA has set National Ambient Air Quality Standards (NAAQS) through the Clean Air Act for six major pollutants called *criteria pollutants*. They consist of particulate matter (PM_{10}), sulfur dioxide (SO_2), nitrogen oxides (NO_x), carbon monoxide (CO), ozone (O_3), and lead (Pb). Volatile organic compounds and hydrocarbons are not included in this category but can add to a plant's overall contribution to criteria pollutants through photochemical reactions with ultra-

violet light from the sun. The VOC's and HC's are broken down into radicals (hydroxyl, organic, and peroxy radicals) that then react with NO to form NO_2. NO_2 formation increases the equilibrium concentration of O_3 through the photo stationary state relationship, according to the following relationship:

$$[O_3] = K_{eq} \frac{[NO_2][h\nu]}{[NO]}, \qquad \textit{(1-1)}$$

where K_{eq}, is the equilibrium constant; $[O_3]$, $[NO_2]$, $[NO]$, are equilibrium concentrations; and $[h\nu]$ is the photon light energy available (dependent upon the light wavelength or frequency).

Toxic chemicals are classified by the perceived risk to human health and environmental impact. Over 600 chemicals and chemical categories are reported in the Toxic Chemical Release Inventory (TRI) of the US EPA. Many of these chemicals are HC's and VOC's.

Hazardous wastes are defined in the Resource Conservation and Recovery Act (RCRA) as any waste that, "(1) exhibits greater than threshold properties of ignitability, corrosivity, reactivity, or toxicity, or (2) is specifically listed as hazardous by compound or by the generating process or industry". These wastes require "cradle to grave" management once identified. This will increase the cost associated with all phases of the life-cycle of these compounds. Certain VOC's may also be classified as hazardous wastes.

Regulatory requirements, with regards to emission levels, are dependent upon their classification status therefore PPMV concentration limits vary accordingly. Table 1.1 lists several chemical compounds of major concern due to their large estimated levels of release to the atmosphere. In order to reduce levels such as those listed, fugitive emission regulations are becoming more stringent. Long-term objectives in Europe are to reduce leaks to near zero levels for hazardous chemicals and to make substantial reductions for other chemicals. Newly developing regulations

for fugitive emissions in Europe may require in-line emission concentrations of 1 ppmv for hazardous materials (ISO / WD-15848-1.6, 2000). Subsequently, development of new equipment technology that can meet such stringent emission levels will be needed. As well, improved implementation of LDAR programs will be necessary to monitor and report that these regulations are being met.

1.1.2 Estimating Fugitive Emission Levels

There are several methods approved by the US EPA for estimating fugitive emissions. Emission factors are given for Refinery processes and the Synthetic Organic Chemical Manufacturing Industry (SOCMI) and factors have been developed to correspond to specific sources depending on volatility, such as gas service, light liquid service, heavy liquid service, hydrogen gas service, etc. Allen and Rosselot (1997) provide and in depth review of these methods and they are briefly summarized in Table 1.2.

These methods provide a means of reporting, however, their accuracy is limited and they are not capable of accounting for large numbers of small leaks. In addition, for leak sources too small to measure with an organic vapour analyzer (OVA), a default-zero emission rate is used, where the default rate for valves in refinery gas service is:

$$E = 6.56 \times 10^{-7} \text{ kg/hr/source,} \qquad \textbf{(1-2)}$$

where: E = the leak rate correlation (kg/hr/source)

The use of equation *1-2*, implies that there is a need for a technology that can measure and contain leakages that fall below the default-zero emission rates.

Estimation Method	Description of Method and Emission Factors	Estimating Equations	Comments
Average emission factor method:	The number of fugitive emission sources is counted and an average factor is applied to each of these sources and summed. ***The average emission factor for a refinery valve in hydrocarbon gas service is:*** ***f_{av}=0.027 kg/hr/source***	$E = m_{voc} * f_{av}$ *where: E = the emission rate (mass/unit time)* *m_{voc} = mass fraction of VOC in the process stream* *f_{av} = average emission factor (kg/hr/source)*	This method is considered the least accurate.
Leak/No Leak emission factor method:	Utilisation of an OVA (API Method 21) detects the VOC concentration, which is to be compared to the regulatory requirement. Generally, if the leakage rate is above 10,000 ppmv, then the valve is considered leaking and given a leak emission factor. If the concentration is below 10,000 ppmv then the No Leakage emission factor is applied. ***The average emission factor for a refinery valve in hydrocarbon gas service is:*** ***F_L=0.2626 kg/hr/source*** ***F_{NL}=0.0006 kg/hr/source***	$E = m_{voc} * f_{av}$ *where: E = the emission rate (mass/unit time)* *m_{voc} = mass fraction of VOC in the process stream* *f_L or f_{NL} = appropriate Leak or No Leak factor (kg/hr/source)*	The 10,000 ppmv corresponding leakage rate is the level at which repair of the valve is considered economical. Plants with small numbers of fugitive emission sources greater than 10,000 ppmv will obtain lower estimates of overall fugitive emissions than the previous method.
Emission correlation as a continuous function of VOC screening concentration:	Emission rates are given as a function of the OVA concentration determined in the field (API Method 21). ***The leakage rate is given in the next column for refinery valves in hydrocarbon gas service.*** For leakage rates too small to detect with an OVA, a default leakage rate is used, ***where the default rate for refinery gas service is:*** ***6.56×10^{-7} kg/hr/source***	$E = 2.18 \times 10^{-7} C^{1.23}$ *where: E = the leak rate correlation (kg/hr/source)* *C = OVA screening concentration (ppmv)*	This is considered more accurate since the actual emission concentration is measured. For sources too small to measure with an OVA a default-zero emission rate is used.
Bagging method:	An EPA approved, unreactive bag is place over the fugitive emission source and the emission rate is measured directly by a mass flow controller and concentration is measured by a detector. Statistical techniques are used to determine the number of sources that need to be measured in order to calculate the overall system fugitive emission rate. Typically metal foil or Mylar bags are used.	Mass Flow Controller actually measures the flow of leaking gas.	This method provides visual proof since the bag fills with emission gas. This method is time consuming and therefore expensive.

Table 1.2: Summary of fugitive emission estimation methods approved by the US EPA (summarized from Allen and Rosselot, 1997).

1.2 Motivation

There are two general methods in which fugitive emission reductions can occur.

- Development and implementation of improved technology
- Improved management (LDAR) of fugitive emission sources (i.e. asset management)

New regulations in Europe (ISO / WD-15848-1.6, 2000) propose that emission limits do not exceed 1 ppmv in ambient air for certain toxic and carcinogenic air pollutants, 20 ppmv for mutagene/carcinogenic media and up to 100 ppmv for standard hydrocarbons. These are much more stringent than the typical 500 ppmv US EPA general requirement for hazardous substance release into the atmosphere. This has lead to new developments in valve sealing technology such as improved packing, the use of bellows seals, and live loading systems, and proposed improvements in LDAR techniques (Seigell, 1999; Dubois, 1997).

In addition, reduced leakage could potentially be built into the design of piping systems by reducing the overall number of valves that can potentially leak and that require maintenance. However, large numbers of valves are required in the process for control and isolation purposes. Enhanced LDAR of these valves will be necessary and therefore it is anticipated that new technologies for monitoring and control of fugitive emissions will potentially be viable in the market place.

Currently the US Clean Air Act (40 CFR, Part 60) requires that refineries implement LDAR programs to monitor fugitive emissions. Minimum requirements dictate that emissions be reported annually. However, in cases where leaks are more frequent then reporting must be carried out quarterly (in the US, if the population of leaking valves at a given process system,

exceeds 2% of the total population of valves in the system, then more frequent, quarterly, reporting becomes necessary).

Current technology for leak detection and LDAR is labor intensive, expensive, does not contain leaks when they occur, and reduces the flexibility of maintenance scheduling since the task can take up so much of the maintenance resource available. Muller (2000) estimates the cost of valve leak detection to be 35 – 65 GBP (Great Britain Pound) per valve per measurement. This cost may be a contributing factor as to why fugitive gas emissions are typically underestimated. In the United States, it has been calculated that about 80 million pounds per year of VOC fugitive emissions go unreported (Garing, 1999). Leak control consists of changing valve packing, or tightening gland packing once leaks are detected. This approach may cause process control difficulties due to increased friction between control valve stems and the packing leading to increase control valve hysteresis (Langford et al., 2000). However, implementing LDAR techniques and systematically monitoring and controlling valve leakage performance may be less costly due to long term reduction in valve maintenance and reduction in lost product. A 380% - 400% return on investment over a yearly period was found at two South African synthetic fuel plants (Muller, 2000) after implementing new LDAR programs.

1.2.1 Long Term Sensor Development

It is believed that further reductions in fugitive emission limits through improvements in valve sealing technology and LDAR management techniques, will lead to the need for improved monitoring and control techniques for very small leakage rates. The current study is a direct result of emerging regulatory developments and is funded with the aim of determining the technical feasibility of a new monitoring and control technology for fugitive emissions. Much of

the discussion will also be applicable to the containment of fugitive emissions from other process equipment, however, valve stem fugitive emissions are of particular interest.

The potential of a combined metal oxide/adsorbent system is being researched to determine the feasibility of the technology to achieve the sensing and adsorption requirements of typical default valve leakage rates (indicated in Table 1.2 and by equation *1-2*). If deemed feasible, further development of a prototype will have to be carried out and tested. Integration of a management strategy involving LDAR techniques would also have to be developed in order to manage the sensors, regenerate adsorbent, and carry out any valve refurbishment requirements. Cost models should be developed at the prototypical stage to compare costs of the new sensor type with current LDAR cost and compared to any benefit obtained.

In practice, a metal oxide/adsorbent system would be housed in a containment or reaction chamber attached to the valve at a location above the packing and surrounding the valve stem (refer to Figure 1.2). The containment chamber would need to be designed so that it could be retrofit onto existing valves. It is currently conceptualized that a monitoring technician could use a hand held multi-meter (electrical metering device) to check the signal from the leak detector leads. Further automation would be possible where valves utilise smart positioners and controllers. Conceptually, the fugitive emission device could be wired into the current controls to give a signal to operators or maintenance staff.

Design criteria such as sensor repeatability, and robustness should also be carefully studied in the development of a prototype. The influence of O_2, CO_2, H_2O, and other contaminants from the ambient environment or as components in the process could have significant impacts on the conductivity of the system and hence the overall stability, repeatability and robustness of any sensor of this type.

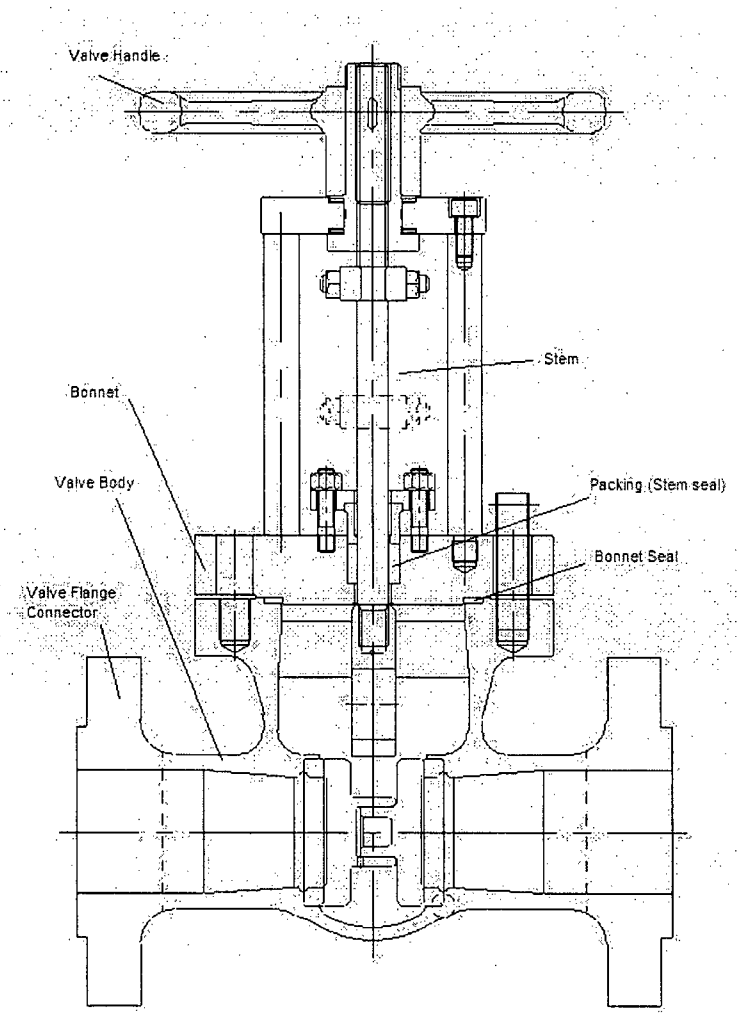

Figure 1.2: X-section of a sliding stem gate valve. Typical valve fugitive emissions result from packing wear with the stem of the valve.

1.3 Objective of the Present Study

The objective of the present study is to determine the effectiveness of metal oxides and adsorbents for the purpose of removing targeted chemical compounds from a flow stream and sensing their uptake. The chosen adsorbent / metal oxide system must be selected such that the metal oxide's electrical conductivity changes when exposed to the emission gas while simultaneously adsorbing the target chemical from the gas stream under ideal conditions.

Chapter 2 - Literature Review

The concept of a combined adsorbent / metal oxide bed for use as a containment and sensing device is novel. There are large amounts of information reported on the development of gas sensing devices from metal oxides and in particular SnO_2. However, there is very little indicating that any work is being carried out investigating the use of both adsorbents and metal oxides in the context of the present study. Reaction mechanisms for catalysts and for metal oxide sensing generally seem to be more sensitive at higher temperatures, unsuitable for adsorbents. Hence adsorption on porous media and gas sensing via metal oxides tend not to be discussed simultaneously.

Presently, elements from literature and theory in the respective areas of adsorption and metal oxide sensing, as applicable to the present study and potential future work, will be reviewed. As well, a review of other "comparable" technologies under development to achieve similar goals in emission prevention and detection or air pollution control will be reviewed.

2.1 Emerging Emission Prevention and Detection

Valve technology and maintenance practices have improved with the use of new stem sealing technology, the use of bursting discs immediately upstream of pressure relief valves and by effective implementation of LDAR programs, as discussed in the previous chapter.

Sealing technology around the shafts of centrifugal pumps to prevent emissions has been in use since the 1950's. Significant developments have been made in the area of mechanical seals for pumps, compressors and bearings of other rotating equipment, along with industry guidelines on implementation of the technology. Advancement in regulations such as the Clean Air Act in the 1970's and its amendments in 1990 have forced mechanical seal developers to improve designs

and plant operators to utilize the best available technology (BAT) and maintain equipment more effectively. Guidelines by the Society of Tribologists and Lubrication Engineers (STLE) have helped manufacturers and operators design and operate mechanical sealing systems capable of meeting targets as low as 50 ppmv in air of emissions on higher specific gravity fluids (Bowden, 1999).

Methods of "open path monitoring" (OPM) such as optical and laser sensing have been field tested and can be used to detect leaks on a plant wide scale or for specific unit operations (Frish and Melnyk, 1996). This technology generates and propagates specific wavelengths of light to a retroreflector. Certain hazardous gases will absorb in the infrared (IR) and ultraviolet (UV) light ranges and hence, a spectral analysis of the reflected light signal will indicate the presence and concentration of certain gases. Chemical Engineering Progress (1993) reports that an optical imaging device was capable of detecting fugitive emission sources from pumps, valves, and flanges for leaks greater than 1 g/h for olefins, in the light wavelength of 9 – 11 μm and that development of the sensor for aliphatic and aromatic compounds are underway. These systems do not quantify equipment leaks and Hashmonay and Yost (1999) combined optical remote sensing with computed tomography (CT), based on micro-meteorological conditions, to estimate the emission flux from the source.

Farrauto and Heck (2000) reviewed a number of studies in the area of environmental catalysis. Catalytic sensors being developed for the automotive industry for on board diagnostics (OBD) are utilized to control the air-fuel ratio based on feedback of O_2 in the exhaust train. These three way catalysts (TWC) also help control hydrocarbon and NO_x levels in the exhaust by optimizing the air-fuel ratio. Miyoshi et al. (1995), report the use of an alkali-earth metal oxide (BaO), incorporated into a TWC, which stores NO_x produced during lean operating periods. The air-to-fuel ratio is forced rich periodically at which time the stored NO_x is reduced on the TWC. It is

reported that complete regeneration is possible in systems with low sulphur content fuel (low catalyst poison) operating at temperatures above 650 °C. This temperature is above the likely operating envelope for fugitive emission capture in industry but may provide clues as to catalytic conversion strategies for fugitive emissions (i.e. high temperature and pure components may be necessary for optimum catalyst/metal oxide activity).

Passive catalytic conversion, requiring little or no control such as heating or gas composition manipulation, is also of interest. Catalysts applied to radiator surfaces have been shown to reduce ambient air ozone levels. In a proprietary technology (PremAir©) a catalytic material is placed on either a mobile or stationary radiator which converts ground level ozone passively to oxygen. Greger et al. (1998) report 95% ozone destruction in tests carried out on automobile radiators in the field. Wu and Kelley (1998) indicate that this technology can also be used to convert other pollutants such as NO_x and HC's. Tests between 25 - 105°C, and varying humidity showed that CO and C_3H_6 could be removed from the air stream and that the conversion efficiency was dependent on catalyst formulation, but more strongly dependent upon catalyst temperature and was suppressed by the presence of H_20. Increased catalyst loading from 2.48 g/l to 4.52 g/l Pt/Al_2O_3 improved C_3H_6 removal from 34 to 48% at 100°C and the addition of 1.3% water vapour decreased efficiency in the temperature range of 30 – 100°C from 24 – 48% to 6 – 26%.

In a separate article, Wu and Kelley (1998) also indicate that for a Pt/Ni catalyst, C_3H_6 converts preferentially over CO but that the presence of CO also inhibits the conversion efficiency of the C_3H_6 between 40 – 80°C. The presence of H_2O suppressed C_3H_6 conversion efficiency by 15 – 20% over the full temperature range. These results are indicative of the challenge of obtaining the desired catalyst activity and selectivity in conditions where water vapour or trace elements of

catalyst poisons are present, especially for lower temperature applications. These issues are also important for metal oxide sensitivity to target gases.

Passive photocatalytic conversion has been reported to reduce atmospheric hydrocarbon levels. Windows of skyscrapers, traffic lights, road sign reflectors, and a host of reflective or sunlight exposed objects can be utilized for hydrocarbon adsorption and subsequent decomposition to carbon dioxide and water passively (Hermann, 1998). This technology may not be feasible for direct fugitive emission reduction, but demonstrates other areas of research with similar goals of reducing ground level air pollution that may be used in a holistic approach to the problem, particularly in densely populated urban areas.

The development of a reactor trap that could utilize a catalyst to oxidise hydrocarbons stoichiometrically to form environmentally harmless products such as carbon oxides and water, is perhaps the most interesting for the reduction of fugitive emissions. Yang and Kung (1994) report the catalytic conversion of toluene, C_3H_6 and C_3H_8 by this method. In this study a gas stream test pulse, composed of 0.01 mol of C_3H_6 and 0.025 mol of O_2, was reacted with 0.20 g of mixed oxide (Cr-Co-Fe-Al). The test pulse was carried in a helium gas stream with either 0% or 2% water vapour to the reactor with a carrier flow rate of 30 mL/min. The results indicate C_3H_6 conversion efficiencies of greater than 90% where no water vapour was present at 25 ^{o}C. However, temperatures of approximately 200 ^{o}C were required to reach the same level of C_3H_6 removal in the presence of 2% water vapour, indicating both the potential for hydrocarbon removal and the inhibition of the hydrocarbon conversion efficiency in the presence of the water vapour at lower temperatures.

In the same study a gas stream test pulse composed of 0.2% of toluene, C_3H_6 or C_3H_8, 0.6% O_2, 0% or 2% CO was used. The test pulse was carried in a helium gas stream with either 0%, 2%,

or 10% water vapour, to a reactor with 0.070g of metal oxide comprised of a 1:1:1:1 atomic ratio of Cr:Co:Fe:Al, with a corresponding space velocity of 30,000 h^{-1}. The temperature of the system was increased at a rate of 150 °C/min. The results, with 10% water vapour and 2% CO, indicate hydrocarbon conversion efficiencies of up to 92%, 78% and 56% for toluene, C_3H_6 and C_3H_8 respectively and also indicates the diminishing reactivity of each species. It is reported that increasing the CO content did not effect the conversion, whereas additional water content from 2% to 10% caused the C_3H_6 conversion to drop from 84% to 78%. The trap also utilized a ZSM-5 adsorbent bed immediately upstream of the metal oxide reactor, the function of which was to trap the hydrocarbon until such time as the temperature in the system increased, allowing desorption of the target gas to the heated metal oxide catalyst bed. When the adsorbent trap was not used the conversion of C_3H_6 dropped from 78 to 44%. The results were repeated for 10 cycles of temperature ramp and regeneration showing no sign of loss of activity. This study shows that passive or active removal of hydrocarbons by catalytic conversion is potentially viable. However, to become more efficient, metal oxides active at lower temperatures should be developed along with adsorbents that can effectively trap hydrocarbons at higher temperatures. This study reinforces the effect of metal oxide contamination by water which reduces its activity and which is an important issue for the development of metal oxide sensors.

Ceramic honeycomb type catalytic reactors are also thought to have great potential for the selective catalytic reduction (SCR) of NO_x and the combustion of hydrocarbons in stationary and mobile sources (Jiang et al., 2003; Kikuchi et al., 2003; Williams, 2001). These monolith type reactors provide high surface area per unit volume due to the existence of thin walls (0.051 – 0.27 mm thick) and a large number of cells per unit area (up to 186 cells/cm^2). They also exhibit low pressure drop at high flow rates, high mechanical strength, and very good thermal and mechanical shock resistance. However ceramic honeycomb reactors typically exhibit laminar

flow regimes and hence low interphase heat/mass transfer rates and suppressed radial mixing. Wire mesh honeycomb (WMH) reactors, constructed of alternating sheets of corrugated and flat wire mesh can improve heat/mass transfer. In the WMH, the wire mesh is coated with a layer of Al_2O_3 particles and sintered to form a porous layer around the mesh. Jiang et al., 2003 utilise a WMH prepared by deposition of Pt on TiO_2 by washcoating and indicate that radial heat/mass transfer effects were improved. Honeycomb reactors can readily be produced utilizing Pd doped SnO_2 and Al_2O_3 (Kikuchi et al., 2003). In addition, activated carbon coated ceramic monoliths have potential for a wide variety of applications including control of VOC emissions (Williams, 2001). Zeolites can be extruded or coated on metal or ceramic substrates by preparation of a zeolite slurry with a binder (colloidal silica or alumina), dipping the monolith and then drying and firing (Williams, 2001).

In a system that combines adsorption and adsorption monitoring, Staudt et al. (1999) report the use of impedance spectroscopic measurements to predict the adsorption equilibria for a number of test gases and to compare the experimental mass adsorbed to that predicted. It is shown that if an adsorbent is placed between the plates of a capacitor, the electric capacitance of the system will change as gas is adsorbed in the system. Calibration of the impedance spectra of a given adsorbent / adsorbate system can provide the parameters necessary to model the change in capacitance (frequency dependent) to the uptake by the adsorbent. The results indicate that the sensitivity of the technique was improved for polar adsorbates over non-polar and for strongly adsorbed gases and show very good agreement between the experimentally measured (via TCD) and the predicted values of mass uptake using both polar (CO, CO_2, H_2S) and non-polar gases (N_2, CH_4) on activated carbon (AC-20) and molecular sieve (MS-5A). Experimental uptakes for CO and CO_2 on 13X molecular sieve measured 5.019 and 52.455 mg/g and compared closely to the impedance predicted uptake of 4.656 and 49.291 mg/g, respectively. Impedance

spectroscopy is typically used for adsorbent characterization studies since capacitance is very sensitive to changes in dipole moment that occur during an adsorption process, however, this study also discusses the possibility of utilizing the method for on-line monitoring of adsorption or regeneration processes and is thus similar to the dual containment and monitoring concept of the present study.

2.2 Adsorbents and Adsorption for Target Gas Containment

Mantell (1951) tells of a Sanskrit manuscript written about 200 BC which states: "It is good to keep water in copper vessels, to expose it to sunlight, and filter it through charcoal." In the 1700's adsorbents were used to remove the colour from sugar and during World War I, gas masks utilizing charcoal adsorbents were put into use to protect against chemical warfare. By the late 1950's a wide variety of adsorbent processes were in use for various separation and purification processes, including hydrocarbon separation, air dehydration, water filtration, and solvent recovery. The discovery of zeolitic materials in 1959, allowed adsorption processes to become much more selective and in the last 20 years the study of adsorbents has become increasingly important to engineering practice as a result of environmental awareness and the drive for ultra-purification of components (Yang, 2003). Air separation, hydrogen purification and storage, methane storage, olefin/paraffin separation, nitrogen/methane separation, desulfurization of transportation fuels, removal of aromatics from fuels, NO_x removal, odour removal and dessicants are several specific areas of modern adsorbent application and hence a large number of adsorbents are available for use. In a combined adsorbent / metal oxide bed the adsorbent's purpose is to contain the target gas passing through the bed (i.e.: a fugitive emission HC or VOC from a valve stem or other process equipment).

2.2.1 Theoretical Basis for Adsorption in a Packed Bed

A packed bed generally consists of a cylindrical column containing one or more granular components for adsorption. As gas flows through the bed, it passes around the adsorbent grains, diffusing into its pores which then preferentially adsorb the gas onto its surface.

Mantell (1951) describes the process as one that takes place at the surface of the adsorbent where the solid and gas come into contact with each other. The net forces present in holding a solid together are unbalanced and tend to create an inward pull on molecules within the solid (the inward pull is greater than the outward force), hence the solid exhibits surface tension. A gas phase in contact with the solid is adsorbed on solid surfaces by the saturation of the unsatisfied forces of the surface atoms by the forces of the gas molecule striking its surface, and hence the surface tension of the solid is diminished. Adsorption is a spontaneous occurrence resulting in a decrease in the free energy of the system and generally occurs via a weak physical attraction known as physisorption or a strong chemical attraction known as chemisorption.

For adsorption to occur an adsorbate must come into contact with an adsorption site on the surface of the porous media, and overcome resistance due to mass transfer effects. Hence, the rate of adsorption depends on the kinetics of the system as follows:

- mass transfer resistances across the fluid boundary to the adsorbent grain,
- mass transfer into the pores of the adsorbent,
- internal microporous mass transfer and,
- intrinsic adsorption surface kinetics.

In designing an adsorption system, it is desireable to maximise the rate of adsorption by reducing adsorbent particle size.

When a gas flows through a packed adsorbent bed, its concentration wave front or mass transfer zone (MTZ) can be affected by dispersive forces. These forces are due to concentration and velocity differences of the fluid within and along the bed causing axial mixing to occur. Such mixing is undesireable since it reduces the efficiency of separation (Ruthven, 1984) and can increase the length of unuseable bed (LUB), approximately ½ the length of the mass transfer zone (Yang, 2003), hence it is a design objective to minimize this effect.

When adsorption occurs in a packed bed, the concentration of the gas is a function of the location in the bed, the concentration of gas at that point and the rate of adsorption. Adsorption in a packed bed, including the effects of axial mixing, can be described by the axially dispersed plug flow model given by the following differential equation (Ruthven, 1984), obtained from a mass balance across an element in the bed:

$$-D_L \frac{\partial^2 c}{\partial z^2} + \frac{\partial}{\partial z}(vc) + \frac{\partial c}{\partial t} + \left(\frac{1-\varepsilon_b}{\varepsilon_b}\right)\frac{\partial \overline{q}}{\partial t} = 0 \qquad \textit{(2-1)}$$

where D_L is the effective axial dispersion coefficient, v is the interstitial velocity, c is the adsorbate concentration, ε_b is the bed voidage and $\overline{q}$ is the adsorbate concentration averaged over the crystal and pellet, z is the distance down the length of the column and t is time. Solutions of equation *2-1* can be found in Ruthven, 1984 and will be used in the present study as further discussed in Chapter 3 and 5. Radial dispersion is not accounted for in equation *2-1*, but is assumed to be present such that the radial concentration of adsorbate remains constant.

2.2.2 Adsorption Equilibrium Isotherm

The amount of target gas contained by an adsorbent material at equilibrium (or the equilibrium uptake capacity) is found from the equilibrium isotherm and is the main factor in adsorbent

selection (Yang, 2003).

Physisorption on a uniform surface at low concentration follows Henry's Law. Therefore the equilibrium relationship will be linear between the fluid phase concentration, c, and the adsorbed phase concentration, q, where the constant of proportionality is called the Henry's constant, K, generally expressed as mole/mole or volume/volume adsorbate to adsorbent as follows:

$$q^* = Kc, \qquad \textit{(2-2a)}$$

where q and c are expressed as molecules or moles per unit volume or mass. Henry's constant is a relative measure of the adsorbent's uptake and is the fundamental parameter of interest for adsorbent selection for low concentration adsorbates.

A power law, the Freundlich Isotherm, can also be used as follows:

$$q^* = k_F c^{1/n}, \qquad \textit{(2-2b)}$$

where k_F is a constant, and $n > 1$. If n = 1 the Freundlich isotherm equates to Henry's law.

At higher partial pressures (or gas concentration), uptake continues only slightly until it becomes almost independent of the pressure. Adsorption isotherms of this type are called Langmuir Isotherms, since they follow the classic adsorption mechanism postulated by Irving Langmuir in 1915:

$$\frac{q}{q_m} = \frac{BP}{1 + BP} \qquad \textit{(2-3)}$$

where B is called the Langmuir constant and q_m is the adsorbed phase concentration at saturation (assumed to be a monolayer).

At low partial pressure, P (or concentration), the Langmuir isotherm reduces to the linear Henry's law form of equation *2-2a,* as illustrated in Figure 2.1. Each point on the isotherm (for a given temperature) represents a concentration for which the adsorbent/adsorbate system is in equilibrium.

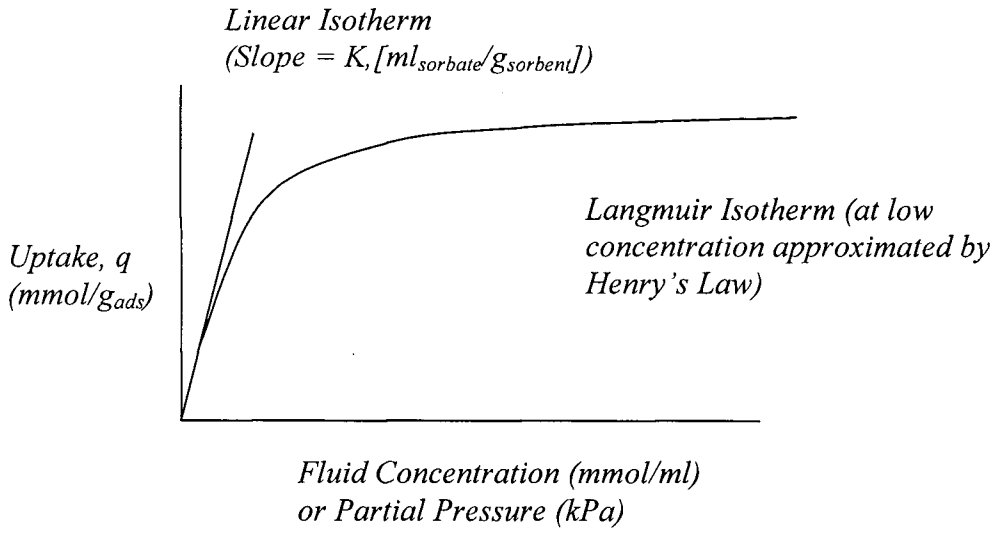

Figure 2.1: Langmuir and Linear Equilibrium Isotherms

2.2.3 Heat of Adsorption, $-\Delta H_{ads}$

Isotherms obtained at different temperatures can be used to determine the heat of adsorption, $-\Delta H_{ads}$. The heat of adsorption generally varies as a function of the adsorption uptake. Therefore, the isoteric heat of adsorption is determined from the Clausius-Clapeyron equation at constant adsorption uptake:

$$\left.\frac{d\ln p}{d\ln(1/T)}\right|_{q^*=const} = \frac{-\Delta H_{ads}}{R}, \qquad \textbf{(2-4a)}$$

At low concentration of adsorbate, in the Henry's law region, and hence for low adsorption uptake, the vant Hoff correlation can be used to determine $-\Delta H_{ads}$ from equation *2-4b*:

$$K = K_o exp(-\Delta H_{ads}/RT), \qquad \textbf{(2-4b)}$$

Where K is the Henry's constant, K_o is the pre-exponential factor, $-\Delta H_{ads}$ is the heat of adsorption obtained from the slope of the plot of ln K vs $1/T$, R is the gas constant, and T is the absolute temperature. As temperature increases, K decreases exponentially.

Adsorption uptake decreases with a rise in temperature and occurs with the evolution of heat. It is therefore an exothermic process where the heat of adsorption, $-\Delta H_{ads}$, is defined as the decrease in the heat content of the system as given by the Gibbs energy which must be negative for significant amounts of adsorption to occur spontaneously (Ruthven, 1984):

$$dG = dH - TdS, \qquad \textbf{(2-4c)}$$

$$dG - dH + TdS = 0$$

$$dS = S_{ads} - S_{gas}$$

Entropy, S_{ads} (adsorbed phase) is always less than S_{gas} (gas phase) and therefore dH must be negative.

The amount of heat evolved in the process is related to the types of forces involved in the adsorption process and can be used to distinguish between physisorption ($1^1/_2$ to 3 times the latent heat of vapourisation) and chemisorption (of the same order of magnitude as the heats of chemical reaction). Hence, $-\Delta H_{ads}$ gives a measure of the strength of the bonding between the adsorbate and the adsorbent surface.

2.2.4 Adsorbent Design/Characterisation

For physical adsorption, the microporous adsorbent/adsorbate interaction potential is dependent upon dispersion-repulsion interactions (van der Waals forces), and electrostatic interactions. Van der Waals forces are dependent upon the relative size and polarization of both the adsorbent and adsorbate atoms. The electrostatic forces result in ionic adsorbents such as zeolites where there is an electric field in the region of the surface and polarization, field-dipole, and field gradient-quadrapole interactions occur (refer to Ruthven, 1984 and Yang, 2003).

Interaction energies are considered pair wise additive (Yang, 2003) and increase when the adsorbate molecule can interact with many adsorbent molecules. They are enhanced further when the adsorbate is between two surfaces (i.e. in a pore), and are dependent upon the geometry of the pore, with a spherical pore providing more interaction potential than a slit-shaped or cylindrical pore, due to the increasing amount of surface atoms available to interact with the adsorbate molecule.

Commercially available adsorbents must be prepared and formed into macroporous pellets with suitable dimensions, porosity and mechanical strength. As previously discussed the mass transfer resistance should be minimized in both the macropores and the micropores for optimal adsorption rates. This requires small crystal sizes to reduce microporous resistance, however, since macropore size is also affected by crystal size, it should not be made too small (Ruthven, 1984). Gross grain size reduction would also reduce macroporous mass transfer resistance, but this is limited by the pressure drop across the bed (increasing inversely with grain diameter). In addition, the surface area of the grains is prepared to provide the maximum amount of surface on which adsorption can occur. Table 2.1 summarises typical geometric properties of some important commercial adsorbents.

Table 2.1: Typical properties of commercial adsorbents (Basmadjian, 1997)

	Densities, g/cm3		Diameter		
Adsorbent	**Bulk**	**Particle**	**Particle (mm)**	**Pore (*Angstrom*)**	**Surface Area (m^2/g)**
Activated Carbon	0.44 – 0.48	0.75 – 0.85	1 - 5	15 - 20	950 – 1250
Activated Alumina	0.60 – 0.85	1.2 – 1.4	2 – 12	25 – 50	250 – 350
Silica Gel	0.40 – 0.75	1.2	1 – 7	20 – 140	350 – 700
Zeolites	0.60 – 0.70	1.0 – 1.7	1 – 5	4 - 10	-

New adsorbents and their isotherms can be designed and modeled based on interaction potential energies between the adsorbent/adsorbate and also on the structure and geometry of the adsorbent (Yang, 2003), however, results based upon the equilibrium isotherm are still required to confirm the properties in real systems due to the large number of variables interacting in the process. Design of adsorbents is not within the current scope, however a number of equilibrium isotherms reported in the literature will be reviewed to compare uptakes of certain adsorbents within the context of the present study.

2.2.5 Adsorbents for HC and VOC Recovery / Separation

Gas adsorption studies on porous media are well established. For example, hydrocarbon uptakes on various zeolites, silica-alumina, silica gel and activated carbons are reported in the literature, and summarized in Table 2.2.

Grande et al. (2002) report equilibrium and kinetic results for propane and propylene adsorption in commercial pellets and crystals of 5A zeolite in the temperature range 323-423 K. The pellet adsorption loading measured by gravimetry was 1.7 mmol/g for propylene and 1.3 mmol/g for propane at 100 kPa and 423 K. The selectivity for propylene over propane increases with temperature and with lower pressure.

Table 2.2: Summary of adsorbent equilibrium capacity, $-\Delta H_{ads}$ and calculated sensor bed life based upon 100g of adsorbent and the default valve fugitive emission rate (6.6×10^{-7} kg/hr).

Adsorbent	Sorb-ate	Temp °C	Uptake* mmol/g	Bed Life** days	$-\Delta H_{ads}$ (kJ/mol)	Reference
13X zeolite	C_2H_4	22	5	884	35.2	Rege et al., 2000
		70	3	530		
	C_3H_6	200	1.0	265	42.5	Da Silva and Rodrigues, 1999
	C_3H_8	200	0.5	139	35.8	
4A zeolite	C_3H_6	200	0.8	212	29.9	
	C_3H_8	200	0.2	56		
5A zeolite	C_3H_6	50	2.4	636	47.5	Grande et al., 2002
		150	1.7	451		
	C_3H_8	50	2.3	639	39.5	
		150	1.3	361		
activated Al_2O_3 @ 5 kPa	C_3H_6	25	0.2	53		Jarvelin and Fair, 1993
	C_3H_8	25	0.1	28		
γ-Al_2O_3	C_2H_4	22	0.5	88	29.3	Rege et al., 2000
		70	0.2	35		
CuCl/γ- Al_2O_3	C_2H_4	25	0.72	127	49.0	Yang and Kikkinides, 1995
		60	0.48	85		
	C_3H_6	25	0.77	204	59.9	
	C_3H_8	60	0.52	144		
Clay support	C_2H_4	30	0.4	71		Choudary et al., 2002
Ag+ impregnated clay support (pi-complexation)	C_2H_4	30	1.17	207	56.5	
		60	0.85	150		
	C_3H_6	30	1.39	369	59.9	
		60	1	265		
carbon molecular sieve (CMS) 4A	C_3H_6	70	1.3	345		Grande et al., 2003
		150	0.9	239		
activated carbon (AC)	C_3H_6	25	5.2	1379		Jarvelin and Fair, 1993
	C_3H_8	25	4.5	1250		
narrow pore silica gel (NSG)	C_3H_6	30	2	530	36.5	Grande and Rodrigues, 2001
		70	1.1	292		
wide pore silica gel (WSG)	C_3H_6	30	0.7	186	29.5	
		70	0.35	93		

* Reported at 100 kPa. Refer to Equation *3-19* for calculation method.

** Refer to Equation 3-20 for calculation method.

Da Silva and Rodriques (1999) report propylene and propane single-adsorption equilibrium isotherms and mass-transfer kinetics over 13X and 4A zeolite pellets. The 13X zeolite shows a higher loading capacity, from 1.0 to 2.5 mmol/g and 0.5 to 2.0 mmol/g for propylene and propane respectively, between 473 K and 303 K and 100 kPa partial pressure. 13X also exhibits lower mass-transfer resistance while 4A zeolite shows the highest selectivity for propylene, however the loading is lower at 0.8 to 1.9 mmol/g for propylene and less than 0.2 mmol/g for propane under the same conditions as above. The isoteric heat of adsorption is reported at 35.8 and 42.5 kJ/mol for propane and propylene respectively on 13X zeolite and 29.9 kJ/mol for propylene on 4A zeolite. Mass transfer resistance in terms of reciprocal time constants range from $10^{-2} - 10^{-1}$ s^{-1} for propylene on 13X compared to $10^{-4} - 10^{-3}$ s^{-1} for propylene on 4A. Grande et al. conclude that though 4A has lower uptake and higher mass transfer resistance than 13X for propylene, its higher selectivity may make it more suitable for selective adsorption.

Grande and Rodriques (2001) have also measured adsorption equilibrium isotherms for propane and propylene on narrow pore silica gel (NSG) and wide pore silica gel (WSG) by gravimetry in the temperature range 303-343 K and at pressures up to 100 kPa. Both adsorbents have a high affinity for propylene. The loading at 303 K and 100 kPa of propylene is 2 and 0.7 mmol/g on NSG and WSG respectively. These loadings are 1.5 times higher than those for propane with both adsorbents.

Choudary et al. (2002) report equilibrium adsorption data for C_2H_4, C_2H_6, C_3H_6, and C_3H_8 measured on Ag^+ impregnated clay support. At 100 kPa and 303 K, ethylene and ethane adsorption capacities were 1.17 and 0.12 mmol/g respectively. Propylene and propane capacities were 1.39 and 0.30 mmol/g respectively. Data for the unimpregnated clay adsorbent indicate that alkene adsorption increased with the Ag^+ impregnation, due to the presence of Ag^+ ions for

π-complexation and that alkane adsorption decreased, corresponding to a reduction in the surface area.

Grande et al. (2003) report the equilibrium adsorption data for propane and propylene adsorption onto a carbon molecular sieve (CMS) 4A in the temperature range of 343 – 423 K and 100 – 300 kPa partial pressure. Uptake is reported at 0.9 mmol/g and 1.2 mmol/g for propane and propylene respectively. They conclude that micropore diffusion controls for both gases. Activation energies of adsorption reported were 33.7 kJ/mol for propane and 30.8 kJ/mol for propylene indicating that propane requires more energy to penetrate the pores.

Rege et al. (2000) studied γ-Al_2O_3, 13X molecular sieve, a natural zeolite (clinoptilolite), and its K^+ and Ca^{2+} ion exchanged forms for air purification pressure swing adsorption (PSA) and temperature swing adsorption (TSA) systems as well as cryogenic distillation systems for liquefied air. Such systems can be used for the purpose of removing trace amounts (a few ppm) of hydrocarbon (CH_4, C_2H_4, C_2H_6), CO and water vapour contaminants from the air prior to the main adsorption process. Golden et al. (1998) indicates that the adsorptive capacity of γ-Al_2O_3 can be improved by alkalizing it with a basic solution such as is formed from K_2CO_3. The natural clinoptilolites and their K^+ and Ca^{2+} ion exchanged forms have also shown potential for removal of CO_2 in PSA/TSA prepurification processes (Bulow et al., 1996). Nitrogen adsorption isotherms were measured and compared and showed that capacity for N_2 from greatest to smallest was for clinoptilolite > K^+ clinoptilolite > 13X zeolite > Ca^{2+} clinoptilolite > γ-Al_2O_3. High loading of N_2 will reduce the capacity of the adsorbent for uptake of impurities and hence Ca^{2+} clinoptilolite and γ-Al_2O_3 were good candidates for prepurification. For CO_2, 13X zeolite had the highest capacity and a steep isotherm making it appropriate for TSA systems. γ-Al_2O_3 had the lowest uptake, but its low slope makes it useful for the regeneration cycle of PSA

systems. Rege et al., also point out that the Ca^{2+} clinoptilolite has poor adsorption uptake at high partial pressures of CO_2, but has a very steep slope at low partial pressures of CO_2, and hence would be an ideal candidate for scavenging trace amounts of CO_2 at the product end of the PSA system. 13X also had superior capacity for water at high partial pressures (> 10^{-4} atm or 100 ppm), but γ-Al_2O_3 showed slightly higher uptake at low partial pressures. 13X had the best capacity for hydrocarbons (expected since 13X is in wide use for pretreatment in industrial units) approximately 5 and 3 mmol/g for ethylene at 295 K and 343 K respectively at 100 kPag. γ-Al_2O_3 uptake was approximately 0.5 and 0.2 mmol/g for the same conditions. Kinetics showed that the uptake of most of the impurities was fast. However CH_4 uptake on Ca^{2+} clinoptilolite was much slower, and hence could lead to a longer mass transfer zone and hence bed length requirement. 13X had the highest $-\Delta H_{ads}$ reported at 35.2 and 31.4 kJ/mol for ethylene and ethane respectively and γ-Al_2O_3 had a $-\Delta H_{ads}$ of 29.3 and 17.6 kJ/mol.

Jarvelin and Fair (1993) studied adsorptive separation of propylene and propane mixtures, comparing different zeolites, activated Al_2O_3, silica gel, and a coconut based activated carbon. Uptake on activated carbon was highest for both propane (4.5 mmol/g) and propylene (5.2 mmol/g) at 298 K and 100 kPa, but had poor selectivity. Activated alumina had very poor uptake for both propane (<0.1 mmol/g) and propylene (<0.2 mmol/g) at 298 K and 5 kPa at which point the isotherms' slope was very low.

The review of adsorbents above indicates that a number of different adsorbents or combinations thereof could be used to contain certain amounts of fugitive gas emissions and could be used in combination as a filtering layer to protect the bed from contaminants. The equilibrium uptake capacity will determine adsorbent volume required to meet annual release targets set by regulations. The $-\Delta H_{ads}$ is useful for evaluating the strength of the adsorption interaction and

hence the ease of regeneration of the adsorbent bed. Table 2.2 summarises some of the key data reviewed above and estimates the sensor life obtainable based on utilization of 100g of adsorbent to contain the default valve fugitive emission (equation *1-2*).

2.3 Metal Oxide Sensing

There are many types of gas sensors available for quantification of target gases. Park and Ackbar (2003) indicate that resistive type sensors based upon ceramic (metal) oxides such as SnO_2 are of particular interest in gas sensing due to low cost, wide range of applications and potential use as an electronic nose ("sniffer").

Watson et al. (1993) indicated that the catalytic pellister and the semi-conductor (metal oxide) type were the most common metal oxide based sensors in the market place. The former consists of a catalytic pellet produced onto a wire filament. Exothermic reactions on the catalytic pellet create temperature changes leading to changes in the electrical resistance of the wire. Ducso et al. (2003) carried out explosion proof detection of hydrocarbons between the lower and upper explosion limits with no protective encapsulation using a micopellister that contained finely dispersed catalysts of Pt, Pd or Rh.

SnO_2 sensors have typically been used for gas alarms in domestic and commercial facilities, for natural gas and methane leakages in oil refineries and mining operations, carbon monoxide detection in parking garages, for alcohol vapour in breathalysers, and in flue and other exhaust applications. Despite these applications, highly selective and sensitive SnO_2 sensors are generally not available and hence the metal oxide has attracted much attention in the area of research and development for gas sensing under atmospheric conditions.

Metal oxide type sensors are characterized by relatively large changes in resistance of the semi-conducting species as a result of reactions with gas molecules in the ambient environment. This leads to one of the following oxide sensor types as differentiated by Park and Ackbar (2003):

- Bulk grain conduction type sensors whereby the bulk phase can maintain stoichiometric equilibrium with the gas species in the surrounding environment,
- Electrode / oxide junction controlled sensors whereby gas phase reactions with the interface create changes to the three phase boundary (electrode/oxide/gas) surface states and,
- Surface layer conductive (inter-granular controlled) which utilizes changes in the concentration of conduction electrons as a result of chemical reactions at the surface with adsorbed gas species.

The present study is primarily concerned with the surface conductive type of sensing metal oxide and will utilize SnO_2 experimentally.

2.3.1 Theoretical Basis of Metal Oxide (SnO_2) Sensing

An SnO_2 sensor is typically prepared as a ceramic by sintering onto to a substrate, usually made up of Al_2O_3. The substrate is heated by passing an electric current through a wire filament embedded within the substrate to obtain optimum operating temperatures. As a target gas comes into contact with the surface of a semiconducting metal oxide, its electrical resistance drops (as a function of increasing target gas concentration). The change in electrical resistance is used as the measurand in a functioning sensor.

Since most metal oxide gas sensing materials act as n-type semiconductors at typical operating temperatures, their electrical conductivity is based on electrons being added or removed from the

conduction band of the sensing layer molecules, leading to large changes in the conductivity of the material. Most of these electrons come from non-stoichiometrical conditions in the material that enable it to donate electrons to the conduction band in the sensing layer (depletion region).

SnO_2 is an n-type semiconductor, in which electron donor levels (for conduction) are formed by oxygen vacancies in the crystal lattice network. The conductance G of a crystal is given by:

$$G = \frac{\sigma W t}{L}, \qquad \textit{(2-5)}$$

where W, t and L are crystal width, thickness and length and σ is the conductivity given by:

$$\sigma = n_b q u_n \qquad \textit{(2-6a)}$$

The temperature dependence of the carrier density, n_b, is also important, the mobility of the carriers, u_n, is also temperature dependent but to a lesser degree, and q is the electronic charge. At high temperatures, defects can be formed in the lattice thereby donating electrons to the conduction band and hence increasing conductivity (hence the negative temperature coefficient of n-type semiconductors). Donors are produced in the semiconductor when a reducing agent to be detected reacts with lattice oxygen, extracting it and hence leaving behind an oxygen vacancy from which donor electrons can be contributed.

The mechanism of SnO_2 surface conduction is such that if oxygen is adsorbed on the surface it forms negative ions thereby removing electrons from the conduction band of atomic species in the surface region of the SnO_2 grain (refer to Figure 2.2) as follows:

$O_2 + 2e^- \rightarrow 2O^-$ *or,*

$O_2 + e^- \rightarrow O_2^-$

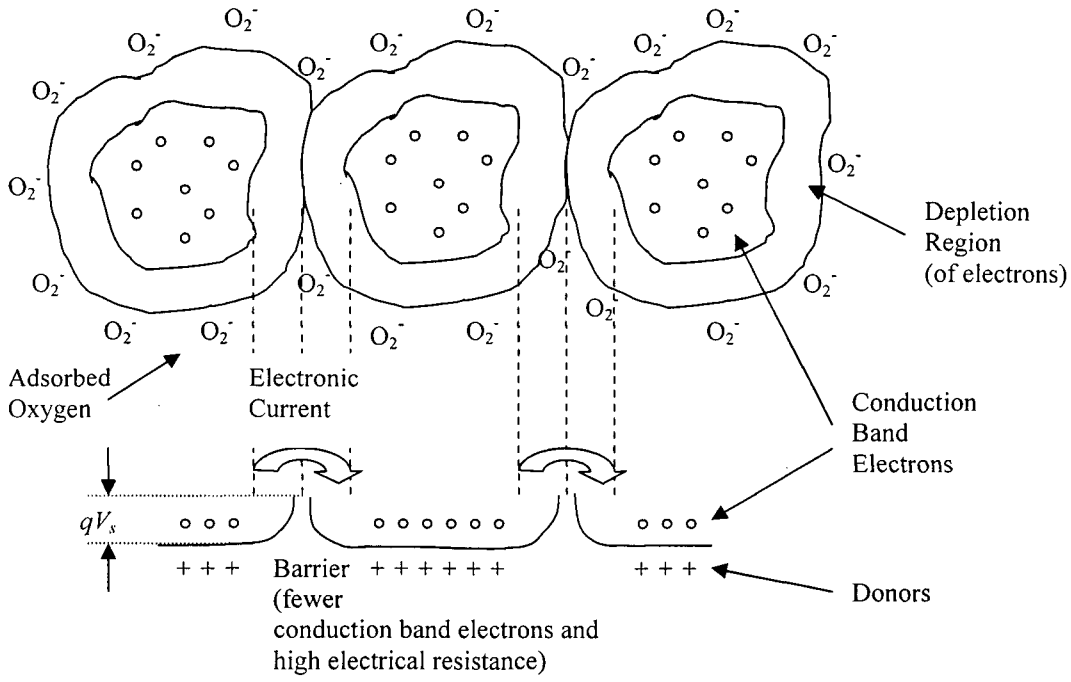

Figure 2.2: Band model for intergranular contact resistance (Madou and Morrison, 1989)

This region therefore is depleted of conduction electrons (called the depletion region) and the surface resistivity of the grain increases. When a reducing gas arrives at the surface, it is adsorbed, combining with oxygen ions thereby releasing electrons which can then freely conduct as follows:

$CO + O^- \rightarrow CO_2 + e^-$ *or,*

$CO + O_2^- \rightarrow CO + O_2 + e^-$

Therefore, surface conductivity is increased and in particular the conductivity at the grain contacts is increased (resistance is reduced) in the presence of a reducing gas. It is this inter-granular contact resistance that dominates the overall resistance in a packed or compressed metal oxide powder. Nemoto and Oda (1981) concluded that the resistance measured across a grain is much smaller than the resistance across a single grain boundary. In addition, since the bulk

resistance of an n-type semiconductor has a negative temperature coefficient, its bulk resistance will decrease as temperature is increased (Watson et al., 1993, Barson and Weimer, 2001), consistent with increasing donor levels.

In cases where the contact resistance between fixed bed particles dominates the resistance, contact resistance is a strong function of mechanical compression (Oloman et. al., 1991) and hence the voidage of the bed. Effective conductivity, σ, can be determined as a function of bed voidage from the Bruggeman equation:

$$\sigma = \sigma_0 (1 - \varepsilon_{inert})^n, \qquad \textit{(2-6b)}$$

where σ_0 is the bulk conductivity of the fixed bed (obtained experimentally) and ε_{inert} is the voidage of non-conductive material, including gas voidage in the bed and n is a power representative of microporous tortuosity usually in the range of 1.5 to 3.

The inter-granular contact resistance is explained fundamentally by using the Fermi energy relation which gives the probability of finding an electron at a given energy level as follows:

$$f = \frac{1}{1 + \exp \frac{E - E_f}{k_b T}} \qquad \textit{(2-7)}$$

where f is the probability of finding an electron with energy level E, and E_f is the energy level where the Fermi probability is ½, k_b is Boltzmann's constant, and T is the temperature. In cases where $E_c - E_f > 2kT$ then the expression can be simplified into a Maxwell Boltzmann equation of the form:

$$n_s = N_c \exp\left[\frac{-(qV_s + E_c - E_f)}{kT}\right] = N_D \exp\left(\frac{-qV_s}{kT}\right)$$

where n_s is the density of electrons on the surface of an n-type semiconductor, N_c is the effective density of states near the edge of the conduction band (~10^{19} cm^{-3}). As n_s increases, E_f approaches the energy of the conduction band, E_c. Hence, as the metal oxide is reduced by removal of oxygen from the oxide or other means of adding electrons are used, in general, E_f moves to higher energy. The energy qV_s is the energy that electrons must attain before they can move to surface energy levels and N_D is the density of donors in the bulk, which is equivalent to the density of electrons n_b in the bulk for simple semiconductors with completely ionized donors. V_s is given by:

$$V_s = qN_s^2 \frac{2}{\varepsilon\varepsilon_0 N_i},$$

where q is the charge carried by an electron, ε and ε_0 are the dielectric constant of the semiconductor and the permittivity of free space respectively, N_s is the density of charged surface states and N_i is the net density of ions in the space charge region. This is an important relation that describes the potential difference between the surface and the bulk as a function of the density of charged surface states, N_s. The charge can be associated with the density of negatively charged adsorbed oxygen (O_2^-). These relations lead to the band model for inter-granular contact resistance of a pressed metal oxide powder (Madou and Morrison, 1989) illustrated in Figure 2.2 and given by the following equation:

$$G = G_0 \exp\left(\frac{-qV_s}{k_b T}\right) \qquad \textit{(2-8)}$$

where G is the conductance of the sensing layer, G_0 is the initial conductance (related to contact area, charge mobility, and other less sensitive factors), qV_s is the energy difference between the

surface and the bulk. The following points can be used to describe the behaviour of the metal oxide during the sensing cycle:

- O_2^- adsorbed on the surface increases the surface resistivity by extracting electrons from the conduction band forming an insulated space charge region,
- Electrons must cross this insulating region to conduct,
- The inter-granular contact region then becomes a region of high resistance relative to the actual grain,
- Transfer of electrons from pellet to pellet requires excitation of the electron over the surface barrier (represented by qV_s).
- C_3H_6, CO or other reducing gas reacts with O_2^- and restores the surface electrons thereby decreases the surface resistivity.
- Intergrannular contact resistance (and hence overall resistance) is reduced providing the measurand for sensing of the reducing gas.

Barson and Weimer (2001) propose the addition of a temperature related diffusion term to the model of Madou and Morrison as follows:

$$G = \frac{G_{0,d}}{T} \exp\left(\frac{-qV_s}{k_b T}\right) \qquad \textit{(2-9)}$$

where the $G_{0,d}/T$ term takes into account surface layer diffusion effects as a function of temperature (i.e. diffusion of electrons from the bulk to surface states).

2.3.2 Sensitivity

Typical reducing gases for metal oxide sensors include CH_4, CO, CO_2, HC's and VOC's. Sensitivity varies greatly depending on the preparation of the sensor, the temperature, reducing

gas concentration, humidity and the presence of other trace contaminants. Sensors typically operate in air at atmospheric conditions and hence it is the presence of ambient oxygen that gives the sensor it's initially high resistance. Sensor resistance typically falls dramatically in the presence of reducing gases according to a power law:

$$R_g \sim K c_g^{-\alpha} \qquad \textit{(2-10)}$$

Where c_g is the concentration of reducing gas in air and K and α are constants.

Sensitivity (absolute), S_A, is defined as the ratio of the sensor resistance in air, R_a to the resistance of the sensor in the reducing gas, R_g and is given as follows:

$$S_A = \frac{R_a}{R_g} \qquad \textit{(2-11)}$$

A normalized sensitivity, S_N, comparing the resistance over a range of 0 – 1 can be defined as the ratio of the difference in resistance between the oxidized state, R_a, and the reduced state R_g, to the resistance in the oxidized state as follows:

$$S_N = \frac{R_a - R_g}{R_a} = 1 - \frac{R_g}{R_a} \qquad \textit{(2-12)}$$

In practice, it is the O^- species that defines the high resistance of SnO_2 in clean air at normal working temperatures of 200 – 400 °C, while only occupying about 2% of the total surface, since oxygen adsorption only occurs on the crystal defects which make chemisorption possible (Madou and Morrison, 1989; Watson et al., 1993; Barson and Weimer, 2001; Park and Ackbar, 2003). At lower temperatures it has been shown that the O_2^- species dominates since the

activation energy is not available to dissociate the O_2^- ion below approximately 175 °C (Barson and Weimer, 2001).

Sensitivity, arises from the consumption of negatively charged oxygen adsorbates at or near the inter-grain contacts by the reducing gas. In other words, the sensitivity of a semiconducting gas sensor is a function of the steady state surface coverage of oxygen adsorbate relative to that in air or its preconditioned state. The lower the surface coverage, relative to its preconditioned state, the higher the sensitivity.

A sensor with a porous structure shows maximum sensitivity at a certain temperature depending on the gas species to be detected because of the following factors:

- Temperature-dependent equilibrium coverage of oxygen adsorbate in air (adsorption rate of oxygen),
- Temperature-dependent equilibrium and time constant of the catalytic reaction between the oxygen adsorbate and the target gas (catalytic activity of sensing element) and,
- Permeability of oxygen and the target gas through the porous medium (diffusivity of gases).

At low temperature, where the equilibrium coverage of oxygen adsorbate in air is high, the catalytic reaction rate of the gas species to be detected with the surface oxygen is low and the sensitivity is low to negligible. On the other hand, at high temperatures, where the rate of removal of oxygen adsorbate is high due to the high catalytic activity, the equilibrium coverage of oxygen in air is low and hence the sensitivity is low. At intermediate temperatures, the sensitivity reaches an optimum. Yamazoe et al. (1983) illustrates this behaviour for C_3H_8, CH_4, CO and H_2 reducing gases over SnO_2 oxides doped with Pt, Pd, or Ag. The results for the optimized temperature and sensitivity ($S_A = R_a/R_g$) are included in Table 2.3. In addition, since

the oxygen consumption related to the conversion of the target gas proceeds at lower temperatures with increasing catalytic activity, the temperature where maximum sensitivity occurs is expected to be inversely proportional to catalytic activity (the higher the catalytic activity the lower the temperature at which the maximum sensitivity occurs).

Park and Ackbar (2003) indicate that in porous media the effective diffusivity, D' of the gas species may be significantly lowered compared to its diffusivity in the ambient, D^o ($D' = 10^{-2} - 10^{-3}\ D^o$) (a function of porosity and tortuosity within pore structures). In addition, the gas is consumed during the diffusion across a thick porous layer at a rate of kc_g, which determines the amount of permeation of the target gas toward the active surface, where k is the reaction rate constant. Thus a gradient in the gas concentration is usually established across the thick porous film which affects the sensitivity and can be described by the following differential equation:

$$\frac{\partial c_g}{\partial t} = D_i' \frac{\partial^2 c_g}{\partial x^2} - kc_g \qquad \textit{(2-13)}$$

To summarise, if a sensing element is highly active, the target gas is almost completely oxidized at the outer region and only a trace amount of the gas species can reach the innermost region where the electrodes are located, leading to low sensitivity. On the other hand, if the element has a moderate activity a considerable amount of gas species can permeate into the innermost region, leading to a high sensitivity. On the contrary the sensor having a negligible activity exhibits a lower sensitivity because of the low consumption of oxygen adsorbate at the innermost region regardless of the almost complete permeation of the gas. Table 2.3 summarises the sensitivity for a number of experimental gas sensor systems, along with their optimum temperature and selectivity.

2.3.3 Selectivity

Selectivity is important to reduce cross-sensitivity which occurs in environments with trace levels of gases not targeted for detection. Selectivity enhancement can be achieved by the some of the following common methods as outlined and reviewed by Park and Ackbar (2003):

- Using an electrode configuration and sensing layer thickness which enables the discrimination of different interfering effects of certain active gases,
- The addition of catalysts/dopants that will enhance or shift the selectivity maximum towards a certain target gas.
- Selection of an optimum operating temperature where the target gas is most active compared to the interfering gases.

Electrodes placed on the top or the sides are more effective for obtaining high sensitivity because of the effectiveness of surface reactions, however, electrodes placed on the bottom of the typical sensor are more beneficial for selectivity. A small gap between the electrode and the sensitive layer will be sensitive to less reactive gases in the presence of highly reactive gases, since the highly reactive gas will be removed while diffusing into the sensing layer, but the less reactive gas remains in tact. On the other hand if the bottom electrodes have a large gap compared to the thickness of the sensor, the highly reactive gas can be detected in the presence of a poorly reactive gas because the conducting channel is formed through the surface region that is most affected by the reactive gas.

The use of physical or catalytic filters above the sensing layer can preferentially adsorb interfering gases and allow more permeable target gases to pass through to the sensing layer. If a

catalytic layer is utilized it can react with interfering compounds thus eliminating them but allowing the targeted gas to pass through to the sensing layer.

Phani et al. (1999) carried out electrical sensitivity experiments between 50 – 450 °C for a semi-conducting SnO_2 gas sensor with different weight percent of Pd and $Al_2Si_2O_7$ added in order to optimise this material as a gas sensor. The optimum sensitivity and selectivity for liquid petroleum gas (LPG) was found with a composition of SnO_2 : $Al_2Si_2O_7$ (35 wt%) : Pd (1.5 wt%) at an operating temperature of approximately 350°C. Sensitivity tests were carried out in varying concentrations of LPG, from 0 – 20,000 ppm in air. Data from the study showed that the S begins to plateau at a concentration of approximately 10,000 ppm. The relationship can be expressed in the form of, $S_N = Kc_g^{\alpha}$ (where α = the exponential factor derived from the data). Trials of this sensor indicate that it maintained sensitivity to within +/- 3% over a 6-month period. Test concentrations in field trials varied from 1,000 – 200,000 ppm, and successfully set off the alarm signals.

Kocemba et al. (2001) indicate that strongly pressed SnO_2 based H_2 sensors increase sensitivity and stability with the addition of 40% by volume of a non-electrically conductive additive such as glass or alumina, and proposed the mechanism that allows this to happen. This finding is promising in that it reinforces the potential for the principle that should allow for a mechanical mixture of SnO_2 and alumina to be used together without impacting the ability of the sensing component to achieve a good electrical sensitivity to the target gas.

Highly specific and sensitive SnO_2 gas sensors are not yet available. The present study does not experiment with the effect of additives, however, varying crystal structure and morphology with the use of additives has been shown to improve gas sensor sensitivity for specific compounds.

This may be important for future work as evidenced by the range of sensitivity, selectivity and operating temperature exhibited by experimental gas sensors summarized in Table 2.3.

Table 2.3: Comparison of maximum sensitivity, selectivity and optimum operating temperature for different sensing materials.

Sensor Material	Comments	Sensitivity @ (Conc. in ppm) $S_A = R_a/R_g$	Selectivity	Optimum T (max. S_A) °C	Reference
SnO_2	No additives	1.35 (100)	CH_4	500	Firth et al., 1975
		1.4 (100)	CO	400	
Pt - SnO_2	0.5% Pt	3600 (8000)	H_2	25	Yamazoe et al., 1983
		50 (2000)	C_3H_8	275	
		25 (5000)	CH_4	300	
		>150 (200)	CO	25	
Pd - SnO_2	0.5% Pd	125 (8000)	H_2	150	
		75 (2000)	C_3H_8	250	
		25 (5000)	CH_4	350	
		<5 (200)	CO	250 – 350	
Ag - SnO_2	0.5% Ag	666 (8000)	H_2	100	
		90 (2000)	C_3H_8	350	
		25 (5000)	CH_4	425	
		<5 (200)	CO	110	
4 wt% Pd/SnO_2	Low power sensor, 50% RH	33 (10,000)	C_3H_8	$P = 145\ mW$	Kim et al., 1997
SnO_2 : $Al_2Si_2O_7$ (35 wt%) : Pd (1.5 wt%)	Pd sensitizer and $Al_2Si_2O_7$ stabiliser, $S=KC^{0.64}$	1.8 (1000)	LPG	350	Phani et al., 1999
		12.5 (10,000)	LPG	350	
SnO_2 nanocrystallites	crystal growth at 800°C, ~34 nm crystallites	12 (1000)	CO	425	Cirera et al., 1999
		6 (10)	NO_2	275	
	crystal growth at 500°C, ~6 nm crystallites	8 (1000)	CO	500	
		33 (10)	NO_2	325	
SnO_2 Pressed Pellets with 40% inert structure	Sensitivity related to porosity,	7 (150)	H_2	350	Kocemba et al., 2001
Ru – SnO_2	Spin coated thin film	672 (NA)	LPG	300	Niranjan and Mulla, 2003
SnO_2	400-500nm film thickness, 60-100 nm crystallites	1.4 (150)	CO	275	Savage, 2002 (in Park and Ackbar, 2003)
TiO_2	85 nm film thk, 10 nm crystallites	30 (NA)	CO	200	
TiO_2	34 nm crystallites	0.1 (100)	CO	190	
Porous silicon (PS)	Conduct-imetric Sensor	10 (50 ppb)	NO_2		Pancheri et al., 2004

2.3.4 Effects of H_20 and CO

Metal oxide sensing materials typically exhibit a sigmoidal resistance versus temperature behaviour in the presence of water. The lower temperature resistance occurs at approximately 200 – 250 °C and the high temperature maximum resistance occurs around 350 – 400 °C. The surface conductivity is proportional to the total concentration of adsorbates among which oxygen ions (O^-, O_2^-, O^{-2}) and OH^- increase resistance by taking electrons from the surface, but H_2O^+ donates an electron thereby decreasing resistance. The resistance of a given sensor geometry can therefore be expressed as:

$$R = f\left([O^-]_s, [OH^-]_s, 1/[H_2O^+]\right), \qquad \textit{(2-14)}$$

where $[\ ]_s$ is the surface density of adsorbate on the sensor surface. At low temperatures, adsorbed water molecules are physisorbed as reviewed by Barnes and Weimer (2001) and Park and Ackbar (2003). The water molecules act as donors, blocking the equilibrium sorption of oxygen, giving lower oxygen ion surface concentration. In this case the electrons donated by the adsorbed water molecule are accumulated near the surface and reduce the sensor resistance. As the temperature rises, water molecules desorb, due to their weak bonding interaction with the oxide and allow enhanced surface oxygen ion concentration. In addition, with increasing temperature, dissociative water adsorption can occur generating a negative hydroxyl group. TPD and IR studies show that water molecules are no longer present at the surface above 200 °C. Barnes and Weimer (2001) discuss hydroxyl groups appearing as a result of acid/base reactions with OH sharing its electron pair with the Lewis acid site (Sn) and leaving the hydrogen atom available for reaction with the Lewis base (lattice oxygen) or adsorbed oxygen. These combined effects increase resistance. At even further increases in temperature, beyond the maximum

sigmoidal resistance, the combined effect of OH^- desorption and the negative temperature coefficient of metal oxide materials reduce resistance further.

At temperatures that are of interest to chemical and gas sensors, preadsorbed water or water that is adsorbed during manipulation (handling, experiment, etc) can affect the conductivity (Caldararu et al., 1995, 1996, 2001 and Stoica et al., 1999, 2000). Caldararu (1996) indicates that at low temperature, SnO_2 shows low lattice oxygen mobility and AC conductance preventing rapid equilibrium between bulk and surface and is very susceptible to the history of the sample, in particular the presence of water (humidity). It is postulated that water adsorption interferes with oxygen adsorption by blocking some of the surface anionic vacancies with stable species (coordinately adsorbed water and surface hydroxyl groups) consistent with the conclusions of Barnes and Weimer (2001) and Park and Ackbar (2003).

The presence of carbon monoxide (CO) increases surface conduction in SnO_2 at typical sensor operating temperatures (150 – 450 °C) for all studies reviewed by Barson and Weimer (2001), consistent with the fact that SnO_2 is utilized extensively as a CO detector. The studies indicate that CO reacts with adsorbed or lattice oxygen to form carbonate (between 150 – 400 °C), carboxylate (250 – 400 °C) or CO_2 (200 – 370 °C) directly or from the previous reactions.

2.3.5 Typical Sensor Construction and Preparation

Metal Oxide gas sensors typically contain the following components:

- The sensitive layer composed of the metal oxide
- A substrate upon which the metal oxide is deposited
- Electrodes to detect changes in electrical conductivity of the sensing layer

- A heating element to maintain the unit at the optimum operating temperature, which is electrically isolated from the sensing layer

Taguchi prepared the first commercially successful sensor design (Madou and Morrison, 1989) consisting of a hollow ceramic tube, the primary ingredient of which was Al_2O_3 (3 mm long by 1.5 mm diameter) containing a heating element within the tube wall. SnO_2 was coated on the outside wall of the tube. Gold electrodes sputtered onto the tube were used as contacts and catalysts could be added, usually by impregnation, supported on the oxide. The oxide layer was prepared as a paste and applied as a thick film. Filter layers could also be added to the outside to help reduce the effect of poisons or nuisance gases or to help improve selectivity. Planar Taguchi sensors were also prepared using screen printing techniques, made using more economical batch processes.

The Figaro (Figaro Engineering Co. Inc. of Japan) sensor is another commercially successful design. Watson et al. (1993) indicates that it is manufactured using thin film microchip technology for mass production. The preparation consists of the following steps:

- High purity SnO_2 is dissolved in acid, followed by the addition of an alkali to precipitate out tin hydroxide. This is heat dried to give a very pure powder.
- The tin hydroxide is calcined (heated at ~450 ^{o}C) to give a pure SnO_2 powder. The crystallite size is closely related to the final sensor properties and is determined by the temperature and length of the calcination step.
- Equal weight of Al_2O_3 powder is added to the high purity SnO_2 powder with distilled water to make a paste, for strength enhancement and to modify the conductivity of the final ceramic.

- Binder is added and the paste applied to a substrate, usually composed of Al_2O_3 and containing an isolated heating element. This is allowed to air dry.
- The sintering process (typically heating over 700 °C) is the final stage, causing the crystallites of SnO_2 to fuse together and increasing the strength of the final product. The addition of tetraethyl orthosilicate as a binder leaves silica in the final SnO_2 ceramic. This improves the strength and also reduces resistance by up to a factor of 10 (perhaps as a result of changing the sensor porosity), thus allowing for simplified circuitry in the sensor electronics.
- Additives such as Pd and Pt can be added prior to the calcination stage in order to modify sensitivity or selectivity.

A flow diagram illustrating a preparation procedure for a tin dioxide based LPG sensor, successfully tested in field trials, is shown in Figure 2.3 (Phani et al., 1999).

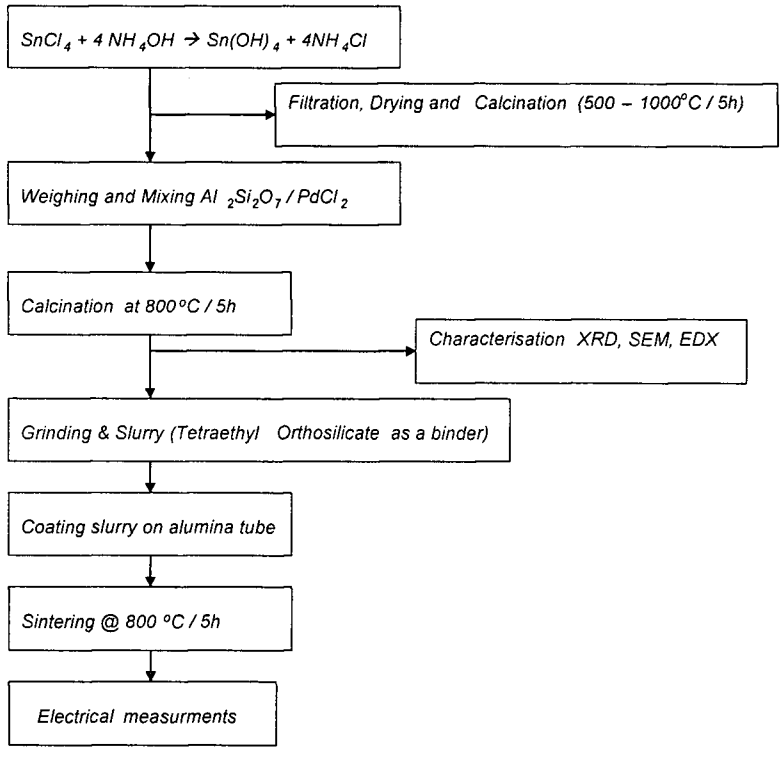

Figure 2.3 Typical SnO_2 sensor preparation methodology (Phani et al., 1999).

The potential for multiple gas composition detection has been demonstrated on nano-crystalline thick films deposited on micro-machined substrates (Heilig et al., 1997). Further work by Heilig et al. (1999) has been used to simultaneously monitor temperature (similar to pellistor technology) and resistance changes upon gas exposure to the same sensing layer. Correlations of the change in sensitivity and the gas specific change in temperature, in the range of 1 – 2 °C, of the sensing layer, using artificial neural networks were used, to discriminate between CO, CH_4, and C_2H_5OH detection and concentration on 0.2% Pt doped SnO_2 at 400 °C. Similarly, they found that H_2 could be discriminated in the same system with CO and CH_4 at 310 °C at 30%, 50% and 70% relative humidity with 0.2% Pd doped SnO_2. The temperature decrease is thought to be a result of the net energy balance in the sensor system as a result of the reaction mechanism (exothermic), adsorption (exothermic) and desorption (endothermic) heat effects.

Kim et al. (1997) developed and tested a 4wt% Pd doped SnO_2 sensor for low power consumption and detection of C_3H_8/C_2H_6 in air with a threshold level of 100 ppm. Compared to the widely used Figaro Sensor discussed above, which utilise approximately 400 mW to 1 W of power for heating requirements, the developed sensor utilised 100 mW at 2 V (specified for field use battery supplied sensor). The sensor is two sided to reduce the size of the sensing chip (1.5 mm x 0.3 mm x 0.15 mm) and heating requirements and is placed on an alumina substrate. The average grain size was measured by SEM and found to be 0.1 μm and the BET surface area was $18m^2g^{-1}$. Fabrication of the sensor components were carried out based on thick film printing technology. The sensor was tested in a 1.0 vol% C_3H_8/air mixture at 50% RH and the maximum sensitivity was found to be 33 with a sensor power output of 145 mW.

2.3.6 Circuitry

Transduced sensor signals must be carried by an electrode to an electronic circuit. These circuits usually consist of a voltage dividing circuit where the output voltage V_{out} is given by:

$$V_{out} = \frac{R_L}{R_L + R_S} V_c \qquad \textit{(2-15)}$$

where R_L is a load resistance, R_S is the sensor resistance and V_c is the operating voltage of the circuitry. Output voltage is a function of R_S/R_L as shown in Figure 2.4 for a typical operating voltage of 5V. The figure indicates that the most sensitive region of the sensor is in the range $0.1 < R_S/R_L < 10$. In addition, the figure indicates that in order to operate in the sensitive region of the plot, the load resistance R_L should be less then 10 times the sensor resistance R_S. Park and Ackbar, 2003 indicate that the lower limit of the sensor resistance is dictated by the nature of sensor self heating and that for a CH_4 sensor operating at 2000 ppm in air, it should be approximately 0.6 kohm and 0.1 kohm for 5V and 2V operating voltage respectively. They point out that these values are well below typical values exhibited by doped SnO_2 devices.

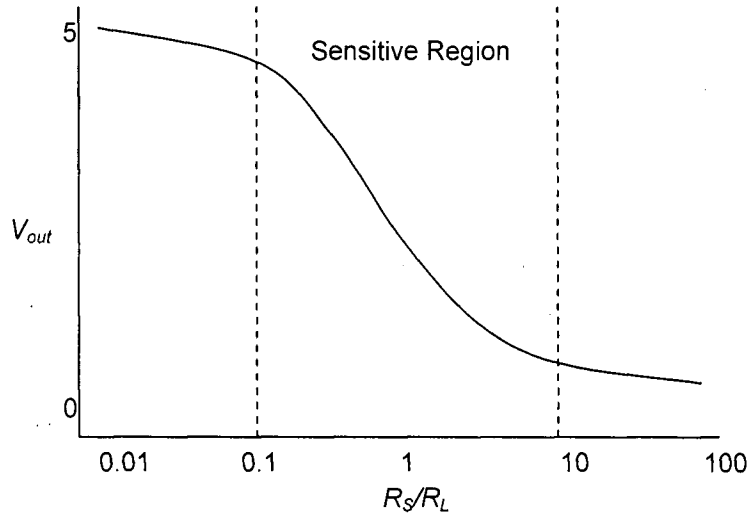

Figure 2.4: Practical Sensor Characteristic Response (Park and Ackbar, 2002).

Chapter 3 - Experimental Methods and Analysis

This chapter will describe the experimental methods undertaken to simultaneously carry out electrical resistance and adsorption uptake measurements of a mixed bed of metal oxide (SnO_2) and adsorbent (Al_2O_3). These measurements will be used to correlate the change in electrical resistance to the amount of target gas uptake in the bed. The method of analysis will also be presented.

3.1 Flow Diagram and Apparatus

A laboratory "bench scale" packed bed reactor was designed such that the conductivity of the metal oxide / adsorbent bed could be measured, simultaneously, along with the adsorption breakthrough of the bed. The experimental flow system and reactor are illustrated in Figure 3.1, and Figures 3.2 and 3.3 respectively. Appendix A discusses selection criteria for individual components of the flow system.

The quartz reactor measured 25 mm in diameter by approximately 100 mm in length and contained two co-centric tantalum electrodes. The electrodes were connected by tungsten wires through the reactor wall to an industrial type multi-meter capable of measuring electrical resistance (direct current) up to 500 MΩ. A packed bed made up of 22.5 ml of mixed metal oxide (SnO_2) and adsorbent (Al_2O_3) material was placed between the electrodes. The resistance properties of the metal oxide / adsorbent system were monitored at intervals of 0.5 seconds to measure changes during experimentation. The time average of these readings were taken every 10 seconds and logged. Adsorption breakthrough was monitored using thermal conductivity detection of the exit gas stream from the reactor. These readings were monitored and logged at 0.5 second intervals. A heating and temperature control system was commissioned allowing

ramp and soak temperature profiles to be utilized. Experiments were carried out between 25 and 350 °C and the static operating pressure was between 120 – 145 kPag. The mass flow controller's (MFC) were calibrated over the range of experimental flow rates, from 80 sccm to 200 sccm, for 1 – 10% C_3H_6 in He mixtures and for pure air and He.

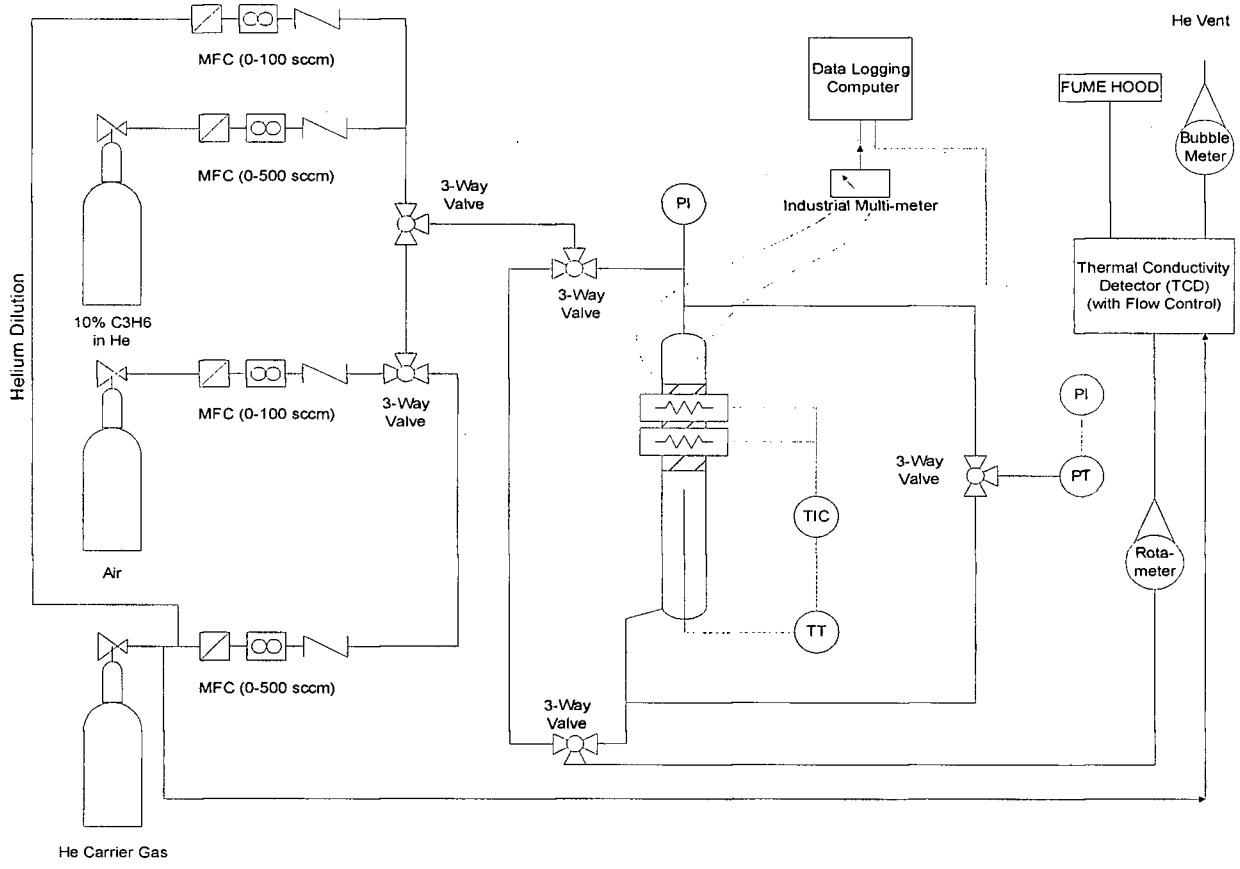

Figure 3.1: Flow diagram for simultaneous measurements of electrical resistance and adsorption breakthrough curves over a metal oxide / adsorbent bed.

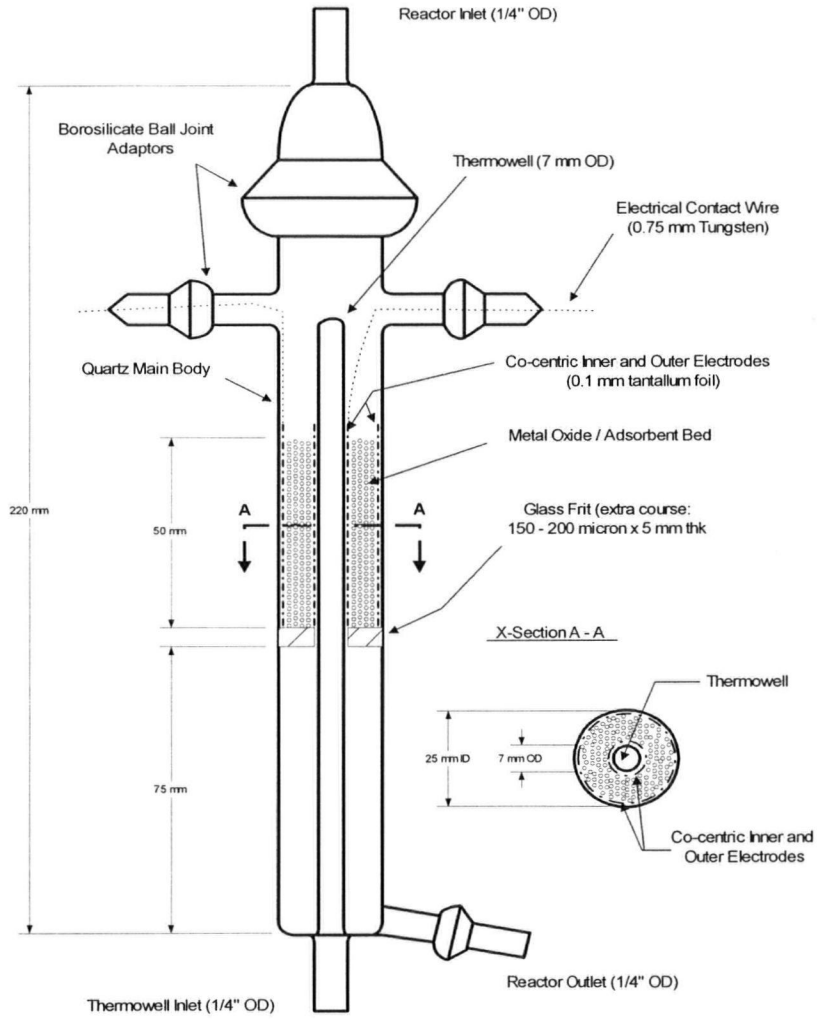

Figure 3.2: Detailed reactor design

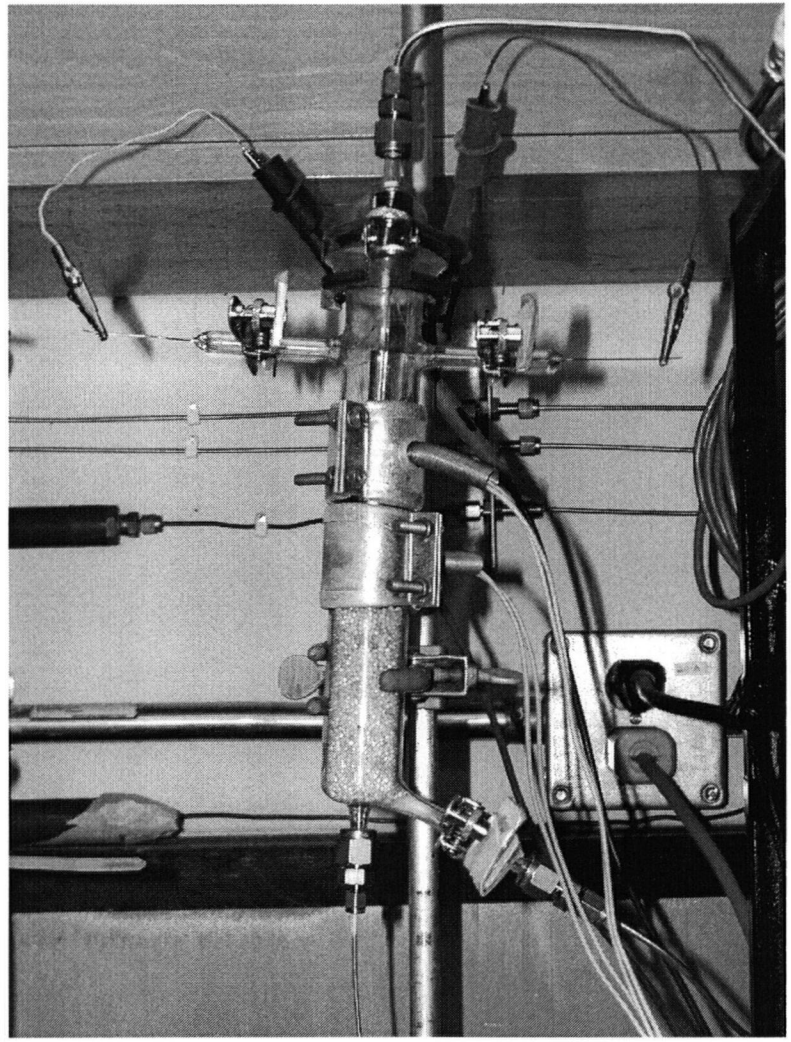

Figure 3.3: Actual reactor installation including electrical leads and band heaters.

3.2 Experimental Approach

Data were obtained by simultaneously monitoring the in-situ electrical resistance of the bed while carrying out an adsorption breakthrough experiment and were carried out over a range of conditions.

During preliminary investigations, both pure metal oxide (SnO_2) and pure adsorbent (Al_2O_3) were used to test the experimental system and to determine practical operational limits that would yield meaningful results for each component.

The primary experiments were carried out utilizing three variables:

1. % volume of adsorbent (ranging from 10 – 70% volume in SnO_2),
2. gas concentration (ranging from 1 – 10% volume C_3H_6 in He),
3. temperature (ranging from 50 – 150 ^{o}C).

Initially, varied % volume compositions of the metal oxide / adsorbent bed ranging from 10 - 70% adsorbent were studied varying the temperature only. A subsequent set of tests at constant metal oxide / adsorbent bed composition was undertaken, varying the concentration of the target gas. For each metal oxide / adsorbent bed composition and for each gas concentration, the bed temperature was varied between 50 and 150 ^{o}C. In addition, for each temperature, two series of experiments were undertaken in order to check the repeatability of the results.

The first series of experiments consisted of three cycles of oxidation (1 hr, 15 min, 15 min) and reduction, with He flushes in between each oxidation and each reduction. This is illustrated in Figure 3.4. These tests were specifically designed so that the change in electrical resistance of the bed could be monitored during both adsorption and desorption of the target gas, however, it

is the correlation of the electrical resistance to the adsorption breakthrough that is of particular interest for this research project.

The second series of experiments followed immediately after the first series and consisted of adsorption / desorption breakthrough experiments between He and C_3H_6. These experiments were specifically designed to determine the parameters of the axially dispersed plug flow model for adsorption using moment analysis (Ruthven, 1984). Flow rates were varied between 80 - 200 sccm for the target fugitive emission gas (C_3H_6) and He. The breakthrough curve data was logged and plotted as illustrated in Figure 3.5. The data were then analysed and the parameters of the model extracted.

In all cases the sensor bed mixture was prepared on the bench and poured through a funnel into the reactor which was then lightly tapped to level the bed. In this way the bed was assumed to be loosely packed and compression affects on resistance were assumed constant.

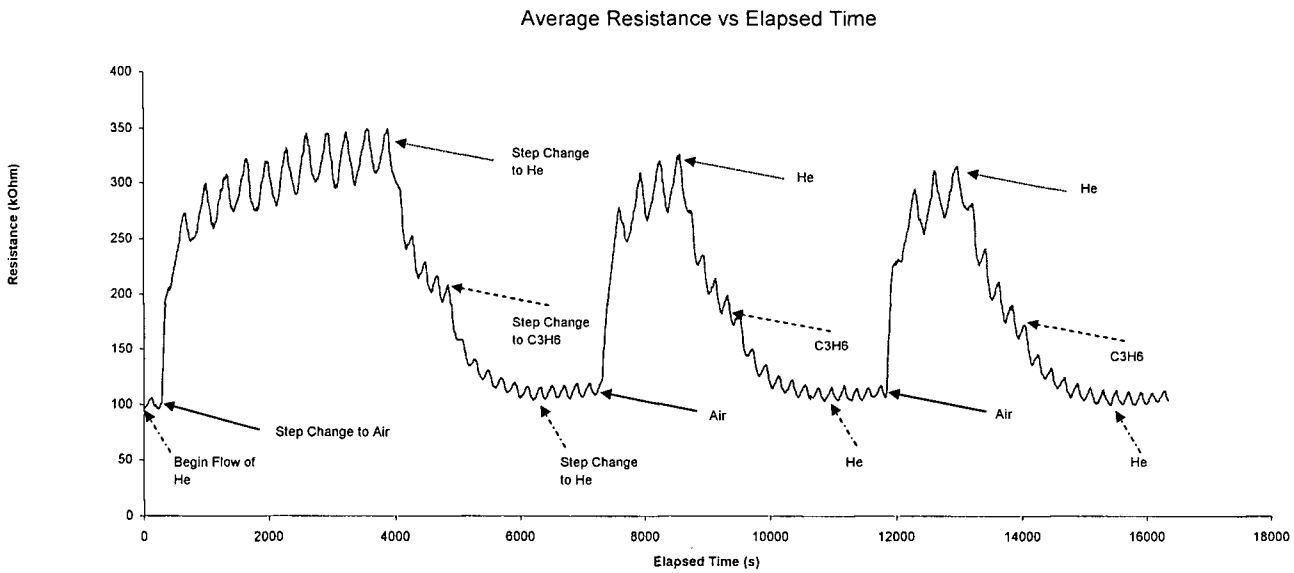

Figure 3.4: The general procedure of a 1 hour oxidation in air followed by two 15 min cycles of an oxidation in air, He flush, 10% C_3H_6 reduction and He flush.

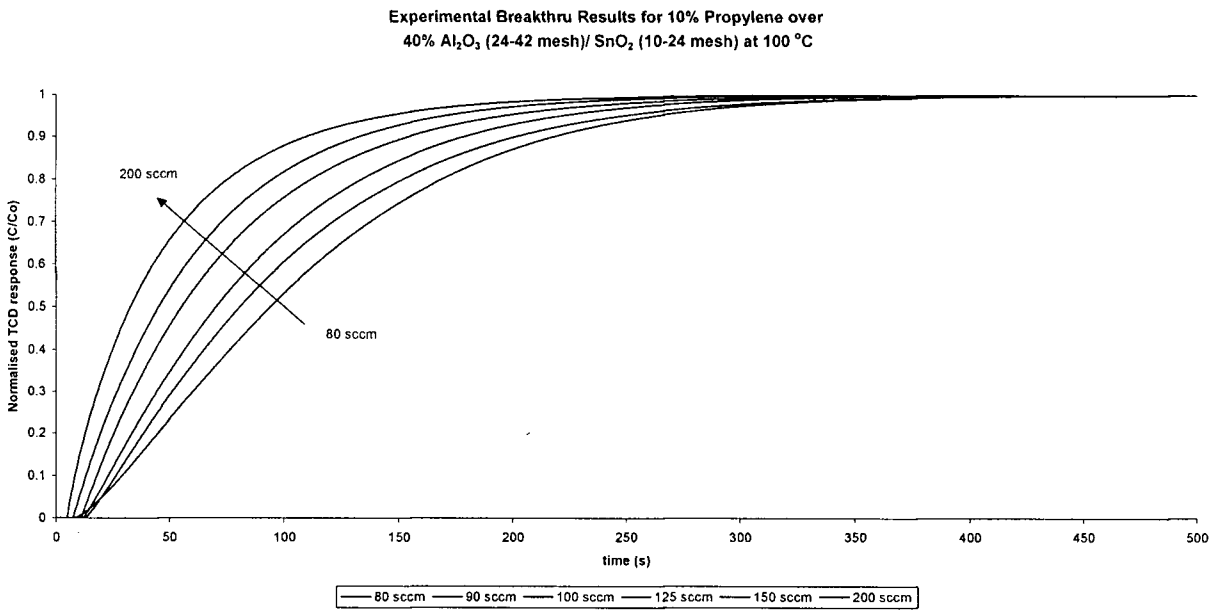

Figure 3.5: Typical plot indicating the adsorption breakthrough curves for the adsorption of 10% C_3H_6 from 80 - 200 sccm from right to left respectively.

3.3 Experimental Operating Procedure

The following sections detail the procedures used to carry out the experiments. Reference to Figure 3.1 illustrating the experimental flow diagram should be made. Initially these tests were carried out utilizing a fixed concentration of adsorbate, 10%vol. C_3H_6 in He, and varying the metal oxide / adsorbent bed composition between 10 - 70% adsorbent. Further tests were then carried out with fixed, 40%vol., adsorbent and varying the gas concentration from 10% to 1% C_3H_6 in He.

3.3.1 Preparation and Pretreatment

Metal oxide (SnO_2) and adsorbent (Al_2O_3) were obtained commercially and ground to the required size with a mortar and pestle. Metal oxide was ground and filtered to obtain 10 – 24 mesh particle sizes. The adsorbent was ground to 24 – 42 mesh particle size. These particles

were then measured in a graduated cylinder to obtain the percent volume mixture specification for each experiment.

Initially a 10% by volume mixture of adsorbent to metal oxide was prepared. Subsequent mixtures required additional adsorbent and hence new adsorbent was added to the previous mixture. In each case 22.5 ml of mixture was placed in the reactor for experimentation.

The mixture was then flushed in He while the temperature was raised to 350 ^{o}C after which a step change to 80 sccm of air was made. The metal oxide / adsorbent sample was oxidised in air for one hour. After one hour the flow was switched back to He via the three way valve. The temperature set point was then adjusted to the first test temperature (50 ^{o}C) via the temperature controller and an additional one hour oxidation was carried out, followed by a He flush and a reduction in C_3H_6. It was found that initially after oxidation at 50 ^{o}C, a C_3H_6 reduction of the bed was required to obtain consistent electrical resistances. This may have been due to the different species of O_2 ion that exists at high temperature (O^-, O^{-2}) versus the O_2 ion found at low temperature (O_2^-).

After the reduction in C_3H_6, the reactor was again flushed with He for 15 minutes (or the length of time for complete desorption of the C_3H_6). The reactor was then shut-in via the three way valves connected to the reactor bypass. The reactor would generally sit in a static environment until the next day, when a complete set of experiments for electrical resistance and adsorption would be carried out.

3.3.2 Simultaneous Electrical Resistance and Adsorption Breakthrough

During start-up of each experimental procedure, the Fluke multi-meter was turned on to monitor the electrical resistance of the bed. Helium gas was turned on to 80 sccm and the reactor opened

to the flow of gas by switching the bypass valves to the reactor side. *FlukeView* software was set to begin logging the electrical resistance once flow was established in the reactor. Helium flowed for 5 minutes at 80 sccm and then a step change was made to air by switching the three way valve on the air supply (MFC's were preset and the TCD was warmed up for at least one hour, with TCD sensitivity @ 2 (100 mA) and TCD "block" temperature @ 150 °C).

After the bed was oxidized in air for one hour, a step change to He at 80 sccm was made for 15 minutes, followed by a step change to C_3H_6 at 80 sccm for 15 minutes (or until complete adsorption occurred). A step change back to He flush at 80 sccm was then made. After this point, two cycles of oxidation in air (15 minutes), He flush (15 minutes), reduction in C_3H_6 (15 minutes or until complete adsorption), and He flush (15 minutes or until complete desorption) were made. A second cycle of oxidation / flush / reduction was performed to check the repeatability of results (refer to Figure 3.4).

Simultaneous gas adsorption measurements were taken from the discharge of the reactor, which flows through the TCD to the fume hood, for each step change in gas composition.

3.3.3 Gas Adsorption Breakthrough Experimental Procedure

The second series of experiments made were used to obtain the data necessary to extract the parameters of the axially dispersed plug flow model for adsorption. In this series of experiments a set of adsorption and desorption breakthrough curves were generated by cycling the flow from He to C_3H_6 in step changes through different flow rates and hence interstitial bed velocities.

From these data the mean residence time and variance was calculated and used to extract the axial dispersion number (D_L), lumped mass transfer resistance (*LMTR*), and Henry's constant (K)

from the model. The flow rates were varied from 80, 90, 100, 125, 150 and 200 sccm for each adsorption / desorption trial.

Initially the gas flow was set to He. The *Labtech Notebook* software was initialized and a step change to C_3H_6, at the given flow rate, was undertaken after 30 seconds. After complete adsorption the data logger was reinitialised and a step change to He was undertaken until complete desorption.

MFC's were set to the next flow rate specified and after waiting approximately 15 minutes, for equilibrium to occur, the next adsorption / desorption cycle was carried out. Typical adsorption breakthrough curves for this series of experiments are illustrated in Figure 3.5.

3.4 Method of Analysis

Analysis of adsorption breakthrough data was utilized to determine parameters K, D_L, and the *LMTR*. Electrical conductivity data was used to determine the sensitivity S of the system for each given set of operating conditions. In addition, the energy barrier, qV_s, was analysed.

3.4.1 Adsorption Breakthrough Analysis

Ruthven (1984) details the theoretical background and presents a number of models in use for adsorption studies. The present study is based on single component adsorption and hence the analysis is greatly simplified.

For ideal conditions of plug flow with no resistance to mass transfer and no dispersive forces, the concentration profile of gas exiting the bed would match the inlet concentration profile with a time delay corresponding to the adsorbed uptake (hold-up) in the bed. In real systems, the outlet

concentration profile is dispersed due to dispersive and mass transfer effects within the bed. Therefore, measurement of the time delay provides information that can be used to extract the adsorption equilibrium of the system and measurement of the dispersion of the response can be used to extract kinetic information about the system.

Moment Analysis:

Mean residence time μ and the variance σ^2 of the step response are obtained from moment analysis. The first and second moments correspond to the mean and variance of the response:

First Moment: $$\mu = \bar{t} = \int (1 - c/c_0) dt \qquad (3\text{-}1)$$

Second Moment: $$\sigma^2 = 2\int (1 - c/c_0) dt - \mu^2 \qquad (3\text{-}2)$$

Where c/c_0 is the concentration of adsorbate, as a ratio of the inlet concentration c_0, measured at the exit of the adsorbent bed at time t, after injection of the step input of adsorbate into the bed. In practice the concentration is injected via a tubing system which leads to the bed and then from the bed to the TCD. Therefore the dead volume of the space leading to and from the adsorbent bed needs to be taken into account.

Parametric equations representing the first and second moments are as follows (Ruthven, 1984):

$$\mu = \bar{t} = \frac{L}{v}\left[1 + \left(\frac{1-\varepsilon_b}{\varepsilon_b}\right)K\right] \qquad (3\text{-}3)$$

$$\frac{\sigma^2}{2\mu^2} = \frac{D_L}{vL} + \frac{\varepsilon_b v}{L(1-\varepsilon_b)}\left(\frac{R_p}{3k_f} + \frac{R_p^2}{15\varepsilon_p D_p} + \frac{r_c^2}{15KD_c}\right)\left(1 + \frac{\varepsilon_b}{(1-\varepsilon_b)K}\right)^{-2} \qquad (3\text{-}4)$$

For strongly adsorbed species (large K) the last term of equation *3-4* reduces to approximately 1 and hence can be neglected from the analysis. The equation reduces to the following:

$$\frac{\sigma^2}{2\mu^2} = \frac{D_L}{vL} + \frac{v}{L}\left(\frac{\varepsilon_b}{1-\varepsilon_b}\right)\left(\frac{R_p}{3k_f} + \frac{R_p^2}{15\varepsilon_p D_p} + \frac{r_c^2}{15KD_c}\right) \qquad \textit{(3-5)}$$

axial film macropore micropore

The arrows above indicate the linearly additive contributions to the second moment of axial dispersion, external film mass transfer resistance, macropore diffusion resistance, and micopore diffusion resistance.

For the simple Linear Driving Force (LDF) rate model as discussed in Ruthven (1984):

$$\frac{d\bar{q}}{dt} = k_{eff}(q^* - q) \qquad \textit{(3-6)}$$

where $\bar{q}$ is the average adsorbate concentration over a grain, q^* is the equilibrium adsorbate concentration and q is the local adsorbate concentration, the rate coefficient, k_{eff}, is the overall effective mass transfer coefficient taking into account the last term in equation *3-5* for external, macropore and micropore diffusion resistance which can be simplified to give:

$$\frac{\sigma^2}{2\mu^2} = \frac{D_L}{vL} + \frac{v}{L}\left(\frac{\varepsilon_b}{1-\varepsilon_b}\right)\frac{1}{k_{eff}K} \qquad \textit{(3-7)}$$

and hence:

$$\frac{1}{k_{eff}K} = \left(\frac{R_p}{3k_f} + \frac{R_p^2}{15\varepsilon_p D_p} + \frac{r_c^2}{15KD_c} \right) \qquad \textit{(3-8)}$$

$$k_{eff} = \frac{1}{\left(\frac{KR_p}{3k_f} + \frac{KR_p^2}{15\varepsilon_p D_p} + \frac{r_c^2}{15D_c} \right)} \qquad \textit{(3-9)}$$

Equation *3-9* allows for a determination of the micropore resistance term and hence microporous diffusivity (not carried out in the present study), by obtaining successive sets of experimental data at identical conditions but varying the particle radius, R_p, and determining whether micro or macro diffusion dominates the adsorption kinetics.

Adsorption Equilibrium Constant *K* (Henry's Constant):

Once the first moment is determined from the experimental breakthrough curve, the adsorption equilibrium constant, K, can be found by substituting $v = F/(\varepsilon_b A)$ into equation *3-3* and rearranging to give:

$$\mu = \bar{t} = L(\varepsilon_b A)\left[1 + \left(\frac{1-\varepsilon_b}{\varepsilon_b}\right)K\right]\frac{1}{F} \qquad \textit{(3-10)}$$

where t, L, A, ε_b, K and F are the mean retention time, bed length, cross section area of the bed, bed voidage, Henry's constant and gas flow rate respectively. A plot of the corrected mean μ_{corr} (corrected mean retention time which takes into account reactor dead volume, explained further in Chapter 4) versus $1/F$ is approximately linear, from which the slope, S, yields Henry's constant, K, as follows:

$$K = \frac{\left(\frac{S}{L(\varepsilon_b A)} - 1\right)}{\left(\frac{1-\varepsilon_b}{\varepsilon_b}\right)} \qquad (3\text{-}11)$$

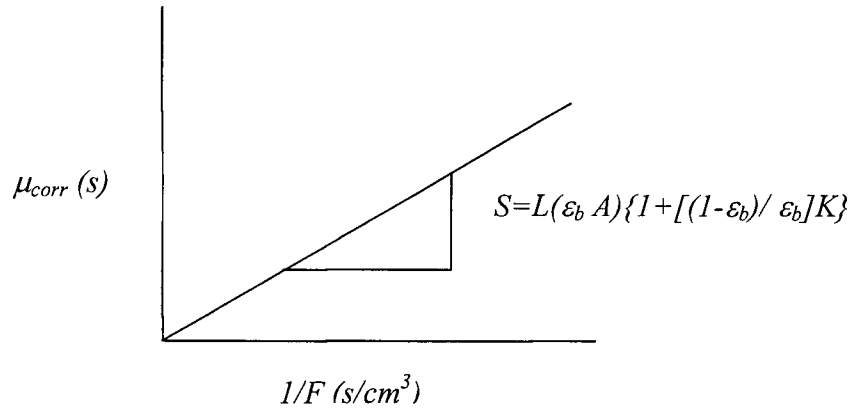

Figure 3.6: Extraction of Henry's constant from slope of μ_{corr} versus *1/F*.

Axial Dispersion Coefficient D_L and the Lumped Mass Transfer Resistance, *LMTR*:

Multiplying the second moment by L/v and rearranging gives:

$$\frac{\sigma^2}{2\mu^2}\frac{L}{v} = D_L\frac{1}{v^2} + \left(\frac{\varepsilon_b}{1-\varepsilon_b}\right)\frac{1}{k_{eff}K} \qquad (3\text{-}12)$$

The axial dispersion coefficient, D_L, and the lumped mass transfer resistance, *LMTR*, can be determined from a plot of $(\sigma^2/2\mu^2)(L/v)$ versus $1/v^2$, where the slope, S, will give the axial dispersion coefficient, D_L, directly and the intercept I will yield the *LMTR* and the effective mass transfer coefficient, k_{eff}, as follows:

$$I = LMTR = \left(\frac{\varepsilon_b}{1-\varepsilon_b}\right)\frac{1}{k_{eff}K} = \left(\frac{\varepsilon_b}{1-\varepsilon_b}\right)\left(\frac{R_p}{3k_f} + \frac{R_p^2}{15\varepsilon_p D_p} + \frac{r_c^2}{15KD_c}\right) \qquad (3\text{-}13)$$

$$k_{eff} = \left(\frac{\varepsilon_b}{1-\varepsilon_b} \right) \frac{1}{K} \frac{1}{I} \qquad (3\text{-}14)$$

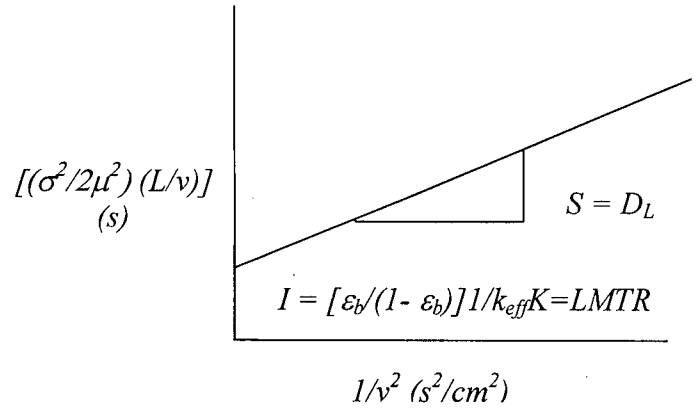

Figure 3.7: Extraction of axial dispersion coefficient D_L, and the lumped mass transfer resistance *LMTR*.

The parameters described above can be obtained by repeating a number of breakthrough experiments under identical conditions and varying only the flow rate. The above analysis was carried out to obtain K, D_L, and the *LMTR*.

3.4.2 Electrical Resistance Analysis

The sensitivity of the metal oxide / adsorbent bed to target gas adsorption was defined by equations *2-11* and *2-12* as follows:

$$S_A = \frac{R_a}{R_g} \qquad (2\text{-}11)$$

$$S_N = \frac{R_a - R_g}{R_a} = 1 - \frac{R_g}{R_a} \qquad (2\text{-}12)$$

The electrical resistance of a granular metal oxide exposed to reducing gases is inversely proportional to the electrical conductivity and is modeled based on the inter-granular contact resistance model (Madou and Morrison, 1989) and which has been modified to include diffusional effects at the surface of the grain as was given by equation *2-9* (Barson and Weimer, 2001). Taking the natural logarithm of both sides and expanding this equation leads to equation *3-15*:

$$G = \frac{G_{0,d}}{T}\exp\left(\frac{-qV_s}{k_b T}\right) \qquad \textbf{(2-9)}$$

$$\ln G = \ln G_{0,d} - \ln T + \left(\frac{-qV_s}{k_b}\right)\frac{1}{T} \qquad \textbf{(3-15)}$$

Equation *3-15* is of the form:

$$y = a + b\ln(x) + \frac{c}{x} \qquad \textbf{(3-16)}$$

which is a non-linear equation as a function of T. This equation was solved by plotting ln G versus T and finding the root of the best fit. *TableCurve-2d* software was utilized to fit the data and solve for the parameters where,

$y = \ln G$,

$x = T$,

$a = \ln G_{0,d}$ **(3-17)**

b = -1, and

$$c = -qV_s / k_b \qquad \textit{(3-18)}$$

Equations *3-17* and *3-18* can be used to obtain $G_{0,d}$ and qV_s respectively. $G_{0,d}$ is difficult to interpret physically but can be used to qualitatively compare conductivities of the bed at different conditions. The qV_s term represents an effective energy barrier for electrons to conduct from one metal oxide grain over the depletion region to another metal oxide grain.

3.4.3 Calculation of Sensor Bed Life

Sensor bed life, or the time until regeneration of the adsorbent, is calculated based on the amount of time (days) it would take to theoretically saturate the adsorbent component of the bed (it is assumed that 100% of the uptake is adsorbed in the adsorbent material). In practice the amount of adsorbent that can be utilized will be limited to a finite volume dependent upon the size and geometry of the valve and the actual fugitive emission rate allowance for a particular valve. However, for the present study, a mass of 100 g of adsorbent was used to calculate the sensor life for comparison purposes at different operating conditions. Calculations were then made based on the default valve fugtive emission rate of Equation *1-2*, $E = 6.56 \times 10^{-7}$ *kg/hr/source,* to determine the length of time that it would take 100 g of the bed to be saturated by the default flow rate given the Henry's constant or the equilibrium uptake of a given adsorbent material. The equilibrium uptake q^* (mmol/g) is calculated as follows from the Henry's constant, K:

$$q^*(mmol/g) = \left(\frac{K}{22414}\right)\left(\frac{273}{273+T}\right)\left(\frac{1000}{\rho_p}\right)c \qquad \textit{(3-19)}$$

where: K is Henry's constant ($vol._{adsorbate}$ / $vol._{bed}$) and it is assumed that significant adsorption only occurs on the Al_2O_3 adsorbent component of the bed, 22414 is the molar volume of a gas (cc gas phase/mole gas phase), T is the operating temperature (°C), 1000 is a conversion factor

(1000 mmol gas phase per mole gas phase), and ρ_p is the particle density of adsorbent (1.14 g/cc for Al_2O_3) and c is the concentration of C_3H_6 in the gas phase (mole C_3H_6/mole gas phase).

The sensor life (days) is calculated from the equilibrium uptake, q^*, as follows:

$$SensorLife(days) = (q^*)(MW)\left(\frac{100}{0.66}\right)\left(\frac{1}{24}\right) \qquad \textbf{(3-20)}$$

where: MW is the molecular mass of the adsorbent (42 g/mole for C_3H_6), 100 (g) is the mass of adsorbent assumed to be in the bed, 0.66 is the default valve fugitive emission rate (mg C_3H_6 per hour), and 24 is the number of hours per day.

3.5 Summary

Conceptually, changes in electrical resistance of the metal oxide (SnO_2)/adsorbent (Al_2O_3) fixed bed will be used to monitor the presence of the target gas (C_3H_6) and the adsorption of the gas on the solid will be used to contain the gas. In particular, the changes in electrical resistance, adsorption breakthrough and sensor life will be examined as a function of temperature, adsorbent bed composition and gas concentration. Correlations between sensor (metal oxide) resistance response to the target gas adsorption breakthrough will be made.

Table 1.1 indicates a number of test gases that could be used in the study however tests will focus on propylene (C_3H_6), a key primary refinery product produced by naptha/gas cracking or dehydrogenation of alkanes (Chang, 2000). Tin dioxide (SnO_2), a metal oxide commonly used in the manufacture of gas sensors will be utilized as the sensing material. Alumina (Al_2O_3), an adsorbent commonly used commercially for the adsorption of water vapour, will be utilized as the adsorbent material. Although Al_2O_3 has a low affinity for hydrocarbons, this allowed for a larger number of experiments to be undertaken in a reasonable period of time compared to a

strong adsorbent such as activated carbon and zeolites 4A, 5A, and 13X. This was evidenced by preliminary investigations undertaken for the adsorption of 10% C_3H_6 over zeolite 13X, in which a breakthrough experiment took over 30 minutes compared to less than 10 minutes for the same breakthrough experiment over Al_2O_3. In practice, the use of stronger, higher capacity adsorbents will give higher adsorption uptake. Further discussion of experimental design considerations is given in Appendix A.

Chapter 4 - Results and Discussion

Results of adsorption breakthrough and electrical resistance experiments on the mixed adsorbent / metal oxide bed, also referred to as the sensor bed will be presented and discussed along with their importance to the industrial application. Firstly, certain system and component parameters will be addressed, followed by presentation of preliminary and primary experimental results.

4.1 System Parameters

The root-mean average particle size, the modified Reynolds number, the bed voidage, and the system dead volume were important to understand to ensure that reasonable assumptions were made during analysis of the results.

4.1.1 Root Mean Average Particle Size

Each of the components used in the adsorbent / metal oxide mixtures prepared were sieved to specific Tyler mesh size ranges. A weighted average particle size was determined for each mixture of components, summarized in Table 4.1, and used for calculation purposes. It is assumed that the particles were spherical in diameter, and that the average particle size of each specific component was equivalent to the root-mean average opening size of the screens used in the sieving process. Therefore:

- SnO_2, the metal oxide, was sieved to 10 – 24 Tyler mesh, with sieve openings of 1.68 mm and 0.707 mm respectively, corresponding to a root-mean average screen opening of 1.29 mm.

- Al_2O_3, the adsorbent, was sieved to 24 – 48 Tyler mesh, with sieve openings of 0.707 mm and 0.297 mm respectively, corresponding to a root mean average screen opening of 0.542 mm.

Table 4.1: Weighted Average particle size for adsorbent / metal oxide mixtures utilized

Mixture	d_{Pave}
% vol.	**mm**
100% SnO_2	1.29
10% Al_2O_3 in SnO_2	1.22
20% Al_2O_3 in SnO_2	1.14
30% Al_2O_3 in SnO_2	1.07
40% Al_2O_3 in SnO_2	0.991
70% Al_2O_3 in SnO_2	0.766
100% Al_2O_3	0.542

4.1.2 Modified Reynolds Number

The Reynolds number of the packed bed was calculated for each case using the following modified Reynolds number calculation (Ruthven, 1984):

$$\mathrm{Re}_p = \frac{d_p \cdot u \cdot \rho_g}{\mu_f \cdot (1-\varepsilon_b)}, \qquad \textit{(4-1)}$$

where d_p is the weighted root mean average particle size, u is the superficial velocity, ρ_g is the gas density, μ_f, is the gas viscosity, and ε_b is the void fraction of empty space between particles in the bed. The Reynolds number is a dimensionless parameter that represents the ratio of inertia forces to viscous forces of the flow in the packed bed.

Experimental values of the modified Reynolds number were calculated for flow rates between 80 and 200 sccm for He, and fluid properties based upon temperatures between 50 - 350 °C were considered. The actual adsorbates used experimentally ranged from 1 to 10% C_3H_6 in He, however, values of pure He were used for the calculations as it was assumed that properties would not change significantly with the addition of small amounts of C_3H_6.

The modified Reynolds numbers were calculated to be in the range of 0.15 – 2.6. These values fall within the laminar flow regime and are consistent with laboratory adsorption breakthrough tests (Kovacevic, 2000) and the axially dispersed plug flow model reviewed by Ruthven (1984).

4.1.3 Bed Voidage

Bed voidage, ε_b, is the fraction of empty space between particles compared to the overall bulk space occupied by the particles (refer to Table 4.2). The following equation (Perry and Green, 1997) was utilized to calculate the bed voidage of each pure component comprising the bed (i.e. adsorbent, Al_2O_3, and metal oxide, SnO_2).

$$1 - \varepsilon_b = \frac{\rho_b}{\rho_p}, \qquad \textit{(4-2)}$$

where ε_b, ρ_b, and ρ_p are the bed void fraction, bulk density, and particle density respectively.

Table 4.2: Parameters used to calculate bed voidage.

Composition	ρ_b	ρ_p	ε_b
% vol.	**g/cc**	**g/cc**	V_E/V_T
100% SnO_2	2.28	6.95	0.67
100% Al_2O_3	0.573	1.14	0.50

V_E = Volume of empty space in the bed, V_T = total bed volume

As was done for the modified Reynolds number calculation, a weighted average bed voidage was calculated for the sensor bed, based upon the percent composition of each material in the mixture. Table 4.3 summarizes the bed voidage for each bed composition. However, it was subsequently determined that the actual void fraction should be less than these values, since the smaller adsorbent (Al_2O_3) particles would fill the gaps between the larger SnO_2 particles.

Corrected bed voidage values were determined, based upon the Henry's constant for propylene adsorption on 100% Al_2O_3 and the residence time obtained experimentally for each component mixture based on equation *3-1*. This method assumes that SnO_2 is essentially a non-porous, non-adsorbing component in the mixture, hence the mixture's Henry's constant will be linearly proportional to the % volume of Al_2O_3 in the mixture. Therefore the Henry's constant at each % composition of Al_2O_3 was calculated (from the 100% Al_2O_3 value), followed by a back calculation of the bed voidage required to achieve that Henry's constant, based upon the experimentally obtained residence time for each mixture (equation *3-10)*. The corrected values obtained in this manner are also presented in Table 4.3 and were further confirmed by comparing measured bulk densities of certain mixtures with the bulk density based on the voidage.

Table 4.3: Bed voidage ε_b for adsorbent / metal oxide mixtures.

Mixture	**Weighted Ave ε_b**	**Corrected ε_b**	**Measured ε_b**
% vol.	V_E/V_T	V_E/V_T	V_E/V_T
100% SnO2	0.67	0.67	-
10% Al_2O_3 in SnO_2	0.66	0.53	-
20% Al_2O_3 in SnO_2	0.64	0.51	-
30% Al_2O_3 in SnO_2	0.62	0.47	0.55
40% Al_2O_3 in SnO_2	0.60	0.48	0.51, 0.51
70% Al_2O_3 in SnO_2	0.55	na	0.53
100% Al_2O_3	0.50	0.50	-

V_E = Volume of empty space in the bed, V_T = total bed volume, - not measured

4.1.4 System Dead Volume Response

The mean retention time, μ, and variance, σ^2, of a step change in gas composition are the primary parameters obtained experimentally from adsorption breakthrough analysis. System dead space will impact results of the analysis by increasing the residence time and variance of a system for a given adsorption uptake. Since adsorption occurs only in the packed bed portion of the system, the Henry's constants obtained from the analysis will be lower than the actual value due to the dead space effects. To compensate, the mean residence time and variance of the dead volume were determined experimentally and these values were subtracted from the overall system mean residence time and variance during analysis.

The system dead volume was comprised of the volume in the system excluding the adsorbent / metal oxide bed, and included the reactor (above and below the bed), the tubing and valving, and the TCD. The dead volume was reduced during the design and assembly of the apparatus wherever practicable, however, in the present system the dead space of the reactor was significant since the adsorbent / metal oxide bed comprised only a portion of the complete reactor vessel (Figure 3.2).

In order to measure the dead volume, glass beads were placed in the bed portion of the reactor for the purpose of filling up the volume in that portion of the vessel with a non-adsorbent solid. Tracer experiments were then carried out at experimental conditions between 50 - 200 ^{o}C and between 80 - 200 sccm with 10% C_3H_6 in He. The mean residence time and the variance of the breakthrough curves were obtained by use of curve fitting the TCD response data and then using moment analysis as described by equations 3.1 and 3.2. The results are tabulated in Table 4.4.

Table 4.4: Mean Residence Time (s) and Variance (s^2) of System Dead Volume (from breakthrough of 10% C_3H_6 in He over glass bead).

Mean Residence Time (s) and Variance of System Dead Volume (s^2)						
Flow	80 sccm	90 sccm	100 sccm	125 sccm	150 sccm	200 sccm
μ_{50C}	63.4	60.1	52.0	42.4	35.6	26.7
σ^2_{50C}	1369.0	1070.5	803.1	546.2	386.0	232.9
μ_{75C}	58.5	54.7	48.4	38.7	32.5	24.0
σ^2_{75C}	1187.2	947.1	712.3	477.2	338.9	194.5
μ_{100C}	55.2	51.2	45.9	36.3	30.4	22.3
σ^2_{100C}	1029.5	837.9	631.7	417.0	297.6	162.5
μ_{150C}	50.9	46.6	42.7	33.1	27.7	20.0
σ^2_{150C}	774.2	655.8	496.9	318.3	229.5	113.3
μ_{200C}	48.1	43.6	40.6	31.0	26.0	18.6
σ^2_{200C}	582.2	513.3	390.9	243.0	176.9	79.1

The mean residence time and variance of Table 4.4 are subtracted from the response obtained during experimentation using the adsorbent / metal oxide bed. This methodology introduces a small bias in the calculation of the actual values of axial dispersion (D_L), lumped mass transfer resistance (*LMTR*) and Henry's constant (K). This bias occurs because during the system dead volume measurements, the bed volume was occupied by glass beads in an attempt to fill this volume and hence remove it from the overall system volume during these measurements. In actuality, these glass beads contained a certain volumetric void fraction, and hence the entire volume of the bed portion of the reactor vessel was not removed from influencing the mean residence time and variance of the system dead volume. It is postulated that this led to a marginal increase in the mean residence time and variance of the system response and hence a bias towards decreased values of axial dispersion, lumped mass transfer resistance and Henry's constant.

However, since the uptake on the adsorbent in the bed is assumed to dominate the residence time, it is thought that this bias will lead to an insignificant error during conditions at which high uptake occurs and hence the Henry's constant is relatively large (i.e low temperature and/or high % volume of adsorbent in the sensor bed). The error will be larger during conditions for which uptake is small and hence the residence time is dominated by the bed voidage.

4.2 Pure Adsorbent and Metal Oxide Component Results

Preliminary experiments using only pure components were designed to test the apparatus and experimental procedures. This was done to determine the range of conditions over which reliable data, consistent with theory, could be practicably obtained, and to provide baseline data for electrical resistance and adsorption breakthrough measurements.

4.2.1 Bulk Electrical Resistance of Pure Metal Oxide (SnO_2)

Electrical resistance measurements were made on bulk samples of SnO_2 of different particle size. This was done in order to determine a practical particle size of metal oxide that would be utilized in subsequent experiments. Commercially available sintered SnO_2 [Alfa Aesar tin (IV) oxide, 99.9% (metals basis)] was ground using a mortar and pestle to particle sizes ranging from 80 mesh (less than 0.2 mm) to 10 mesh (greater than 2 mm). Bulk resistance measurements of 10 ml samples were made in a 25 ml beaker by placing electrodes at diametrically opposite sides of the beaker. This was repeated three times for each sample. A constant reading could not be established so the range of resistances measured is presented for each particle size and is tabulated in Table 4.5. It was determined that 10 – 24 mesh SnO_2 was relatively low in electrical resistance (as compared to SnO_2 samples of smaller size), an important consideration in order to

ensure that initial metal oxide resistance could be monitored by the apparatus. Subsequent experimentation was carried out utilizing 10 – 24 mesh SnO_2 particles.

Table 4.5: Effect of particle size on electrical resistance of sintered bulk SnO_2 (untreated).

Taylor Mesh Size	d_p (mm)	R (MΩ)
> 80	< 0.2	430 - 500
42 - 80	0.2 - 0.4	260 - 540
24 - 42	0.4 - 0.7	170 - 260
10 - 24	0.7 - 2	26 - 50
< 10	> 2	19 - 22

The bulk resistance values are consistent with the results of Namoto and Oda (1981) which indicate that the resistance across a single grain boundary is greater than the resistance across a single grain. In Table 4.5, as the particle size increased, the number of inter-granular contacts decreased, as did the bulk resistance measurement across the bed.

4.2.2 In-situ Electrical Resistance of 100% Metal Oxide (SnO_2)

Electrical resistance tests were carried out on pure 10 – 24 mesh SnO_2 at temperatures ranging from 150 – 350 °C. This was done to determine whether the resistance could be measured over a range of operating conditions and to check the consistency of the operating procedure. At each temperature a series of step changes in gas composition were made in which the test gas was cycled between He, Air, He, and 10% C_3H_6 in He for 15 minutes each, following pretreatment and a 1 hour oxidation period. Figure 4.1 illustrates the experimental results of electrical resistance on a continuous basis for data at 150, 200, and 275 °C.

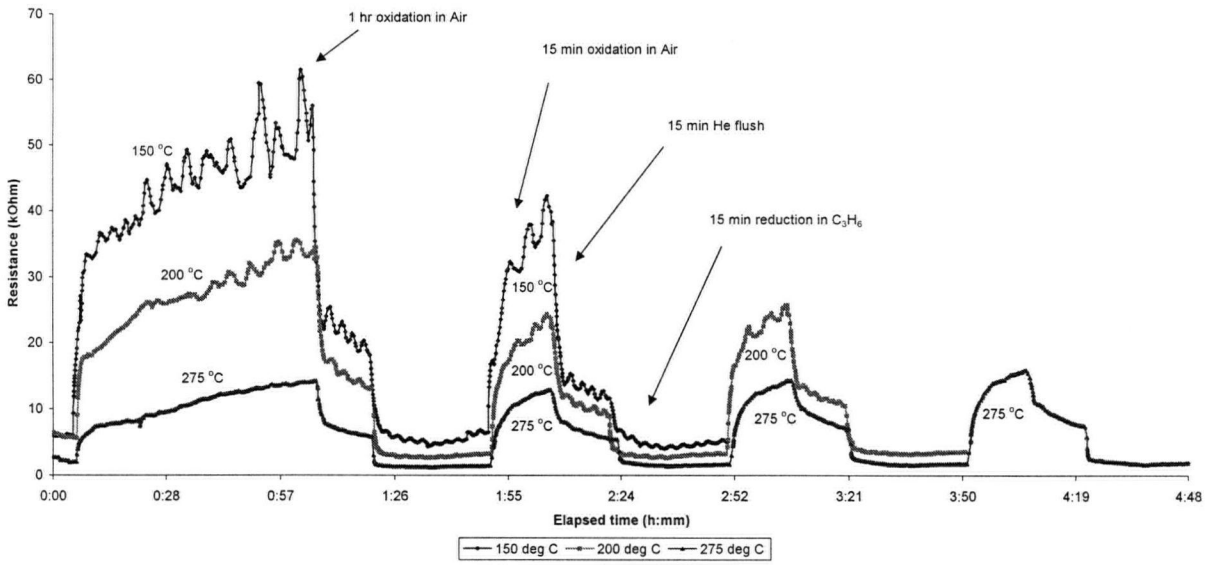

Figure 4.1: Electrical resistance measurements for 100% SnO_2 while gas cycling between oxidation in Air / He flush / C_3H_6 reduction at temperatures of 150, 200, and 275 °C.

The results show that after oxidation, the resistance of the SnO_2 sample increased significantly and that after both the He flush and the reduction in 10% C_3H_6, the sample's resistance dropped significantly. These data are summarized further in Table 4.6 for points corresponding to the end of both the 1hr and the 15 minute oxidation cycles, R_a, and the beginning and end of the C_3H_6 reduction cycles, $R_{a,He}$ (the same as the end of the 15 minute He flush) and R_g respectively. The sensitivity of the pure SnO_2 to changes in gas composition is also given in Table 4.6 and shown in Figure 4.2.

Table 4.6: Summary of electrical resistance results, for pure SnO_2 between 150 – 350 °C.

Temp	R_a	$R_{a,He}$	R_g	S_1	S_2
°C	kΩ	kΩ	kΩ	S_N (S_A)	S_N (S_A)
1 hour oxidation data					
150	56.00	19.15	4.38	0.92 (12.8)	0.77 (4.4)
200	35.55	13.82	2.61	0.93 (13.6)	0.81 (5.3)
275	14.20	5.98	1.22	0.91 (11.6)	0.80 (4.9)
350	10.50	3.15	0.82	0.92 (12.8)	0.74 (3.8)
qV_s	0.245	0.254	0.238	**eV**	
90% CI	0.302	0.326	0.264	**eV**	
90% CI	0.187	0.182	0.213	**eV**	
$G_{0,d}$	6.00E+03	2.05E+04	6.56E+04	**kmho**	
R_0	1.67E-04	4.87E-05	1.52E-05	**kΩ**	
15 min oxidation data					
Temp	R_a	$R_{a,He}$	R_g	S_3	S_4
150	42.26	11.23	4.02	0.90 (10.5)	0.64 (2.8)
200	24.30	8.86	2.63	0.89 (9.2)	0.70 (3.4)
275	12.85	5.39	1.31	0.90 (9.8)	0.76 (4.1)
350	10.27	3.20	0.85	0.92 (12.1)	0.73 (3.8)
qV_s	0.209	0.187	0.224	**eV**	
90% CI	0.251	0.244	0.250	**eV**	
90% CI	0.167	0.129	0.197	**eV**	
$G_{0,d}$	3.20E+03	5.74E+03	4.68E+04	**kmho**	
R_0	3.12E-04	1.74E-04	2.14E-05	**kΩ**	

Key:
R_a = Resistance in the oxidized state (after 1 hour oxidation or after 15 min)
$R_{a,He}$ = Resistance in the oxidized state but after 15 minutes of He flush
R_g = Resistance in the reduced state (after 10% C_3H_6 passed through the bed for 15 minutes)
S_1, S_2, S_3, S_4 = Sensitivity as given in figure below
S_N = normalized sensitivity
S_A = absolute sensitivity

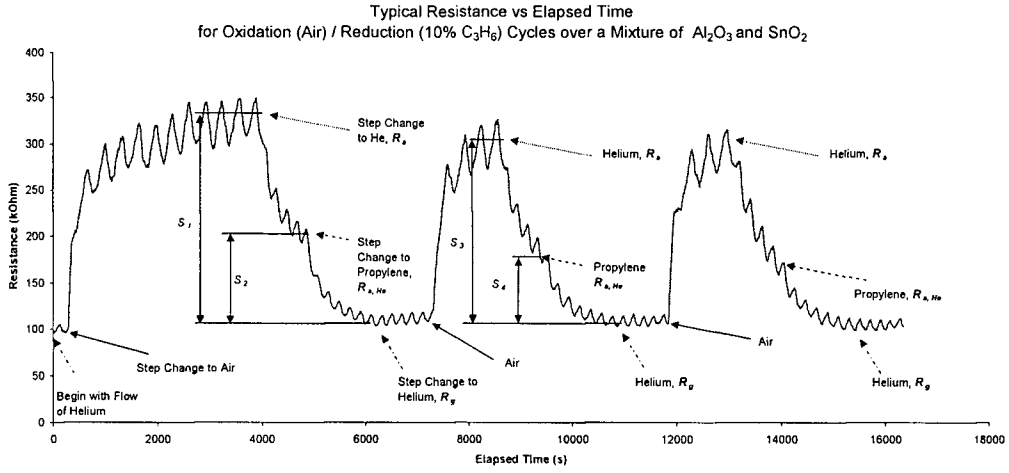

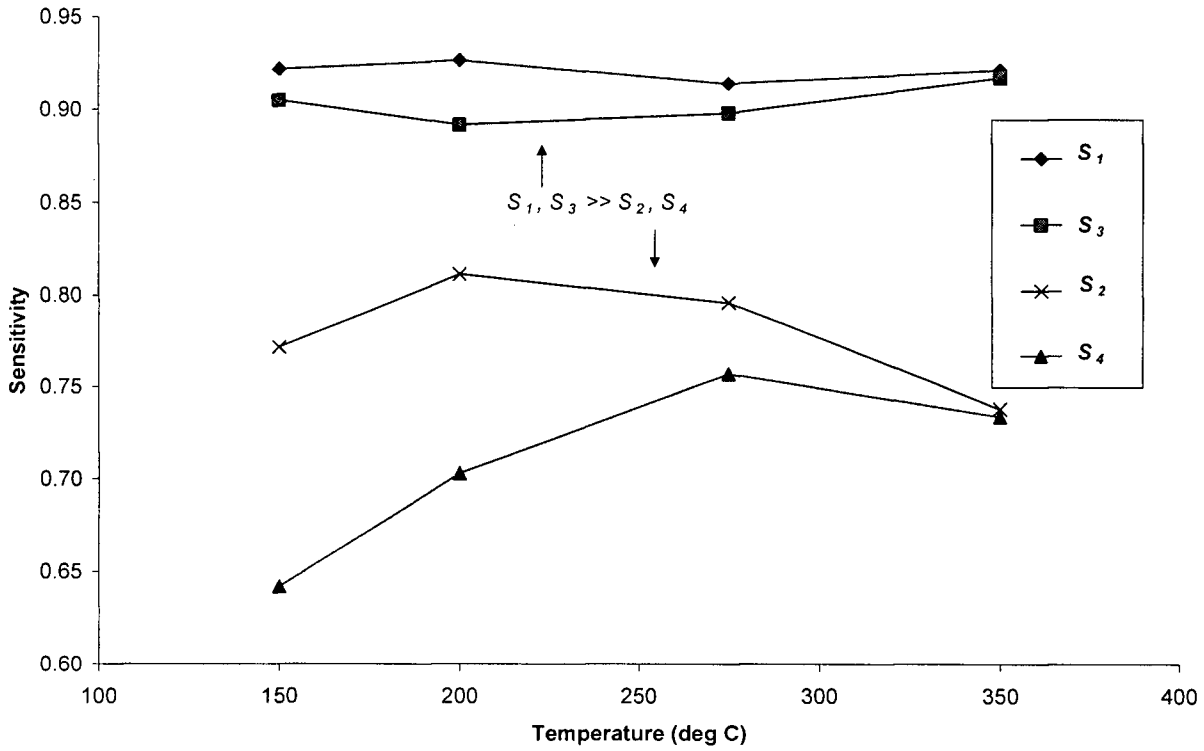

Figure 4.2: Comparison of sensitivity of pure SnO_2 after 1 hr oxidation in air, 15 min oxidation in air and for reduction in 10% C_3H_6 after 1 hr oxidation and 15 min oxidation, respectively (refer also to the key of Table 4.6).

Figure 4.2 illustrates that the sensitivity of pure SnO_2 was quite high at all temperatures between the fully oxidized state (for both 1 hour, and 15 minute, oxidation cycles) and the fully reduced state (which includes both a flush with He and a reduction with C_3H_6), given by the upper two sets of data points, S_1 and S_3. Also, the sensitivity was marginally higher when the metal oxide was oxidized for a full hour, compared to when the material was only oxidized for the 15 minute cycle, S_1 compared to S_3.

The sensitivity, defined for the C_3H_6 reduction phase only is somewhat lower (the lowest two sets of data points, S_2 and S_4) as expected since the beginning of the C_3H_6 reduction phase corresponds to the end of the He flush phase, seen in Figure 4.1, by which time the electrical resistance of SnO_2 has already decreased as a result of desorption of O_2.

The results also indicated that as the temperature was increased between subsequent trials, the electrical resistance decreased exponentially. These results are consistent with the modified inter-granular contact resistance model as outlined by Madou and Morrison (1989) and Barson and Weimer (2001). Electrical resistance versus temperature is plotted in Figures 4.3.

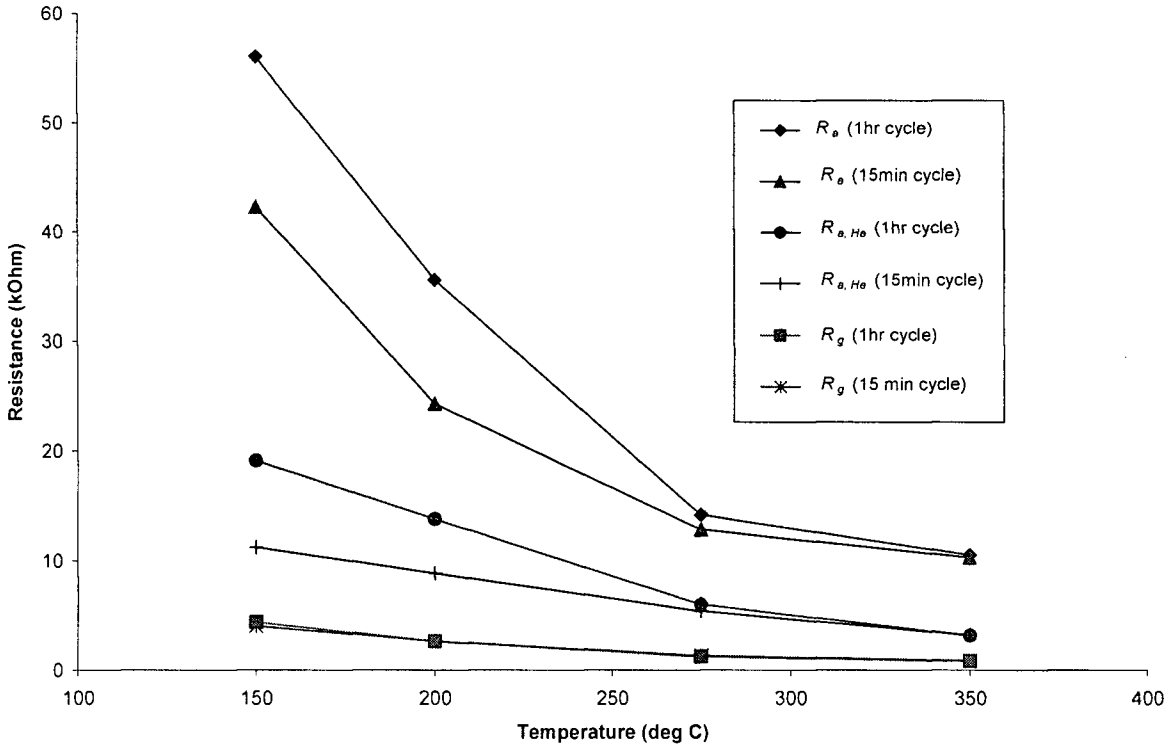

Figure 4.3: Comparison of R vs T for SnO_2 for both 1 hour and 15 minute oxidation cycles, and for 10% C_3H_6 reduction cycle.

The plot of ln ($1/R$) versus T is shown in Figure 4.4 and provides details into the surface state of the metal oxide conductor (SnO_2). According to the model, the fitting parameters of equation *3-16* were used to determine the energy barrier, qV_s, that electrons must overcome in order to cross from one grain of metal oxide to the next, and hence conduct electricity. Therefore, when the qV_s energy barrier term increases, the contact resistance between the grains of the metal oxide also increases. During the oxidation cycle performed experimentally, the adsorption of oxygen

extracts electrons from the surface region, indicated by the space charge region of Figure 2.2, and for electrons to conduct they must obtain enough energy, qV_s, to cross this insulating barrier, hence resistance increases.

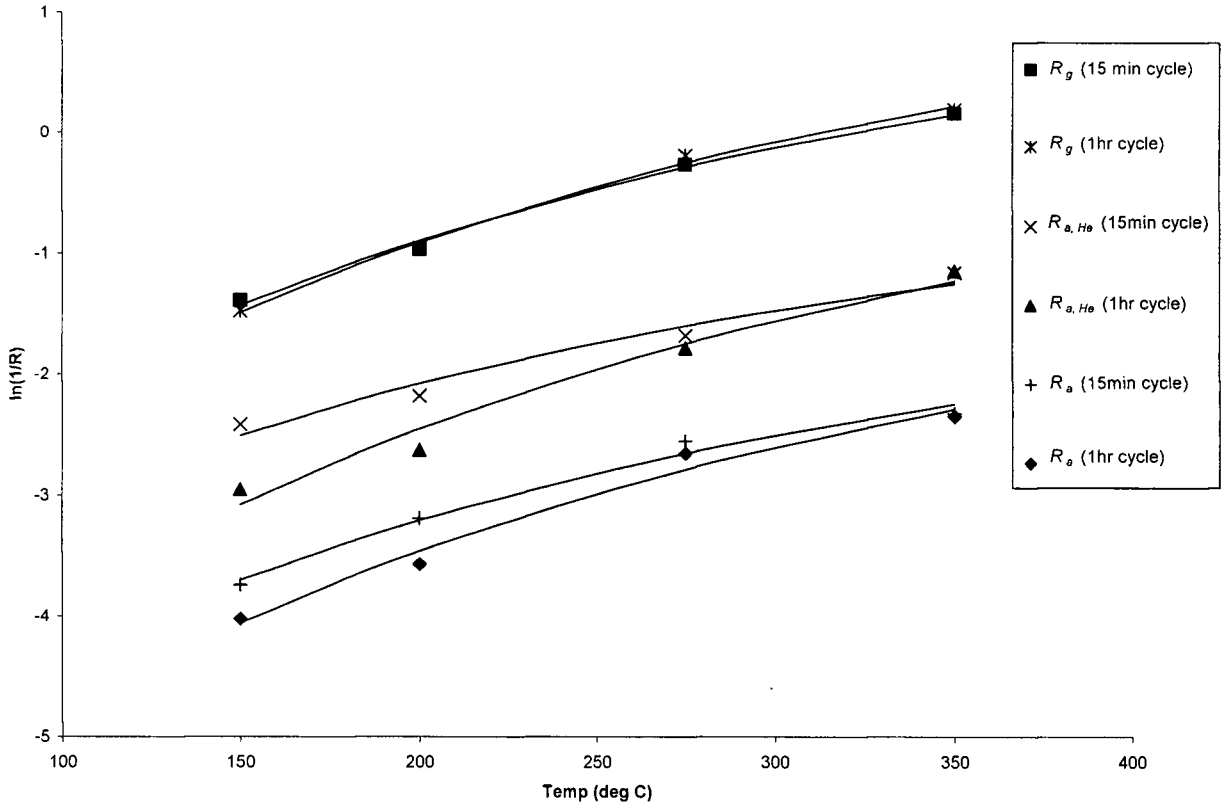

Figure 4.4: Plot of ln ($1/R$) vs T for SnO_2 after oxidation for 1 hr, 15 min, at the beginning of the 10% C_3H_6 reduction phase, and in the completely reduced phases.

Figure 4.4 and Table 4.6 indicate that the energy barrier varies depending on the length of the oxidation cycle, however, given the confidence intervals, it is not clear as to whether the mechanism of surface resistance change is the key factor in determining overall resistance. The energy barrier was greater for the case where the sample was oxidized for 1 hour as compared to when the sample was oxidized for only 15 minutes for all cycles and this general trend is consistent with the model for inter-granular resistance. For example the qV_s energy associated with the resistance of the 1 hour oxidized state was 0.245 eV compared to 0.209 eV for the 15

minute oxidation cycle. Similarly, the qV_s energy barrier was higher at the initiation of the C_3H_6 cycle that was previously oxidized for 1 hour compared to the 15 minute cycle with qV_s energies of 0.254 eV and 0.187 eV respectively. At the completely reduced point in the oxidation/reduction cycles the qV_s energies were 0.238 eV and 0.224 eV for the 1 hour and 15 minute oxidation cycles respectively. The energy barrier decreases as the sample undergoes a corresponding reduction in surface resistance however these changes are very small and may reflect that the actual surface barrier does not have as great an impact as initially postulated for the present system, or that other factors such as diffusion or the temperature coefficient of resistance for the SnO_2 are more dominant. Given the confidence intervals on these trends, no conclusive explanation can be drawn and these results may be indicative that the slope actually remains fairly constant overall

On the other hand, $G_{0,d}$, does show significant changes between oxidation and reduction cycles. It is representative of other factors that affect the conductance of the material, such as electron mobility, inter-granular contact area (a function of bed compression), and other less sensitive factors determining the conductance G, or inversely accounting for resistance, R. Figure 4.4 and Table 4.6 indicate that the relative change in $G_{0,d}$ is greater than qV_s during gas cycling.

4.2.3 Adsorption Breakthrough of 100% Adsorbent (Al_2O_3)

Adsorption breakthrough measurements were carried out over 24 - 42 mesh Al_2O_3 at temperatures between 50 - 200 °C and at flow rates between 80 - 200 sccm. This work was valuable in obtaining baseline adsorption data for the Al_2O_3.

The mean residence time, μ, and the variance, σ^2, of the adsorption breakthrough curves were determined by moment analysis. Breakthrough curves are presented in Appendix B and analysis, including summaries of residence time and variance, Henry's constant, K, axial dispersion, D_L,

and lumped mass transfer resistance, *LMTR* are presented in Appendix C. A summary of the adsorption parameters determined from the analysis is given in Table 4.7.

Table 4.7: Summary of parameters obtained from breakthrough analysis of 10% C_3H_6 in He over 100% Al_2O_3.

T	*K*	*q**	D_L	*LMTR*	k_{eff}
°C	*vol./vol.*+	mmol/g	cm^2/s	s	s^{-1}
50	36.5	0.12	0.432	3.56	0.008
100	9.38	0.027	0.893	3.67	0.029
150	2.77	0.007	1.17	5.35	0.067
200	1.19	0.003	3.54	6.01	0.138

\+ $volume_{adsorbate}$ / $volume_{bed}$ including both adsorbent and metal oxide components of the bed

The Henry's constant was determined from the analysis at each temperature, and was used to calculate the uptake of the adsorbent material. The plot of mean residence time versus the inverse of flow rate is shown in Figure 4.5. The slope of this plot is used to determine the Henry's constant according to the methods described in Section 3.4.1. It can be seen that the slope and therefore the Henry's constant reduces from 36.5 to 1.19 vol./vol. as the temperature increased from 50 to 200 °C, and that above 150 °C, the Henry's constant and uptake becomes negligible for practical purposes, compared to temperatures below 150 °C. This is an important result because it indicates that adsorption would not be practical if the temperature was increased above 150 °C and hence this was made the upper temperature limit of subsequent testing for the present adsorbent (Al_2O_3).

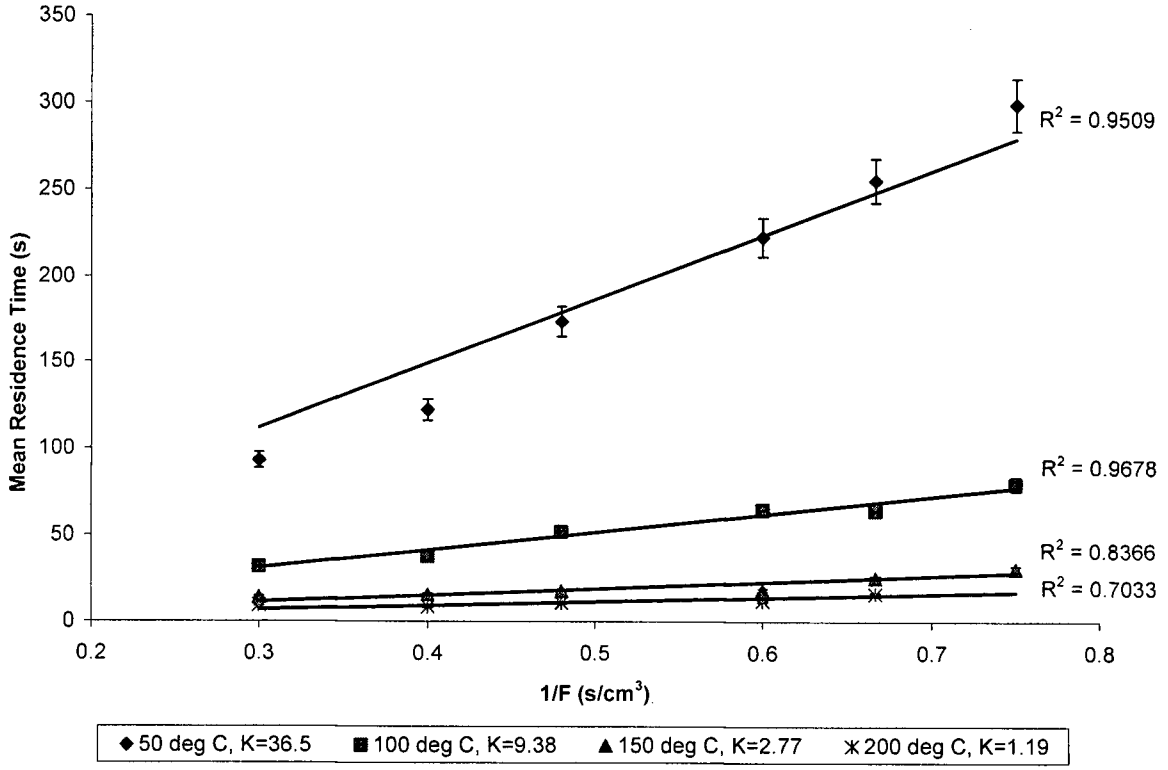

Figure 4.5: Plots of μ vs $1/F$ from which the Henry's constant K was determined (error bars show +/-5%).

The Arrhenius plot of Henry's constant versus temperature for the Al_2O_3 sample at temperatures from 50 – 200 °C is shown in Figure 4.6. The data show a good linear fit (r^2=0.99), from which the heat of adsorption, $-\Delta H_{ads}$ = 29.2 kJ/mol, was obtained. Error bars indicating +/-5% are also included in the plot and show that the data contains very little scatter.

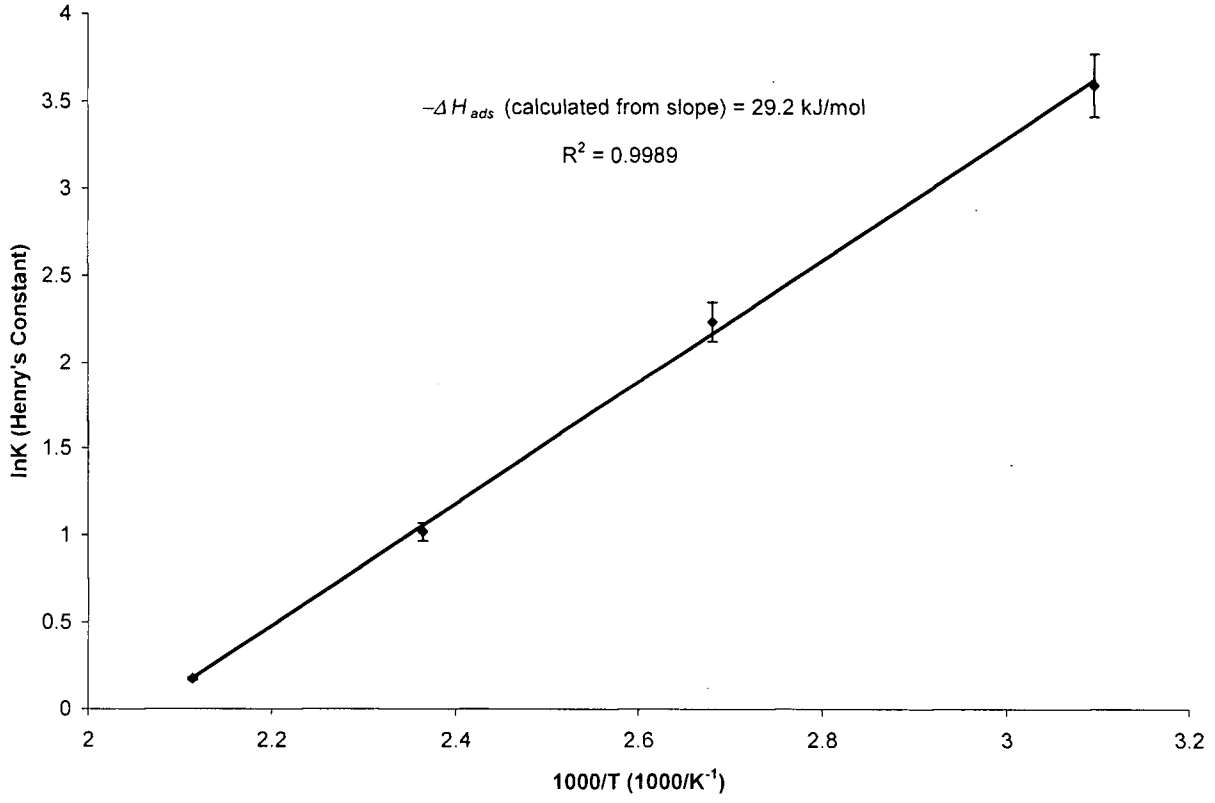

Figure 4.6: Determination of $-\Delta H_{ads}$ for adsorption of 10% C_3H_6 in He over 24 - 42 mesh Al_2O_3 from 50 - 150 °C.

Jarvelin and Fair (1993) report very low equilibrium uptake of < 0.2 mmol/g of C_3H_6 on activated Al_2O_3 at 5 kPa and 25 °C. The present results, from Table 4.7, show similar equilibrium adsorption uptake, at 0.12 mmol/g at 50 °C and approximately 12 kPa (10% C_3H_6 and total pressure of approximately 120 kPa), and heat of adsorption of 29.2 kJ/mol from Table 4.7. Literature was not available to compare the heat of adsorption but the present results are reasonable when compared with data taken for the adsorption of ethylene (C_2H_4) on γ-Al_2O_3 for an air purification study, with an uptake of 0.5 mmol/g at 22 °C and 100 kPa and $-\Delta H_{ads}$ = 29.3 kJ/mol (Rege et al, 2000). The results of the present study and those of the above reference indicate that the uptake of light hydrocarbons on Al_2O_3 is low compared to typically utilised

commercial adsorbents such as zeolites 4A, 5A and 13X; molecular sieves or activated carbon, as reviewed in Chapter 2, Table 2.2.

When $-\Delta H_{ads}$ is small, it suggests that the bonds between the adsorbent and adsorbate are weak, and that as temperature increases the adsorption coverage will be very low. Ruthven (1984) indicates that physisorption is the dominant mechanism when the heat of adsorption is less than 2-3 times the heat of vapourisation. In the present study, physisorption dominates since the heat of adsorption, $-\Delta H_{ads}$= 29.2 kJ/mol, is approximately 2 times the cited heat of vapourisation of C_3H_6, ΔH_{vap} = 16.04 kJ/mol (Majer and Svoboda, 1985). This could be a significant attribute for an industrial sensor since regeneration, preferably carried out at low temperature for economic reasons, would be required once the sensor bed's saturation point is approached.

A plot of $(\sigma^2/2\mu^2)L/v$ vs $1/v^2$, Figure 4.7, directly yields, D_L, and the *LMTR* from the slope and intercept respectively as described in Section 3.4. The results for Al_2O_3 are shown in Table 4.6, and indicate that as the temperature is increased both the axial dispersion (slope) and the *LMTR* (y-intercept) increase. This relationship results, since both parameters are functions of the mean residence time of the breakthrough curve, which decreases with increasing temperature.

Axial mixing (dispersion) will generally occur when a fluid flows through a packed bed and design objectives generally try to reduce this effect since it will reduce the efficiency of the adsorption process. In the case of an industrial sensor bed design however, the flow rate would be very small and limited generally to a value on the scale of the default emission factor for a valve ($E = 6.56 \times 10^{-7}$ *kg/hr/source*), and hence it is expected that certain levels of axial dispersion could not be practically designed out of the system. However, commercial designs should try to minimize this effect, perhaps through the incorporation of a monolith type of bed or WMH.

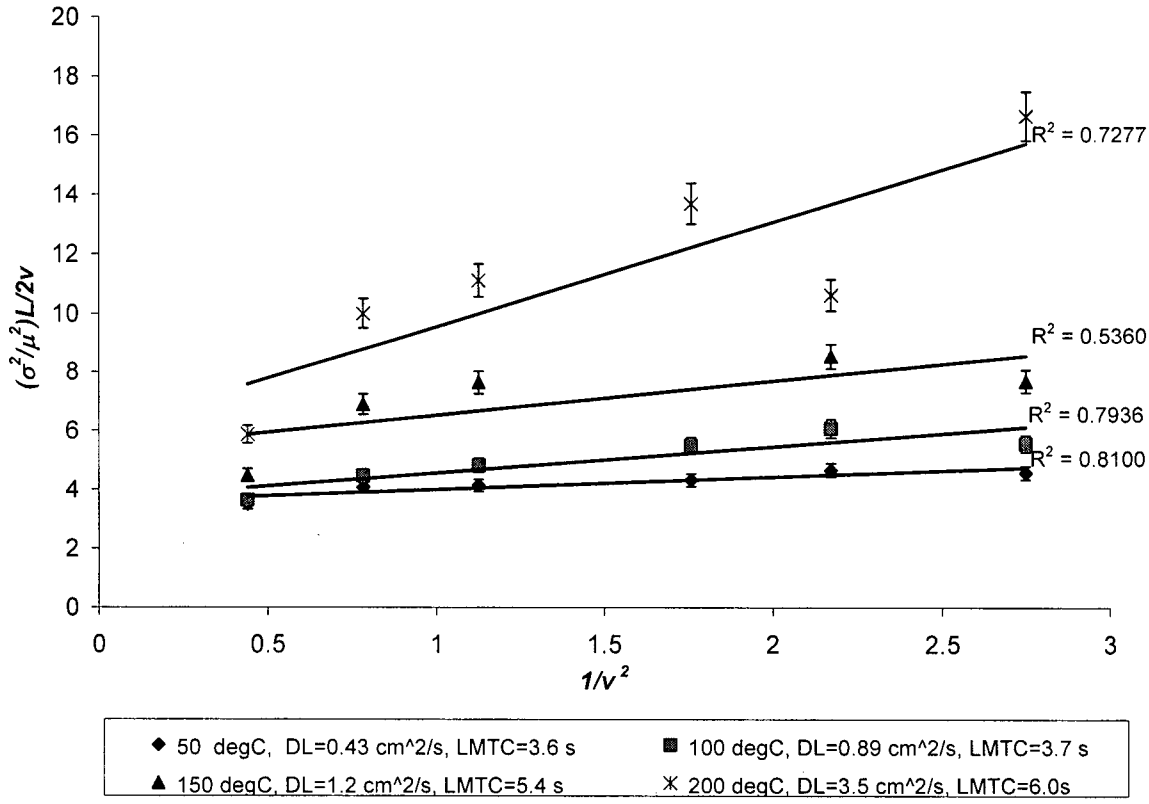

Figure 4.7: Plots of $(\sigma^2/2\mu^2)L/v$ vs $1/v^2$ to determine D_L (slope) and *LMTR* (intercept) for adsorption of 10% C_3H_6 in He over 24-42 mesh Al_2O_3 from 50 - 200 °C (error bars represent +/-5%).

The *LMTR* can be lowered by reducing the size of the adsorbent particles utilized in the sensor bed. The pressure drop across the bed is typically a major design constraint and hence particles need to be sized (i.e. made larger) to reduce this. The *LMTR* can be relatively high in such cases. In an industrial sensor bed for valve stem fugitive emissions the default fugitive emission rate is very small and hence the pressure drop due to viscous effects across the bed will be negligible, as was seen experimentally in the present study. The largest pressure drop observed experimentally was approximately 3.5 kPag where the static operating pressure was 41.5 kPag with flow of 200 sccm of 10% C_3H_6 in He. Smaller adsorbent grains or alternative adsorbent structures such as carbon nonotubes, zeolitic coated monoliths could potentially reduce mass transfer effects and hence increase uptake and reduce the length of unuseable bed (LUB).

4.3 Mixed Adsorbent / Metal Oxide Bed Results

Mixed adsorbent / metal oxide bed (sensor bed) experimental work consisted of two phases.

- Firstly, adsorption breakthrough measurements and electrical resistance measurements were taken simultaneously at constant adsorbate concentration varying the sensor bed composition.
- Secondly, adsorption and electrical resistance measurements were taken simultaneously at a constant adsorbent / metal oxide bed composition, varying the adsorbate concentration.

Adsorption breakthrough experiments were carried out for all conditions independent of the electrical resistance measurements in order to obtain the data for moment analysis. Adsorption breakthrough results will be presented first for both experimental phases, followed by the electrical resistance results for both phases.

4.3.1 Adsorption Breakthrough at Varying Adsorbent / Metal Oxide Concentration

Breakthrough experiments were carried out for sensor bed compositions from 10% Al_2O_3 – 40% Al_2O_3 in SnO_2 and temperatures from 50 – 150 ^{o}C varying the flowrate of adsorbate from 80 - 200 sccm. The concentration of adsorbate was kept constant for each experiment at 10% C_3H_6 in He. K, D_L and $LMTR$ were extracted from the analysis and are shown in Table 4.8. Results for 100% Al_2O_3 are also shown for comparison. The analysis was greatly simplified by the assumption that Henry's Law was applicable.

Table 4.8: Summary of adsorption results for 10% C_3H_6 in He while varying the composition of adsorbent / metal oxide mix and temperature.

T	K (for Bed)	q^* (for Bed)	Sensor Life [++]	D_L	$LMTR$	k_{eff}
°C	*vol./vol.* [+]	mmol/g	days	cm^2/s	s	s^{-1}
10% Al_2O_3, ε_b = 0.531, $-\Delta H_{ads}$ = 30.0 kJ/mol						
50	4.76	0.016	4	0.921	5.55	0.043
75	1.85	0.0057	1.5	0.0133	11.2	0.055
100	1.07	0.0031	1	1.29	7.49	0.141
150	0.0069	2E-05	<1	[+++]	[+++]	[+++]
20% Al_2O_3, ε_b = 0.506, $-\Delta H_{ads}$ = 32.4 kJ/mol						
50	8.88	0.029	8	0.845	4.26	0.027
75	4.57	0.014	4	0.705	4.88	0.046
100	2.27	0.0065	2	1.02	5.77	0.078
150	0.52	0.0013	<1	[+++]	[+++]	[+++]
30% Al_2O_3, ε_b = 0.473, $-\Delta H_{ads}$ = 24.1 kJ/mol						
50	13.7	0.045	12	0.626	4.36	0.015
75	7.48	0.023	6	0.783	4.34	0.028
100	4.41	0.013	3	0.973	4.82	0.042
150	1.63	0.0041	1	1.75	5.45	0.101
40% Al_2O_3, ε_b = 0.477, $-\Delta H_{ads}$ = 25.2 kJ/mol						
50	17.7	0.058	16	0.362	4.08	0.013
75	9.47	0.029	8	0.718	3.85	0.025
100	5.24	0.015	4	0.976	3.96	0.044
150	1.94	0.0049	1	0.869	6.12	0.077
100% Al_2O_3, ε_b = 0.497, $-\Delta H_{ads}$ = 29.2 kJ/mol						
50	36.5	0.12	32	0.432	3.56	0.008
100	9.38	0.027	7	0.893	3.67	0.029
150	2.77	0.007	2	1.165	5.35	0.067
200	1.19	0.0027	1	3.54	6.01	0.138

[+] *$volume_{adsorbate}$ / $volume_{bed}$ including both adsorbent and metal oxide components of the bed*

[++] *values are calculated based on 100g of adsorbent*

[+++] *indicates that these data were very unobtainable due to the scatter in the plot for axial dispersion, D_L, and lumped mass transfer, LMTR when obtained at high temperature and low concentration of adsorbent (Al_2O_3) in the bed (refer to Appendix C for further detail).*

4.3.1.1 Effect of % Volume Composition of Adsorbent / Metal Oxide Mixture

As the percent volume of adsorbent increases in the sensor bed, the Henry's constant based on the total bed volume including metal oxide, and hence the uptake, increases proportionally. This

is expected since the adsorbent is a porous material, and uptake at a given temperature and adsorbate concentration is dependent upon the number of sites per adsorbent particle. The number of sites per particle is assumed constant therefore the total uptake is dependent upon the volume of adsorbent material utilized. This trend also agrees with the assumption that SnO_2 is essentially a non-porous, non-adsorbing material. The relationship can be seen in Figure 4.8.

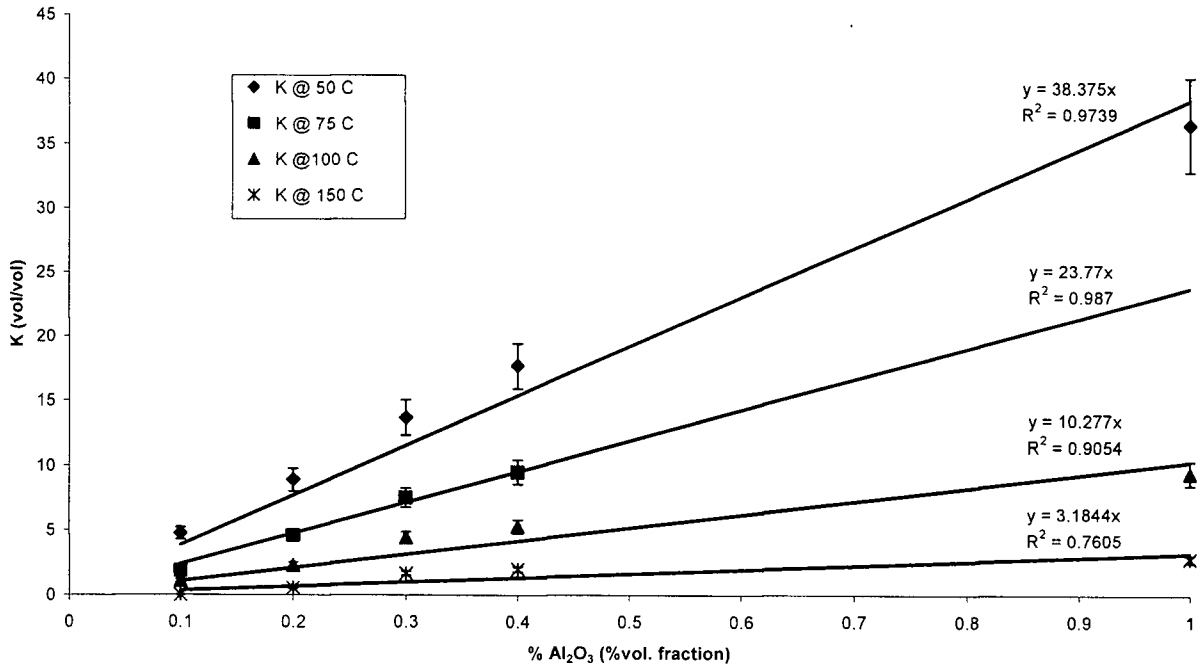

Figure 4.8: Henry's constant, *K*, as a function of % volume of adsorbent and temperature (error bars represent +/-10%).

The Henry's constant at 10% Al_2O_3 and 50 °C was determined to be 4.76 ($vol._{adsorbate}/vol._{bed}$), increasing to 17.7 at 40% Al_2O_3 and 36.5 at 100% Al_2O_3. This indicates that the total uptake of the target gas and hence the sensor life increase as a function of the %volume of adsorbent utilized. In a practical containment application, it is desirable to maximize the volume adsorbed

and hence in a mixed bed, the maximum %volume of adsorbent should be utilized that would also exhibit a practical sensor resistance response to the target gas.

The sensor life, given in Table 4.8, is the amount of time that it would take the default emission to fully breakthrough the adsorbent bed, based upon the experimentally obtained Henry's constant and 100g of adsorbent. It is based upon the default-zero valve fugitive emission rate (*$E = 6.56 \times 10^{-7}$ kg/hr/source*), given in Section 1.1.2 and calculated according to equation *3-20*.

The sensor bed containing 10% Al_2O_3 had a maximum sensor life of 4 days at 50 °C, whereas the sensor bed containing 40% Al_2O_3 had a maximum sensor life of 16 days at 50 °C. If the sensor bed contained 100% Al_2O_3 then it would have a sensor life of 32 days at 50 °C, but only 2 and 1 days at 150 and 200 °C respectively. In addition, the pure Al_2O_3 bed had a very large electrical resistance, greater than the resistance measurement capability of the instrumentation utilized, and consequently it would not be a practical sensor composition in itself.

Sensor life could be improved by making the sensor bed larger, thereby allowing for a proportionally larger volume of adsorbent material. In addition, the adsorbent selected would be optimized so that it has a more effective equilibrium uptake capacity than Al_2O_3 (used only for experimental purposes). Section 2.2.5 reviewed a number of such adsorbents. As can be seen in Table 2.2, zeolite 13X would yield a bed life of 265 days at 200 °C; zeolite 4A gives a bed life of 212 days at 200 °C; zeolite 5A gives a bed life of 636 and 451 days at 50 and 150°C respectively; and activated carbon gives a bed life of 1380 days at 25°C.

4.3.1.2 Effect of Temperature

Table 4.8 and Figure 4.8 show that Henry's constant, and hence the uptake and sensor life decrease as a function of increasing temperature for each sensor bed composition. The lines of Figure 4.9 illustrate the effect of temperature on Henry's constant for each sensor bed composition and indicate qualitatively that the relationship is exponential in nature.

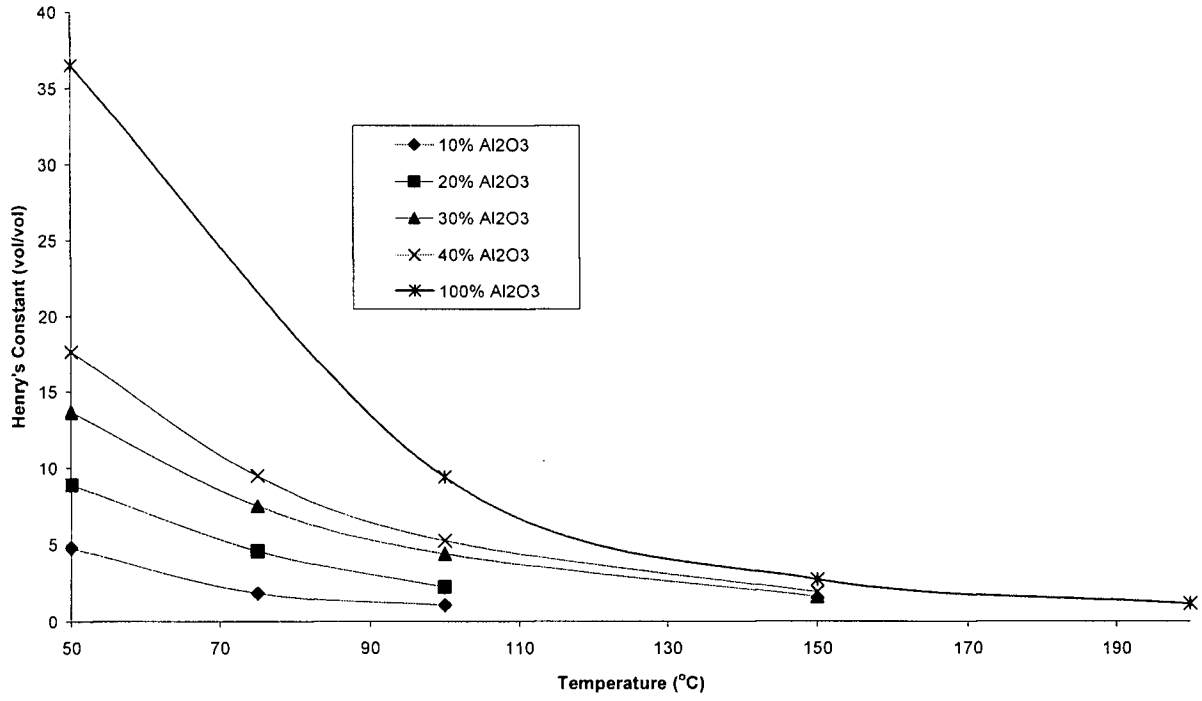

Figure 4.9: Henry's constant, *K*, versus temperature, *T*, for varying sensor bed composition.

4.3.1.3 Heat of Adsorption

Figure 4.9 illustrates that at 40% Al_2O_3 (typical), Henry's constant decreases from 17.7 to 1.94 from 50 to 150 °C. Henry's constant is an Arhennius temperature dependent relationship given by the vant Hoff correlation (equation *2-4b*) and hence this behavior is expected.

If an Arhennius plot of the Henry's constant and temperature is made then the heat of adsorption can be obtained from the slope. Such a plot of ln K versus $1/T$ is shown in Figure 4.6 for 100% Al_2O_3. Similarly, plots were made for each sensor bed composition and the heat of adsorption determined. The results are given in Table 4.8. The heat of adsorption for each sensor bed composition varies (between approximately 10-18%) from the value of 29.2 kJ/mol. for the 100% Al_2O_3 bed. This scatter may be related to the effect of surface adsorption on SnO_2 present in the bed.

In each case however, the values obtained for the heat of adsorption indicate that the system is dominated by physisorption rather than chemisorption. This is an important result, since for adsorbent regeneration, it may be possible to carry out a simple flush of the commercial unit with an inert gas and capture the desorbed gas on the downstream side of the bed. However, if chemisorption was the dominant adsorption process, then raising the temperature would be necessary, increasing the complexity of the process, energy requirements and cost. Experimentally, regeneration of the adsorbent bed was achieved by simply passing pure He through the bed at the given test operating temperatures.

4.3.1.4 Axial Dispersion, D_L and Lumped Mass Transfer Resistance, *LMTR*

The axial dispersion and the lumped mass transfer resistance obtained are shown in Table 4.8. Practical commercial systems will likely have flow regimes characterized by certain amounts of axial dispersion. The trends observed in the present study are consistent with the experimental factors of temperature and bed voidage. Therefore, there is an increase in axial dispersion as the temperature increases, for example, from 0.36 to 0.87 cm^2/s over 40% Al_2O_3, from 50 to 150 °C respectively.

The values of the lumped mass transfer resistance also follow expected trends, increasing with increasing temperature (since the *LMTR* is inversely proportional to *K* from equation *3-13*). Values of the *LMTR* varied, for example, from 4.08 to 6.12 s over 40% Al_2O_3, from 50 to 150 °C respectively. The high values of mass transfer resistance are perhaps explained by the choice of adsorbent and gas velocities used experimentally. Since Al_2O_3 does not have a high uptake for C_3H_6, the breakthrough curves were very steep, and therefore the variance of the bed itself very small. This low variance in the bed may contribute to error in assessing the magnitude of the mass transfer resistance compared to other more favourable adsorbents such as certain zeolites and molecular sieves. In addition, the low gas velocities traveling through the bed may allow a relatively high film thickness to exist over which mass transfer must occur from the bulk fluid phase to the adsorbent phase.

The effective mass transfer coefficient, k_{eff}, is inversely proportional to the *LMTR* and was determined to range from 0.013 to 0.077 s^{-1} for 50 to 150 °C. Reduction of the *LMTR* (increasing k_{eff}) can be achieved by decreasing particle size thereby increasing the surface area to bulk ratio. Reducing the particle diameter will typically increase the pressure drop across the sensor bed, however, in the case of the current application pressure drop across the bed will be negligible due to low fugitive emission leakage rates. Increased adsorption efficiency could still potentially be realized though, by decreasing the particle size, thereby reducing the LUB (length of unused bed), but potentially increasing regeneration time due to pressure drop.

4.3.2 Adsorption Breakthrough at Varying Adsorbate Concentration

The adsorbate concentration was varied from 10% C_3H_6 to 5% C_3H_6 and then to 1% C_3H_6 while the sensor bed composition was held constant at 40% Al_2O_3 in SnO_2 and the temperature was held constant at 100 °C. The results are given in Table 4.9.

Table 4.9: Summary of adsorption results for varying adsorbate concentration from 10% C_3H_6 to 1% C_3H_6 at constant sensor bed composition and temperature.

T	*K* (for Bed)	*q** (for Bed)	Sensor Life ++	D_L	*LMTR*	k_{eff}
°C	vol./vol.+	mmol/g	days	cm^2/s	s	s^{-1}
40% Al_2O_3, ε_b = 0.477, 10% C_3H_6						
100	5.24	0.015	4	0.976	3.96	0.044
40% Al_2O_3, ε_b = 0.477, 5% C_3H_6						
100	7.40	0.011	3	0.668	2.33	0.055
40% Al_2O_3, ε_b = 0.477, 1% C_3H_6						
100	9.25	0.0026	<1	1.24	0.809	0.132

+ *$volume_{adsorbate}$ / $volume_{bed}$ including both adsorbent and metal oxide components of the bed*
++ *values are calculated based on 100g of adsorbent*

As the concentration of adsorbate was reduced from 10% to 1%, the value of K increased from 5.24 to 9.25 ($vol._{adsorbate}$ / $vol._{bed}$). However, the equilibrium uptake per mass of adsorbent decreased and hence the total uptake and sensor life diminished for lower concentration of adsorbate, from 4 days to <1 day, when the adsorbate concentration was changed from 10 to 1% C_3H_6. In effect, the adsorbent becomes less efficient at lower concentration of adsorbate. These uptakes are too low to be practical for an industrial containment system but real systems would utilize a strong adsorbent selective to the particular gas being targeted (refer to Table 2.2 for comparison with other adsorbents).

4.3.2.1 Equilibrium Adsorption Isotherm

Figure 4.10 illustrates a plot of the equilibrium isotherm. The experimentally observed data suggest that the isotherm is not linear, as assumed, but rather may be of the Freundlich or Langmuir type. Isotherms are shown using Henry's Law and Freundlich types for comparison.

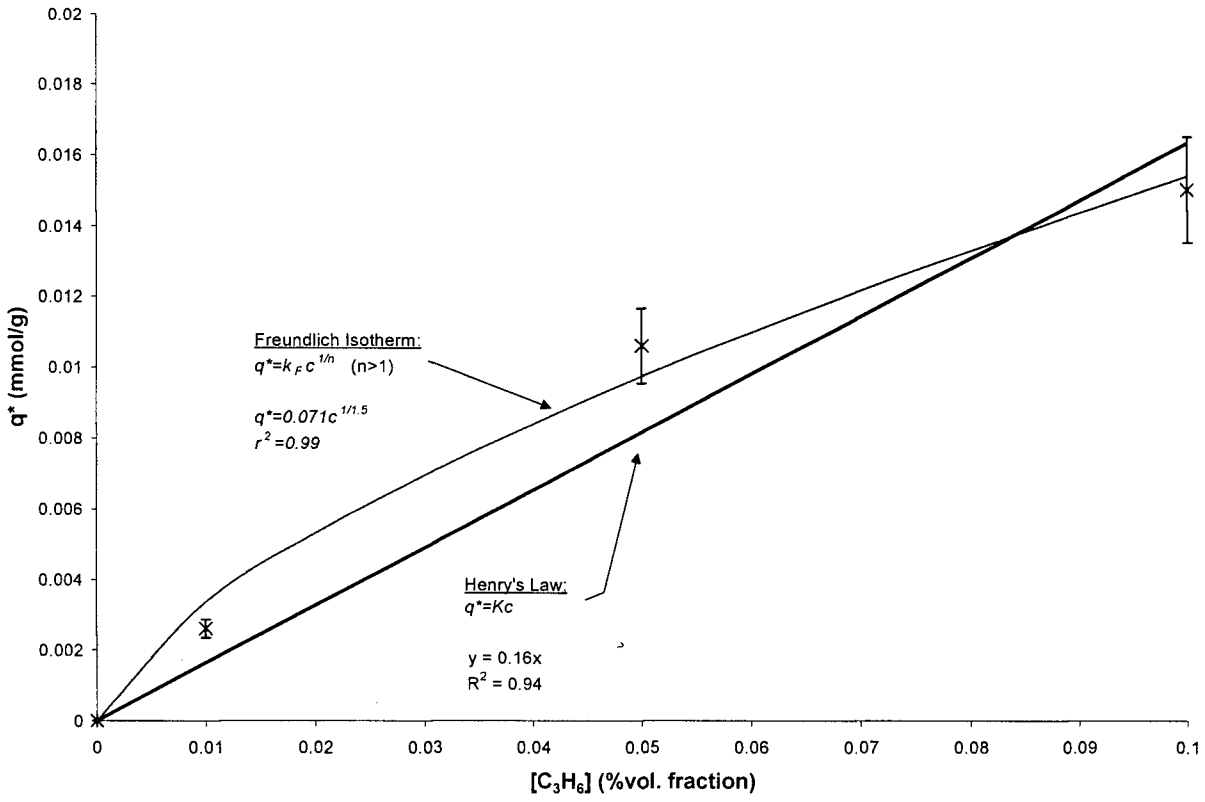

Figure 4.10: Equilibrium adsorption isotherm of C_3H_6 uptake on 40% Al_2O_3 at 100 °C. Error bars indicate +/-10%.

The error bars indicated +/- 10%, thus the Henry's Law assumption shows greater than 10% error from the experimentally observed points except at 10% C_3H_6, where both Henry's law and the Freundlich Isotherm are within 10% of the experimentally observed adsorption uptake. It should be noted though, that the relevant practical discussion will be based on the experimentally determined *K* values rather than the fitted points.

4.3.2.2 Axial Dispersion, D_L and Lumped Mass Transfer Resistance, *LMTR*

Axial dispersion varies from 0.67 cm^2/s at its minimum for 5% C_3H_6, increasing to 0.98 and 1.24 cm^2/s for 10% C_3H_6 and 1% C_3H_6 respectively. Theoretical values for axial dispersion can be approximated from equation *4-3* (Ruthven, 1984) where D_m is the molecular diffusivity of the gas, approximately equal to 0.74 cm^2/s (Satterfield, 1981):

$$D_L = 0.7D_m \qquad \textbf{(4-3)}$$

D_m for a binary gas mixture is given by the Lennard-Jones expression for intermolecular forces (Hirschfelder et al., 1954):

$$D_m = D_{12} = \frac{0.001858T^{3/2}\left[(M_1 + M_2)/M_1M_2\right]^{1/2}}{P\sigma_{12}^2\Omega_D} \qquad \textbf{(4-4)}$$

where T is the absolute temperature, M is the species molecular weight, P is the total pressure, σ_{12} a force constant, and Ω_D is the "collision integral" (a function of k_bT/ε_{12}, where k_b is the Boltzmann constant and ε_{12} is also a force constant in the model).

It is apparent from equation *4-4* that the molecular diffusivity is proportional to temperature, $T^{3/2}$ and inversely proportional to total pressure P. Therefore, the concentration within the binary mixture (C_3H_6 in He) should not influence the molecular diffusivity nor the axial diffusion according to equation *4-3*. This is the case for bulk diffusion or diffusion in large pores as described by equation *4-4* (Satterfield, 1981). Therefore the spread in data reported above are likely indicative of the scatter of axial dispersion measurement although the magnitude of the results seem reasonable considering D_m = 0.74 cm^2/s as reported above.

The lumped mass transfer resistance decreased from 4.0 to 0.81 s as the adsorbate concentration decreased from 10% C_3H_6 to 1% C_3H_6 indicating a large reduction in overall mass transfer resistance at lower concentration, consistent with the increasing trend in K over the same concentration range. Laboratory studies by Kovacevic (2000) reported that axial dispersion and *LMTR* values were prone to scatter. Evaluation of the data used to extract D_L and the *LMTR* for the present study show scatter in some cases (refer to Figure 4.7 and the moment analysis of Appendix C) and in some cases a shift in slope seems to occur at the high gas velocity range of the data. This suggests that if additional data points were collected at higher gas velocity, then smoother fits may have been obtained along with higher D_L and lower *LMTR*. However, if the sensor bed is operating at low gas velocity, as in the present study and presumably as a system would in the field, then high mass transfer resistance may be expected and hence reduced particle size or other means to reduce the mass transfer resistance should be undertaken as discussed previously.

4.3.3 Electrical Resistance at Varying Adsorbent/Metal Oxide Composition

It is the change in the electrical resistance of the sensor bed that provides information regarding the target gas uptake in the sensor bed system. In the present study, C_3H_6 adsorption on various bed compositions was monitored. In the initial phase, C_3H_6 adsorbate concentration was kept constant at 10% in He and the sensor bed composition was varied from 10% Al_2O_3 to 40% Al_2O_3 in SnO_2. For each bed composition, experiments were carried out at temperatures from 50 to 150 °C as previously described. Averaged values for two cycles of initial resistance in a more oxidized state, $R_{a,He}$, and final resistance in a more reduced state, R_g, and the sensitivity, S_4, of the system while undergoing the C_3H_6 reduction phase of the procedure are reported in Table 4.10, along with Sensor Life. The standard deviation of each averaged sensitivity is also given.

Table 4.10: Summary of electrical resistance at varying adsorbent / metal oxide concentration and temperature.

Temp	R_a	R_g	S_4^*	Stand. Dev.	S_4^*	Stand. Dev.	Sensor Life
°C	MΩ	MΩ	S_N		S_A		days
10% Al_2O_3, ε_b = 0.531, 10% C_3H_6							
50	0.265	0.202	0.24	0.010	1.31	0.018	4
75	0.144	0.0657	0.54	0.001	2.20	0.001	1.5
100	0.0950	0.0304	0.68	0.018	3.12	0.178	1
150	0.0222	0.00482	0.78	0.003	4.60	0.061	<1
20% Al_2O_3, ε_b = 0.506, 10% C_3H_6							
50	0.622	0.351	0.44	0.023	1.77	0.074	8
75	0.456	0.130	0.71	0.037	3.50	0.452	4
100	0.195	0.0552	0.72	0.010	3.54	0.126	2
150	0.0764	0.0182	0.76	0.025	4.21	0.440	<1
30% Al_2O_3, ε_b = 0.473, 10% C_3H_6							
50	1.54	1.08	0.30	0.004	1.43	0.009	12
75	0.95	0.35	0.64	0.029	2.76	0.217	6
100	0.66	0.18	0.72	0.004	3.60	0.056	3
150	0.53	0.11	0.78	0.038	4.61	0.791	1
40% Al_2O_3, ε_b = 0.477, 10% C_3H_6							
50	10.4	6.22	0.40	-	1.67	-	16
100	2.14	0.676	0.68	-	3.16	-	4
150	1.44	0.272	0.81	-	5.29	-	1
(*Alternate Pretreatment*), 40% Al_2O_3, ε_b = 0.477, 10% C_3H_6							
50	0.412	0.293	0.28	-	1.41	-	16
75	0.269	0.178	0.34	0.005	1.51	0.011	8
100	0.176	0.108	0.39	0.015	1.63	0.039	4
150	0.127	0.0662	0.48	0.001	1.92	0.003	1

\- indicates that a repeat test was not carried out.

* Refer to key in Table 4.6 for explanation of S_4, S_N, *and* S_A.

Table 4.10 indicates that as the % volume of Al_2O_3 increases from 10% to 40%, both the initial resistance and the final resistance of the sensor bed increase as expected (by approximately two orders of magnitude). At 50 °C, for example, the initial and final resistances for the 10% Al_2O_3 bed are 0.265 and 0.202 MΩ respectively, compared to 10.4 and 6.22 MΩ respectively for the 40% Al_2O_3 bed. An electrical resistance experiment was also carried out for a bed composition of 70% Al_2O_3 in SnO_2, however, the resistance of the bed had become too high to measure with the current apparatus therefore no results are reported. Figures 4.11a and b indicate the

conductance (1/R) as a function of the fraction of SnO_2 in the bed for varying temperature and for varying oxidation state (from equation *2-6b*) and indicate a very good correlation.

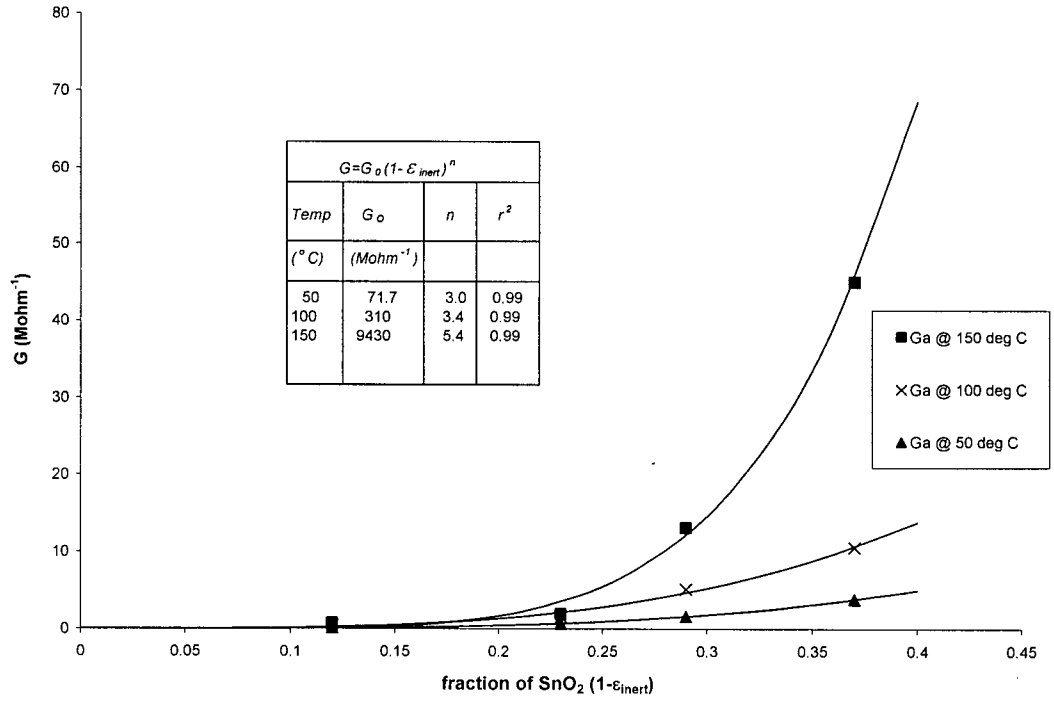

Figure 4.11a: Conductance vs fraction of SnO_2 in the bed for varying temperature (shown for the oxidized surface state only).

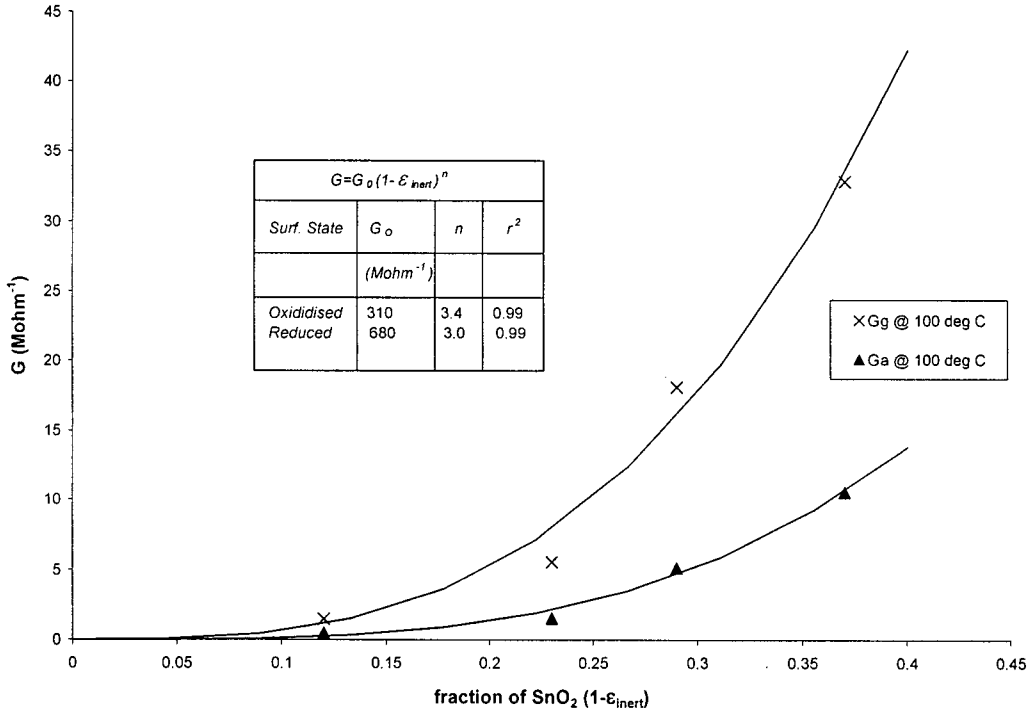

Figure 4.11b: Conductance vs fraction of SnO_2 in the bed for varying surface state (shown for 100 ^{o}C only).

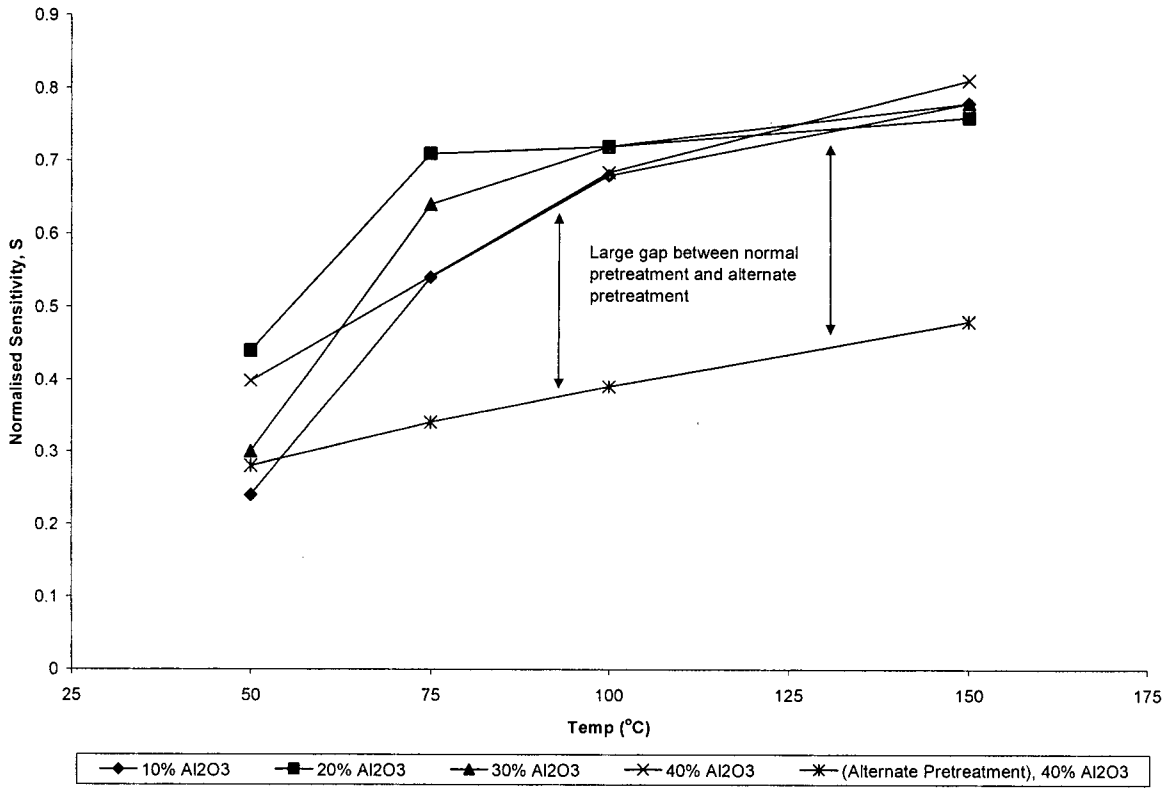

Figure 4.11c: Normalised sensitivity versus temperature for varying %volume of adsorbent in the sensor bed.

A plot of sensitivity versus bed composition is given in Figure 4.11. The figure clearly shows that sensitivity increases with increasing temperature for all sensor bed compositions and that the range of sensitivity becomes relatively narrow at 100 to 150 °C compared to the large spread in the data shown below 100 °C. The difference between the data that underwent a normal pretreatment and that of the alternate pretreatment will be discussed separately in a later section.

Absolute sensitivity (S_A of Table 4.10) results are reasonable compared to other experimental results involving hydrocarbons (refer to Table 2.3). Phani *et al.* (1999) report the sensitivity for a doped SnO_2 sensor for LPG of 1.8 and 12.5 for 1000 and 10,000 ppm at 350 °C. Firth et al (1975) report the sensitivity of an undoped CH_4 sensor at 100 ppm and 500 °C at 1.35 and

Kocemba et al (2001) report for a pressed SnO_2 pellet containing 40% Al_2O_3 a sensitivity of 7 for 150 ppm of pure H_2 at 350 °C.

The comparison for hydrocarbon's is good, however, the sensitivity results of the present study are in the low range of experimental results involving other reducing gases such as CO, even though the adsorbate concentration was quite high (10,000 to 100,000 ppmv). This may be due to the relatively low temperature range of the present study compared to most other studies for gas sensors, the lack of dopants used in the present study to improve sensitivity and selectivity for C_3H_6 and also by the fact that the system was flushed with He prior to each C_3H_6 reduction, substantially reducing the initial resistance value from R_a (after oxidation with no He flush) to $R_{a,He}$ (with He flush).

4.3.4 Electrical Resistance at Varying Adsorbate Concentration

The effect of varying the adsorbate concentration was tested and the initial resistance, $R_{a,He}$, final resistance, R_g, and sensitivity, (S_A and S_N), determined. This information along with the standard deviation of the sensitivity and estimated sensor life for the given conditions are shown in Table 4.11.

When the adsorbate concentration was decreased from 10 to 1% C_3H_6, both the initial resistance and the final resistance increased. For example, at 50 °C, the initial resistance was 10.4 MΩ and the final resistance was 6.23 MΩ after adsorption of 10% C_3H_6, compared to an initial resistance of 13.3 MΩ and a final resistance of 8.81 MΩ after adsorption of 1% C_3H_6. Similarly, the resistances were found to be higher at all other conditions when the bed was exposed to lower concentration of reducing gas as compared to higher concentrations.

Table 4.11: Summary of electrical resistance at varying adsorbate concentration

Temp	R_a	R_g	S_4	Stand. Dev.	S_4	Stand. Dev.	Sensor Life
°C	MΩ	MΩ	S_N		S_A		days
40% Al_2O_3, ε_b = 0.477, 10% C_3H_6							
50	10.4	6.23	0.40	-	1.66	-	-
100	2.14	0.676	0.68	-	3.17	-	4
150	1.44	0.272	0.81	-	5.31	-	-
40% Al_2O_3, ε_b = 0.477, 5% C_3H_6							
50	11.1	7.16	0.35	-	1.54	-	-
100	3.25	1.11	0.65	0.082	2.98	0.71	3
150	1.91	0.445	0.77	-	4.29	-	-
40% Al_2O_3, ε_b = 0.477, 1% C_3H_6							
50	13.3	8.81	0.34	-	1.51	-	-
100	5.02	1.39	0.72	0.045	3.65	0.59	1
150	3.98	0.50	0.87	0.010	7.97	0.66	-

- indicates that a repeat test was not carried out.

Sensitivity generally fluctuates very little as a function of adsorbate concentration in the present study, however, it increases with increasing temperature as seen in Figure 4.12. The discussion of sensitivity previously given also applies for the present set of data. According to the literature (Park and Ackbar (2003), Watson et al. (1993)) the sensitivity should generally increase according to a power law of target gas concentration. This was not evident with the present study, and may again be a result of the temperature range of the study and the number of points taken, issues with the history of the sample or the cycle times used for adsorption/desorption compared to letting the sensor bed come to equilibrium over a long period of time under exposure to a certain reducing gas concentration.

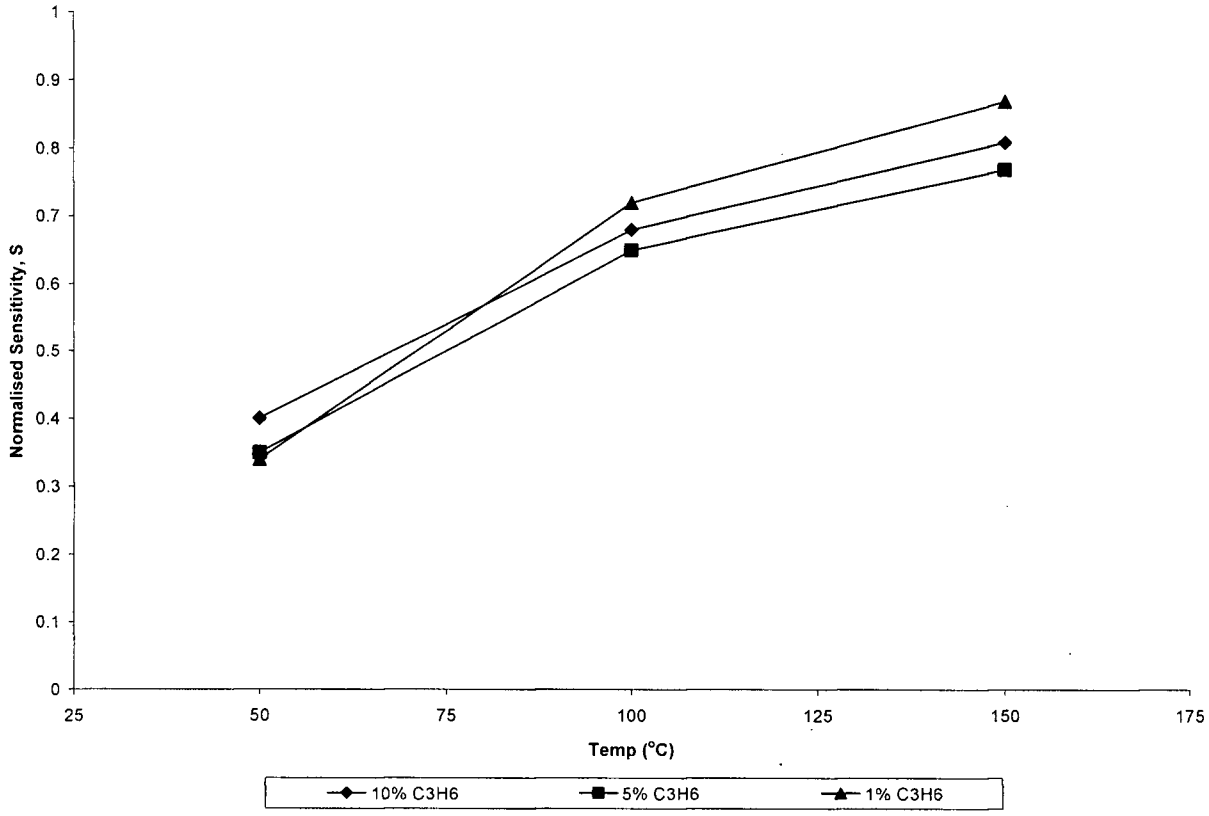

Figure 4.12: Normalised sensitivity versus temperature for varying %volume of adsorbate in the sensor bed.

4.4 Effect of Adsorbent Pretreatment on Electrical Resistance

Experiments were performed in order to determine whether the pretreatment of the material affects its electrical properties. The pretreatment of the bed was varied to include a 15 minute C_3H_6 reduction at 350 °C, following the normal 1 hour oxidation cycle at that temperature. The sample was then flushed with He while the temperature was reduced to 50 °C. The normally prescribed procedure was then followed consisting of oxidation and reduction cycles. Electrical resistance was monitored during the adsorption of C_3H_6 while maintaining constant temperature. The procedure was repeated for temperatures between 50 and 150 °C. Comparison is made

between the alternately pretreated sample and a sample that underwent the nominal pretreatment (i.e. no high temperature C_3H_6 reduction) and the results are shown in Table 4.10.

The results indicate that electrical resistance is reduced substantially (approximately one order of magnitude) for the sample that underwent the alternate pretreatment as compared to the sample that underwent the nominal pretreatment. For example, at 50 °C, the initial resistance of the sample (prior to adsorption) was 0.412 MΩ for the alternately pretreated sample, compared to 10.4 MΩ, for the nominally pretreated sample.

A similar trend can be seen for the final state of the sensor bed after adsorption of C_3H_6, however, proportionally, the change in electrical resistance after C_3H_6 adsorption, is much less for the sample that underwent the alternate pretreatment. This can be seen by comparing the sensitivity, which essentially represents the percent difference between the initial electrical resistance and the final electrical resistance. The alternate pretreatment (reduced at 350 °C) yields lower sensitivity than the nominal pretreatment (unreduced at 350 °C), and its sensitivity does not increase appreciably with an increase in temperature (S_N = 0.28 to 0.48 compared to S_N = 0.33 to 0.87 from 50 to 150 °C respectively) as can be seen in Figure 4.11.

This is an important result which reinforces the need to control the pretreatment and history of the sample, since its variation can cause significant changes in electrical properties and sensitivity. In addition, it provides a general guideline as to what the initial state of the sensor bed should be in order to optimize its sensitivity to reducing gases. That is, to maximize sensitivity, the bed must be in an oxidized state, normally achieved in a sensor by exposure to atmospheric oxygen.

4.5 Effect of Temperature and Energy Barrier, qV_s

Results indicate that for each sensor bed composition, as the temperature was increased from 50 to 150 °C the electrical resistance, $R_{a,He}$ and R_g decreased (similar to Figure 4.9) consistent with the Arhennius relationship of the model for inter-granular contact resistance. Solutions to the non-linearized form of the model using equation *3-16* (from plots similar to Figure 4.4) were used to determine qV_s. Appendix D, summarizes the electrical resistance results and the qV_s data.

In general these results indicate that the energy barrier term increased by approximately 0.15 eV between the beginning of the C_3H_6 reduction phase and the end of the phase. This is contrary to the model for inter-granular contact resistance which predicts a decrease in the energy gap as the sensor is reduced. These results are not explained within the context of the present study, however, the low operating temperature of the present system compared to other experimental systems may be a factor since mobility of donor electrons is lower than for typical sensor operating temperatures and sensing mechanisms may also be kinetically different. In addition, the presence of trace amounts of water vapour in the propylene or He supply could possibly contribute to surface conduction effects that impact these values.

It is noteworthy however that the energy barrier determined for the alternately pretreated sample compared to the typically pretreated sample does give results consistent with the model. The sample pretreated at high temperature with C_3H_6 has lower resistance indicating that its energy gap for conduction should also be smaller. This is confirmed by analysis which yields a qV_s term for the alternately pretreated sample of 0.11, 0.17 and 0.21 eV compared to the typically pretreated sample 0.13, 0.27, 0.41 eV for the oxidized state, the He flushed state and the C_3H_6 reduced state.

4.6 Experimental Error and Reproducibility

In general each simultaneous electrical resistance and adsorption breakthrough experiment was repeated. It can be seen qualitatively, by examining the plots, that repeatability of these data is very good in controlled laboratory conditions and that the adsorbent / metal oxide bed becomes reoxidised to approximately the same state, and is reduced to approximately the same state with the successive experiment (refer to Figures 3.4 and 4.1). A more quantitative approach also shows good agreement between repeat experiments. Tables 4.10 and 4.11 indicate reasonable standard deviations between repeated experiments. It has also been shown experimentally that variation of the pretreatment can result in significant changes in the electrical properties of the materials as discussed in Section 4.4.

The literature also suggests that metal oxides and adsorbents are susceptible to the influence of water vapour and non targeted gases. Keeping this in mind, once an adsorption bed becomes saturated it will have to be regenerated. Successive use of the bed after regeneration appears viable due to its repeatability given consistent pretreatment of the bed. However, controlled conditions of temperature, relative humidity and level of contaminants would have to exist within the sensor bed to ensure that sensor output can be interpreted meaningfully. The use of filtering layers and/or high operating temperature to reduce the effect of poisons and physisorbed water vapour may be necessary to ensure reliability due to the presence of "non-laboratory" conditions.

4.7 Summary of Results

Sensor bed characteristics are the result of a combination of adsorption and sensing properties. In the present study, combined Al_2O_3 adsorption and SnO_2 sensing experiments were carried out.

Adsorption equilibrium parameters were obtained by moment analysis and indicate that adsorption of C_3H_6 on Al_2O_3 is relatively low compared to adsorption on other solid adsorbents (Table 2.2). This fact was suitable for the present study in order to maximize the number of tests that could be carried out. Adsorption equilibrium uptake and sensor life was increased with increasing % volume of adsorbent in the sensor bed. Increasing the temperature reduced uptake and sensor life.

Adsorption results indicate, with good correlation (r^2=0.99), the inverse relationship between Henry's constant, K, and increasing temperature, T. The plot of ln K vs $1/T$, shown in Figure 4.6, illustrates the linear trend from which the heat of adsorption, $-\Delta H_{ads}$ = 29.2 kJ/mol, was obtained indicating that physisorption is the dominant adsorption mechanism.

Additional adsorption design parameters could also be measured for axial dispersion, D_L and the lumped mass transfer resistance, *LMTR*. These parameters indicated that axial dispersion was present in the system and that mass transfer resistance was high, or k_{eff} was small, perhaps a result of the low flow rates and gas velocities utilized experimentally combined with the use of a relatively weak adsorbent in Al_2O_3.

SnO_2 was utilized for metal oxide sensing. Since the bulk 10 – 24 mesh SnO_2 tested was relatively low in electrical resistance, all subsequent tests were carried out using the same mesh size of SnO_2. Subsequent electrical resistance monitoring with pure SnO_2 in-situ at a variety of temperatures in both the oxidized and reduced state was carried out. Empirical parameters were extracted from these tests indicating that the energy barrier increases as the sample is oxidized for greater periods of time (1 hour versus 15 min) consistent with the model for inter-granular contact resistance. However, qV_s also increased as the sample was reduced in 10% C_3H_6, in contrast to the model for inter-granular contact resistance, but which is possibly explained by the

presence of water vapour, operating temperature and or the use of a flow system not necessarily reaching full equilibrium during the oxidation and reduction cycles. Alternating the pretreatment of SnO_2 by reducing it at 350 °C (where surface kinetics are expected to be very rapid) did show that the energy barrier was lowered compared to samples that were not reduced at 350 °C.

Resistance decreased and sensitivity increased marginally with increasing temperature, consistent with literature, but was relatively high overall (S_A > 9.2) for all temperatures when calculated from the 1 hour (S_1) and the 15 minute (S_3) oxidation states, and was somewhat lower (S_A > 3.4) when calculated from the C_3H_6 reduction phase only (S_2 and S_4) in the 150 to 350 °C temperature range. Sensitivity over the C_3H_6 reduction phase (S_4) is reduced (S_A ~ 1.3 – 8.0) in the 50 to 150 °C range, comparable to other studies for hydrocarbons (Table 2.3).

Implications for the mixed sensor bed are that as temperature increases, sensitivity increases, however, adsorption capacity decreases as seen in Table 4.8. A balance should be determined between sensitivity and adsorption uptake and may necessitate the use of dopants and/or new adsorbent materials. In addition, consistent operating conditions are necessary to ensure reliability and repeatability of the sensor which could also benefit from increasing the operating temperature and the use of filtering layers to reduce or eliminate the influence of water vapour and contaminants (non-target gases).

Chapter 5 - Model

The purpose of modeling the results of the present study was to correlate the electrical resistance response of the sensor bed to the adsorption uptake. That is, to determine the relationship between electrical resistance as a function of adsorption uptake. In practice, this relationship could be used to quantify the amount of gas adsorbed into the sensor bed from the target fugitive emission and thereby allow a decision to be made as to whether a significant fugitive leak has occurred or not.

A simple model will be used to describe the relationship, which will directly relate the electrical resistance of the bed to the concentration profile of adsorbate in the bed. The electrical parameters required are the initial resistance of the bed (in the oxidized state) and the final resistance of the bed (in the reduced state), both of which were determined experimentally. Adsorption parameters are required for the Henry's constant, K, and the axial dispersion coefficient, D_L, given that the physical properties, size and voidage, of the bed are known. In addition, a fitting parameter, a, representing the rate constant of the surface reaction, k_a, is obtained by fitting the model to the experimental data. The activation energy, E_a, is also determined by comparing the rate constant at three different temperatures.

5.1 Model for Adsorption

Adsorption of a single component through a packed bed is described by the following differential equation (given previously in Chapter 2):

$$-D_L \frac{\partial^2 c}{\partial z^2} + \frac{\partial}{\partial z}(vc) + \frac{\partial c}{\partial t} + \left(\frac{1-\varepsilon_b}{\varepsilon_b}\right)\frac{\partial \overline{q}}{\partial t} = 0 \qquad \textit{(2-1)}$$

This equation can be further simplified assuming that the propagation velocity, v, of the mass transfer front through the bed is constant, and the equation reduces to:

$$-D_L \frac{\partial^2 c}{\partial z^2} + v\frac{\partial c}{\partial z} + \frac{\partial c}{\partial t} + \left(\frac{1-\varepsilon_b}{\varepsilon_b}\right)\frac{\partial \bar{q}}{\partial t} = 0 \qquad \textit{(5-1)}$$

The adsorption rate expression is obtained from a mass balance on a single adsorbent particle given by:

$$\frac{\partial \bar{q}}{\partial t} = f(q,c) \qquad \textit{(5-2)}$$

This is a simplified expression taking into account all diffusion terms and mass transfer effects. The dynamic response of the column at any point and time [$c(z, t)$, $\bar{q}(z, t)$] is given by the solution of equations *5-1* and *5-2*, subject to the boundary conditions of an initially adsorbate free column with a step change in adsorbate concentration at the inlet of the bed $(z = 0)$ at time zero $(t = 0)$ as follows:

At $\quad t < 0,\ q(0, z) = c(0, z) = 0$

and $\quad t > 0,\ c(0, t) = c_0 \qquad \textit{(5-3)}$

The nature of a mass transfer zone that propagates through a packed adsorbent bed is dependent upon the equilibrium isotherm. The shape of the mass transfer zone is affected significantly by kinetic effects. Isotherms can be favourable, linear or unfavourable depending on the equilibrium relationship. These concepts are fully detailed in Ruthven (1984), however for the present study it is important to note that the equilibrium relationship is assumed to be linear and therefore adsorption and desorption processes are symmetrically equivalent. This assumption

allows for analytical solution to the above differential equations and signifies that the mass transfer zone will broaden as the front propagates through the packed bed in a dispersive manner.

Solutions to the differential equations *5-1* and *5-2* are summarized in Ruthven, 1984. A model for axially dispersed plug flow will be utilized to represent adsorption in the sensor bed based on the following assumptions:

- A *linear isotherm* approximates equilibrium conditions and the mass transfer zone exhibits dispersive behaviour.
- The system is *isothermal* and hence heat transfer effects can be neglected. Therefore, the spreading of the concentration front through the bed is due entirely to dispersive and mass transfer effects.
- The gas composition acts as a *trace system* where changes in fluid velocity across the mass transfer zone are negligible.
- *Axially dispersed plug flow* exists in the system such that the axial dispersion term D_L is significant and retained in the solution.
- The *kinetic rate model* for adsorption utilizes an overall effective mass transfer resistance (i.e. a single lumped mass transfer resistance parameter) and is governed by the linear rate expression of equation *3-6*:

$$\frac{d\bar{q}}{dt} = k_{eff}(q^* - q) \qquad \textbf{(3-6)}$$

Analytic solutions for the breakthrough curves of linear, isothermal, trace component systems are summarized by Ruthven, 1984. For the linearized rate expression, the solution of Levenspiel and Bischoff (1963) can be used. The solution gives an analytical solution for the breakthrough

curve as a function of time, t, and position along the column, z, given the parameters K, D_L and ε_b and determining the interstitial velocity, v, from the flow rate and bed geometry:

$$\frac{c}{c_0} = \frac{1}{2} erfc\left\{ \frac{1 - \frac{t}{\bar{t}}}{2\left[\frac{D_L}{vz}\left(\frac{t}{\bar{t}}\right)\right]^2} \right\}, \qquad \textit{(5-4)}$$

where:

$$\bar{t} = \frac{z}{v}\left\{1 + K\left(\frac{1-\varepsilon_b}{\varepsilon_b}\right)\right\} \qquad \textit{(5-5)}$$

5.2 Electrical Resistance as a Function of Adsorption Breakthrough

The electrical resistance was modeled as a function of the adsorption breakthrough by considering that the sensor bed can be portrayed as a system of parallel electrical resistors as illustrated in Figure 5.1.

The model can be rationalized by considering the following points and Figure 5.1:

- Each parallel resistance, given by R_i, represents an infinitesimally thin layer of the sensor bed.
- Each parallel resistance is composed of two resistors in series, whose resistance is determined by whether that portion of the bed is in the oxidized state, $R_{O,i}$ (initial state) or the reduced state $R_{R,f}$ (final state):
- The value of each parallel resistance, R_i, is a function of time, t, and position, z, along the length of the sensor bed which is dependent upon the propagation of the adsorbate mass transfer zone through the bed and hence adsorbate concentration c/c_0. Therefore:

$$R_i\,(t,\,z) = R_{O,i} + R_{R,i} = R_{O,0}\,(1 - c/c_0) + R_{R,f}\,(c/c_0) \qquad \textit{(5-6)}$$

where: $R_{O,i}$ = Layer resistance: oxidized component of parallel layer

$R_{R,i}$ = Layer resistance: reduced component of parallel layer

$R_{O,0}$ = each layer resistance at $t = 0$,

$R_{R,f}$ = each layer resistance at $t = t_f$

- As the reducing gas flows through the sensor bed, under the influence of axially dispersive forces, the resistance of components within each layer changes. As time increases, the mass transfer front moves further down the length of the sensor bed.
- Initially, it was assumed that reaction kinetic effects do not influence the electrical resistance of each layer. That is, when a layer component is reduced, its resistance undergoes an immediate step change in resistance, with no effect due to the rate of the surface reduction process. It is the cumulative effect of all resistances in the bed that influence the total electrical resistance response of the system.
- The total electrical resistance of the system is the equivalent resistance of the network of the parallel resistors; of which each value changes with time according to the adsorption breakthrough response:

$$1/R_T = 1/R_1 + 1/R_2 + 1/R_3 + \cdots + 1/R_n \qquad \textit{(5-7)}$$

which is equivalent to:

$$R_T\Big|_{t=t_j} = \frac{1}{\sum_{i=1}^{n} \frac{1}{R_n}} \qquad \text{(where } n = 1000 \text{ for the present study)} \qquad \textit{(5-8)}$$

Electrical response of the sensor bed for each time, t_j (where i is the index for the number of parallel resistance layers modeled in the sensor bed and j is the index used for time) is obtained by applying equation *5-8*.

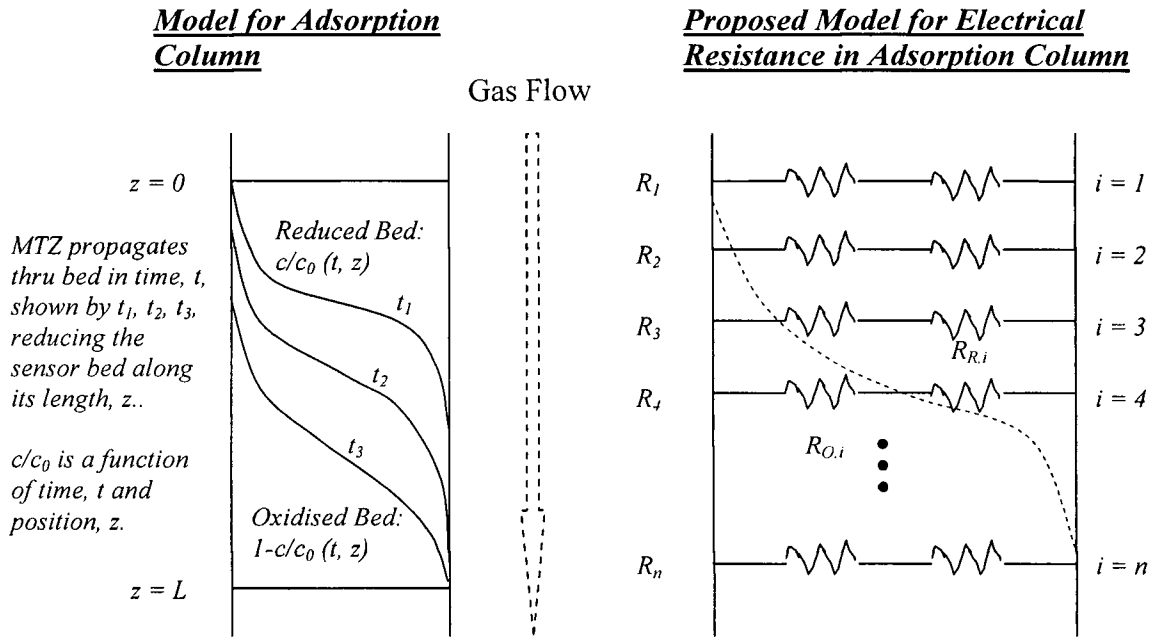

$$\frac{c}{c_0}(t,z) = \frac{1}{2}\,erfc\left\{\frac{1-\frac{t}{\bar{t}}}{2\left[\frac{D_L}{vz}\left(\frac{t}{\bar{t}}\right)\right]^2}\right\}$$

where:

$$\bar{t} = \frac{z}{v}\left\{1+K\left(\frac{1-\varepsilon_b}{\varepsilon_b}\right)\right\}$$

$$R_i(t,z) = R_{O,i}+R_{R,i}=R_{O,0}(1-c/c_0)+R_{R,f}(c/c_0)$$

where: $R_{O,i}$ = Layer resistance: oxidized
$R_{R,i}$ = Layer resistance: reduced

$R_{O,0}$ = each layer resistance at $t = 0$,
$R_{R,f}$ = each layer resistance at $t = t_f$

Total bed resistance at time, *t*:

$$1/R_T \;\Big|_{t=t_j} = 1/R_1+1/R_1+1/R_3+\ldots+1/R_n$$

Figure 5.1: Proposed model for electrical resistance of an adsorption column with no reaction kinetic effects.

5.2.1 Resistance and Adsorption Versus Time

Typical time based curves for normalized resistance (R/R_0) and normalized adsorption breakthrough (c/c_0) of 10% C_3H_6 over 40% Al_2O_3/SnO_2 are given in Figures 5.2a for both the experimentally observed data and the predicted data based on the model of Figure 5.1.

It is important to note that the experimentally observed breakthrough and electrical response curves are based on raw data and have not been corrected for dead volume in the reactor. In contrast, the modeled curves have been calculated based on experimentally obtained parameters from the breakthrough and electrical resistance analysis, which *are* corrected for dead volume.

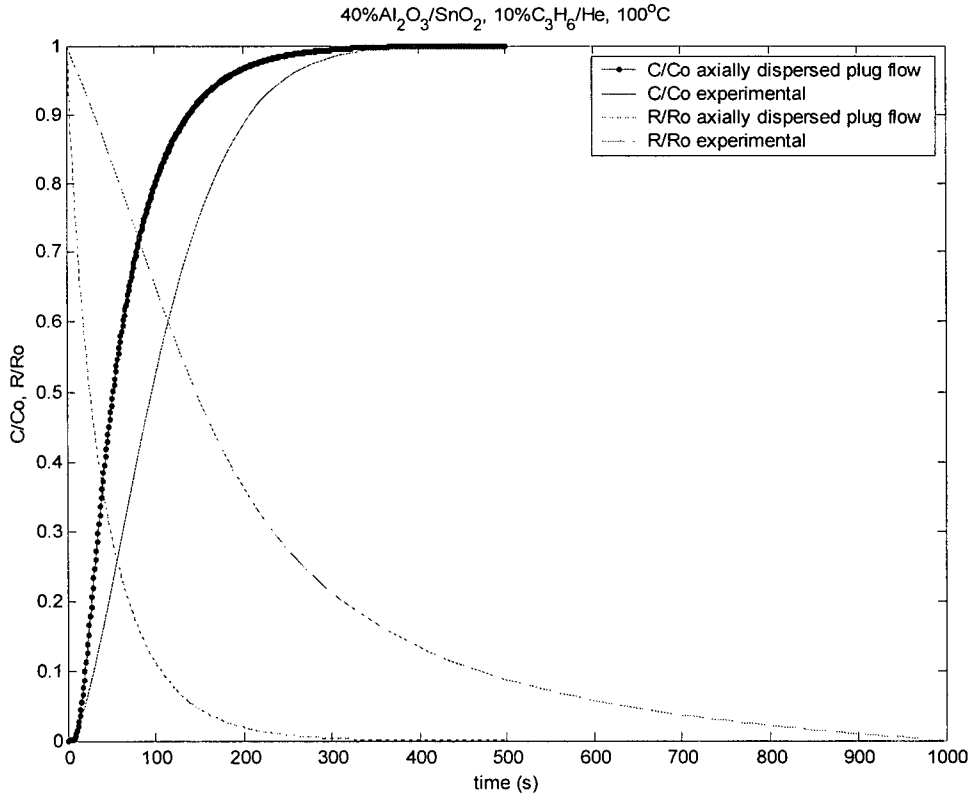

Figure 5.2a: Experimental and modeled R/R_0 and c/c_0 vs time curves for 10% C_3H_6 over 40% Al_2O_3/SnO_2 at 100 °C.

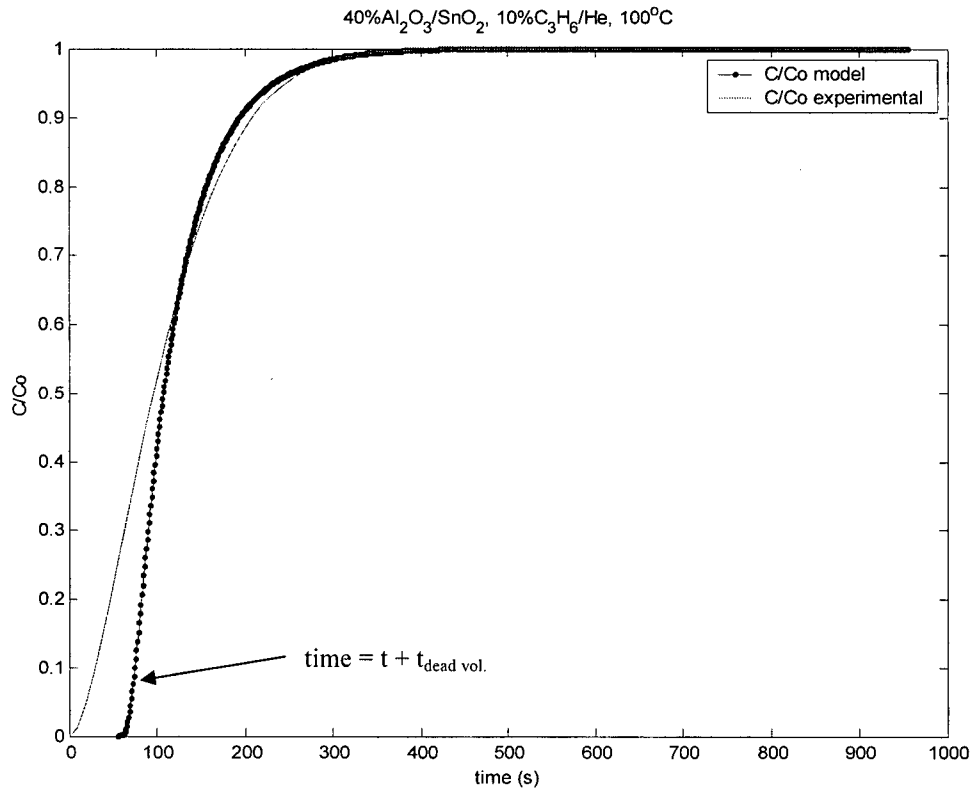

Figure 5.2b: Experimental and modeled c/c_0 vs time curves for 10% C_3H_6 over 40% Al_2O_3/SnO_2 at 100 °C.

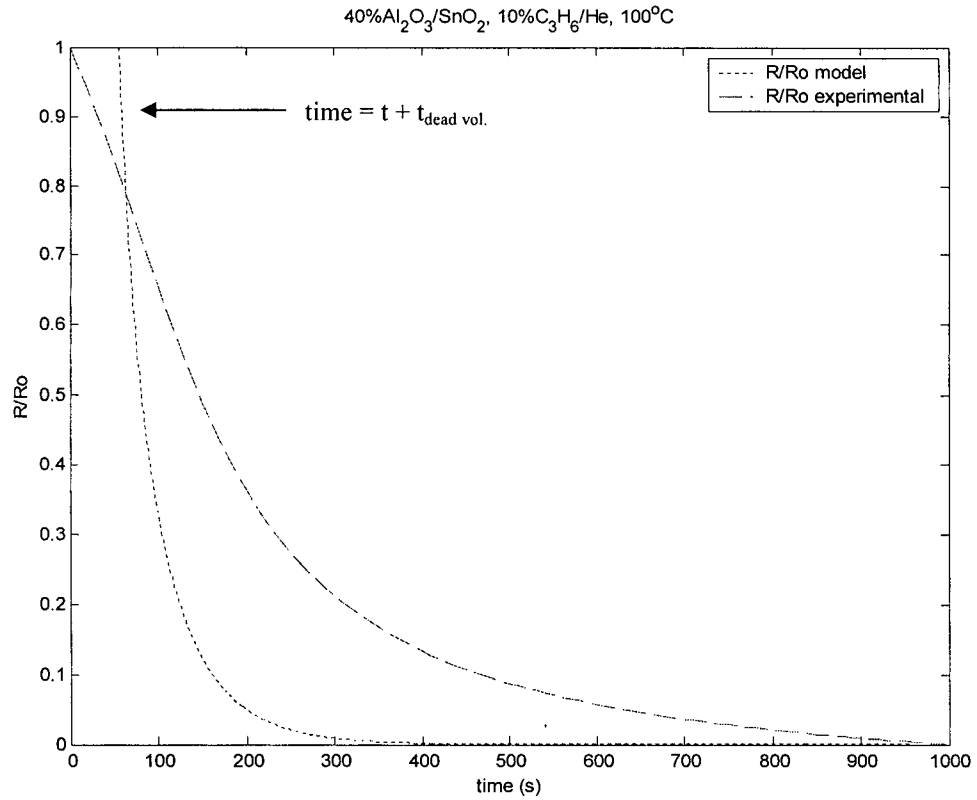

Figure 5.2c: Experimental and modeled R/R_0 vs time curves for 10% C_3H_6 over 40% Al_2O_3/SnO_2 at 100 °C.

Discrepancies can be seen between the experimental and modeled curves. In particular, the tails (representing axial dispersion) are much greater for the experimentally obtained curves, since they contain the influence of the dead space variance. The mean residence time, on the other hand, can generally be corrected for the effects of dead volume. This is done by offsetting the modeled curves by a time equivalent to the mean residence time of the dead space and it can be seen from the curves in Figure 5.2b that the mean residence time matches reasonably well for c/c_0. In addition, it is evident from the curves of Figure 5.2c that at 100 °C the modeled resistance response is much faster than the experimental response, reaching $R/R_0 = 0$ (the final normalized resistance state) significantly earlier than the actual experimental response.

In summary, it is evident from Figure 5.2a-c that direct comparison is not possible with time scale analysis. Therefore, in order to remove the effects of dead space, the time axis was removed from the analysis by plotting the resistance response (R/R_0) versus the breakthrough response (c/c_0). Typical plots of these data are presented and discussed in section 5.2.2.

5.2.2 Resistance Response versus Breakthrough

To account for the convolution present in the experimental data as a result of dead volume in the system, the normalized resistance response (R/R_0) was plotted against the breakthrough response (c/c_0) of the system. This method is independent of time and yields a direct correlation between R/R_0 and c/c_0 (the primary purpose of the study). Typical plots are given in Figures 5.3a through 5.3c for 10% C_3H_6 over 40% Al_2O_3 in SnO_2 over the temperature range of 150 to 50 °C.

The characteristic of the R/R_0 response to adsorption breakthrough is generally linear in nature at 150 and 100 °C, and becomes more "on-off" at 50 °C. Depending on the application either characteristic may be desirable. That is, it may be useful to monitor the uptake (linear) or alternatively obtain an alarm only when the signal exceeds a limiting value ("on-off").

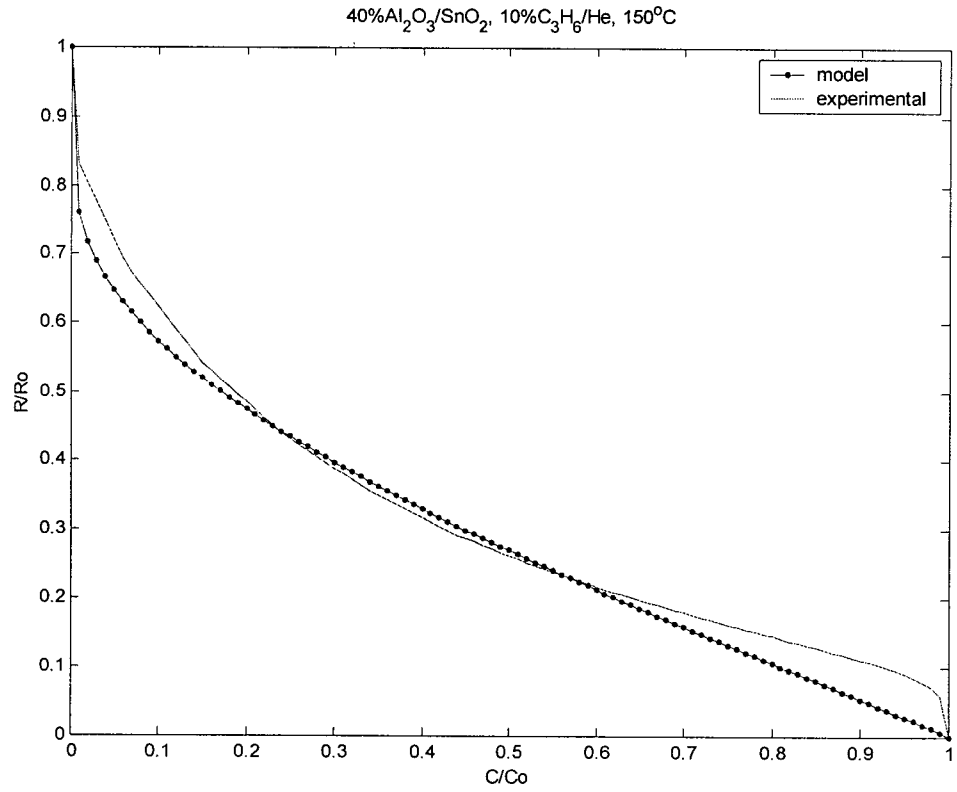

Figure 5.3a: R/R_0 **vs** c/c_0 **for 10% C_3H_6 over 40% Al_2O_3/SnO_2 at 150 °C.**

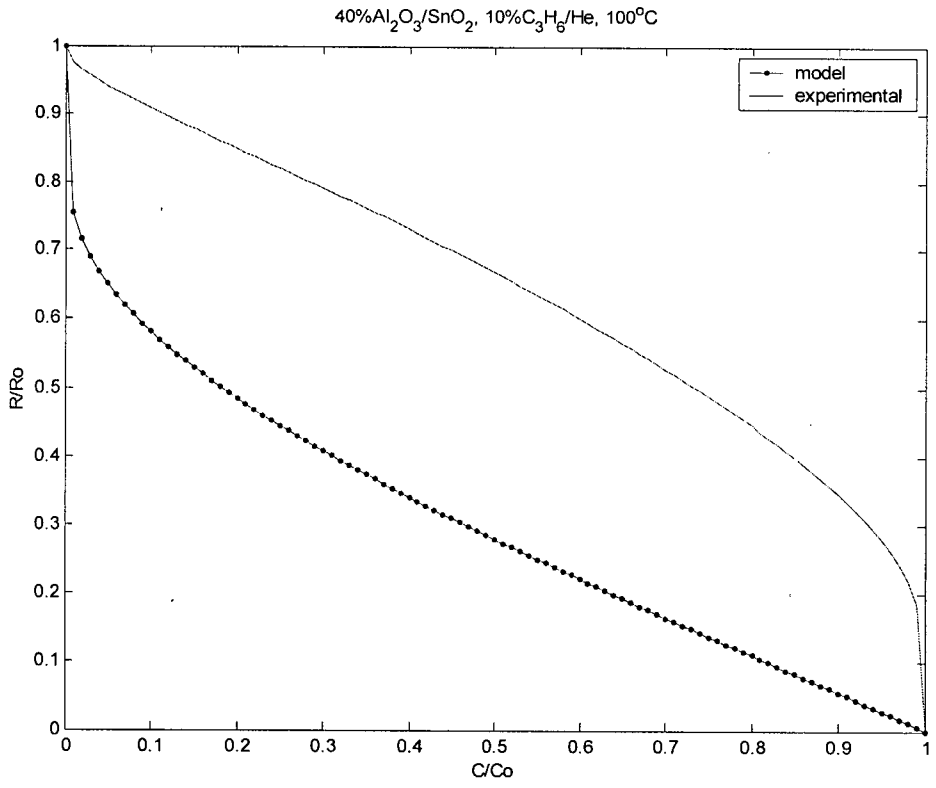

Figure 5.3b: R/R_0 **vs** c/c_0 **for 10% C_3H_6 over 40% Al_2O_3/SnO_2 at 100 °C.**

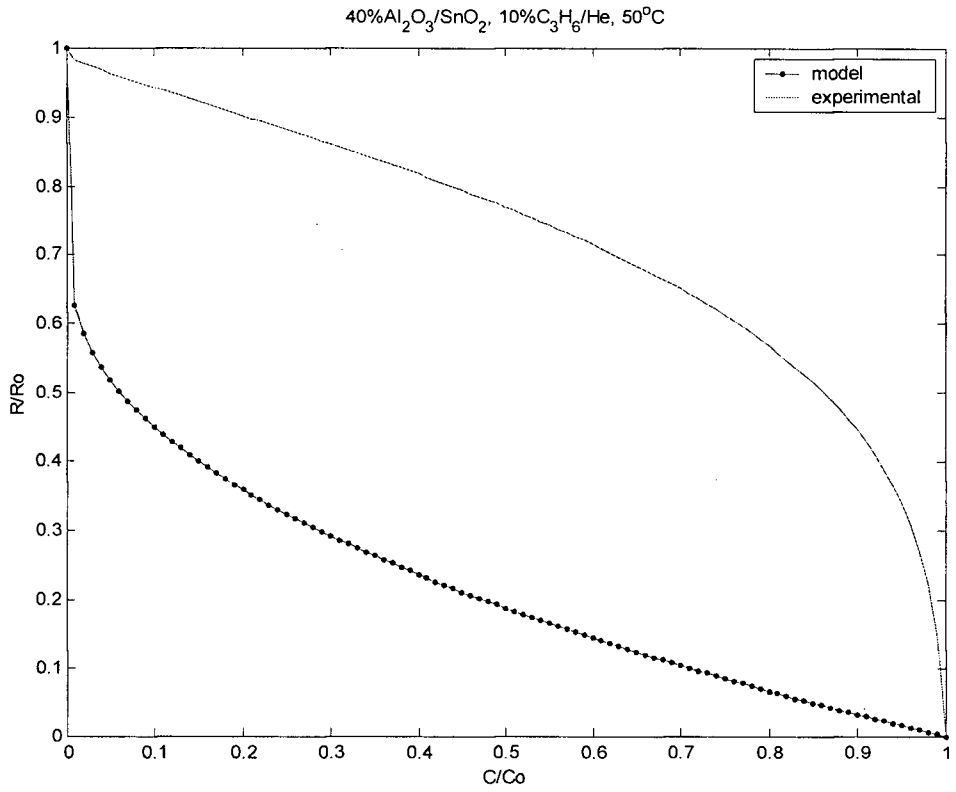

Figure 5.3c R/R_0 vs c/c_0 for 10% C_3H_6 over 40% Al_2O_3/SnO_2 at 50 °C.

5.2.3 Discussion of the Present Model

Resistance response versus time data (typical of Figure 5.2c) show that the experimental resistance response lags behind the modeled response significantly, even though the residence time has been corrected in the breakthrough response (Figure 5.2b). Also, it can be seen that the dispersion effects, seen in the nose and tail of the breakthrough response curves of Figure 5.2b, cannot be accounted for by simply shifting the time axis by the residence time of the dead space.

Examination of Figures 5.3a-c shows that the time lag of experimental resistance to the breakthrough becomes greater as temperature is reduced from 150 - 50 °C. That is, the experimentally observed bed resistance is less responsive at lower temperature than at higher temperature compared to the modeled response. This is consistent with results of the previous

chapter (and literature) indicating that sensitivity is reduced at lower temperatures. The reason for this is not clear from the present study but may be associated with kinetic effects due to mass transfer resistance in the sensing component or kinetic effects due to the reaction mechanism of the sensing. Below 150 °C, the physisorbed O_2^- ion that is present on the surface may not be as reactive to the reducing species compared to higher temperature. In addition, donor mobility is reduced at lower temperatures which may impact the rate at which electrons can move to and from the depletion region of the metal oxide.

Figures 5.3 a-c show this effect dramatically. At 150 °C (Figure 5.3a) the resistance response versus the breakthrough response shows by inspection qualitatively good correlation between experimentally observed and modeled curves. That is, the response of the SnO_2 is well matched kinetically with the breakthrough of C_3H_6 through the adsorption bed. At 100 and 50 °C, the model predicts a much more responsive system than is experimentally observed.

This is consistent with the fact that the model does not take into account kinetic effects, but rather, assumes that as the adsorbate moves through the bed the sensor response will be immediate (i.e. no rate limiting steps via mass transfer or reaction kinetics). At 150 °C this assumption seems valid, but it appears that rate limiting mechanisms must be included below this temperature and hence the resistance response does not follow the breakthrough directly.

5.3 Inclusion of Reaction Rate into the Present Model

An additional parameter was added to the model which is postulated to account for the reaction at the surface of the metal oxide and its temperature dependent effect on the resistance response to the adsorption breakthrough. The model assumes a simple first order reaction whereby the reduced portion of each parallel resistive layer in the bed is affected by the rate of reaction of the

reducing gas with the adsorbed oxygen on the surface of the depletion region. The following points are used to develop the model:

- First recall equation *5-6*, describing the resistance in each parallel resistor:

$$R_i(t, z) = R_{O,i} + R_{R,i} = R_{O,0}(1 - c/c_0) + R_{R,f}(c/c_0) \qquad \textbf{(5-6)}$$

- A surface displacement reaction is assumed in which oxygen ions are displaced by the reducing gas thereby liberating electrons. Electrons then migrate back into the depleted region increasing conductivity (decreasing resistance). The process is represented by equation *5-9* with forward reaction rate constant k_a:

$$C_3H_6 + O_2^- \xrightarrow{k_a} C_3H_6 + O_2 + e^- \qquad \textbf{(5-9)}$$

- Assuming that surface resistance is directly proportional to the conduction electrons present in the surface region, n_s :

$$R \propto n_s .$$

If the total number of electrons, N_T, is constant, and are either available for conduction (represented by n_s) or are associated with an oxygen ion (represented by $[O_2^-]$) and therefore not available for conduction, then:

$$N_T = n_s + [O_2^-] \qquad \textbf{(5-10)}$$

The rate of change in conductivity is then proportional to the rate of change in conduction electrons as given by:

$$\frac{dn_s}{dt} = k_a P_R \left[O_2^-\right] = k_a P_R \left(N_T - n_s\right) = a\left(N_T - n_s\right), \text{ hence} \qquad \textit{(5-11)}$$

$$\frac{dn_s}{dt} + k_a P_R n_s = k_a P_R N_T$$

The solution to the above differential equation is as follows:

$$n_s = N_T + \alpha e^{-k_a P_R t} \qquad \textit{(5-12)}$$

- Applying boundary conditions to equation *5-12* gives:

at $t = 0$: $\quad n_s = \dfrac{1}{\beta R_{O,0}}, \quad$ and hence: $\alpha = \dfrac{1}{\beta R_{O,0}} - N_T$

and at $t = \infty$: $n_s = \dfrac{1}{\beta R_{R,f}} = N_T, \quad$ and hence: $\alpha = \dfrac{1}{\beta R_{O,0}} - \dfrac{1}{\beta R_{R,f}}$, therefore:

$$n_s = \frac{1}{\beta R_{R,f}} + \left(\frac{1}{\beta R_{O,0}} - \frac{1}{\beta R_{R,f}}\right) e^{-k_a P_R t} = \frac{1}{\beta R_{R,i}}$$

Combining terms and rearranging to a form useable in the present algorithm yields:

$$\frac{1}{R_{R,i}} = \frac{1}{R_{R,f}}\left(1 - e^{-k_a P_R t}\right) + \frac{1}{R_{O,0}} e^{-k_a P_R t}, \text{ and therefore:}$$

$$R_{R,i} = \frac{1}{\left(\dfrac{1}{R_{R,f}}\left(1 - e^{-k_a P_R t}\right) + \dfrac{1}{R_{O,0}} e^{-k_a P_R t}\right)} \qquad \textit{(5-13)}$$

- Letting $a = k_a P_R$, and inserting equation *5-13* into equation 5-6, yields the revised model with fitting parameter, a, directly proportional to the rate constant k_a:

$$R_i(t,z) = R_{0,i} + R_{R,i} = R_{O,0}\left(1 - c/c_0\right) + \frac{1}{\left(\frac{1}{R_{R,f}}\left(1 - e^{-at}\right) + \frac{1}{R_{O,0}}e^{-at}\right)}\left(c/c_0\right) \qquad \textbf{(5-14)}$$

In addition, the model assumes:

- adsorption of C_3H_6 in the sensor bed follows Henry's Law,
- radial dispersion is high and hence radial concentration of adsorbate is constant,
- $-\Delta H_{ads}$ is constant (i.e. adsorption is occurring where $-\Delta H_{ads}$ is independent of coverage),
- fitting parameter a, is independent of P_R (i.e. the surface reduction process is zero order in P_R and first order in $[O_2^-]$.

The model was optimized by using the method of least squares in which parameter a was changed to give the best fit between the modeled response and the experimentally observed response. A *Matlab* program was developed to carry out the modeling and is shown in Appendix F. Figures 5.4a-c are typical of the optimized results which strongly indicate that the rate of reaction step is critical to the success of the model.

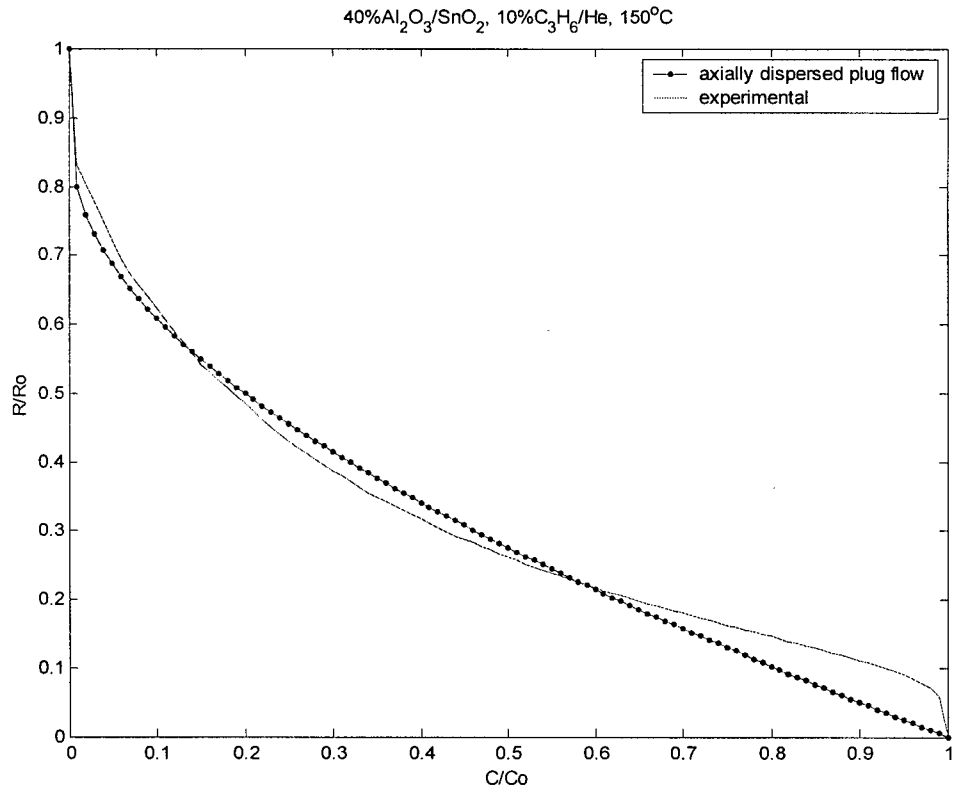

Figure 5.4a: Optimised R/R_0 vs c/c_0 for 10% C_3H_6 over 40% Al_2O_3/SnO_2 at 150 °C.

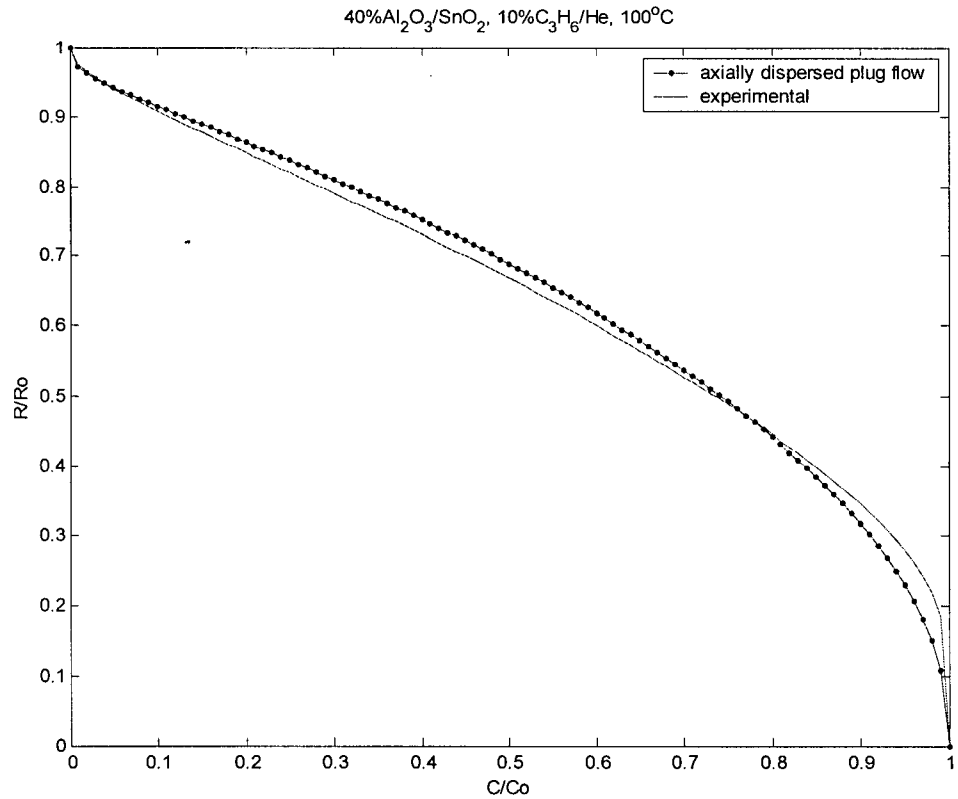

Figure 5.4b: Optimised R/R_0 vs c/c_0 for 10% C_3H_6 over 40% Al_2O_3/SnO_2 at 100 °C.

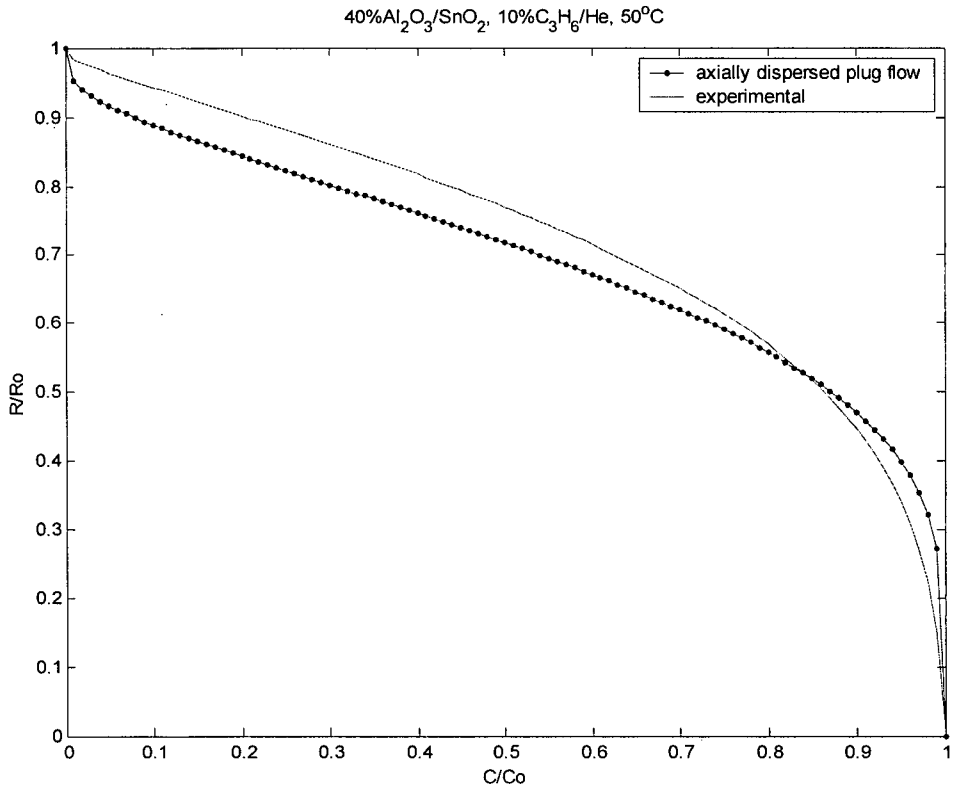

Figure 5.4c: Optimised R/R_0 vs c/c_0 for 10% C_3H_6 over 40% Al_2O_3/SnO_2 at 50 °C.

Figures 5.4a-c indicates reasonably good fits of the model to the experimental results. In particular, at temperatures below 150°C, decreasing the reaction rate constant was effective in decreasing the modeled response thereby matching the model to the experimental results. Table 5.1 gives the fitting parameter *a* (directly proportional to the rate constant) and the error sum of squares, obtained from the optimization at 50, 100 and 150 °C for 40%vol. Al_2O_3 in SnO_2, the alternately pretreated bed, and for varying concentration of C_3H_6 from 10 – 1%vol.

Table 5.1: Rate constant fitting parameter, a, and activation energy, E_a.

T	a	Sum of Squares	E_a
°C	s^{-1}		kJ/mol
40% Al_2O_3 in SnO_2, 10% C_3H_6			
50	0.0015	0.24	42.4
100	0.004	0.051	
150	0.07	0.11	
***Alt. Pretreatment*, 40% Al_2O_3 in SnO_2, 10% C_3H_6**			
50	0.0015	0.45	29.0
100	0.0045	0.14	
150	0.02	0.91	
40% Al_2O_3 in SnO_2, 5% C_3H_6			
100	0.003	0.065	-
40% Al_2O_3 in SnO_2, 1% C_3H_6			
100	0.0008	0.23	-

- Activation Energy not available

Results of the optimization show that as temperature increases from 50 to 150 °C the first order rate of reaction increases. Therefore the resistance is more responsive to the breakthrough of the reducing gas as the temperature increases (i.e. the surface reaction is enhanced). These results are consistent with the sensitivity found in the present study, which increases with increasing temperature. In addition, comparing the data for the alternately pretreated bed, the data is similar with the exception of the 150 °C point, for which the rate is much lower than for the typically pretreated bed. These values are consistent with the fact that sensitivity was lower for the alternately pretreated bed, particularly at 100 and 150 °C (seen by referring to Figure 4.11).

5.3.1 Activation Energy

The activation energy is related to the rate of reaction by the Arhennius equation:

$$k_a(T)=A_0 exp(-E_a/RT) \qquad (5\text{-}15)$$

Plotting the rate of reaction versus the inverse of temperature for a specific bed composition yields the activation energy for the surface reaction from the slope. Figure 5.5 compares the

plots for 40% Al_2O_3 in SnO_2 for the normally pretreated bed and the alternately pretreated bed. E_a is reduced for the alternately pretreated bed where E_a=29.0 kJ/mol compared to E_a=42.4 kJ/mol for the normally pretreated bed. The lower E_a, indicative that the bed resistance response is less temperature dependent, is consistent with the reduced sensitivity found in the alternately pretreated bed (refer to Figure 4.11).

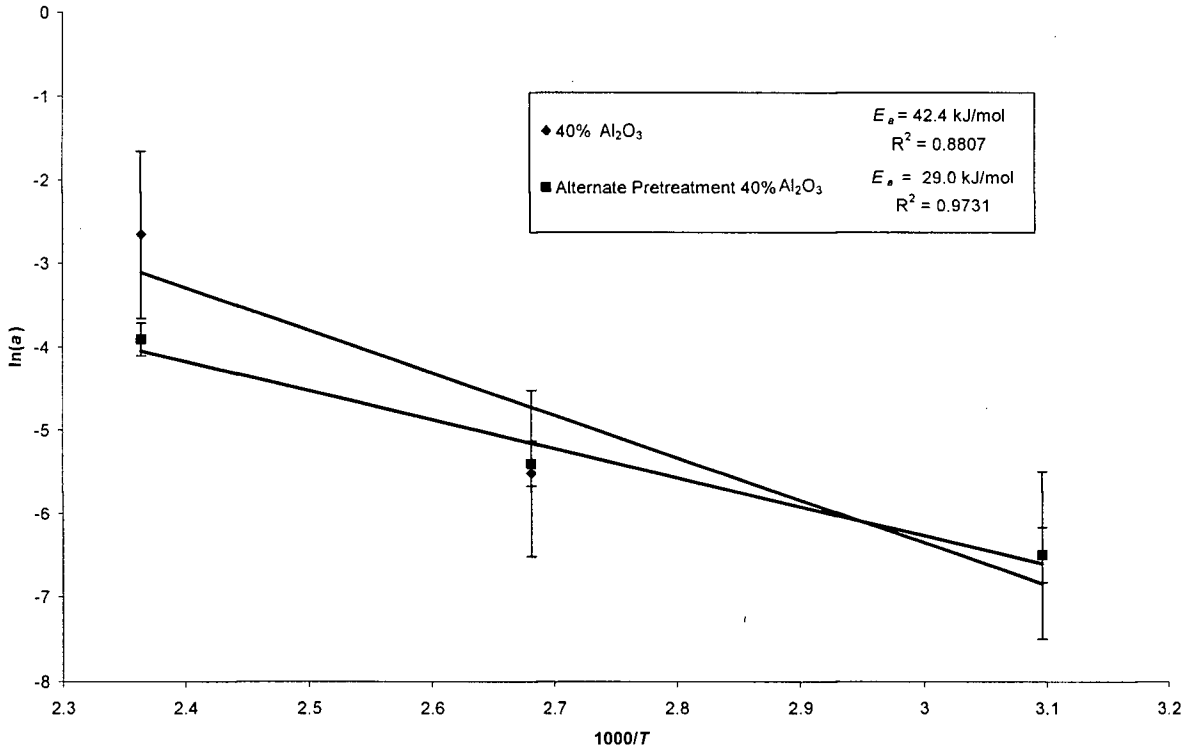

Figure 5.5: Arrhenius plot of rate ($a=k_aP_R$) vs temperature to obtain E_a normally and alternately pretreated samples of 40% Al_2O_3/SnO_2 (error bars are +/- 5%).

The low value of E_a agrees with the assumption that only weak bonds are made between the oxygen ion and the SnO_2 surface and that the oxygen ion is easily desorbed by propylene. In addition propylene may not be reactive with the oxygen ion in the temperature range of 50 – 150 ^{o}C, indicating that physisorption may be the dominant phenomenon in the metal oxide system in this temperature range.

5.3.2 Discussion of the Revised Model

The revised model fitting parameter, $a = k_a P_R$, is defined according to equations *5-9* and *5-11:*

$$C_3H_6 + O_2^- \xrightarrow{k_a} C_3H_6 + O_2 + e^- \qquad \textit{(5-9)}$$

$$\frac{dn_s}{dt} = k_a P_R \left[O_2^-\right], \qquad \textit{(5-11)}$$

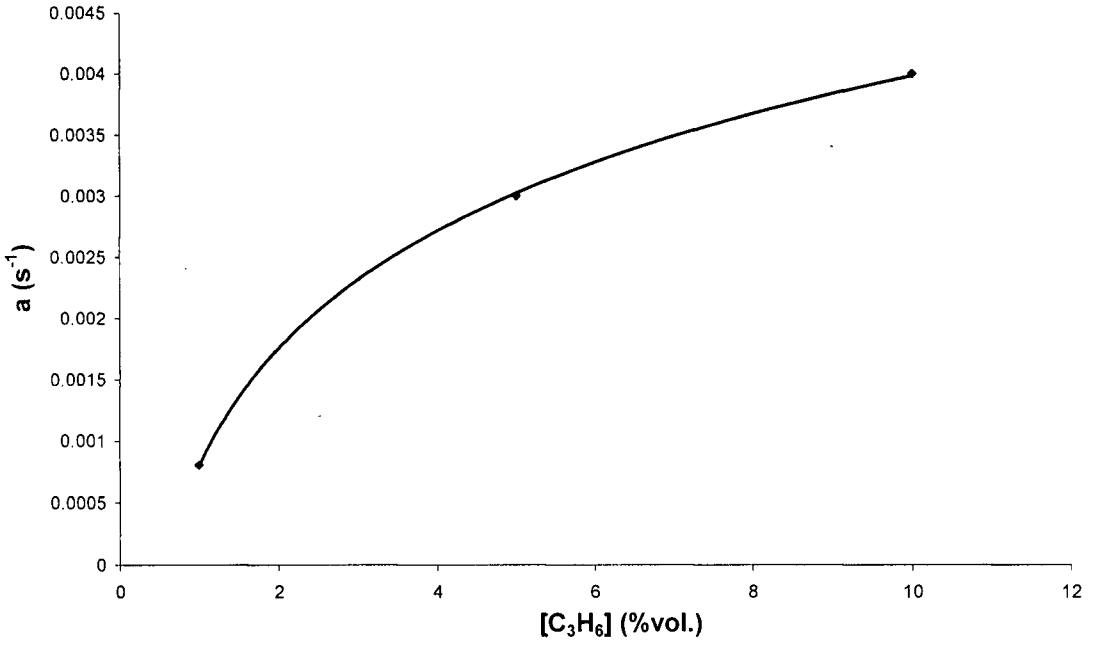

Figure 5.6: Rate constant fitting parameter *a* vs C_3H_6 concentration.

and $a = k_a P_R$ is assumed independent of P_R in the model calculations. Figure 5.6, obtained from the varying C_3H_6 concentration results (refer to Table 5.1) shows that as the concentration of C_3H_6 increases, the parameter a also increases. However, since Al_2O_3 is a weak adsorbent, the mass transfer zone is narrow and the breakthrough curve is steep. Therefore, the concentration gradient across the mass transfer zone should be small favouring the assumption that a is independent of P_R during each adsorption breakthrough. Therefore in the present model the

overall reaction can be thought of as first order in $[O_2^-]$, as has been assumed. For such a case, a preliminary adsorption step in the surface reaction whereby C_3H_6 adsorbs to saturation on a surface adsorption site may be used to describe the reaction mechanism as follows:

$$C_3H_6 + S \Leftrightarrow C_3H_6 \cdot S,$$

where S is a surface site. If this is followed by the reassociation step for O_2^- then:

$$C_3H_6 \cdot S + O_2^- \xrightarrow{k_a} C_3H_6 \cdot S + O_2 + e^- \qquad \textit{(5-16)}$$

In closing, as illustrated by comparing figures 5.4a-c with figures 5.3a-c, it can be seen that the addition of the reaction rate provides a good empirical fit with the experimental data and that overall the model matches the experimental data very well, thereby allowing for prediction of the state of adsorption from the resistance data. The proposed mechanism given by Equation *5-16* is one possible explanation for the rate limiting effect on resistance response.

5.4 Comparison with Modified Plug Flow Model

It is useful to compare the analytical solution of the present model (the axially dispersed plug flow model of Levenspiel and Bischoff (1963)) to the modified plug flow model outlined by Ruthven (1984) in order to determine if any benefit would be obtained. Experimental data from the adsorption bed containing 40% Al_2O_3 in SnO_2 at 100°C were used as a test case to make a comparison between the two approaches.

The analytical solution of the axially dispersed plug flow model includes the assumption that the bed has no mass transfer limitation (which can be seen from Equation *5-4* and *5-5* and which do not include any mass transfer term, namely k_{eff}). The solution assumes that the effective mass transfer coefficient, k_{eff}, is very large and hence the mass transfer resistance (or the lumped mass

transfer resistance, *LMTR*) is very small. Recalling equations *3-12* and *3-13,* indicating that the *LMTR* is proportional to the inverse of k_{eff} and Henry's Constant, *K*:

$$\frac{\sigma^2}{2\mu^2}\frac{L}{v} = D_L\frac{1}{v^2} + \left(\frac{\varepsilon_b}{1-\varepsilon_b}\right)\frac{1}{k_{eff}K}, \qquad \textit{(3-12)}$$

$$LMTR = \left(\frac{\varepsilon_b}{1-\varepsilon_b}\right)\frac{1}{k_{eff}K} = \left(\frac{\varepsilon_b}{1-\varepsilon_b}\right)\left(\frac{R_p}{3k_f} + \frac{R_p^2}{15\varepsilon_p D_p} + \frac{r_c^2}{15KD_c}\right), \qquad \textit{(3-13)}$$

and noting that the variance (second moment) σ^2 is comprised of the additive dispersive term and the mass transfer term of the RHS of Equation *3-12* allows the limiting case, where mass transfer can be neglected, to be evaluated. This can be found by rearrangement of equation *3-12* to give:

$$\frac{\sigma^2}{2\mu^2}\frac{L}{v} = \frac{D_L}{v^2}\left[1 + \left(\frac{\varepsilon_b}{1-\varepsilon_b}\right)\frac{v^2}{D_L}\frac{1}{k_{eff}K}\right],$$

and hence if:

$$\left(\frac{\varepsilon_b}{1-\varepsilon_b}\right)\frac{v^2}{D_L}\frac{1}{k_{eff}K} >> 1, \qquad \textit{(5-17)}$$

then the mass transfer term will dominate the variance in the bed. In the present test case (40% Al_2O_3, 10% C_3H_6 at 100 °C) the LHS of Equation *5-17* is equal to 1.6, which is not much greater than 1. Therefore both axial dispersion and mass transfer contribute (approximately by the same order of magnitude) to the variance in the breakthrough curves, and hence the model for plug flow, modified to include axial dispersion effects and mass transfer effects, was evaluated.

Ruthven (1984) gives the approximate analytical solution for the linear rate plug flow model by the following:

$$\frac{c}{c_0} = \frac{1}{2} erfc\left(\sqrt{\xi} - \sqrt{\tau} + \frac{1}{8\sqrt{\xi}} + \frac{1}{8\sqrt{\tau}} \right), \qquad \textit{(5-18)}$$

where:

$$\tau = k_{eff}\left(t - \frac{z}{v} \right), \text{ and } \xi = \frac{k_{eff} Kz}{v}\left(\frac{1-\varepsilon_b}{\varepsilon_b} \right)$$

Dispersive effects are included in the plug flow model by defining an overall effective rate coefficient, k'_{eff} whereby:

$$\frac{1}{k'_{eff}\, K} = \frac{D_L}{v^2}\left(\frac{\varepsilon_b}{1-\varepsilon_b} \right) + \left(\frac{R_p}{3k_f} + \frac{R_p^2}{15\varepsilon_p D_p} + \frac{r_c^2}{15KD_c} \right) \qquad \textit{(5-19)}$$

and redefining the dimensionless parameters τ and ξ as follows:

$$\tau' = k'_{eff}\left(t - \frac{z}{v} \right) \qquad \textit{(5-20)}$$

$$\xi' = \frac{k'_{eff}\, Kz}{v}\left(\frac{1-\varepsilon_b}{\varepsilon_b} \right) \qquad \textit{(5-21)}$$

Substituting τ' and ξ' back into Equation *5-18* gives:

$$\frac{c}{c_0} = \frac{1}{2} erfc\left(\sqrt{\xi'} - \sqrt{\tau'} + \frac{1}{8\sqrt{\xi'}} + \frac{1}{8\sqrt{\tau'}} \right) \qquad \textit{(5-22)}$$

Equations *5-20, 5-21*, and *5-22* describe the approximate analytical solution for plug flow inclusive of axial dispersion effects and mass transfer effects for the breakthrough response. A comparison of the modeled adsorption breakthrough curves is illustrated in Figure 5.7 for the

axially dispersed plug flow model (Equation *5-4*) the modified plug flow model (Equation *5-22*) and the experimentally observed curve. Figure 5-8 illustrates the modeled bed resistance response (R/R_0) versus adsorption breakthrough response (c/c_0) for the two models and the experimentally observed data.

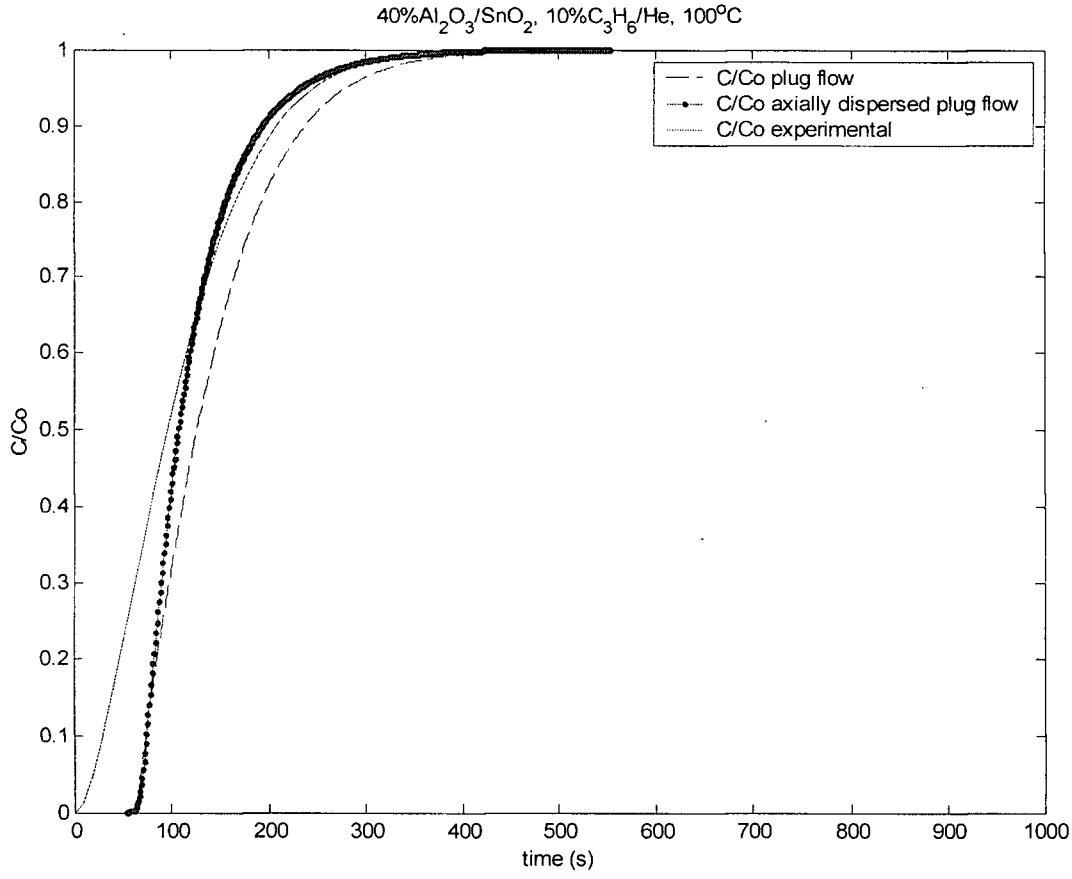

Figure 5.7: Experimental and modeled c/c_0 vs time curves for 10% C_3H_6 over 40% Al_2O_3/SnO_2 at 100 °C for the axially dispersed plug flow model and the modified plug flow model.

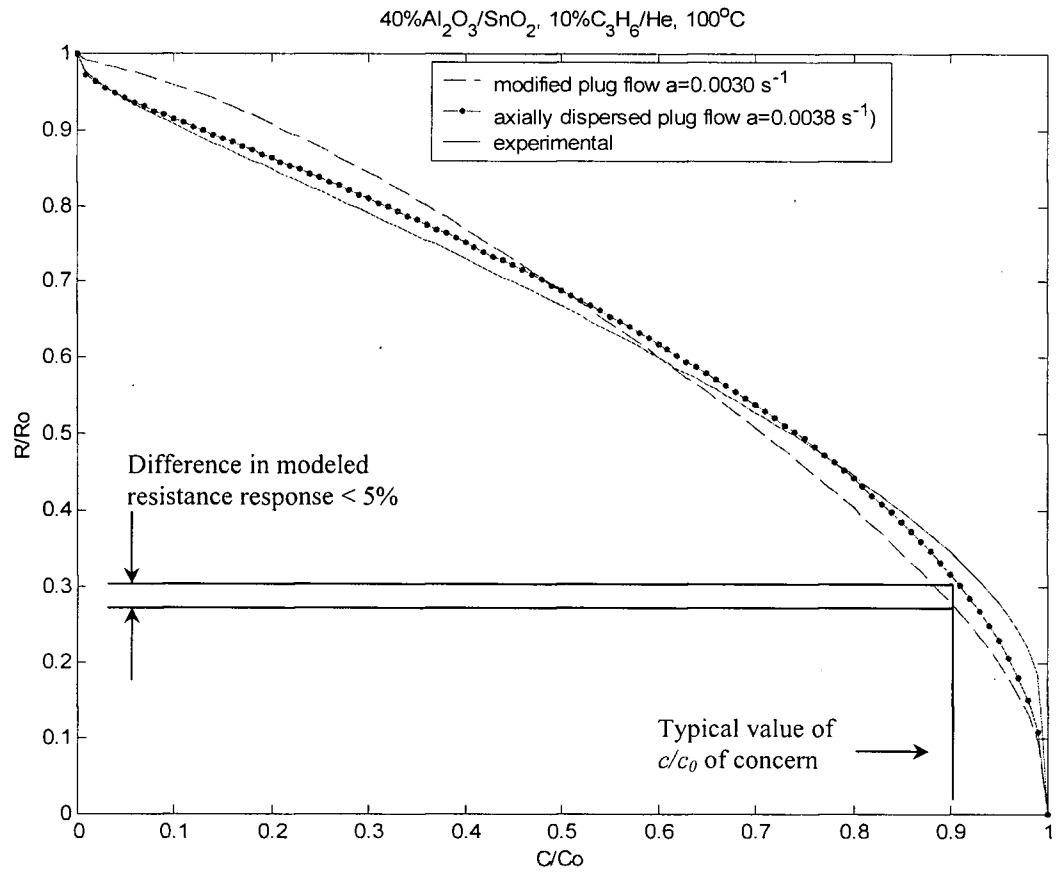

Figure 5.8: Optimised R/R_0 vs c/c_0 for 10% C_3H_6 over 40% Al_2O_3/SnO_2 at 100 °C for the axially dispersed plug flow model and the modified plug flow model.

The modeled breakthrough curves of Figure 5.7 have been offset by the mean residence time of the dead volume of the reactor. By examination of Figure 5.7 it can be seen that the breakthrough curve representing the modified plug flow model generally is not as steep as the curve for axially dispersed plug flow which is consistent with the inclusion of the additional resistance due to mass transfer in the model, thereby increasing the variance of the modeled breakthrough response.

Modeled R/R_0 *vs* c/c_0 curves from Figure 5.8 show reasonable fit with the experimental data, but that qualitatively the axially dispersed plug flow model was able to match the experimental data closer than the modified plug flow model. This is reinforced by comparison of the sum of squares error from the optimization of parameter a, shown in Table 5.2.

Table 5.2: Comparison of fitting parameter, *a*, and least squares error for the modified plug flow model and the axially dispersed plug flow model for the test case (40% Al_2O_3 in SnO_2, 10% C_3H_6, 100 °C).

Model	Parameter *a* (s^{-1})	Sum of Squares
Axially Dispersed Plug Flow (Equation *5-4*)	0.0038	0.048
Modified Plug Flow (Equation *5-21*)	0.0030	0.21

A pragmatic evaluation of the models shows that the difference between them is inconsequential. For the test case it is shown in Figure 5.8 that at c/c_0 equal to 0.9, the difference in R/R_0 between the two models is less than 5% of the full scale of R/R_0.

5.5 Summary of Modeling

The time axis comparison of breakthrough curves and resistance is difficult due to the influence of dead volume. Modeling the R/R_0 vs c/c_0 eliminates the time scale from the comparison allowing for direct comparison of the model to the experimental data. It was postulated that surface reaction kinetics account for the temperature dependent lag of resistance R/R_0 to the breakthrough of the reducing gas. Results of the model including an empirical reaction rate term show reasonably good fits under all conditions. This is substantiated qualitatively by examination of the modeled response given in Appendix E for the data determined from the adsorption over 10 - 40%vol. Al_2O_3 in SnO_2, the alternately pretreated case and the varying C_3H_6 concentration case. Comparison of the axially dispersed plug flow model to the modified plug flow model (including dispersive effects of mass transfer) do not show any benefit for the test case.

6.0 – Conclusions and Recommendations for Future Work

Development of tighter fugitive emission regulations has lead to new technologies to help maintain valve leakage integrity. In addition, improvements in the management of Leak Detection and Repair (LDAR) programs can provide substantial reductions in emissions and lost product thereby reducing overall maintenance and operating costs for process equipment including valves, pumps, compressors and piping systems. However, meeting even more stringent emission limits as has been proposed by the European Regulatory bodies, for example, will require significant improvements in valve sealing technology and LDAR management techniques and will create a need for monitoring and control techniques for very small leakage limits and concentrations (to 1 ppm). A number of potential solutions were presented in the literature review, such as the catalytic conversion of emissions in a reactor trap and passive and photocatalytic conversion. In the present study, the potential of a combined adsorbent / metal oxide sensor bed was studied to determine the feasibility of the technology to achieve adsorption and monitoring at levels consistent with typical default valve leakage rates and whether the electrical resistance response could be modeled as a function of the adsorption breakthrough of the sensor bed.

6.1 Conclusions

The following conclusions are made based on the present research:

- Adsorption uptake of a default valve fugitive emission can be achieved by utilization of a mixed adsorbent / metal oxide bed and has been shown to be practical for 1 year bed life span if strong adsorbents are used.

The practicality of the adsorption uptake is greatly diminished as temperature increases and utilization of strong adsorbents for targeted emissions could improve the uptake significantly for temperatures in the 150 – 200 °C range. In particular, activated carbon, carbon molecular sieves, zeolite 4A and 5A and potentially newly developed pi-complexation adsorbents are recommended for use in practical systems involving light hydrocarbon target gases.

In the present system, Al_2O_3 adsorbent, was found to have insignificant conductive properties ($R \sim 500$ MΩ) compared to SnO_2 metal oxide ($R < 10$ MΩ). However, the electrical characteristics of other adsorbent materials of interest should be studied to determine if they interact with the electrical properties of the metal oxide.

- Sensitivity of the mixed adsorbent / metal oxide bed increases with increasing temperature for the present study and is within lower limits of the sensitivity of other experimental gas sensing studies and within practical sensor resistance limitations imposed by sensor electronics. Sensitivity below 150 °C is limited by kinetic effects and deemed to be impractical unless additives or dopants can be utilized to enhance it. In addition, below 150 °C, the presence of physisorbed water vapour reduces resistance by donating electrons to the depletion region.

- The sensor bed electrical resistance response, represented as a number of parallel resistors, was modeled successfully as a function of the adsorption breakthrough from the model for axially dispersed plug flow (Levenspiel and Bischoff, 1963) at 150 °C where the experimental and modeled response were well matched.

- At temperatures below 150 °C kinetic effects dominate the electrical resistance response of the experimental system and hence the model, which assumes no rate limiting steps,

predicts that the electrical resistance of the bed is much more sensitive and responsive to the adsorption breakthrough than actually occurs (as evidenced by Figures 5.3 b and c).

The addition of an empirical parameter, $a = k_a P_R$, successfully predicted the experimental data based on a simple first order reaction mechanism in $[O_2^-]$ for the temperature range of 50 to 150 °C.

- Comparison of the modified plug flow model (inclusive of axially dispersive and mass transfer effects) outlined by Ruthven (1984) to the axially dispersed plug flow model of Levenspiel and Bischoff (1963) indicated that no additional benefit was obtained for the test case (40%vol. Al_2O_3 in SnO_2, 10%vol. C_3H_6 at 100 °C) by using the modified plug flow model.

6.2 Recommendations for Future Work

Much has been learned from the present study in areas of both adsorbent/adsorption phenomenon and metal oxide sensing. It is recommended that future work be undertaken to progress the concept of the combined adsorbent / metal oxide sensor in the following areas:

- Optimal performance of the combined adsorbent / metal oxide sensor bed can be achieved by maximizing the life of the adsorbent component of the bed on the one hand and by maximizing the sensitivity of the metal oxide sensing component of the bed on the other hand. Sensor life is maximized by increasing the %volume of adsorbent in the bed and by reducing the operating temperature. Sensitivity, in contrast, is inversely proportional to the operating temperature and is relatively unaffected by the %volume of adsorbent at 100 and 150 °C. Therefore a balance between sensor life and sensitivity can be obtained depending on the operating temperature of the mixed sensor bed.

It is recommended that strong adsorbents yielding relatively high uptake for target gases at elevated temperatures (150 – 200 ^{o}C) and enhancement of metal oxide sensing performance by use of additives such at Pt, and Pd should be studied, thereby improving sensitivity and/or selectivity in the same temperature range.

- It is recommended that different sensor preparation techniques and bed geometries be studied to try and improve performance and incorporate heating elements into the bed. Monolith and in particular wire mesh honeycomb reactors are of interest since the wire mesh could be designed to incorporate heating elements and/or electrodes. The literature suggests that zeolites (which have high affinity for light hydrocarbons) can be incorporated into WMH designs.

- Impregnation techniques of metal oxide and additives on adsorbent support in combination with or as the substrate should be studied to determine whether Al_2O_3 or other adsorbent supported SnO_2 will exhibit useful adsorption and sensing properties.

- Determination of the mechanisms and rate limiting steps associated with the sensing at each test temperature (i.e. the mechanism at 150 ^{o}C compared to 100 and 50 ^{o}C) should be undertaken to improve the model over a wider range of operating temperature and to further validate the empirical reaction rate parameter *a*.

Enhancement of the experimental apparatus is also recommended in order to improve the accuracy and quality of the experiments and reduce the labour required to carry them out. These recommendations are as follows:

- Redesign of the reactor to include less dead space, thereby reducing as much as possible the convolution between the experimental data and the modeled data. This

should reduce error associated in particular with the variance of the dead volume associated with the present system.

- To build the reactor from more robust material to improve handling. The current quartz design was more fragile than anticipated. Austenitic stainless steel, possibly applied with an electrically insulating internal glass coating is recommended as one possible material specification.

- Automation of the valving and data acquisition would greatly improve the labour to carry out the work, which presently involved manual operation in timing and valve switching every 15 minutes. *FlukeView* software (utilized with the hand held multi-meter) proved troublesome and would "lock-up" frequently, hence it is recommended to use simplified data acquisition software.

- Utilisation of heating elements that deliver lower power heating and that have a larger heat "reservoir" in order to improve the precision of the temperature control would be beneficial. Longer term development should include a prototypical heating element located directly within the sensor bed.

- Development of testing procedures and techniques for target gas concentration down to 1 ppm and for pure gases to broaden the capability of the sensor and model to a wide range of concentration would be beneficial.

6.3 Summary of Feasibility and Prototype Development

The current research supports the use of a combined adsorbent / metal oxide bed to contain and monitor fugitive emission gas leaks whereby the electrical resistance of the sensor bed correlates the adsorption uptake of the bed. As was concluded above, the correlation was good at 150 ^{o}C with no mathematical representation for kinetic effects. With the addition of reaction kinetics,

the model was capable of predicting the experimental results from 50 – 150 °C. In addition, other factors such as humidity and sensor poisons need to be studied and may require the addition of filtering layers in the bed to prevent sensor contamination. Sensor design parameters such as equilibrium adsorption uptake, sensitivity, selectivity, and temperature need to be further studied for different sensor preparations and geometries, such as WMH reactors, to obtain the best design.

Prototype development and field work should await further research into the above mentioned areas requiring at least an additional 3 years of research and development, based on experience with the present study. In addition, future implementation of the present technology would require the development of strategies similar to LDAR techniques to manage the sensors' field operations, particularly in the following areas:

- to monitor the signal,
- to schedule sensor bed regeneration and
- to schedule and carry out any valve refurbishment requirements.

Management strategy development and cost models should be developed in parallel with prototype development in order to compare costs of the sensor bed's implementation with current LDAR costs and compare any benefit obtained.

In addition, the success of the dual purpose sensor of the present study suggests that other areas of application, which would benefit from simultaneous containment and monitoring, should be examined. In particular, the detection and separation of trace amounts of target elements such as CO from H_2 for fuel cell applications and/or other adsorptive separation processes should be explored.

References

Allen, D.T. and Rosselot, K.S., Pollution Prevention for Chemical Processes, John Wiley and Sons, Inc, New York, 1997, Ch. 2, 5, and 7.

Anonymous, *Faster, easier detection of fugitive emissions*, Chemical Engineering Progress, 99:9 (2003) 16.

Barson, N. and Weimar, U., *Conduction model of metal oxide gas sensors*, Journal of Electroceramics, 7 (2001) 143-167.

Basmadjian, D., The Little Adsorption Book: A Practical Guide for Engineers and Scientists, CRC Press, New York, 1997, Ch. 1, 2, 7, 8.

Bowden, P.E., *Design and selection of mechanical seals to minimize emissions*, Institute of Mechancial Engineers, 213 (J) (1999) 177-188.

Caldararu, M., Popa, V.T., Sprinceana, D., Ionescu, N.I., *Surface dynamics in tin dioxide-containing catalysts I. Surface dynamics of tin dioxide interaction with propene-containing feed in presence of residual water*, Applied Catalysis A: General 125 (1995) 247-256.

Caldararu, M., Popa, V.T., Sprinceana, D., Ionescu, N.I., *Surface dynamics in tin dioxide-containing catalysts II. Competition between water and oxygen adsorption on polycrystalline tin dioxide*, Sensors and Actuators B, 30 (1996) 35-41.

Caldararu, M., Postole, G., Hornoiu, C., Gratan, V., Dragan, M., Ionescu, N.I., *Electrical conductivity of gamma-Al_2O_3 at atmospheric pressure under dehydrating/hydrating conditions*, Applied Surface Science 181 (2001) 255-264.

Chang, T., Oil and Gas Journal, April 3 (2000) 56-67. In Industrial Engineering Chemistry Research, 41 (11) (2002) 2728-2734.

Choudary, N.V., Kumar, P., Bhat, T.S.G., Cho, S.H., Han, S.S., Kim, J.N., *Adsorption of light hydrocarbon gases on alkene-selective adsorbent*, Industrial Engineering Chemistry Research, 41 (2002) 2728-2734.

Chung, K.S., Jiang, Z, Gill, B.S., Chung, J.S., *Oxidative decomposition of o-dichlorobenzene over V_2O_5/TiO_2 catalyst washcoated onto wire-mesh honeycombs*, Applied Catalysis A: General, 237 (2002) 81-89.

Chwieroth, B., Patton, B.R., Wang, Y., *Conduction and gas-surface reaction modeling in metal oxide gas sensors*, Journal of Electroceramics, 6:1, (2001) 27-41.

Cirera, A., Dieguez, A., Diaz, R., Cornet, A., Morante, J.R., *New method to obtain stable small-sized SnO_2 powders for gas sensors*, Sensors and Actuators B, 58 (1999) 360-364.

Da Silva, F.A., Rodrigues, A.E., *Adsorption equilibria and kinetics for propylene and propane over 13X and 4A zeolite pellets*, Journal of Industrial and Engineering Chemistry Research, 38 (1999) 2051-2057.

Dubois, J.P., *New developments in the design of shell safety tightness for quarter-turn valves*, Valve World, Vol. 2, Iss. 5 (October, 1997) 31-33.

Farrauto, R.J. and Heck, R.M., *Environmental catalysis into the 21st century*, Catalysis Today, 55 (2000) 179-187.

Fisher-Rosemount, Control Valve Handbook, Fisher Controls International Inc, Marshalltown, Iowa, Third Edition, 1999, Ch. 1, 3, 8.

Frish, M.B. and Melnyk, J.M., *Detect fugitive emissions with lasers*, Hydrocarbon Processing, 75 (5) (1999) 99.

Garing, K., *Proper monitoring essential to reducing 'Fugitive Emissions' under Leak Detection and Repair programs*, EPA Enforcement Alert, United States Environmental Protection Agency, Vol. 2, No. 9 (October, 1999) 1-4 (EPA 300-N-99-014).

Golden *et al.* (1998) in: Rege, S.U., Yang, R.T., Buzanowski, M.A., *Sorbents for air prepurification in air separation*, Chemical Engineering Science, 55 (2000) 4827-4838.

Grande C.A., Silva, V.M.T.M., Gigola, C., Rodriques A.E., *Adsorptioin of propane and propylene onto carbon molecular sieve*, Carbon, 41 (2003) 2533-2545.

Grande, C.A., Gigola, C., Rodrigues, A.E., *Adsorption of propane and propylene in pellets and crystals of 5A zeolite*, Journal of Industrial and Engineering Chemistry Research, 41 (2002) 85-92.

Grande, C.A. and Rodrigues, A.E., *Adsorption equilibria and kinetics of propane and propylene in silica gel*, Journal of Industrial and Engineering Chemistry Research, 40 (2001) 1686-1693.

Hashmonay, R.A. and Yost, M.G., *Innovative approach for estimating fugitive gaseous fluxes using computed tomography and remote optical sensing techniques*, Journal of the Air and Waste Management Association, 49 (9) (1999), 966-972.

Haynes, H.W. and Sarma, P.N., *A model for the application of gas chromatography to measurements of diffusion in bidisperse structured catalysts*, AIChE Journal, 19 (5) (1973) 1043-1046.

Heilig, A., Barson, N., Weimar, U., Gopel, W., *Selectivity enhancement of SnO_2 gas sensors: simultaneous monitoring of resistances and temperatures*, Sensors and Actuators B, 58 (1999) 302-309.

Hirschfelder, J.O., Curtiss, C.F., Bird, R.B., Molecular Theory of Gases and Liquids, Wiley, New York, 1954.

ISO / WD-15848-1.6 (ISO-TC153/SC1/WG10-N17), *Industrial valves – fugitive emissions – measurement, test and qualification procedures.* Part 1 – 3 (consisting of: proof of design, type testing, quality control, in plant tests). Release 25-1-2000.

Ihokura, K., *The effectgs of crystallite size in sintered tin dioxide on changes in electrical conductivity in deoxydisable gases*, Sensor and Actuators, 50 (1982) 99.

Imelik, B. and Vedrine, J.C., Catalyst Characterisation: Physical Techniques for Solid Materials, Plenum Press, New York, 1994, Chapter 20: Applications of Electrical Conductivity Measurements in Heterogeneous Catalysis (Herrmann, J.M.) 559-584.

Janata, J., Principles of Chemical Sensors, Plenum Press, New York, 1989, Ch. 1, 2, 4.

Jarvelin, H. and Fair, J.R., *Adsorptive separation of propylene-propane mixtures*, Industrial Engineering Chemistry Research, 32 (1993) 2201-2207.

Jiang, Z., Chung, K.S., Kim, G.R., Chung, J.S., *Mass transfer characteristics of wire-mesh honeycomb reactors*, Chemical Engineering Science, 58 (2003) 1103-1111.

Kikuchi R., Maeda, S., Sasaki, K., Wennerstrom, S., Ozawa, Y., Eguchi, K., *Catalytic activity of oxide-supported Pd catalysts on a honeycomb for low-temperature methane oxidation*, Applied Catalysis A: General, 239 (2003) 169-179.

Kim, J.H., Sung, J.S., Son, Y.M., Vasiliev, A.A., Malyshev, V.V., Koltypin, E.A., Eryshkin, A.V., Godovski, D.Y., Pisyakov, A.V., Yakimov, S.S., *Propane/butane semiconductor gas sensor with low power consumption*, Sensors and Actuators B, 44 (1977) 452-457.

Kocemba I., Szafran, s., Rynkowski, J., Paryjczak, T., *The properties of strongly pressed tin oxide-based gas sensors*, Sensors and Actuators B, 79 (2001) 28-32.

Korolkoff, N.O., *Survey of toxic gas sensors and monitoring systems*, Solid State Technology, December (1989) 49-69.

Kovacevic, S.B., *Screening adsorbents for a layered adsorbent bed for hydrogen separation using breakthrough experiments*, MASc Thesis, University of British Columbia (2001).

Langford, G.C., Senior, K.A., Paul, B.O., *Control valves impact profitability, affect air quality*, Chemical Processing, 63 (June 2000) 42-50.

Levenspiel, O. and Bischoff, K.B., Advances in Chemical Engineering, Vol. 4, 95, Academic Press, New York, 1963.

Madou M.J., Morrison, S.R., Chemical Sensing with Solid State Devices, Academic Press, Inc., Toronto, 1989. Ch. 1, 2, 3, 5, 10, 12, 13.

Majer, V. and Svoboda, V., Enthalpies of vapourization of organic compounds: A critical review of data compilation, Blackwell Scientific Publications, Oxford (1985) 300.

Mantell, C.L., Adsorption, McGraw-Hill Book Company, Inc., New York, 1951, Ch. 1-4.

Muller, A., *Sasol Synthetic Fuels Ltd valve gland repacking programme,* Valve World, Vol. 5, Iss. 5 (October 2000) 61.

Nemoto, H. and Oda, I., *Direct examination of electrical properties of single grain boundaries in barium titanate (IV) PTC ceramics*, Advanced Ceramics, 1 (1981) 167.

Oloman, C., Matte, M., Lum, C., Electronic conductivity of graphite fiber fixed-bed electrodes, Journal of the Electrochemical Society, 138 (8) (1991) 2330-2334.

Park, C.O. and Akbar, S.A., *Ceramics for chemical sensing*, Journal of Materials Science, 38 (2003) 4611-4637.

Perry, R.H. and Green, D., Perry's Chemical Engineers' Handbook, Sixth Edition, McGraw Hill, New York, 1984.

Phani, A. R., Manorama, S., Rao, V.J., *Preparation, characterization and electrical properties of SnO2 based liquid petroleum gas sensor*, Materials Chemistry and Physics, 58 (1999) 101-108.

Rege, S.U., Yang, R.T., Buzanowski, M.A., *Sorbents for air prepurification in air separation*, Chemical Engineering Science, 55 (2000) 4827-4838.

Romanow-Garcia, S., *Use optical sensing to detect fugitive emissions*, Hydrocarbon Processing, 75 (5) (1996), 15.

Ruthven, D.M., Principles of Adsorption and Adsorption Processes, John Wiley & Sons, New York, 1984, Ch. 1, 2, 3, 4, 5, 6, 7, 8.

Satterfield, C.N., Mass Transfer in Heterogeneous Catalysis, Robert E. Krieger Publishing Company, New York, 1981, Chapters 1 and 2.

Sear, D., *Emissions Control Special*, Valve World, Vol. 4, Iss. 4 (August, 1999) 35-37.

Siegell, J.H., *Developing and LDAR programme database*, Valve World, Vol. 4, Iss. 4 (August, 1999) 38-43.

Staudt, R., Rave, H., Keller, J.U., *Impedance spectroscopic measurements of pure gas adsorption equilibria on zeolites*, Adsorption, 5 (1999) 159-157.

Stoica, M., Caldararu, M., Ionescu, N.I., Auroux, A., *Protonic conductivity of Pt/Al_2O_3 in hydrogen – and – water containing atmospheres*, Applied Surface Science, 153 (2000) 218 – 222.

Stoica, M., Caldararu, M., Rusu, F., Ionescu, N.I., *Some experimental evidences for hydrogen spillover on Pt/Al_2O_3 catalysts by electrical conductivity transient response*, Applied Catalysis A: General 183 (1999) 287-293.

Sukharev, V.Y., *Percolation model of adsorption-induced response of the electrical characteristics of polycrystalline semiconductor adsorbents*, Chemical Society Faraday Transactions, 89 (3) (1993) 559-572.

Van Santen, R.A. and Niemantsverdriet, J.W., Chemical Kinetics and Catalysis, Plenum, NewYork, 1995, Ch. 2.

Wark, K., Warner, C.F., Davis, W.T., Air Pollution: Its Origin and Control, Addison-Wesley, Menlo Park, California, 1998, Ch. 2, 6, 9, 10.

Watson, J., Ihokura, K., Coles, G.S.V., *The tin dioxide gas sensor*, Measurment Science Technology, 4 (1993) 711-719.

Williams, J.L., *Monolith structures, materials properties and uses*, Catalysis Today, 69 (2001) 3-9.

Wu, M.C. and Kelly, N.A., *Clean air catalyst system for on-road applications: I. Evaluation of potential catalysts*, Applied Catalysis B: Environmental, 18 (1998) 79-81.

Wu, M.C. and Kelly, N.A., *Clean air catalyst system for on-road applications: II. Mechanistic studies of pollutant removal*, Applied Catalysis B: Environmental, 18 (1998) 93-104.

Yamazoe, N., *Effects of additives on semiconductor gas sensors*, Sensors and Actuators, 4 (1983) 283-289.

Yang, B.L. and Kung, H.H., *Reactor trap to remove hydrocarbons from engine exhaust during cold start*, Environmental Science Technology, 28 (1994) 1561-1564.

Yang, R.T., Adsorbents: Fundamentals and Applications, John Wiley & Sons Inc, Hoboken, New Jersey, 2003, Chapters 1, 2, 3, 6, 10.

Appendix A

System and Reactor Design Considerations

System Design Considerations

The following system design considerations were taken into account:

- **Measuring and logging the electrical resistance of the packed bed**: The electrical resistance was monitored throughout the duration of each experimental procedure. An industrial multi-meter, *Fluke 189*, which has a capacity to measure resistance up to 500 mega ohms, was used to obtain these measurements. The meter was connected directly to the logging computer via the RS-232 port and the data logged via Fluke documenting software, *FlukeView Forms*. The sampling rate was set at 2 samples per second (1 sample per 0.5 seconds). Logging of the data occurs based on the time average of the data over 10 second intervals (1 logged time average sample per 10 seconds). Therefore 6 samples per minute are taken to reduce the data storage and handling requirements of the data set.
- **Monitoring the adsorption breakthrough curves**: This was done by utilizing the thermal conductivity detection (TCD) capabilities of a *Hewlett Packard 5710 A* gas chromatograph unit. This unit had a dedicated data logging computer and used *Labtech Notebook/XE* software to manage and display the data. The sampling rate was set to 2 samples per second. The sensitivity of the TCD was adjusted to 100 amps for 5 – 10% C_3H_6 and 120 amps for 1% C_3H_6 in order to obtain a reasonable change between the initial signal and the final signal. However, increasing the unit's sensitivity can cause overheating of the sensor and therefore the TCD was limited by sensitivity to a lower limit of gas concentration of approximately 1% (10,000 ppmv).
- **Step change in gas concentration:** A step change in gas concentration was required to obtain the breakthrough data from the TCD. A series of three-way valves with specially machined working tolerances (to eliminate any leakage between flow paths) were utilized

to allow the flow of gas to be manually changed from one flow stream to another instantaneously. The gas flow rates were preset via the mass flow controllers (MFC) and hence a step change in gas composition would occur each time a three-way valve was switched.

- **Gas (target fugitive emission) Selection / Safety:** Propylene was utilised as the target fugitive emission gas. It is an important primary refining product and as can be seen from Table 1.1, it is a major contributor of fugitive emissions from process equipment (contributing nearly 7,900,000 lbs/yr). Propylene concentrations of 10% in helium to 1% in helium were utilized. A number of target gases could have been selected however propylene is relatively easy to work with in the lab due to its lack of toxicity compared to other gases.
- **Metal / Oxide Selection**: Tin dioxide (SnO_2) was selected as the sensing component of the metal oxide / adsorbent bed. As discussed in the literature review, SnO_2, is a widely researched and utilized material for gas sensing. It is sensitive to hydrocarbon gases through a range of operating temperatures and pressures which makes it an ideal candidate for this research.
- **Adsorbent Selection**: Alumina (Al_2O_3) was selected as adsorbent material for the metal oxide / adsorbent bed. As discussed in the literature review a number of adsorbents could be used that are selective towards the uptake of propylene. Alumina has a lower uptake capacity for propylene than a number of other industrial adsorbents such as zeolite 13X, 4A, and 5A, for example. Its reduced uptake capacity for propylene gas reduced the time required for each breakthrough experiment, thereby allowing for a larger number of tests to be carried out.
- **Temperature Control:** Temperature control for the experiments (including preliminary procedures) was required for set-points between 50 and 350 degrees Celsius. A feedback

temperature control system was used as illustrated in Figure 3.1. This system includes a K-type thermocouple, a PID controller (*Omega model CN8261-DC1-AL1-C2*), and two, 200 Watt band heaters (*Omega model MBH-1215-200-B/120*). The system was insulated by wrapping a fitted piece of fibre-glass blanket insulation around the reactor, up to and including the inlet and outlet connections.

- **Pressure Control:** The pressure was maintained in the reactor between 120 kPag and 145 kPag. The maximum pressure drop across the reactor was no greater than 2 kPa at up to 200 sccm of 10% propylene flow and less than 0.2 kPa at 80 sccm of 10% propylene flow.
- **Ease of Construction, Cost, and Maintainability:** In general, components readily available in the catalysis laboratory were utilized wherever possible to reduce cost. However, the apparatus for breakthrough analysis was redesigned specifically for this project. New 316 stainless steel tubing and valving was utilized and rerouted to simplify the equipment layout and simplify further modifications and maintenance if necessary.

Reactor Design Considerations

The following reactor design considerations were taken into account:

- **Diameter:** The diameter of the reactor was specified in order to reduce or eliminate any wall effects of the flow of gas through the bed and to ensure that good electrical contact and resistance measurements could be obtained. Dautzenberg (1988) recommends that the diameter of the reactor should be at least 10 times greater than the particle diameter. Caldararu (2001) recommends from experience that if the outer wall diameter exceeds 25 mm (with an inner wall diameter limited to 7 mm for practicality of fitting the inner electrode) then the quality of the electrical resistance signal is diminished.

In specifying the reactor diameter, the distance between the inner and outer wall was utilized in the calculation. The particle diameters utilized in this project were 24 - 42 mesh (approximately 0.4 – 0.7 mm) for Al_2O_3 to a maximum of 24 – 42 mesh (approximately 0.7 - 2 mm) for SnO_2. Since the mixture of Al_2O_3 in SnO_2 ranged from 10% to 40% for the main set of experiments, then the lower limit of Dautzenberg's recommendation may not be met at lower percent mixtures of Al_2O_3. However, to meet Caldararu's recommendation, the outer diameter of the bed was specified at 25 mm.

- **Volume / Length:** The volume of the bed was designed to be sufficient to be able to contain enough metal oxide / adsorbent material to obtain a reasonable residence time in the reactor through all of the experimental procedures. That is, the time required to complete each breakthrough experiment should be short enough to allow for a full set of experiments to be completed during each day for practical reasons. With pretreatment and repeat experiments being carried out, this meant that the longest breakthrough experiment should last approximately 30 minutes and hence the volume of the bed was specified at 22.5 ml of mixed metal oxide / adsorbent material.
- **Length:** The minimum length of the reactor was dictated by the volume of the metal oxide / adsorbent bed, and the predetermined diameters of the reactor and thermowell. Therefore, the reactor was designed long enough to contain the metal oxide / adsorbent bed volume, as determined above and hence the bed length was contained within the 50 mm length of the electrodes. Other dimensional considerations included ease of operability, maintenance and heating requirements of the reactor.
- **Temperature Effects:** Radial thermal gradients were considered negligible due to the short distance between the outer wall and the inner wall of the bed. In addition, heat effects from surface reactions are minimal in this system and the length of the bed is

temperature controlled, therefore it is assumed that no axial temperature effects were present.

- **Electrical Contact**: Two co-centric tantalum electrodes were placed in the reactor to make contact with the metal oxide / adsorbent bed and hence allow for the measurement of electrical resistance across the bed throughout the experimental procedures. These contacts were placed co-centrically, as illustrated in Figure 3.2, in order to maximize their surface contact with the bed. Tantalum was utilized as the electrode material in order to reduce any reactivity between the electrodes and either the metal oxide / adsorbent material or the gas flow.
- **Thermowell:** A thermowell was placed into the reactor to allow for temperature feedback to the temperature controller. The thermowell also acts as the support for the tantalum inner electrode and was specified at 7 mm (outer diameter) to ensure that it could be fit with the inner electrode.
- **Ease of operability, construction, cost and maintainability:** The reactor was designed to be robust enough to allow for reasonable handling practices. It was constructed from quartz to make it less fragile than typical borosilicate glass. In addition, fittings were made to connect via borosilicate ball joints, to allow for easy replacements if damaged (fittings being deemed most fragile). The main joint in the reactor wall allows for access to pack and unpack the bed, solder the tantalum electrodes to the tungsten wire leads and clean the reactor. It was designed to withstand a static reactor pressure of 345 kPag (approximately 50 psig), however, all experimental tests were carried out between 120 and 145 kPag. The reactor was relatively expensive, but robust and easily maintained.

Appendix B

Experimental Breakthrough Curves

(In order of increasing % volume of Al_2O_3 in SnO_2 to 100% Al_2O_3)

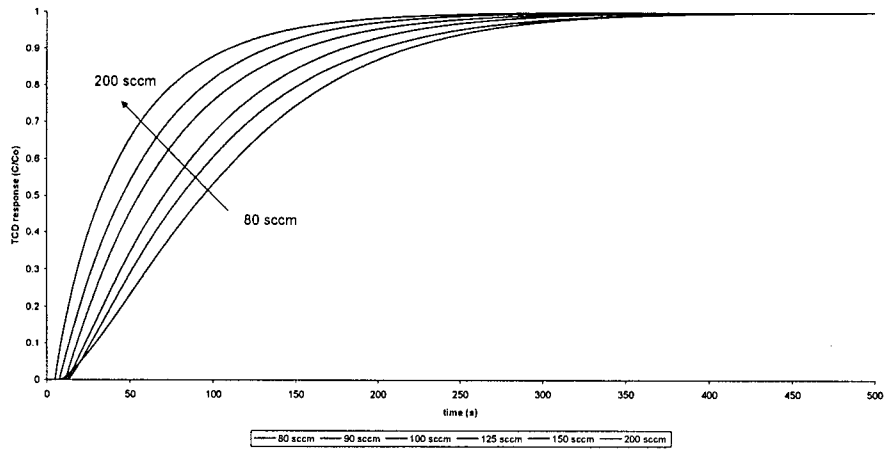

Key: Typical plot indicating the adsorption breakthrough curves for the adsorption of 1-10% C_3H_6. Curves are for 80 - 200 sccm from right to left respectively.

Experimental Breakthru Results for 10% C_3H_6 over
10% Al_2O_3 (24-42 mesh)/ SnO_2 (10-24 mesh) at 50°C

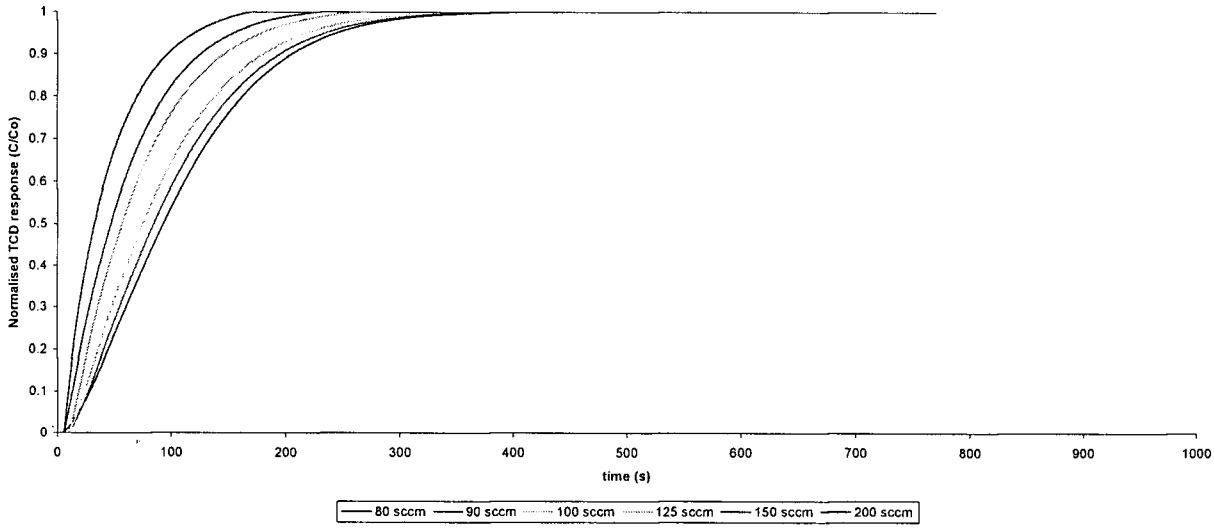

Experimental Breakthru Results for 10% Propylene over
10% Al_2O_3 (24-42 mesh)/ SnO_2 (10-24 mesh) at 75°C

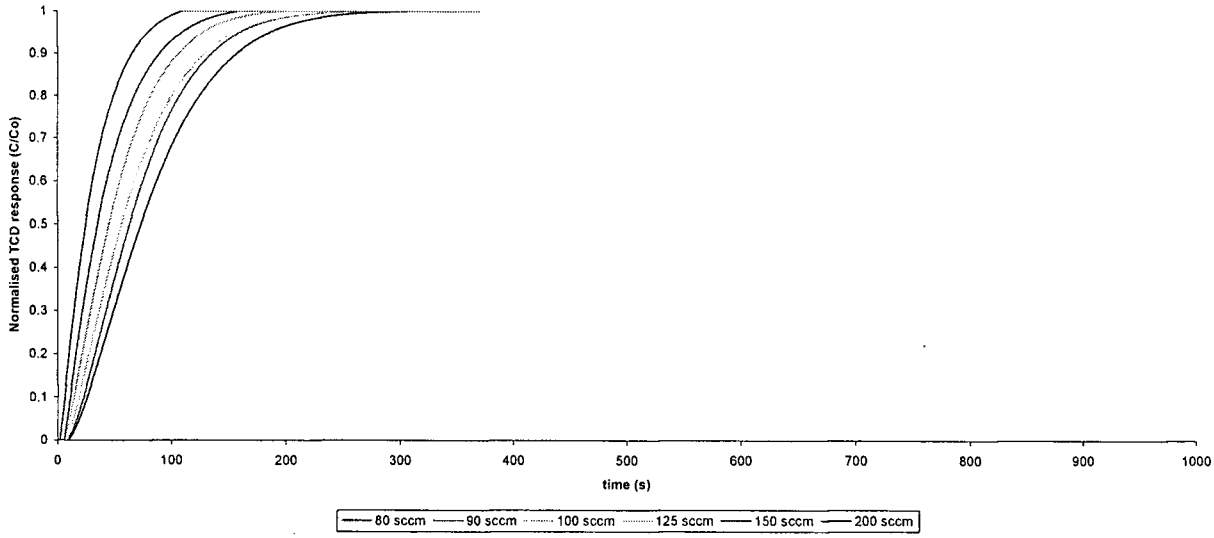

Experimental Breakthru Results for 10% Propylene over
10% Al_2O_3 (24-42 mesh)/ SnO_2 (10-24 mesh) at 100°C

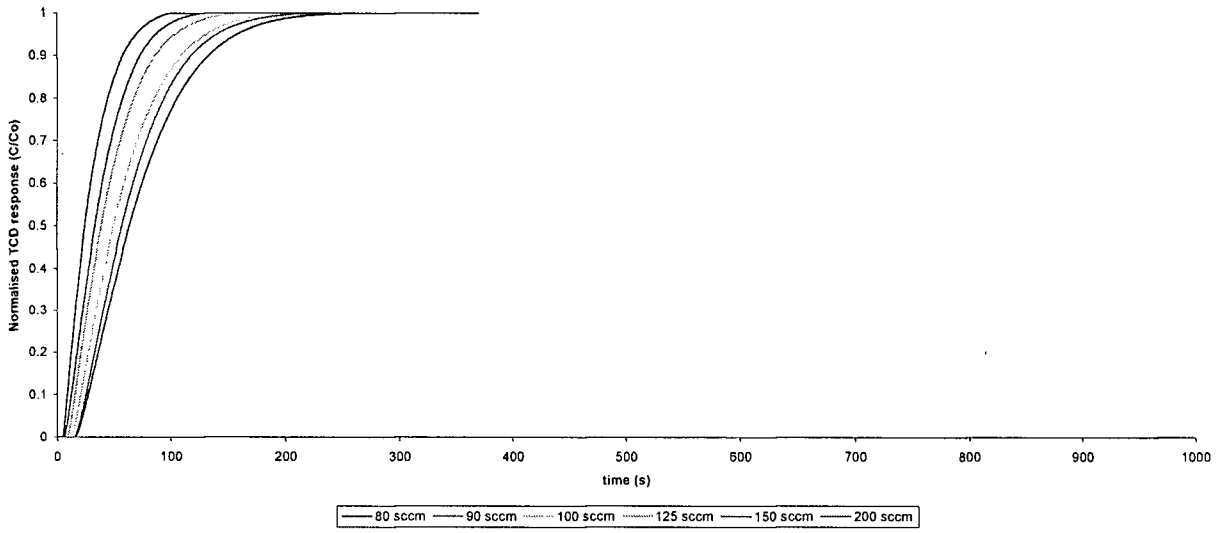

Experimental Breakthru Results for 10% Propylene over
10% Al_2O_3 (24-42 mesh)/ SnO_2 (10-24 mesh) at 100°C

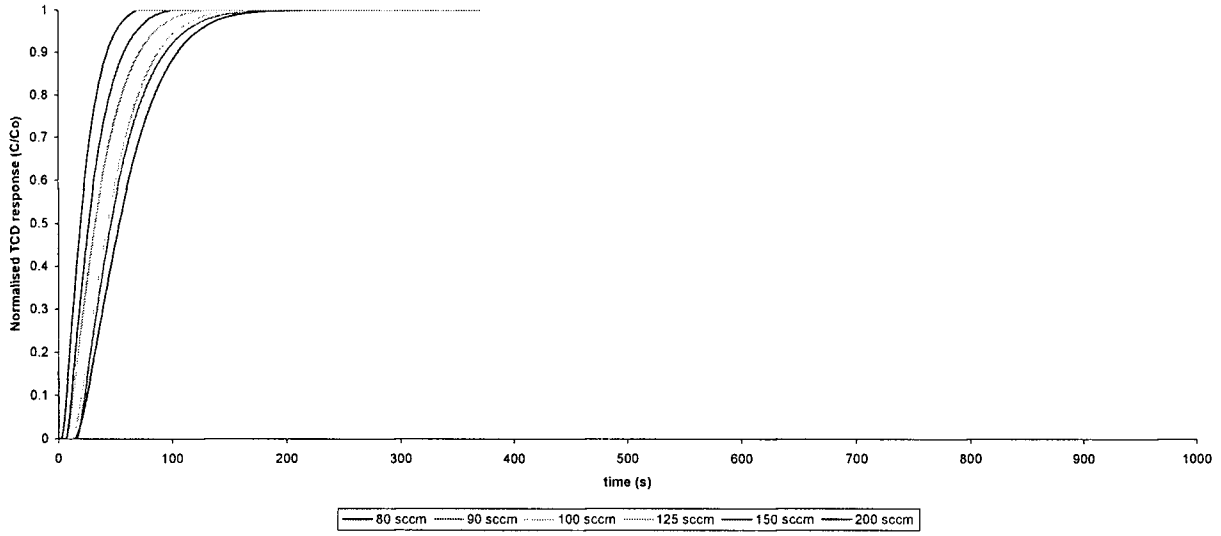

Experimental Breakthru Results for 10% Propylene over
20% Al_2O_3 (24-42 mesh)/ SnO_2 (10-24 mesh) at 50°C

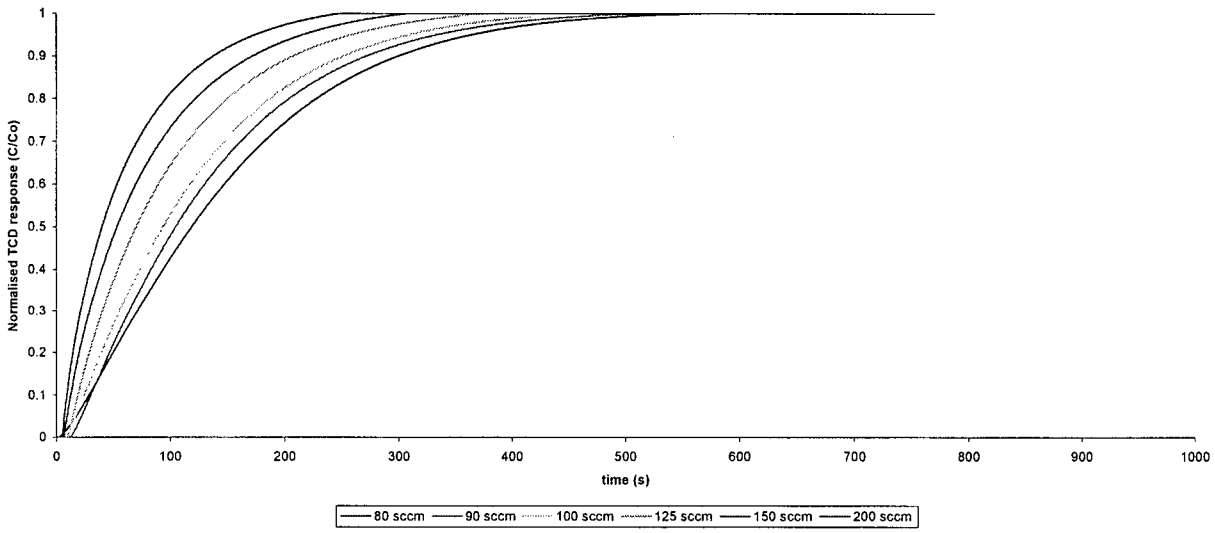

Experimental Breakthru Results of 10% Propylene over
20% Al_2O_3 (24-42 mesh)/ SnO_2 (10-24 mesh) at 75°C

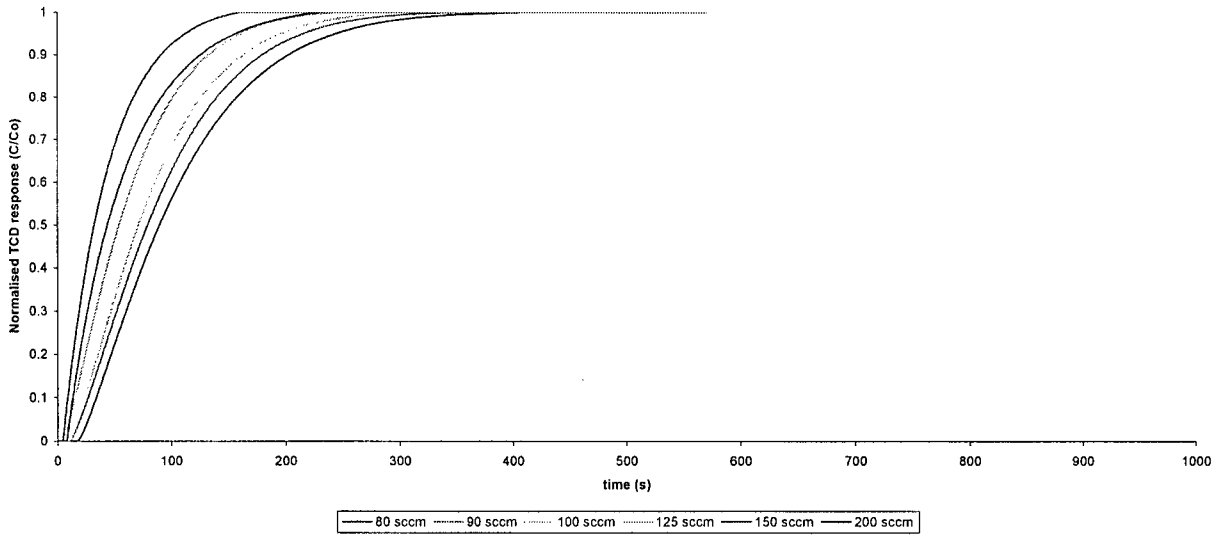

Experimental Breakthru Results of 10% Propylene over
20% Al_2O_3 (24-42 mesh)/ SnO_2 (10-24 mesh) at 100°C

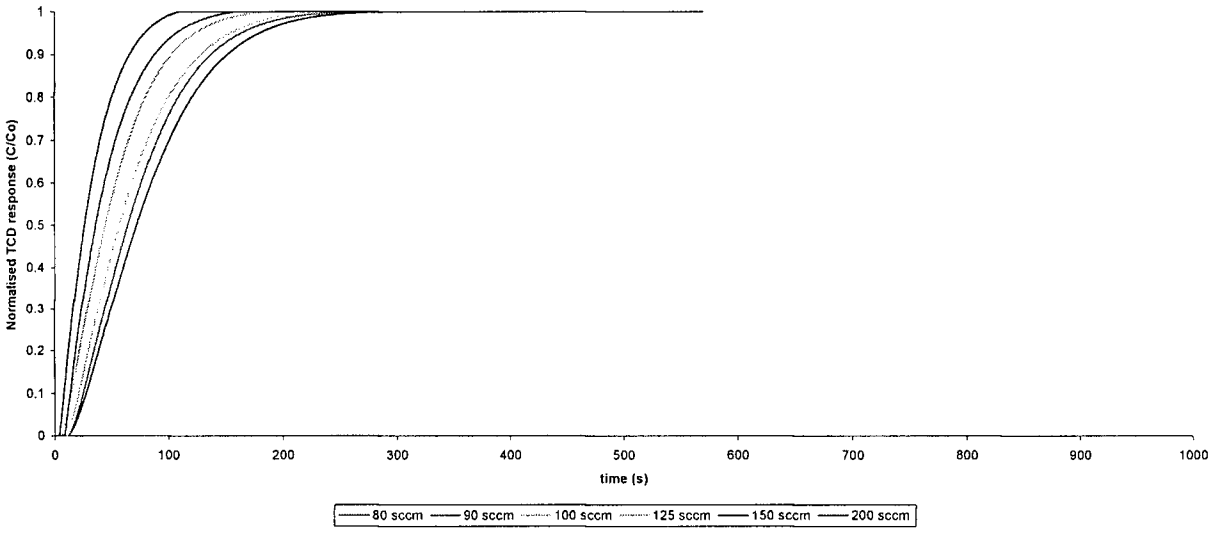

Experimental Breakthru Results for BT of 10% Propylene over
20% Al_2O_3 (24-42 mesh)/ SnO_2 (10-24 mesh) at 150°C

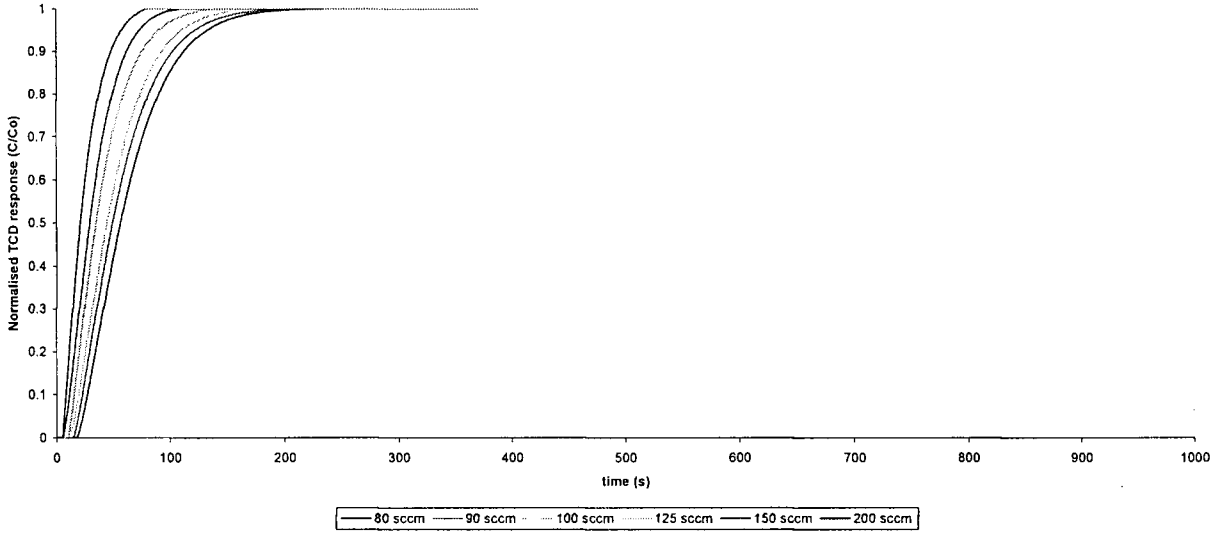

Experimental Breakthru Results for 10% Propylene over
30% Al_2O_3 (24-42 mesh)/ SnO_2 (10-24 mesh) at 50°C

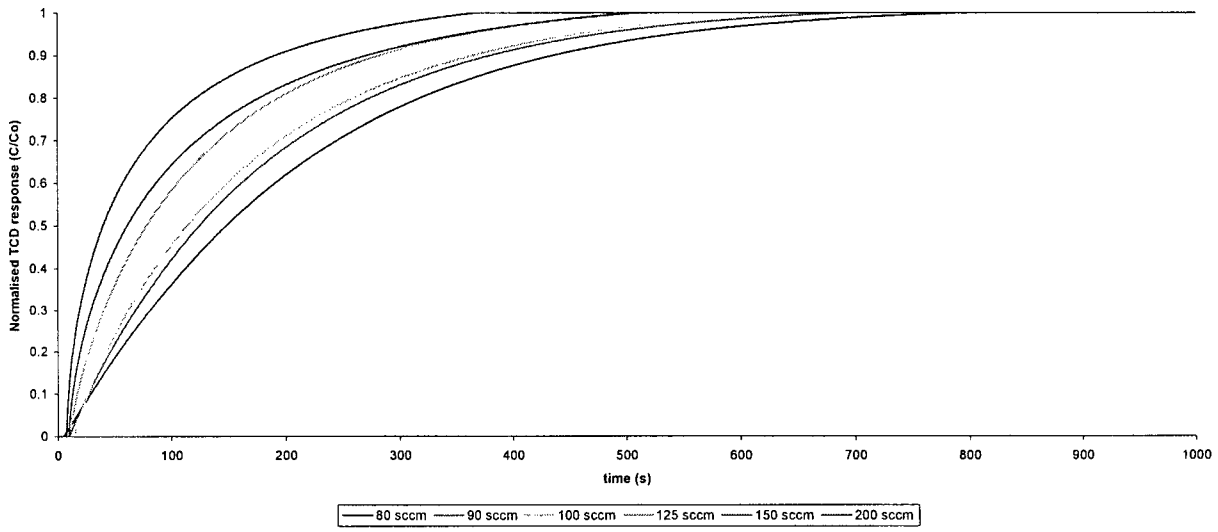

Experimental Breakthru Results of 10% Propylene over
30% Al_2O_3 (24-42 mesh)/ SnO_2 (10-24 mesh) at 75 °C

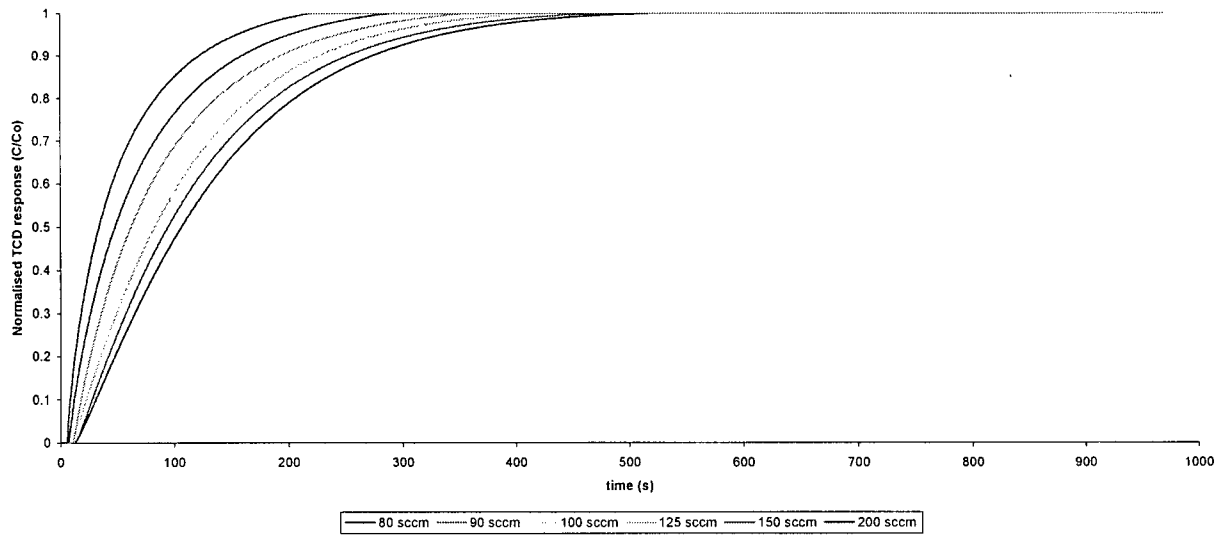

Experimental Breakthru Results for 10% Propylene over
30% Al_2O_3 (24-42 mesh)/ SnO_2 (10-24 mesh) at 100 °C

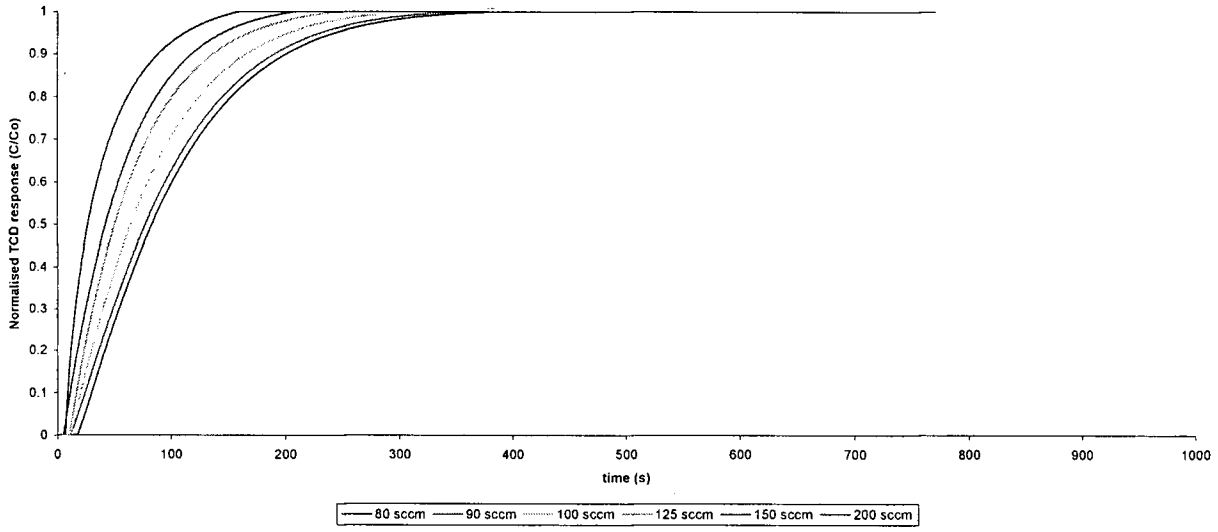

Experimental Breakthru Results for 10% Propylene over
30% Al_2O_3 (24-42 mesh)/ SnO_2 (10-24 mesh) at 150 °C

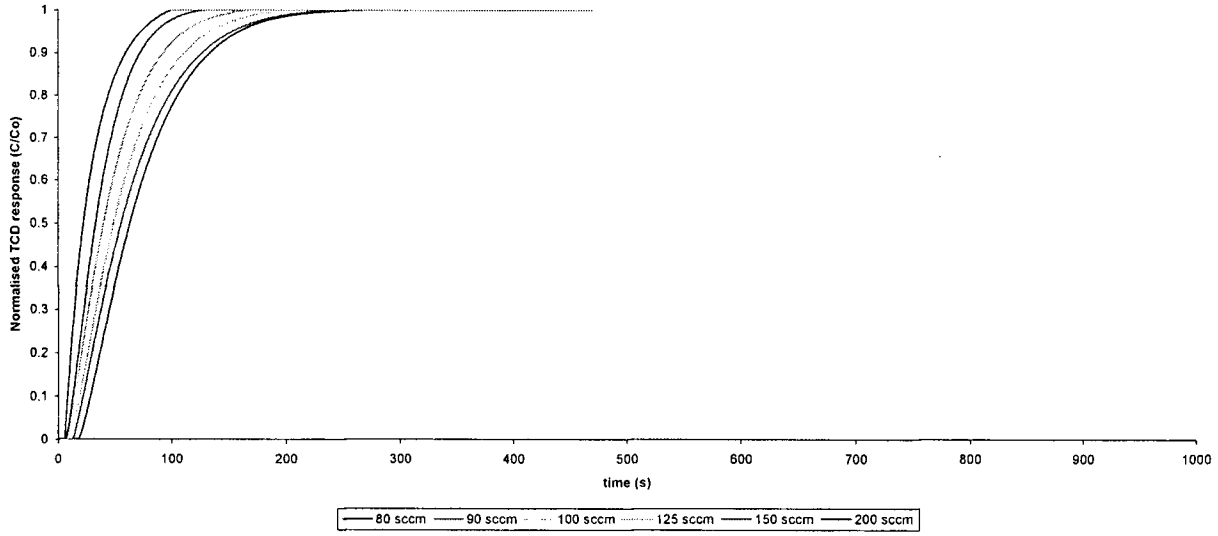

Experimental Breakthru Results of 10% Propylene over
40% Al_2O_3 (24-42 mesh)/ SnO_2 (10-24 mesh) at 50°C

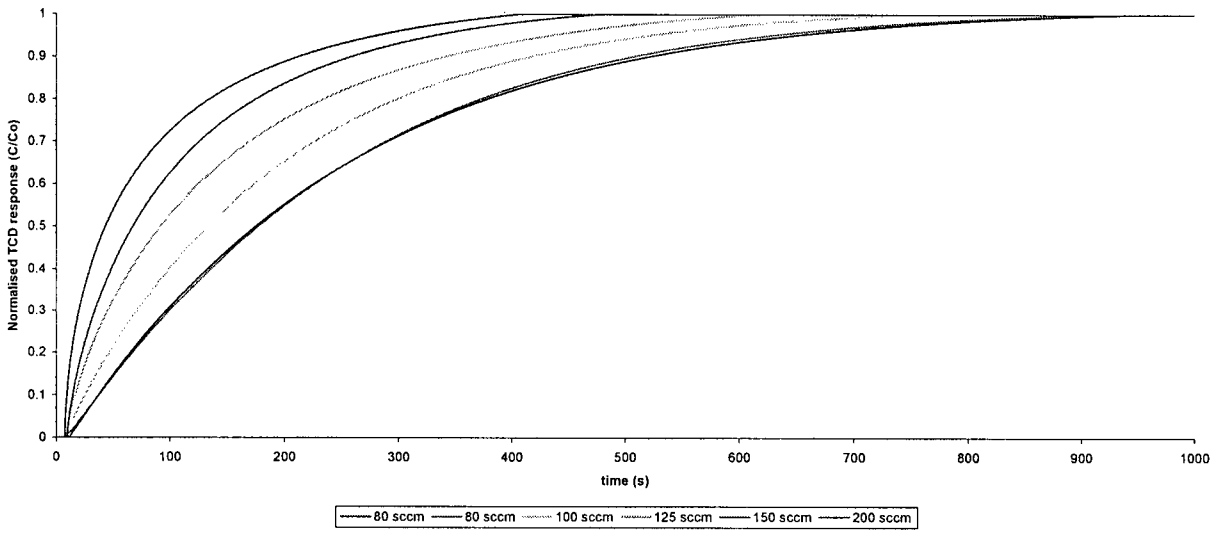

Experimental Breakthru Results of 10% Propylene over
40% Al_2O_3 (24-42 mesh)/ SnO_2 (10-24 mesh) at 75 °C

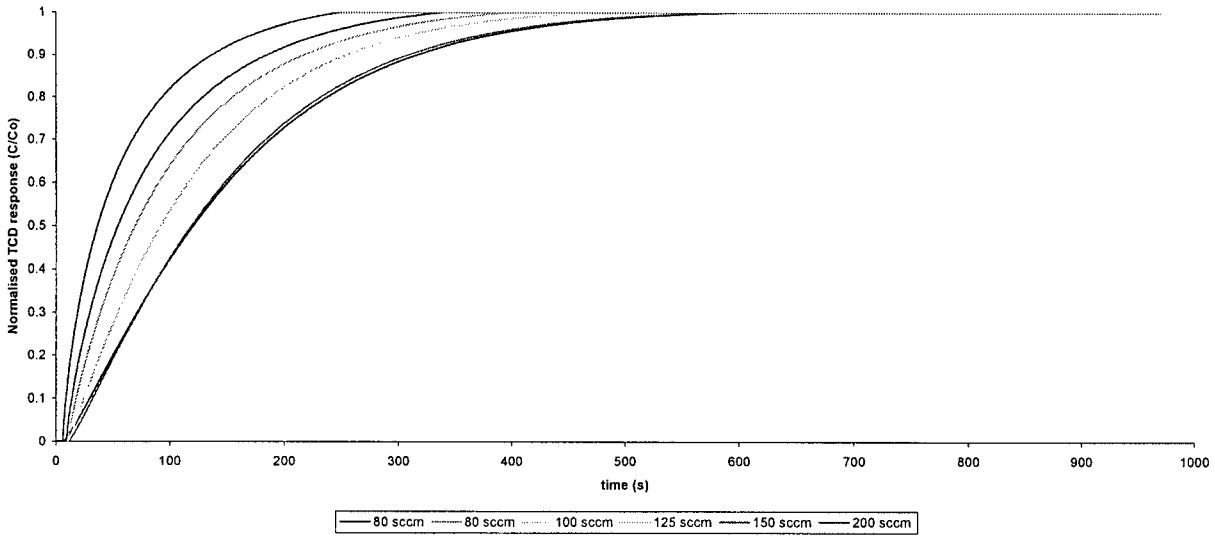

Experimental Breakthru Results of 10% Propylene over
40% Al_2O_3 (24-42 mesh)/ SnO_2 (10-24 mesh) at 100 °C

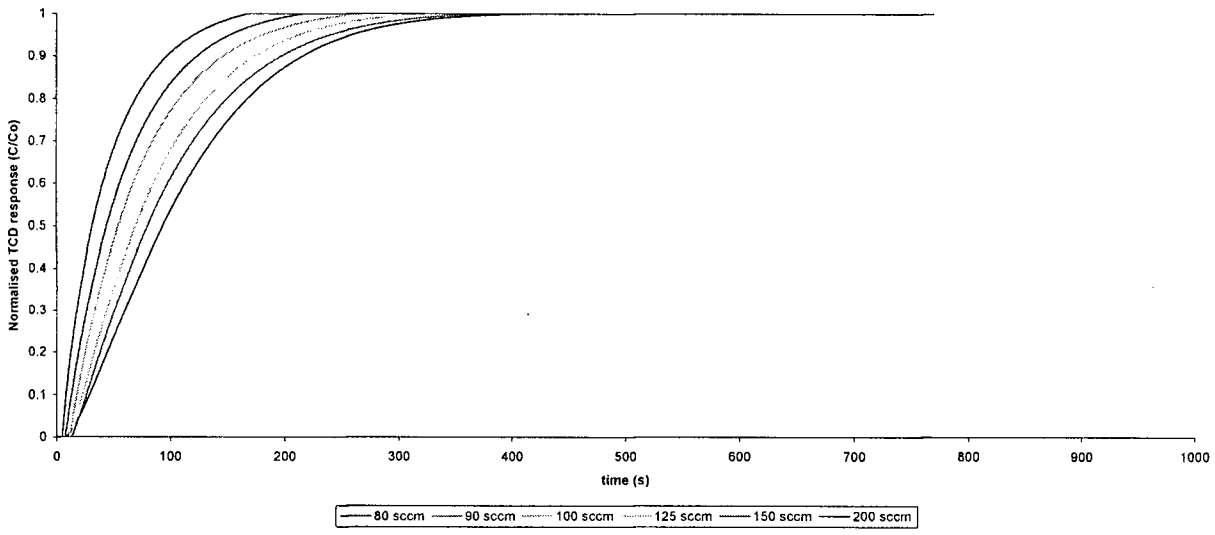

Experimental Breakthru Results of 10% Propylene over
40% Al_2O_3 (24-42 mesh)/ SnO_2 (10-24 mesh) at 150 °C

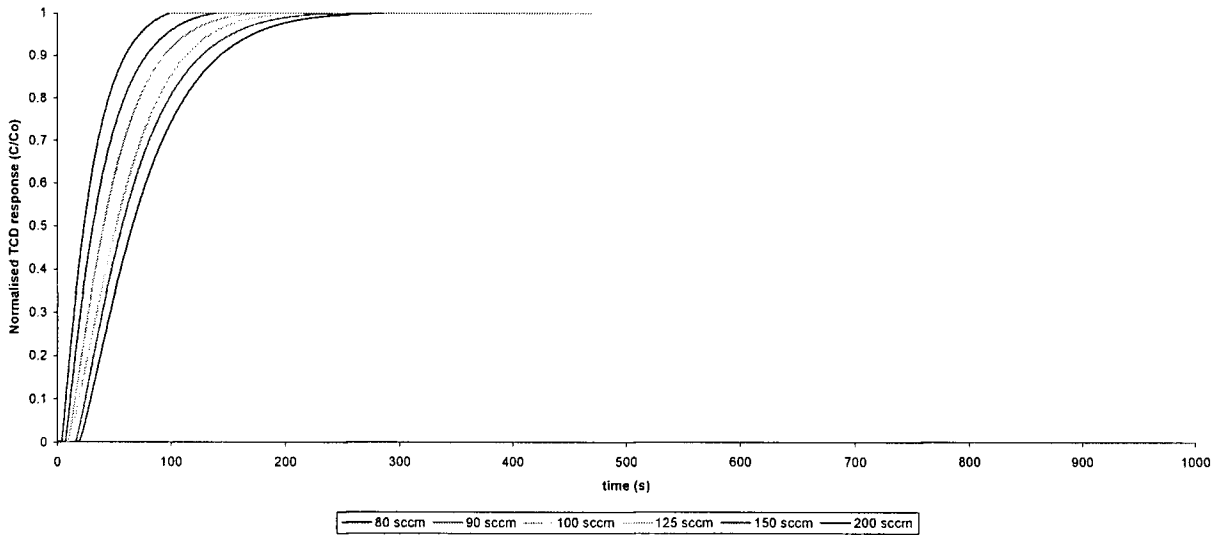

Experimental Breakthru Results of 5% Propylene over
40% Al_2O_3 (24-42 mesh)/ SnO_2 (10-24 mesh) at 100°C

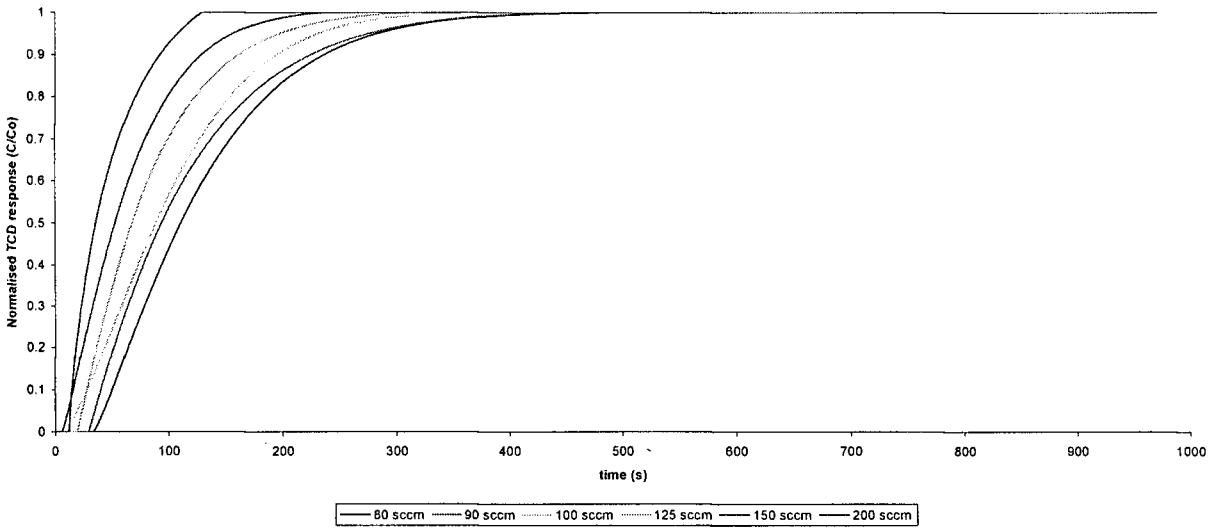

Experimental Breakthru Results of 1% Propylene over
40% Al_2O_3 (24-42 mesh)/ SnO_2 (10-24 mesh) at 100°C

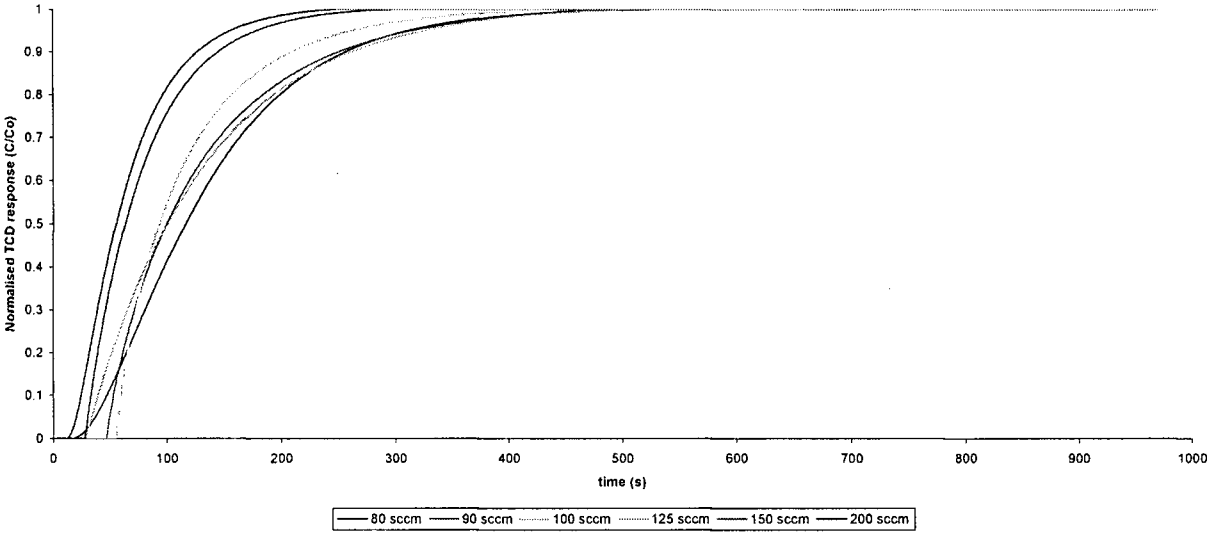

Experimental Breakthru Results of 10% Propylene over
100% Al_2O_3 (24-42 mesh) at 50°C

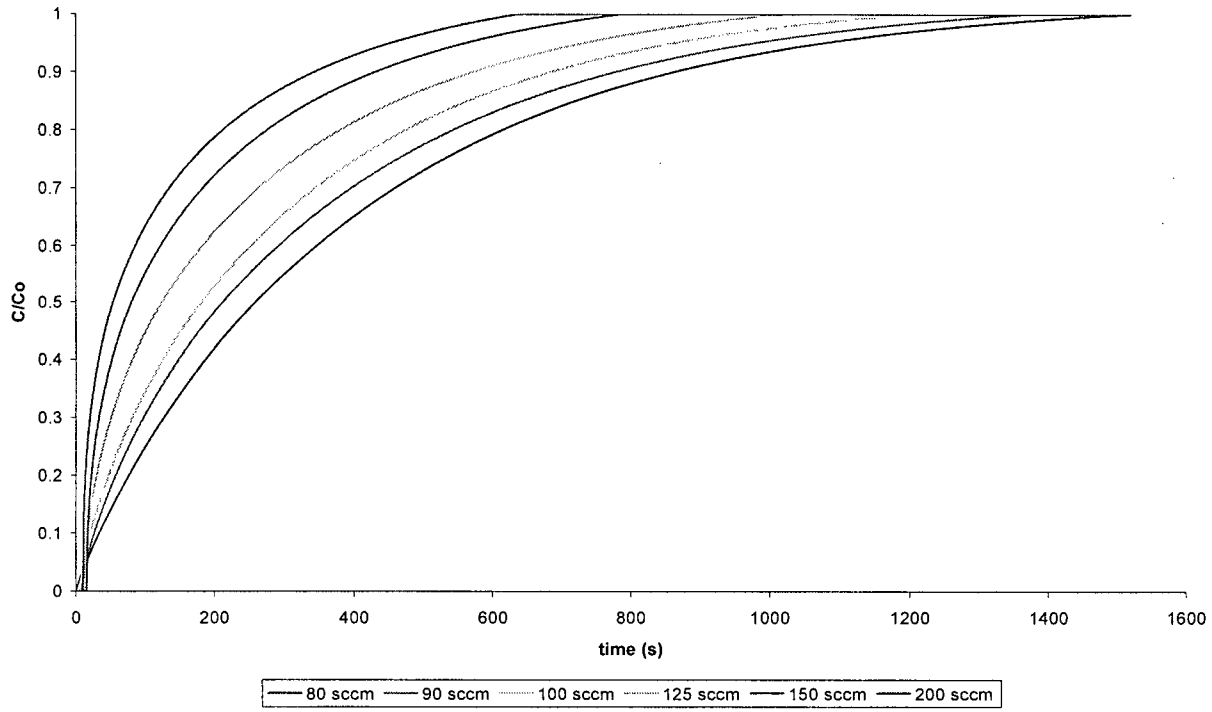

Experimental Breakthru Results of 10% Propylene over
100% Al_2O_3 (24-42 mesh) at 100°C

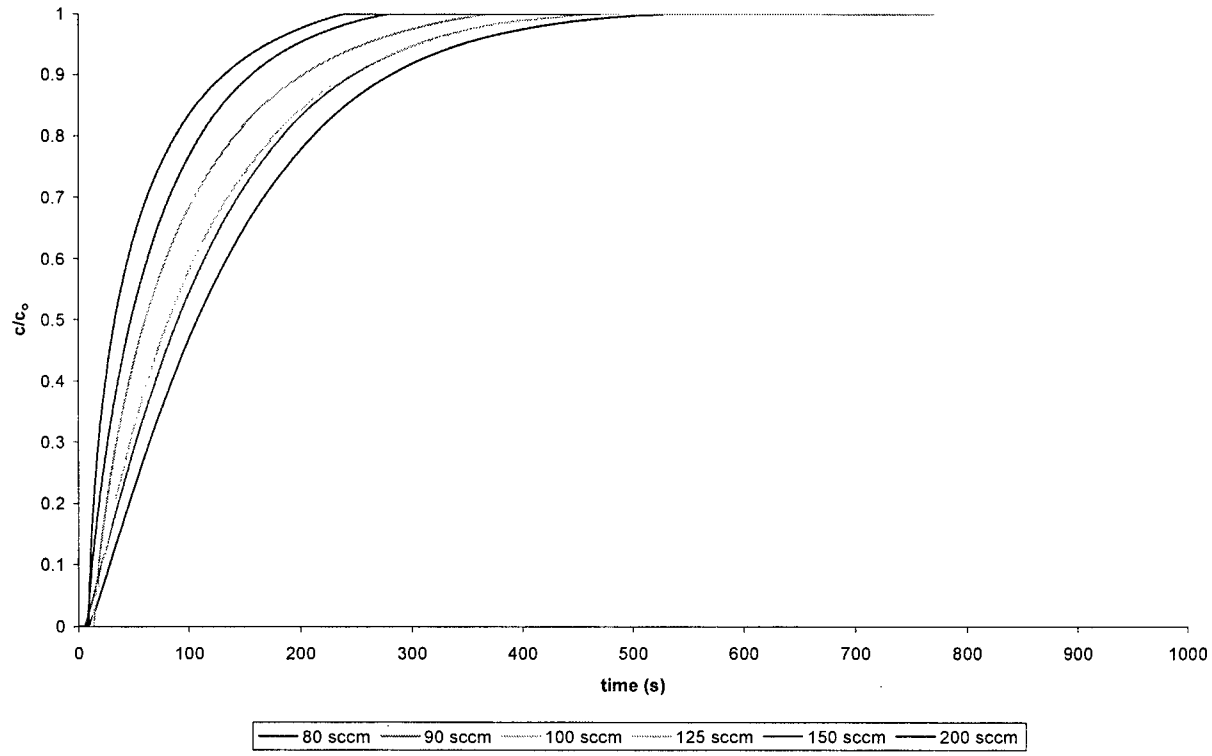

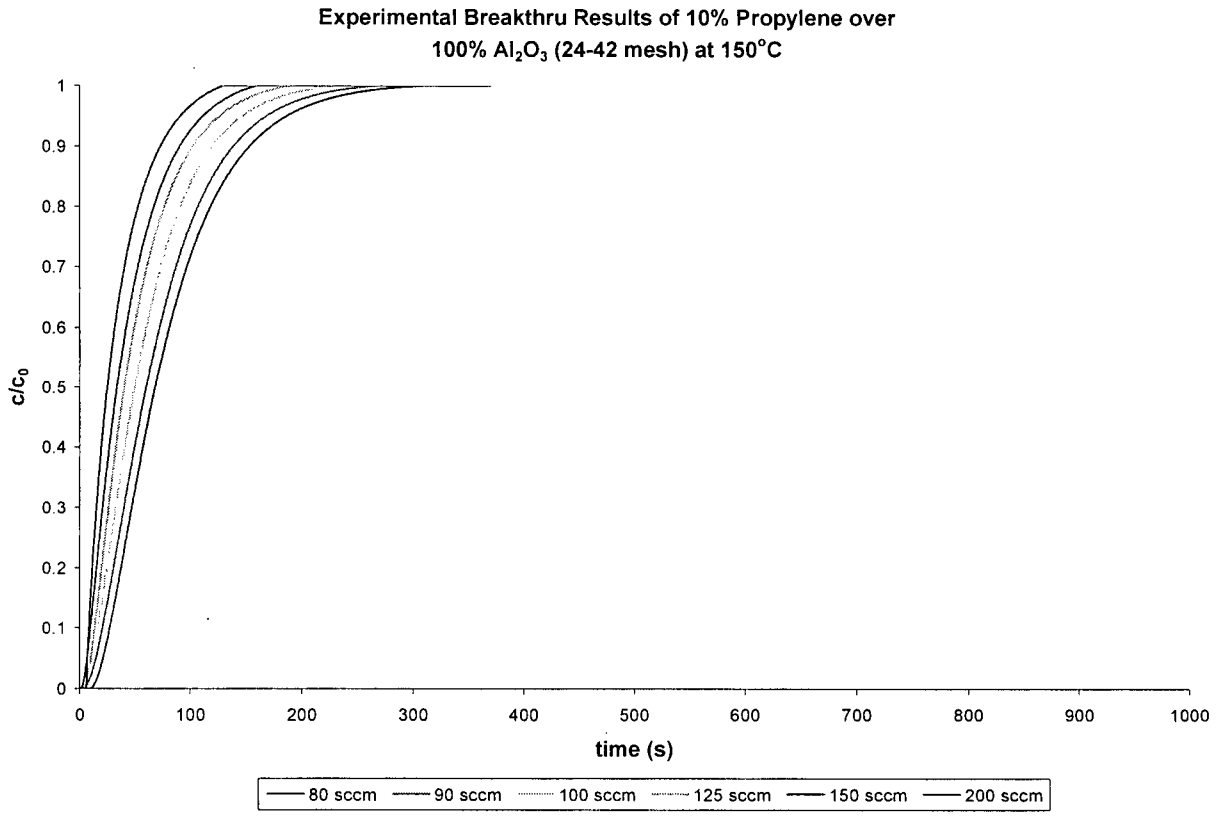
Experimental Breakthru Results of 10% Propylene over
100% Al_2O_3 (24-42 mesh) at 150°C
c/c_0
time (s)
80 sccm
90 sccm
100 sccm
125 sccm
150 sccm
200 sccm

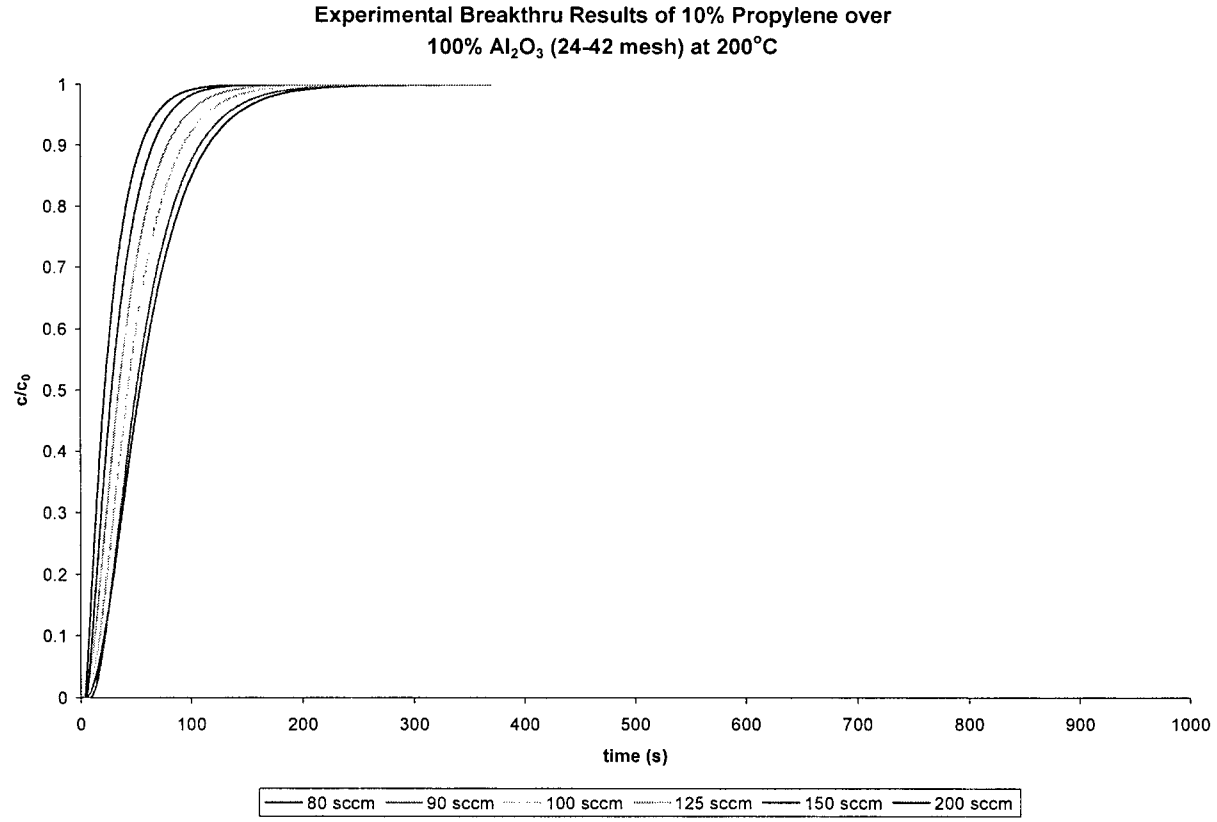
Experimental Breakthru Results of 10% Propylene over
100% Al_2O_3 (24-42 mesh) at 200°C
c/c_0
time (s)
80 sccm
90 sccm
100 sccm
125 sccm
150 sccm
200 sccm

Appendix C

Summary of Moment Analysis

(in order of increasing % volume of Al_2O_3 in SnO_2 to 100% Al_2O_3)

Detemination of Axial Dispersion (D_L) and the Lumped Mass Transfer Resistance (LMTC)

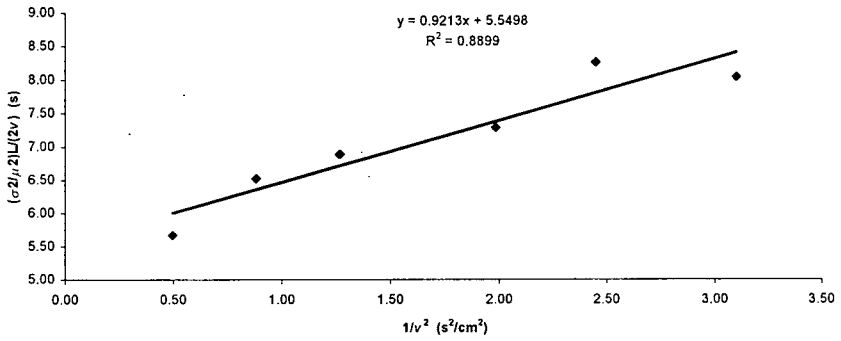

Determination of Henry's Constant (K)

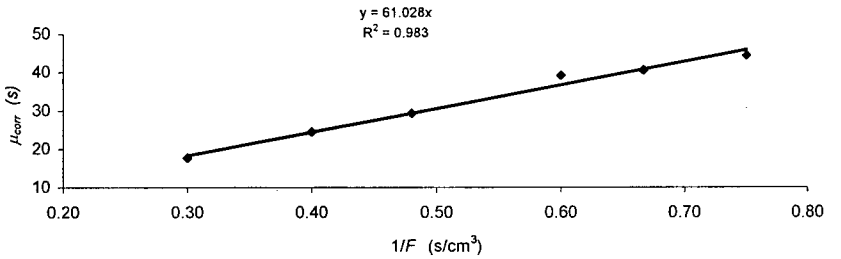

Correction for Dead Space in Reactor (carried out BT calculations with empty reactor (glass bead))									
Flow	(sccm)		F	80	90	100	125	150	200
residence time uncorrected			μ	107.61	100.51	91.10	71.73	60.03	44.32
variance			σ^2	4941.12	4523.28	3971.33	2645.04	2049.61	1238.11
residence time dead space			μ_{50C}	63.39	60.08	51.98	42.43	35.57	26.66
variance dead space			σ^2_{50C}	1369.04	1070.50	803.07	546.20	385.96	232.86
residence corrected			μ_{corr}	44.22	40.43	39.12	29.30	24.46	17.66
variance corrected			σ^2_{corr}	3572.08	3452.78	3168.26	2098.84	1663.65	1005.24
HETP uncorrected			$(\sigma^2/\mu^2)L$	2.13	2.24	2.39	2.57	2.84	3.15
HETP corrected			$(\sigma^2/\mu^2)L$	9.13	10.56	10.35	12.23	13.90	16.12

Determination of Axial Dispersion Coefficient and Lumped Mass Transfer Coefficient:								
C_3H_6 over Alumina (24-42 mesh)		**80**	**90**	**100**	**125**	**150**	**200**	**sccm**
HETP (corrected)	$(\sigma^2/\mu^2)L$	9.13	10.56	10.35	12.23	13.90	16.12	**cm**
Interstitial Velocity	v	0.57	0.64	0.71	0.89	1.07	1.42	**cm/s**
x-axis	$1/v^2$	3.10	2.45	1.98	1.27	0.88	0.50	**s^2/cm^2**
y-axis	$(\sigma^2/\mu^2)L/(2v)$	8.04	8.26	7.29	6.89	6.53	5.67	**s**

Determination of Henry's Constant								
C_3H_6 over Alumina (24-42 mesh)		**80**	**90**	**100**	**125**	**150**	**200**	sccm
Residence time, μ	**s**	44.22	40.43	39.12	29.30	24.46	17.66	**s**
F	**sccs**	1.33	1.50	1.67	2.08	2.50	3.33	**cm^3/s**
1/F	**1/sccm**	0.75	0.67	0.60	0.48	0.40	0.30	**s/cm^3**
(1-E)/E	**(denominator)**	0.88						
(1-S/LA)	**(numerator)**	4.20						
K	**$vol_{adsorbate}$ / $vol_{adsorbent}$**	4.76						

Summary of moment analysis for 10% Al_2O_3 in SnO_2 10% Propylene at 50 °C

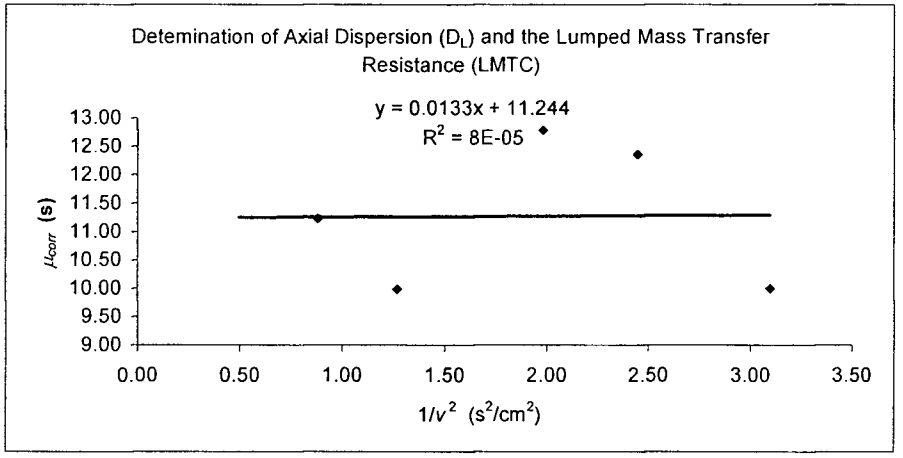

Correction for Dead Space in Reactor (carried out BT calculations with empty reactor (glass bead)								
Flow			80	90	100	125	150	200
residence time uncorrected		μ =	84.48	72.95	66.98	54.28	44.07	31.18
variance		σ^2	2724.55	1997.10	1972.82	1337.97	984.32	539.08
residence time dead space		μ_{75C}	58.46	54.71	48.35	38.70	32.45	23.99
variance dead space		σ^2_{75C}	1187.22	947.08	712.26	477.22	338.91	194.50
residence corrected		μ =	26.02	18.23	18.63	15.58	11.62	7.19
variance corrected		σ^2	1537.34	1050.02	1260.56	860.75	645.41	344.57
HETP uncorrected		$(\sigma^2/\mu^2)L$	1.91	1.88	2.20	2.27	2.53	2.77
HETP corrected		$(\sigma^2/\mu^2)L$	11.35	15.79	18.16	17.73	23.92	33.30

Determination of Axial Dispersion Coefficient and Lumped Mass Transfer Coefficient:								
C_3H_6 over Alumina (24-42 mesh)		80.000	90.000	100.000	125.000	150.000	200.000	sccm
HETP (corrected)	$(\sigma^2/\mu^2)L$	11.35	15.79	18.16	17.73	23.92	33.30	cm
Interstitial Velocity	v	0.57	0.64	0.71	0.89	1.07	1.42	cm/s
x-axis	$1/v^2$	3.10	2.45	1.98	1.27	0.88	0.50	s^2/cm^2
y-axis	$(\sigma^2/\mu^2)L/(2v)$	9.99	12.35	12.79	9.99	11.23		s

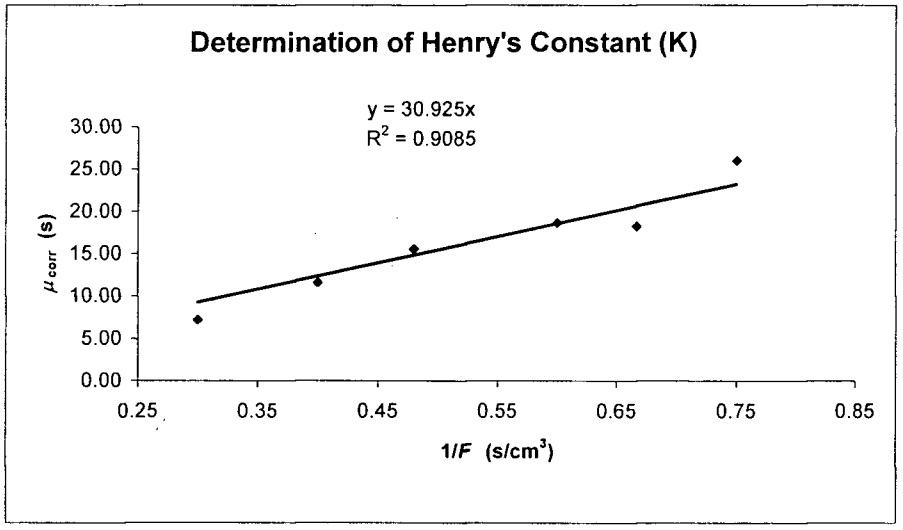

Determination of Henry's Constant								
C_3H_6 over Alumina (24-42 mesh)		80.000	90.000	100.000	125.000	150.000	200.000	sccm
Residence time	μ	26.02	18.23	18.63	15.58	11.62	7.19	s
F	sccs	1.33	1.50	1.67	2.08	2.50	3.33	
1/F	1/sccm	0.75	0.67	0.60	0.48	0.40	0.30	s/cm^{-3}
(1-E)/E	denominator	0.88						
(1-S/LA)	numerator	1.64						
K		1.85						

Summary of moment analysis for 10% Al_2O_3 in SnO_2 10% Propylene at 75 °C

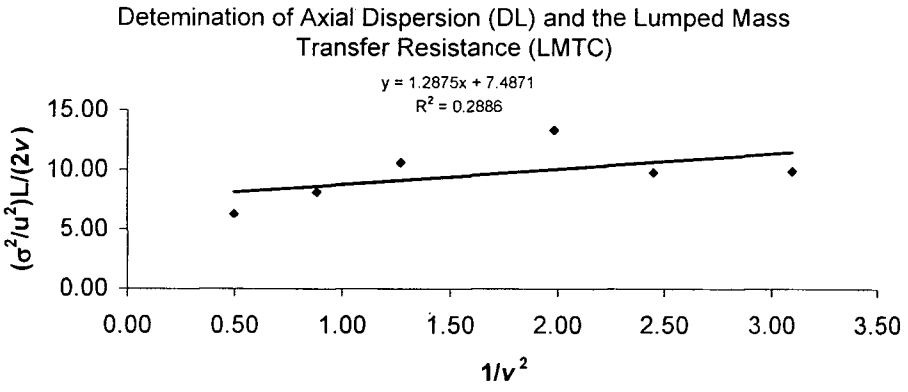

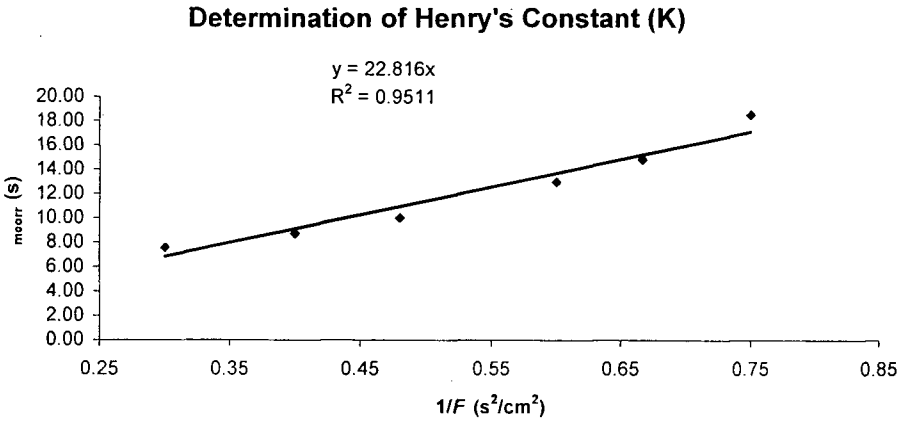

Correction for Dead Space in Reactor (carried out BT calculations with empty reactor (glass bead)									
Flow				80.00	90.00	100.00	125.00	150.00	200.00
residence time uncorrected			μ =	73.72	66.04	58.92	46.28	39.14	29.83
variance			σ^2	1798.98	1388.15	1269.82	795.66	561.80	367.66
residence time dead space			μ_{100C}	55.20	51.20	45.93	36.26	30.41	22.25
variance dead space			σ^2_{100C}	1029.54	837.89	631.72	416.96	297.59	162.46
residence corrected			μ =	18.52	14.84	12.98	10.02	8.74	7.58
variance corrected			σ^2	769.44	550.26	638.11	378.70	264.21	205.20
HETP uncorrected			$(\sigma^2/\mu^2)L$	1.66	1.59	1.83	1.86	1.83	2.07
HETP corrected			$(\sigma^2/\mu^2)L$	11.21	12.50	18.93	18.87	17.31	17.88

Determination of Axial Dispersion Coefficient and Lumped Mass Transfer Coefficient:								
C_3H_6 over Alumina (24-42 mesh)		80.00	90.00	100.00	125.00	150.00	200.00	sccm
HETP (corrected)	$(\sigma^2/\mu^2)L$	11.21	12.50	18.93	18.87	17.31	17.88	cm
Interstitial Velocity	v	0.57	0.64	0.71	0.89	1.07	1.42	cm/s
x-axis	$1/v^2$	3.10	2.45	1.98	1.27	0.88	0.50	s^2/cm^2
y-axis	$(\sigma^2/\mu^2)L/(2v)$	9.87	9.78	13.33	10.63	8.13	6.29	s

Determination of Henry's Constant								
C_3H_6 over Alumina (24-42 mesh)		80.00	90.00	100.00	125.00	150.00	200.00	sccm
Residence time	μ	18.52	14.84	12.98	10.02	8.74	7.58	s
F	sccs	1.33	1.50	1.67	2.08	2.50	3.33	
1/F	1/sccm	0.75	0.67	0.60	0.48	0.40	0.30	s/cm^3
(1-E)/E		0.88						
Numerator (use slope of graph)		0.94						
K		1.07						

Summary of moment analysis for 10% Al_2O_3 in SnO_2 10% Propylene at 100 °C

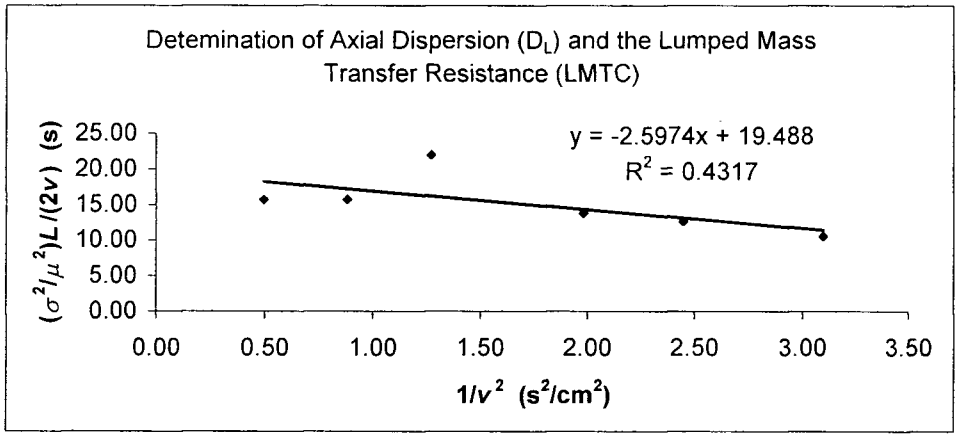

Correction for Dead Space in Reactor (carried out BT calculations with empty reactor (glass bead)								
Flow			80.00	90.00	100.00	125.00	150.00	200.00
residence time uncorrected		μ =	60.78	53.96	50.35	38.37	31.58	22.93
variance		σ^2	1008.07	829.81	724.79	537.62	328.58	188.59
residence time dead space		μ_{150C}	50.90	46.63	42.73	33.08	27.74	20.02
variance dead space		σ^2_{150C}	774.23	655.82	496.93	318.30	229.46	113.35
residence corrected		μ =	9.87	7.33	7.62	5.30	3.84	2.91
variance corrected		σ^2	233.84	174.00	227.86	219.32	99.12	75.24
HETP uncorrected		$(\sigma^2/\mu^2)L$	1.36	1.43	1.43	1.83	1.65	1.79
HETP corrected		$(\sigma^2/\mu^2)L$	12.00	16.21	19.62	39.07	33.59	44.50

Determination of Axial Dispersion Coefficient and Lumped Mass Transfer Coefficient:								
C_3H_6 over Alumina (24-42 mesh)		80.00	90.00	100.00	125.00	150.00	200.00	sccm
HETP (corrected)	$(\sigma^2/\mu^2)L$	12.00	16.21	19.62	39.07	33.59	44.50	cm
Interstitial Velocity	v	0.57	0.64	0.71	0.89	1.07	1.42	cm/s
x-axis	$1/v^2$	3.10	2.45	1.98	1.27	0.88	0.50	s^2/cm^2
y-axis	$(\sigma^2/\mu^2)L/(2v)$	10.56	12.68	13.82	22.01	15.77	15.67	s

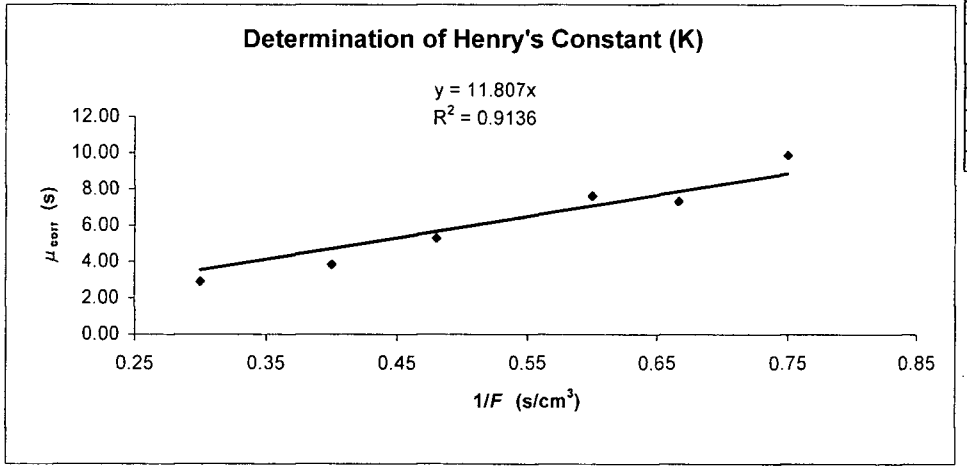

Determination of Henry's Constant								
C_3H_6 over Alumina (24-42 mesh)		80.00	90.00	100.00	125.00	150.00	200.00	sccm
Residence time	μ	9.87	7.33	7.62	5.30	3.84	2.91	s
F	sccs	1.33	1.50	1.67	2.08	2.50	3.33	
1/F	1/sccm	0.75	0.67	0.60	0.48	0.40	0.30	s/cm^3
(1-E)/E		0.88						
Numerator (use slope of graph)		0.0061						
K		0.0069						

Summary of moment analysis for 10% Al_2O_3 in SnO_2 10% Propylene at 150 °C

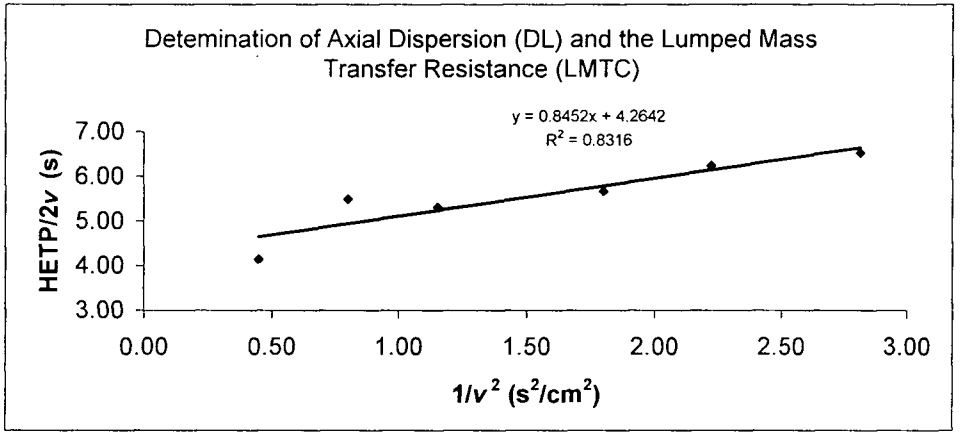

Correction for Dead Space in Reactor (carried out BT calculations with empty reactor (glass bead)									
Flow				80.00	90.00	100.00	125.00	150.00	200.00
residence time uncorrected			μ =	145.23	131.60	119.10	94.46	75.15	58.80
variance			σ^2	11796.59	9634.38	8424.24	5907.65	4229.94	2787.30
residence time dead space			μ_{60C}	63.39	60.08	51.98	42.43	35.57	26.66
variance dead space			σ^2_{60C}	1369.04	1070.50	803.07	546.20	385.96	232.86
residence corrected			μ =	81.84	71.52	67.12	52.03	39.58	32.14
variance corrected			σ^2	10427.54	8563.88	7621.17	5361.45	3843.98	2554.44
HETP uncorrected			$(\sigma^2/\mu^2)L$	2.80	2.78	2.97	3.31	3.74	4.03
HETP corrected			$(\sigma^2/\mu^2)L$	7.79	8.37	8.46	9.90	12.27	12.37

Determination of Axial Dispersion Coefficient and Lumped Mass Transfer Coefficient:								
C_3H_6 over Alumina (24-42 mesh)		**80.00**	**90.00**	**100.00**	**125.00**	**150.00**	**200.00**	sccm
HETP (corrected)	$(\sigma^2/\mu^2)L$	7.79	8.37	8.46	9.90	12.27	12.37	**cm**
Interstitial Velocity	v	0.60	0.67	0.75	0.93	1.12	1.49	**cm/s**
x-axis	$1/v^2$	2.81	2.22	1.80	1.15	0.80	0.45	**s^2/cm^2**
y-axis	$(\sigma^2/\mu^2)L/(2v)$	6.53	6.24	5.67	5.31	5.49	4.15	**s**

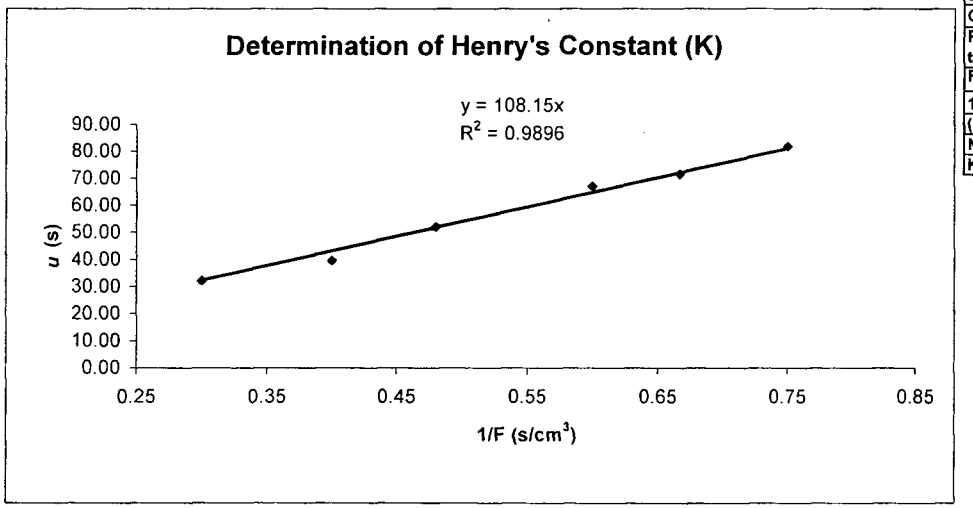

Determination of Henry's Constant								
C_3H_6 over Alumina (24-42 mesh)		**80.00**	**90.00**	**100.00**	**125.00**	**150.00**	**200.00**	sccm
Residence time	μ	81.84	71.52	67.12	52.03	39.58	32.14	**s**
F	sccs	1.33	1.50	1.67	2.08	2.50	3.33	
1/F	1/sccm	0.75	0.67	0.60	0.48	0.40	0.30	**s/cm^3**
(1-E)/E		0.98						
Numerator (use slope of graph)		8.67						
K		8.88						

Summary of moment analysis for 20% Al_2O_3 in SnO_2 10% Propylene at 50 °C

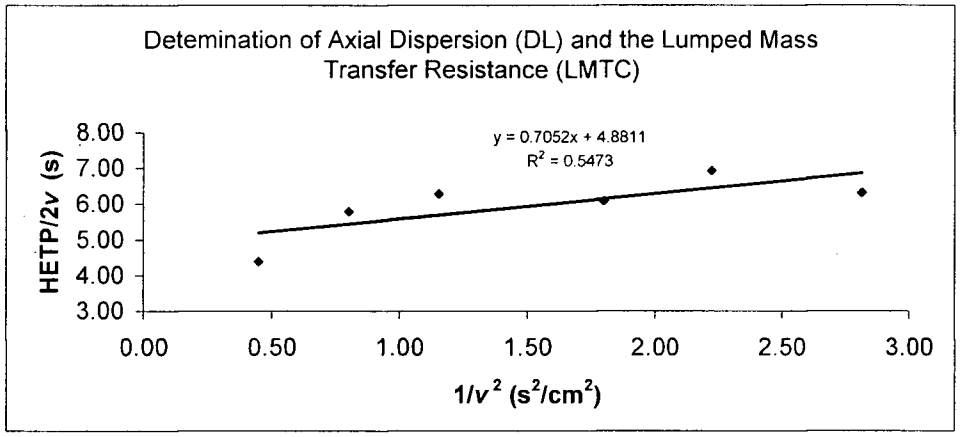

Correction for Dead Space in Reactor (carried out BT calculations with empty reactor (glass bead)								
Flow				80.00	90.00	100.00	125.00	150.00	200.00
residence time uncorrected			μ =	106.75	93.55	84.61	65.92	58.51	42.47
variance			σ^2	4695.44	3750.70	3101.47	2210.06	2098.28	1088.70
residence time dead space			μ_{75C}	58.46	54.71	48.35	38.70	32.45	23.99
variance dead space			σ^2_{75C}	1187.22	947.08	712.26	477.22	338.91	194.50
residence corrected			μ =	48.29	38.83	36.26	27.21	26.06	18.48
variance corrected			σ^2	3508.22	2803.61	2389.21	1732.83	1759.37	894.19
HETP uncorrected			$(\sigma^2/\mu^2)L$	2.06	2.14	2.17	2.54	3.06	3.02
HETP corrected			$(\sigma^2/\mu^2)L$	7.52	9.30	9.09	11.70	12.96	13.09

Determination of Axial Dispersion Coefficient and Lumped Mass Transfer Coefficient:								
C_3H_6 over Alumina (24-42 mesh)			**80.00**	**90.00**	**100.00**	**125.00**	**150.00**	**200.00**	sccm
HETP (corrected)	$(\sigma^2/\mu^2)L$		7.52	9.30	9.09	11.70	12.96	13.09	**cm**
Interstitial Velocity	v		0.60	0.67	0.75	0.93	1.12	1.49	**cm/s**
x-axis	$1/v^2$		2.81	2.22	1.80	1.15	0.80	0.45	**s^2/cm^2**
y-axis	$(\sigma^2/\mu^2)L/(2v)$		6.31	6.93	6.10	6.28	5.80	4.39	**s**

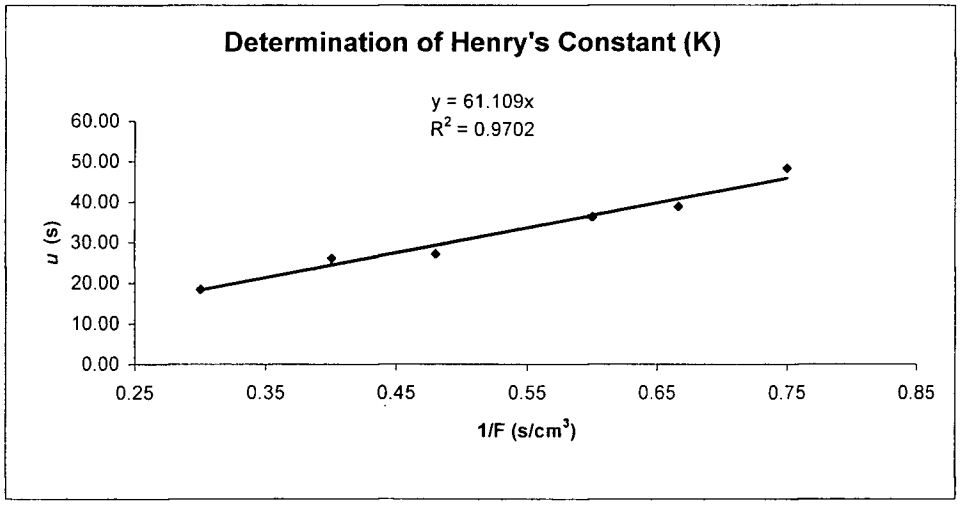

Determination of Henry's Constant									
C_3H_6 over Alumina (24-42 mesh)			**80.00**	**90.00**	**100.00**	**125.00**	**150.00**	**200.00**	sccm
Residence time	μ		48.29	38.83	36.26	27.21	26.06	18.48	**s**
F	sccs		1.33	1.50	1.67	2.08	2.50	3.33	
1/F	1/sccm		0.75	0.67	0.60	0.48	0.40	0.30	**s/cm^3**
(1-E)/E			0.98						
Numerator (use slope of graph)			4.46						
K			4.57						

Summary of moment analysis for 20% Al_2O_3 in SnO_2 10% Propylene at 75 °C

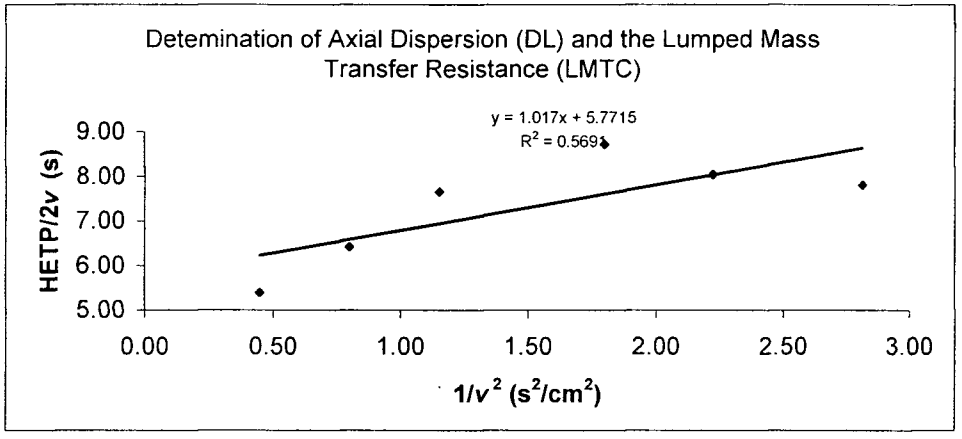

Correction for Dead Space in Reactor (carried out BT calculations with empty reactor (glass bead)								
Flow			80.00	90.00	100.00	125.00	150.00	200.00
residence time uncorrected		μ =	82.85	74.71	67.66	53.08	44.85	32.63
variance		σ^2	2452.85	2029.63	1858.62	1223.74	895.74	508.44
residence time dead space		μ_{100C}	55.20	51.20	45.93	36.26	30.41	22.25
variance dead space		σ^2_{100C}	1029.54	837.89	631.72	416.96	297.59	162.46
residence corrected		μ =	27.65	23.51	21.73	16.82	14.44	10.37
variance corrected		σ^2	1423.31	1191.74	1226.91	806.78	598.15	345.97
HETP uncorrected		$(\sigma^2/\mu^2)L$	1.79	1.82	2.03	2.17	2.23	2.39
HETP corrected		$(\sigma^2/\mu^2)L$	9.31	10.78	13.00	14.26	14.35	16.07

Determination of Axial Dispersion Coefficient and Lumped Mass Transfer Coefficient:								
C_3H_6 over Alumina (24-42 mesh)		80.00	90.00	100.00	125.00	150.00	200.00	sccm
HETP (corrected)	$(\sigma^2/\mu^2)L$	9.31	10.78	13.00	14.26	14.35	16.07	cm
Interstitial Velocity	v	0.60	0.67	0.75	0.93	1.12	1.49	cm/s
x-axis	$1/v^2$	2.81	2.22	1.80	1.15	0.80	0.45	s^2/cm^2
y-axis	$(\sigma^2/\mu^2)L/(2v)$	7.80	8.04	8.72	7.65	6.42	5.39	s

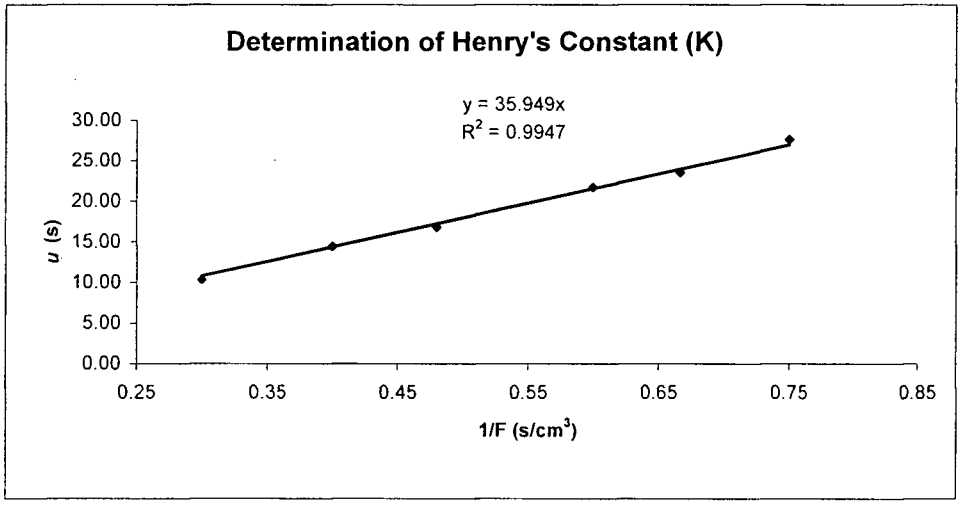

Determination of Henry's Constant								
C_3H_6 over Alumina (24-42 mesh)		80.00	90.00	100.00	125.00	150.00	200.00	sccm
Residence time	μ	27.65	23.51	21.73	16.82	14.44	10.37	s
F	sccs	1.33	1.50	1.67	2.08	2.50	3.33	
1/F	1/sccm	0.75	0.67	0.60	0.48	0.40	0.30	s/cm^3
(1-E)/E		0.98						
Numerator (use slope of graph)		2.21						
K		2.27						

Summary of moment analysis for 20% Al_2O_3 in SnO_2 10% Propylene at 100 °C

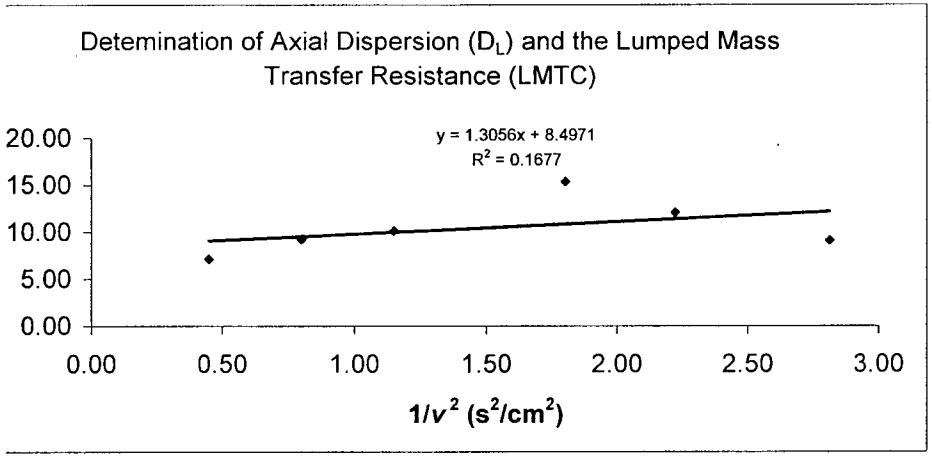

Correction for Dead Space in Reactor (carried out BT calculations with empty reactor (glass bead)									
Flow				80.00	90.00	100.00	125.00	150.00	200.00
residence time uncorrected			μ =	64.69	57.54	51.72	41.39	33.96	25.45
variance			σ^2	1186.00	1041.81	866.98	578.79	389.23	239.08
residence time dead space			μ_{150C}	50.90	46.63	42.73	33.08	27.74	20.02
variance dead space			σ^2_{150C}	774.23	655.82	496.93	318.30	229.46	113.35
residence corrected			μ =	13.78	10.91	8.99	8.31	6.22	5.43
variance corrected			σ^2	411.77	385.99	370.05	260.50	159.77	125.73
HETP uncorrected			$(\sigma^2/\mu^2)L$	1.42	1.57	1.62	1.69	1.69	1.85
HETP corrected			$(\sigma^2/\mu^2)L$	10.84	16.21	22.90	18.86	20.65	21.32

Determination of Axial Dispersion Coefficient and Lumped Mass Transfer Coefficient:								
C_3H_6 over Alumina (24-42 mesh)		**80.00**	**90.00**	**100.00**	**125.00**	**150.00**	**200.00**	sccm
HETP (corrected)	$(\sigma^2/\mu^2)L$	10.84	16.21	22.90	18.86	20.65	21.32	**cm**
Interstitial Velocity	v	0.60	0.67	0.75	0.93	1.12	1.49	**cm/s**
x-axis	$1/v^2$	2.81	2.22	1.80	1.15	0.80	0.45	**s^2/cm^2**
y-axis	$(\sigma^2/\mu^2)L/(2v)$	9.09	12.08	15.36	10.12	9.24	7.15	**s**

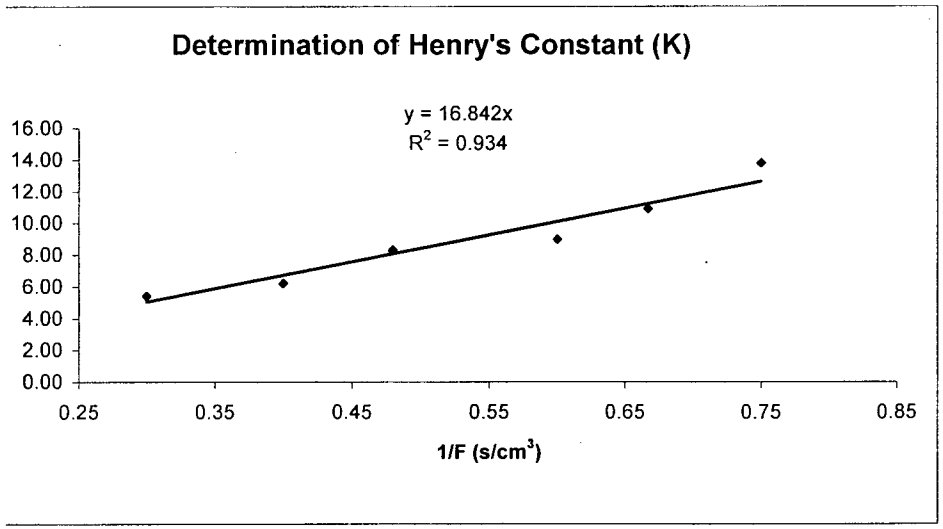

Determination of Henry's Constant								
C_3H_6 over Alumina (24-42 mesh)		**80.00**	**90.00**	**100.00**	**125.00**	**150.00**	**200.00**	sccm
Residence time	μ	13.78	10.91	8.99	8.31	6.22	5.43	**s**
F	sccs	1.33	1.50	1.67	2.08	2.50	3.33	
1/F	**1/sccm**	0.75	0.67	0.60	0.48	0.40	0.30	**s/cm^3**
(1-E)/E		0.98						
Numerator (use slope of graph)		0.51						
K		0.52						

of moment analysis for 20% Al_2O_3 in SnO_2 10% Propylene at 150 °C

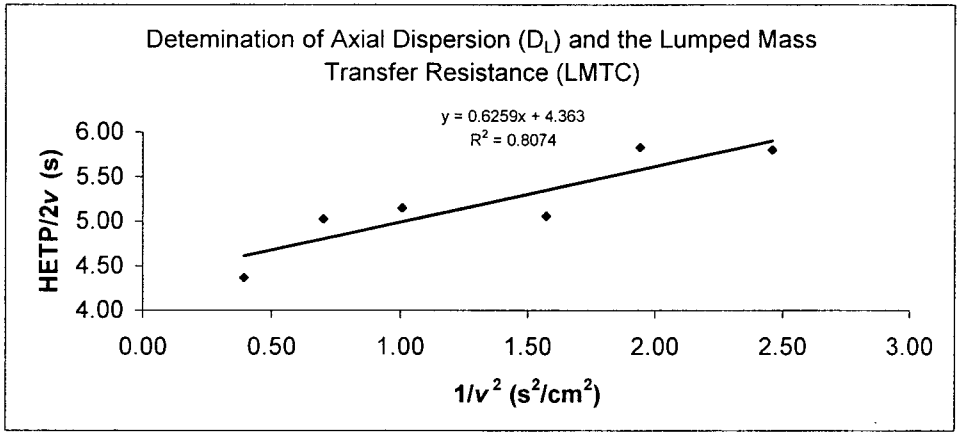

Correction for Dead Space in Reactor (carried out BT calculations with empty reactor (glass bead)									
Flow				80.00	90.00	100.00	125.00	150.00	200.00
residence time uncorrected			μ =	195.29	168.63	159.05	117.28	105.09	72.72
variance			σ^2	27108.40	20777.95	19300.83	12046.94	12002.13	6143.34
residence time dead space			μ_{60C}	63.39	60.08	51.98	42.43	35.57	26.66
variance dead space			σ^2_{60C}	1369.04	1070.50	803.07	546.20	385.96	232.86
residence corrected			μ =	131.90	108.55	107.07	74.85	69.52	46.06
variance corrected			σ^2	25739.36	19707.45	18497.76	11500.74	11616.17	5910.48
HETP uncorrected			$(\sigma^2/\mu^2)L$	3.55	3.65	3.81	4.38	5.43	5.81
HETP corrected			$(\sigma^2/\mu^2)L$	7.40	8.36	8.07	10.26	12.02	13.93

Determination of Axial Dispersion Coefficient and Lumped Mass Transfer Coefficient:								
C_3H_6 over Alumina (24-42 mesh)		**80.00**	**90.00**	**100.00**	**125.00**	**150.00**	**200.00**	sccm
HETP (corrected)	**$(\sigma^2/\mu^2)L$**	7.40	8.36	8.07	10.26	12.02	13.93	**cm**
Interstitial Velocity	**v**	0.64	0.72	0.80	1.00	1.20	1.59	**cm/s**
x-axis	**$1/v^2$**	2.46	1.94	1.57	1.01	0.70	0.39	**s^2/cm^2**
y-axis	**$(\sigma^2/\mu^2)L/(2v)$**	5.80	5.83	5.06	5.15	5.03	4.37	**s**

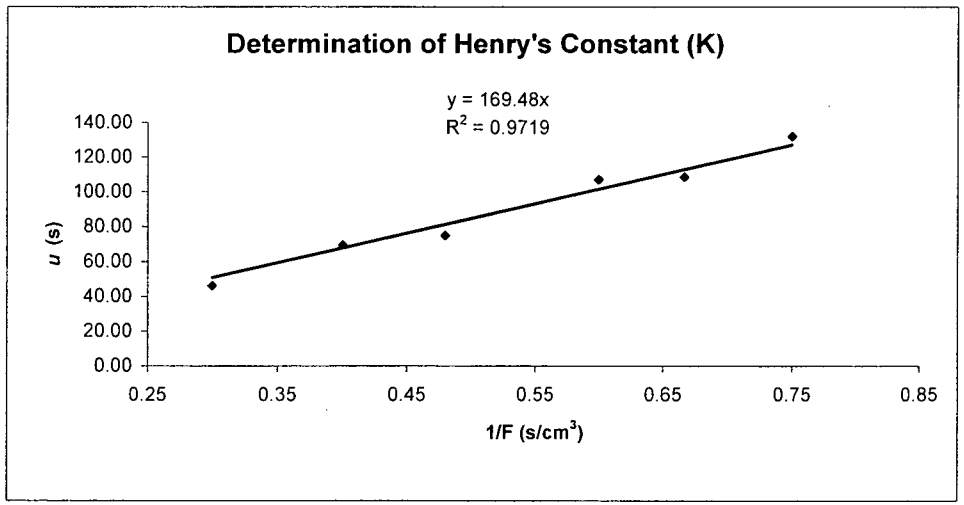

Determination of Henry's Constant								
C_3H_6 over Alumina (24-42 mesh)		**80.00**	**90.00**	**100.00**	**125.00**	**150.00**	**200.00**	sccm
Residence time	**μ**	131.90	108.55	107.07	74.85	69.52	46.06	**s**
F	**sccs**	1.33	1.50	1.67	2.08	2.50	3.33	
1/F	**1/sccm**	0.75	0.67	0.60	0.48	0.40	0.30	**s/cm^3**
(1-E)/E		1.11						
Numerator (use slope of graph)		15.21						
K		13.65						

Summary of moment analysis for 30% Al_2O_3 in SnO_2 10% Propylene at 50 °C

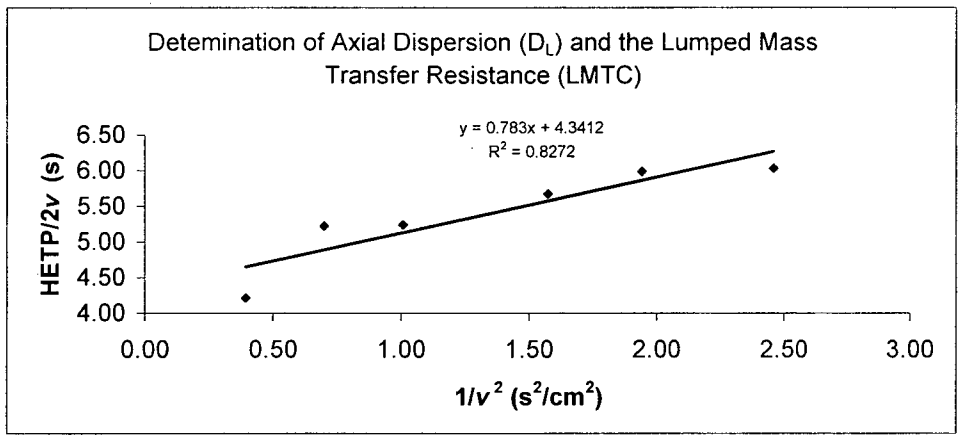

Correction for Dead Space in Reactor (carried out BT calculations with empty reactor (glass bead)								
Flow			80.00	90.00	100.00	125.00	150.00	200.00
residence time uncorrected		μ =	132.85	120.52	106.64	86.47	68.94	51.25
variance		σ^2	9701.61	8390.43	6857.93	5244.37	3664.48	2191.05
residence time dead space		μ_{75C}	58.46	54.71	48.35	38.70	32.45	23.99
variance dead space		σ^2_{75C}	1187.22	947.08	712.26	477.22	338.91	194.50
residence corrected		μ =	74.38	65.81	58.29	47.77	36.49	27.26
variance corrected		σ^2	8514.39	7443.35	6145.67	4767.15	3325.58	1996.55
HETP uncorrected		$(\sigma^2/\mu^2)L$	2.75	2.89	3.02	3.51	3.86	4.17
HETP corrected		$(\sigma^2/\mu^2)L$	7.69	8.59	9.04	10.45	12.49	13.43

Determination of Axial Dispersion Coefficient and Lumped Mass Transfer Coefficient:								
C_3H_6 over Alumina (24-42 mesh)			80.00	90.00	100.00	125.00	150.00	200.00	sccm
HETP (corrected)	$(\sigma^2/\mu^2)L$		7.69	8.59	9.04	10.45	12.49	13.43	cm
Interstitial Velocity	v		0.64	0.72	0.80	1.00	1.20	1.59	cm/s
x-axis	$1/v^2$		2.46	1.94	1.57	1.01	0.70	0.39	s^2/cm^2
y-axis	$(\sigma^2/\mu^2)L/(2v)$		6.03	5.99	5.67	5.24	5.22	4.21	s

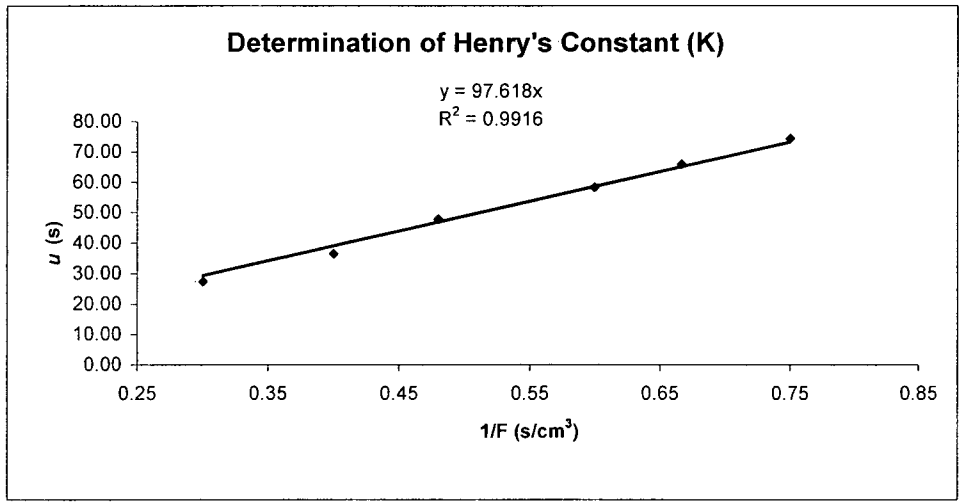

Determination of Henry's Constant									
C_3H_6 over Alumina (24-42 mesh)			80.00	90.00	100.00	125.00	150.00	200.00	sccm
Residence time	μ		74.38	65.81	58.29	47.77	36.49	27.26	s
F	sccs		1.33	1.50	1.67	2.08	2.50	3.33	
1/F	1/sccm		0.75	0.67	0.60	0.48	0.40	0.30	s/cm^3
(1-E)/E			1.11						
Numerator (use slope of graph)			8.34						
K			7.48						

Summary of moment analysis for 30% Al_2O_3 in SnO_2 10% Propylene at 75 °C

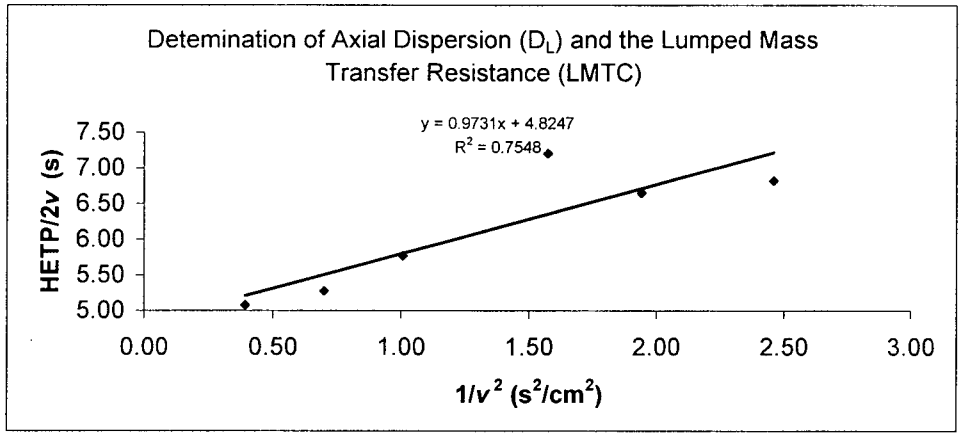

Correction for Dead Space in Reactor (carried out BT calculations with empty reactor (glass bead)								
Flow			80.00	90.00	100.00	125.00	150.00	200.00
residence time uncorrected		μ =	101.92	94.85	81.05	65.42	55.07	39.13
variance		σ^2	4829.92	4475.73	3464.67	2371.82	1833.68	1085.04
residence time dead space		μ_{100C}	55.20	51.20	45.93	36.26	30.41	22.25
variance dead space		σ^2_{100C}	1029.54	837.89	631.72	416.96	297.59	162.46
residence corrected		μ =	46.73	43.65	35.12	29.16	24.67	16.88
variance corrected		σ^2	3800.38	3637.84	2832.95	1954.86	1536.09	922.58
HETP uncorrected		$(\sigma^2/\mu^2)L$	2.32	2.49	2.64	2.77	3.02	3.54
HETP corrected		$(\sigma^2/\mu^2)L$	8.70	9.55	11.49	11.50	12.62	16.19

Determination of Axial Dispersion Coefficient and Lumped Mass Transfer Coefficient:								
C_3H_6 over Alumina (24-42 mesh)		**80.00**	**90.00**	**100.00**	**125.00**	**150.00**	**200.00**	sccm
HETP (corrected)	$(\sigma^2/\mu^2)L$	8.70	9.55	11.49	11.50	12.62	16.19	**cm**
Interstitial Velocity	**v**	0.64	0.72	0.80	1.00	1.20	1.59	**cm/s**
x-axis	$1/v^2$	2.46	1.94	1.57	1.01	0.70	0.39	**s^2/cm^2**
y-axis	$(\sigma^2/\mu^2)L/(2v)$	6.82	6.65	7.20	5.77	5.28	5.08	**s**

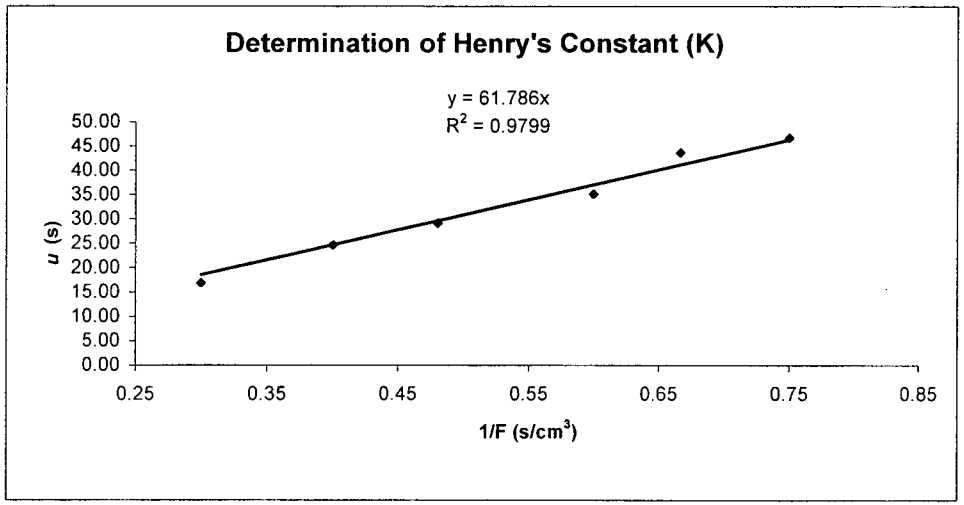

Determination of Henry's Constant								
C_3H_6 over Alumina (24-42 mesh)		**80.00**	**90.00**	**100.00**	**125.00**	**150.00**	**200.00**	sccm
Residence time	μ	46.73	43.65	35.12	29.16	24.67	16.88	**s**
F	**sccs**	1.33	1.50	1.67	2.08	2.50	3.33	
1/F	**1/sccm**	0.75	0.67	0.60	0.48	0.40	0.30	**s/cm^3**
(1-E)/E		1.11						
Numerator (use slope of graph)		4.91						
K		4.41						

Summary of moment analysis for 30% Al_2O_3 in SnO_2 10% Propylene at 100 °C

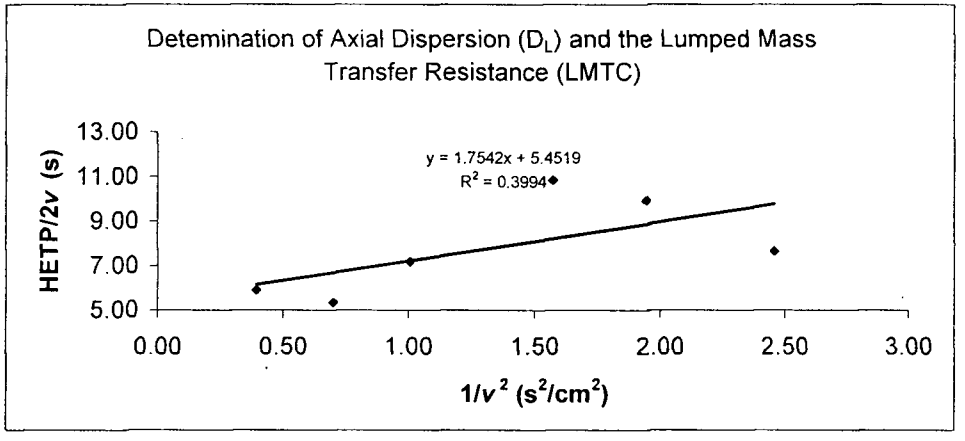

Correction for Dead Space in Reactor (carried out BT calculations with empty reactor (glass bead)								
Flow			80.00	90.00	100.00	125.00	150.00	200.00
residence time uncorrected		μ =	73.89	66.71	58.49	48.08	38.85	28.96
variance		σ^2	1807.77	1804.89	1355.91	963.03	544.77	414.53
residence time dead space		μ_{160C}	50.90	46.63	42.73	33.08	27.74	20.02
variance dead space		σ^2_{160C}	774.23	655.82	496.93	318.30	229.46	113.35
residence corrected		μ =	22.99	20.08	15.76	15.01	11.10	8.94
variance corrected		σ^2	1033.54	1149.07	858.98	644.74	315.31	301.18
HETP uncorrected		$(\sigma^2/\mu^2)L$	1.66	2.03	1.98	2.08	1.80	2.47
HETP corrected		$(\sigma^2/\mu^2)L$	9.78	14.25	17.28	14.32	12.79	18.84

Determination of Axial Dispersion Coefficient and Lumped Mass Transfer Coefficient:								
C_3H_6 over Alumina (24-42 mesh)		80.00	90.00	100.00	125.00	150.00	200.00	sccm
HETP (corrected)	$(\sigma^2/\mu^2)L$	9.78	14.25	17.28	14.32	12.79	18.84	cm
Interstitial Velocity	v	0.64	0.72	0.80	1.00	1.20	1.59	cm/s
x-axis	$1/v^2$	2.46	1.94	1.57	1.01	0.70	0.39	s^2/cm^2
y-axis	$(\sigma^2/\mu^2)L/(2v)$	7.67	9.93	10.84	7.18	5.35	5.91	s

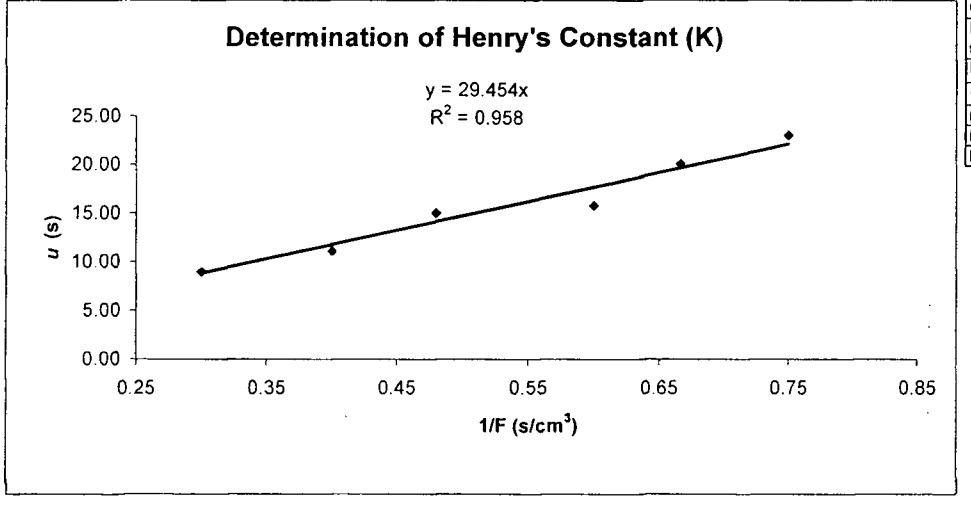

Determination of Henry's Constant								
C_3H_6 over Alumina (24-42 mesh)		80.00	90.00	100.00	125.00	150.00	200.00	sccm
Residence time	μ	22.99	20.08	15.76	15.01	11.10	8.94	s
F	sccs	1.33	1.50	1.67	2.08	2.50	3.33	
1/F	1/sccm	0.75	0.67	0.60	0.48	0.40	0.30	s/cm^3
(1-E)/E		1.11						
Numerator (use slope of graph)		1.82						
K		1.63						

Summary of moment analysis for 30% Al_2O_3 in SnO_2 10% Propylene at 150 °C

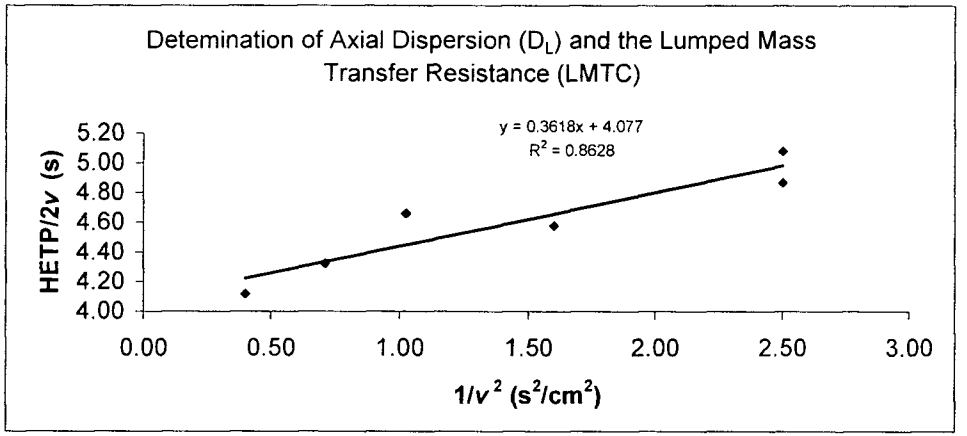

Correction for Dead Space in Reactor (carried out BT calculations with empty reactor (glass bead)								
Flow			80.00	80.00	100.00	125.00	150.00	200.00
residence time uncorrected		μ =	233.28	230.88	182.03	139.65	105.52	80.17
variance		σ^2	38452.33	35909.88	25283.93	17950.54	10418.42	7688.24
residence time dead space		μ_{soc}	63.39	63.39	51.98	42.43	35.57	26.66
variance dead space		σ^2_{soc}	1369.04	1369.04	803.07	546.20	385.96	232.86
residence corrected		μ =	169.88	167.49	130.05	97.22	69.95	53.51
variance corrected		σ^2	37083.28	34540.84	24480.86	17404.35	10032.47	7455.38
HETP uncorrected		$(\sigma^2/\mu^2)L$	3.53	3.37	3.82	4.60	4.68	5.98
HETP corrected		$(\sigma^2/\mu^2)L$	6.42	6.16	7.24	9.21	10.25	13.02

Determination of Axial Dispersion Coefficient and Lumped Mass Transfer Coefficient:								
C_3H_6 over Alumina (24-42 mesh)		**80.00**	**80.00**	**100.00**	**125.00**	**150.00**	**200.00**	sccm
HETP (corrected)	$(\sigma^2/\mu^2)L$	6.42	6.16	7.24	9.21	10.25	13.02	**cm**
Interstitial Velocity	v	0.63	0.63	0.79	0.99	1.19	1.58	**cm/s**
x-axis	$1/v^2$	2.50	2.50	1.60	1.02	0.71	0.40	**s^2/cm^2**
y-axis	$(\sigma^2/\mu^2)L/(2v)$	5.08	4.87	4.58	4.66	4.32	4.12	**s**

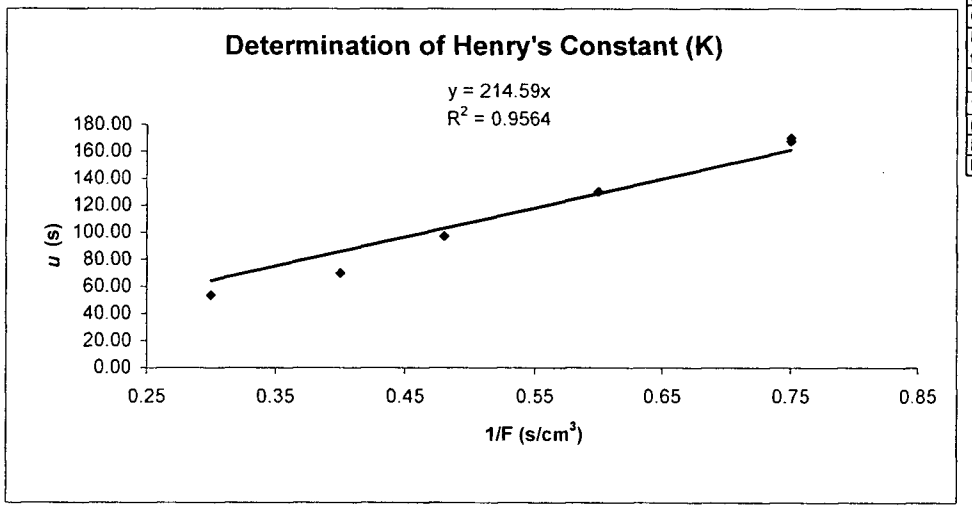

Determination of Henry's Constant								
C_3H_6 over Alumina (24-42 mesh)		**80.00**	**80.00**	**100.00**	**125.00**	**150.00**	**200.00**	sccm
Residence time	μ	169.88	167.49	130.05	97.22	69.95	53.51	**s**
F	sccs	1.33	1.33	1.67	2.08	2.50	3.33	
1/F	**1/sccm**	0.75	0.75	0.60	0.48	0.40	0.30	**s/cm^3**
(1-E)/E		1.10						
Numerator (use slope of graph)		19.36						
K		17.65						

Summary of moment analysis for 40% Al_2O_3 in SnO_2 10% Propylene at 50 °C

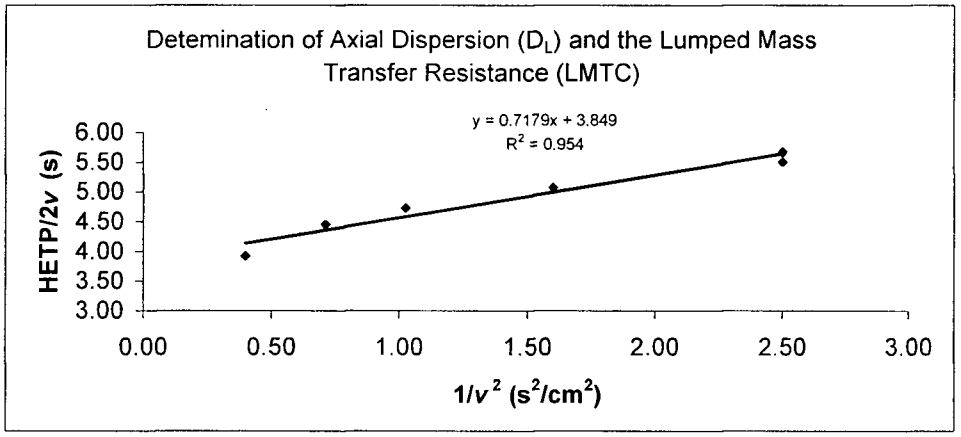

Correction for Dead Space in Reactor (carried out BT calculations with empty reactor (glass bead)								
Flow			80.00	80.00	100.00	125.00	150.00	200.00
residence time uncorrected		μ =	150.77	148.77	119.23	96.47	79.51	56.65
variance		σ^2	13417.54	12555.46	8781.52	6712.47	5015.12	2839.64
residence time dead space		μ_{75C}	58.46	58.46	48.35	38.70	32.45	23.99
variance dead space		σ^2_{75C}	1187.22	1187.22	712.26	477.22	338.91	194.50
residence corrected		μ =	92.30	90.31	70.88	57.76	47.06	32.66
variance corrected		σ^2	12230.32	11368.24	8069.26	6235.25	4676.21	2645.14
HETP uncorrected		$(\sigma^2/\mu^2)L$	2.95	2.84	3.09	3.61	3.97	4.42
HETP corrected		$(\sigma^2/\mu^2)L$	7.18	6.97	8.03	9.34	10.56	12.40

Determination of Axial Dispersion Coefficient and Lumped Mass Transfer Coefficient:								
C_3H_6 over Alumina (24-42 mesh)		80.00	80.00	100.00	125.00	150.00	200.00	sccm
HETP (corrected)	$(\sigma^2/\mu^2)L$	7.18	6.97	8.03	9.34	10.56	12.40	cm
Interstitial Velocity	v	0.63	0.63	0.79	0.99	1.19	1.58	cm/s
x-axis	$1/v^2$	2.50	2.50	1.60	1.02	0.71	0.40	s^2/cm^2
y-axis	$(\sigma^2/\mu^2)L/(2v)$	5.67	5.51	5.08	4.73	4.45	3.92	s

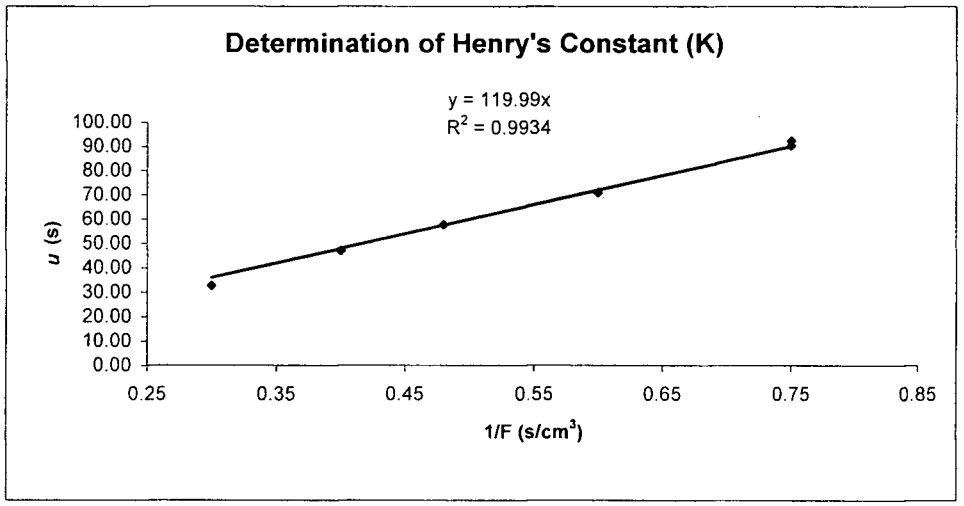

Determination of Henry's Constant								
C_3H_6 over Alumina (24-42 mesh)		80.00	80.00	100.00	125.00	150.00	200.00	sccm
Residence time	μ	92.30	90.31	70.88	57.76	47.06	32.66	s
F	sccs	1.33	1.33	1.67	2.08	2.50	3.33	
1/F	1/sccm	0.75	0.75	0.60	0.48	0.40	0.30	s/cm^3
(1-E)/E		1.10						
Numerator (use slope of graph)		10.38						
K		9.47						

Summary of moment analysis for 40% Al_2O_3 in SnO_2 10% Propylene at 75 °C

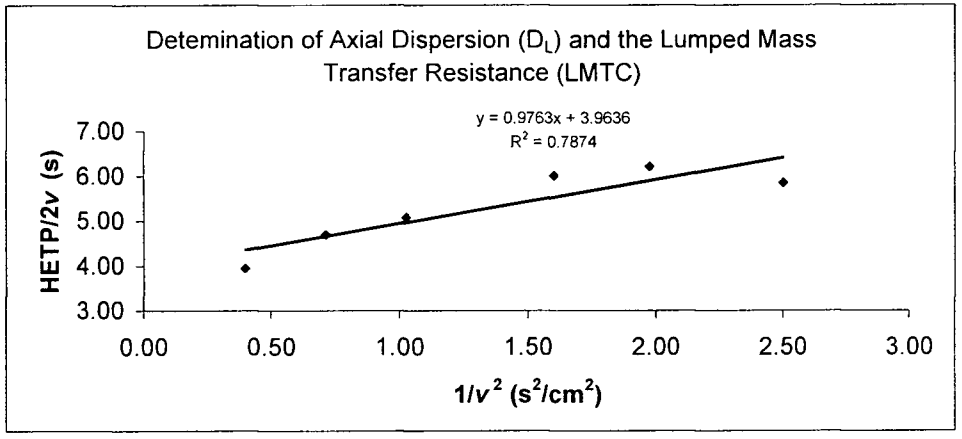

Correction for Dead Space in Reactor (carried out BT calculations with empty reactor (glass bead)								
Flow			80.00	90.00	100.00	125.00	150.00	200.00
residence time uncorrected		μ =	110.73	98.64	86.50	70.31	57.92	43.49
variance		σ^2	5591.18	4818.67	3756.06	2745.78	1984.15	1289.32
residence time dead space		μ_{100C}	55.20	51.20	45.93	36.26	30.41	22.25
variance dead space		σ^2_{100C}	1029.54	837.89	631.72	416.96	297.59	162.46
residence corrected		μ =	55.53	47.44	40.56	34.05	27.52	21.23
variance corrected		σ^2	4561.64	3980.78	3124.35	2328.83	1686.55	1126.85
HETP uncorrected		$(\sigma^2/\mu^2)L$	2.28	2.48	2.51	2.78	2.96	3.41
HETP corrected		$(\sigma^2/\mu^2)L$	7.40	8.84	9.49	10.04	11.14	12.50

Determination of Axial Dispersion Coefficient and Lumped Mass Transfer Coefficient:								
C_3H_6 over Alumina (24-42 mesh)		**80.00**	**90.00**	**100.00**	**125.00**	**150.00**	**200.00**	sccm
HETP (corrected)	$(\sigma^2/\mu^2)L$	7.40	8.84	9.49	10.04	11.14	12.50	**cm**
Interstitial Velocity	v	0.63	0.71	0.79	0.99	1.19	1.58	**cm/s**
x-axis	$1/v^2$	2.50	1.98	1.60	1.02	0.71	0.40	**s^2/cm^2**
y-axis	$(\sigma^2/\mu^2)L/(2v)$	5.85	6.22	6.00	5.08	4.70	3.95	**s**

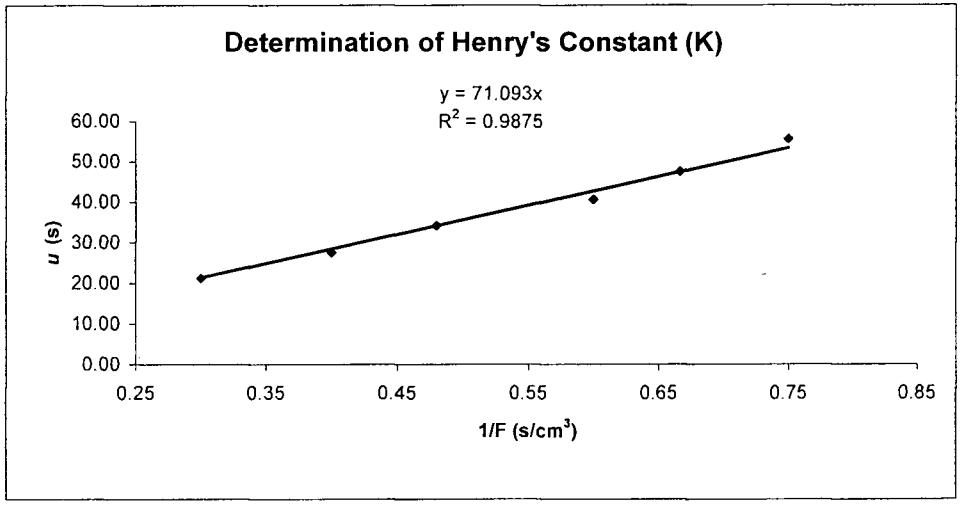

Determination of Henry's Constant								
C_3H_6 over Alumina (24-42 mesh)		**80.00**	**90.00**	**100.00**	**125.00**	**150.00**	**200.00**	sccm
Residence time	μ	55.53	47.44	40.56	34.05	27.52	21.23	**s**
F	sccs	1.33	1.50	1.67	2.08	2.50	3.33	
1/F	1/sccm	0.75	0.67	0.60	0.48	0.40	0.30	**s/cm^3**
(1-E)/E		1.10						
Numerator (use slope of graph)		5.74						
K		5.24						

Summary of moment analysis for 40% Al_2O_3 in SnO_2 10% Propylene at 100 °C

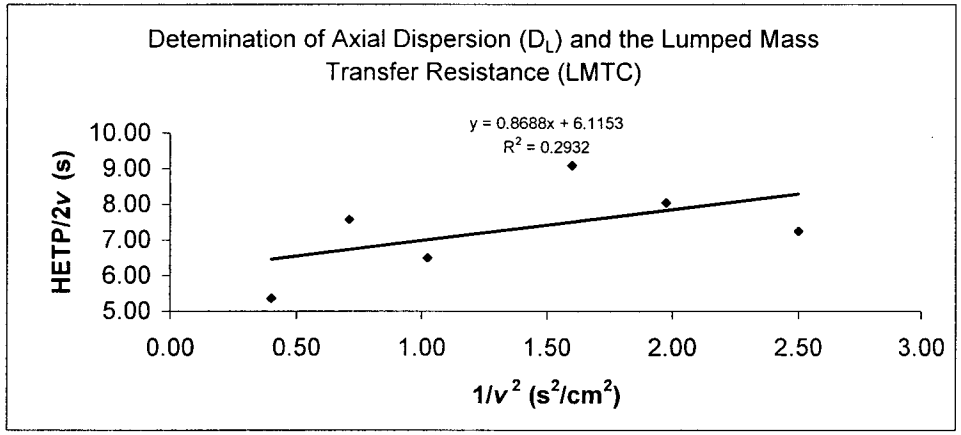

Correction for Dead Space in Reactor (carried out BT calculations with empty reactor (glass bead)									
Flow				80.00	90.00	100.00	125.00	150.00	200.00
residence time uncorrected			μ =	78.24	68.31	60.46	49.31	39.38	29.52
variance			σ^2	2144.09	1732.45	1400.84	995.27	715.82	419.52
residence time dead space			μ_{150C}	50.90	46.63	42.73	33.08	27.74	20.02
variance dead space			σ^2_{150C}	774.23	655.82	496.93	318.30	229.46	113.35
residence corrected			μ =	27.34	21.68	17.73	16.23	11.63	9.50
variance corrected			σ^2	1369.86	1076.63	903.91	676.97	486.36	306.17
HETP uncorrected			$(\sigma^2/\mu^2)L$	1.75	1.86	1.92	2.05	2.31	2.41
HETP corrected			$(\sigma^2/\mu^2)L$	9.17	11.45	14.37	12.85	17.97	16.97

Determination of Axial Dispersion Coefficient and Lumped Mass Transfer Coefficient:								
C_3H_6 over Alumina (24-42 mesh)		80.00	90.00	100.00	125.00	150.00	200.00	sccm
HETP (corrected)	$(\sigma^2/\mu^2)L$	9.17	11.45	14.37	12.85	17.97	16.97	cm
Interstitial Velocity	v	0.63	0.71	0.79	0.99	1.19	1.58	cm/s
x-axis	$1/v^2$	2.50	1.98	1.60	1.02	0.71	0.40	s^2/cm^2
y-axis	$(\sigma^2/\mu^2)L/(2v)$	7.25	8.05	9.09	6.50	7.58	5.37	s

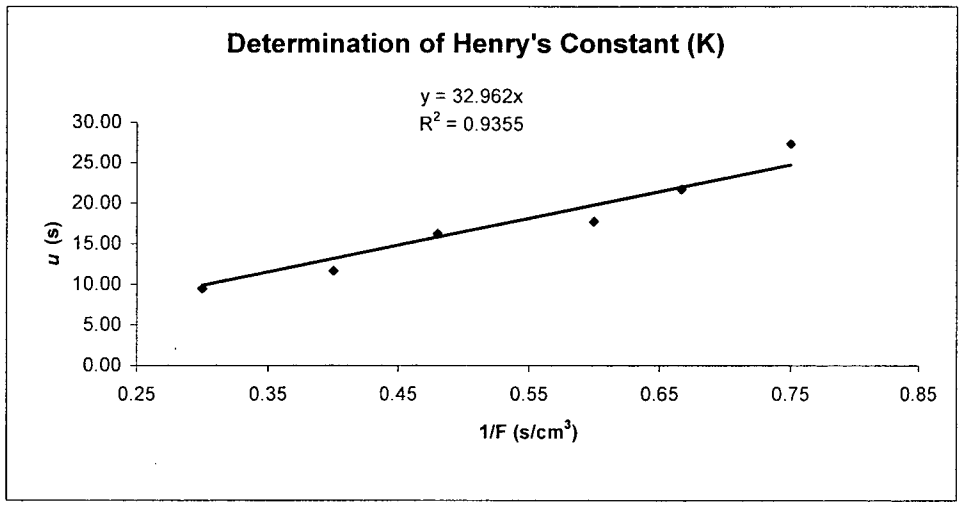

Determination of Henry's Constant								
C_3H_6 over Alumina (24-42 mesh)		80.00	90.00	100.00	125.00	150.00	200.00	sccm
Residence time	μ	27.34	21.68	17.73	16.23	11.63	9.50	s
F	sccs	1.33	1.50	1.67	2.08	2.50	3.33	
1/F	1/sccm	0.75	0.67	0.60	0.48	0.40	0.30	s/cm^3
(1-E)/E		1.10						
Numerator (use slope of graph)		2.13						
K		1.94						

Summary of moment analysis for 40% Al_2O_3 in SnO_2 10% Propylene at 150 °C

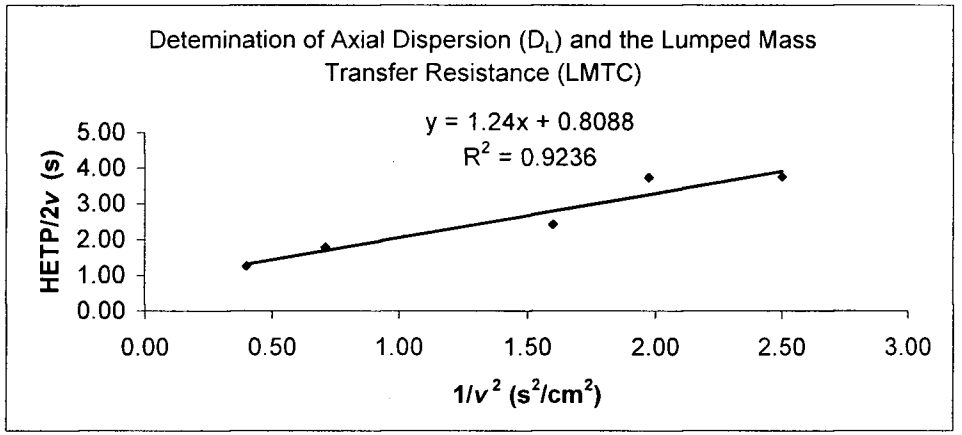

Correction for Dead Space in Reactor (carried out BT calculations with empty reactor (glass bead)								
Flow			80.00	90.00	100.00	125.00	150.00	200.00
residence time uncorrected	μ =		137.58	129.67	117.59	129.18	78.58	67.44
variance	σ^2		7475.84	7366.60	4569.11	8599.39	2262.43	1796.63
residence time dead space	μ_{100C}		55.20	51.20	45.93	36.26	30.41	22.25
variance dead space	σ^2_{100C}		1029.54	837.89	631.72	416.96	297.59	162.46
residence corrected	μ =		82.38	78.47	71.66	92.92	48.17	45.19
variance corrected	σ^2		6446.30	6528.71	3937.39	8182.43	1964.84	1634.16
HETP uncorrected	$(\sigma^2/\mu^2)L$		1.97	2.19	1.65	2.58	1.83	1.97
HETP corrected	$(\sigma^2/\mu^2)L$		4.75	5.30	3.83	4.74	4.23	4.00

Determination of Axial Dispersion Coefficient and Lumped Mass Transfer Coefficient:								
C_3H_6 over Alumina (24-42 mesh)		80.00	90.00	100.00	125.00	150.00	200.00	sccm
HETP (corrected)	$(\sigma^2/\mu^2)L$	4.75	5.30	3.83	4.74	4.23	4.00	cm
Interstitial Velocity	v	0.63	0.71	0.79	0.99	1.19	1.58	cm/s
x-axis	$1/v^2$	2.50	1.98	1.60	1.02	0.71	0.40	s^2/cm^2
y-axis	$(\sigma^2/\mu^2)L/(2v)$	3.76	3.73	2.43		1.79	1.27	s

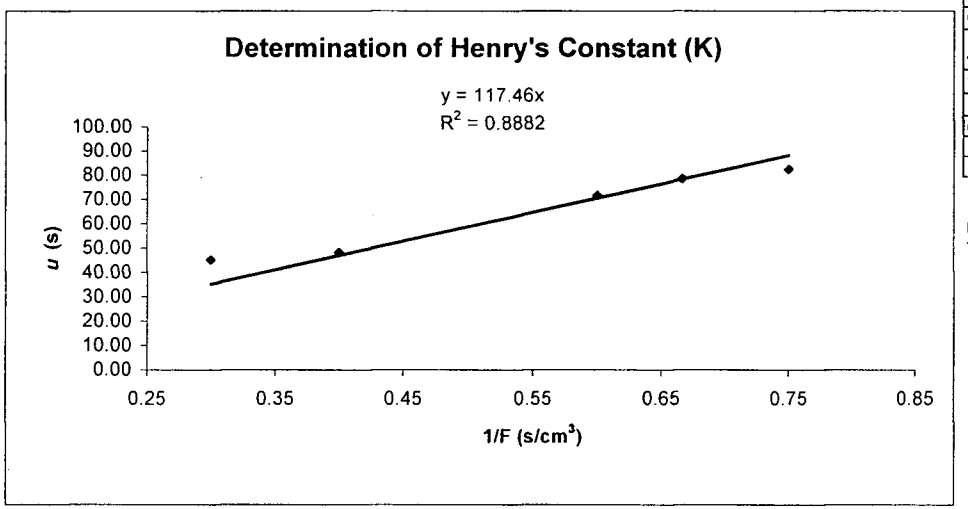

Determination of Henry's Constant								
C_3H_6 over Alumina (24-42 mesh)		80.00	80.00	100.00	125.00	150.00	200.00	sccm
Residence time	μ	82.38	78.47	71.66		48.17	45.19	s
F	sccs	1.33	1.50	1.67	2.08	2.50	3.33	
1/F	1/sccm	0.75	0.67	0.60	0.48	0.40	0.30	s/cm^3
(1-E)/E		1.10						
Numerator (use slope of graph)		10.14						
K		9.25						

NOTE to improve the fit eliminated the 125 point and then recalculate K
This greatly improves the fit and puts this K value in line with others

Summary of moment analysis for 40% Al_2O_3 in SnO_2 1% Propylene at 100 °C

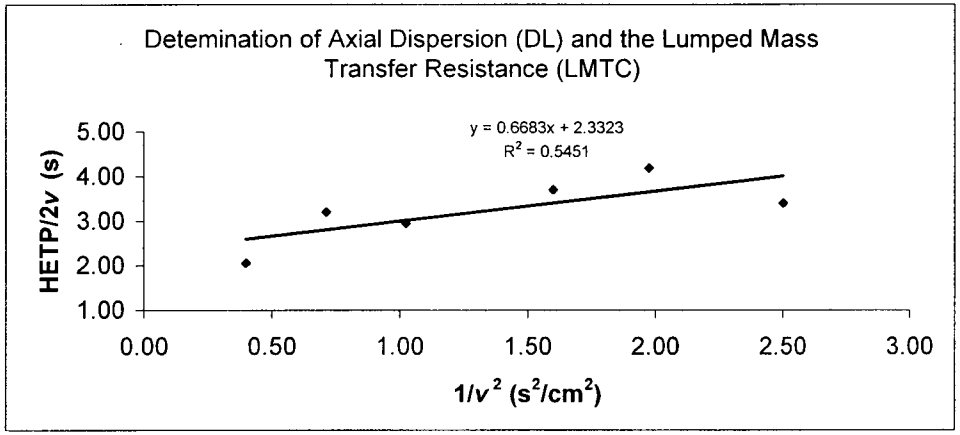

Correction for Dead Space in Reactor (carried out BT calculations with empty reactor (glass bead)								
Flow			80.00	90.00	100.00	125.00	150.00	200.00
residence time uncorrected		μ =	130.36	116.57	102.68	83.87	64.55	45.62
variance		σ^2	5884.69	5928.15	4396.58	3057.03	2064.55	872.88
residence time dead space		μ_{100C}	55.20	51.20	45.93	36.26	30.41	22.25
variance dead space		σ^2_{100C}	1029.54	837.89	631.72	416.96	297.59	162.46
residence corrected		μ =	75.17	65.37	56.74	47.61	34.14	23.37
variance corrected		σ^2	4855.15	5090.26	3764.86	2640.07	1766.95	710.42
HETP uncorrected		$(\sigma^2/\mu^2)L$	1.73	2.18	2.09	2.17	2.48	2.10
HETP corrected		$(\sigma^2/\mu^2)L$	4.30	5.96	5.85	5.82	7.58	6.50

Determination of Axial Dispersion Coefficient and Lumped Mass Transfer Coefficient:								
C_3H_6 over Alumina (24-42 mesh)		**80.00**	**90.00**	**100.00**	**125.00**	**150.00**	**200.00**	sccm
HETP (corrected)	$(\sigma^2/\mu^2)L$	4.30	5.96	5.85	5.82	7.58	6.50	**cm**
Interstitial Velocity	v	0.63	0.71	0.79	0.99	1.19	1.58	**cm/s**
x-axis	$1/v^2$	2.50	1.98	1.60	1.02	0.71	0.40	**s^2/cm^2**
y-axis	$(\sigma^2/\mu^2)L/(2v)$	3.40	4.19	3.70	2.95	3.20	2.06	**s**

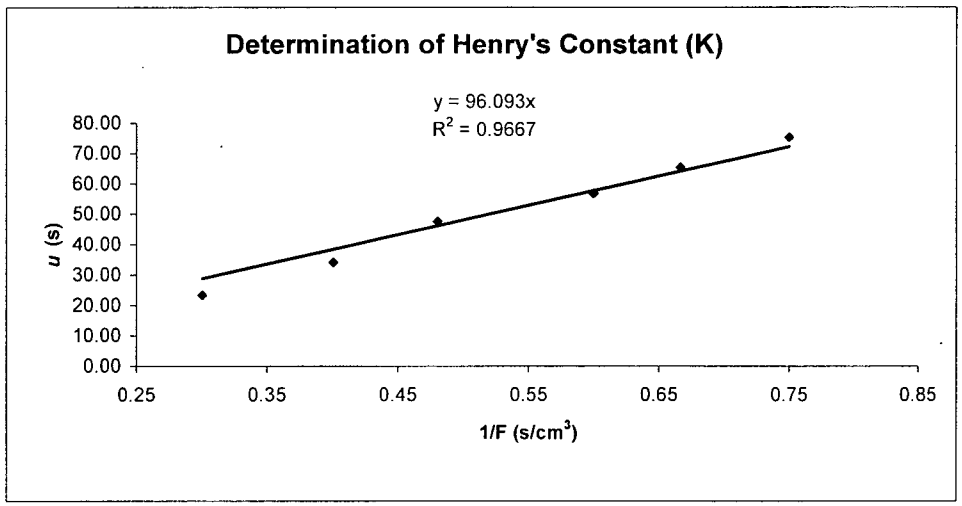

Determination of Henry's Constant								
C_3H_6 over Alumina (24-42 mesh)		**80.00**	**80.00**	**100.00**	**125.00**	**150.00**	**200.00**	sccm
Residence time	μ	75.17	65.37	56.74	47.61	34.14	23.37	**s**
F	sccs	1.33	1.50	1.67	2.08	2.50	3.33	
1/F	1/sccm	0.75	0.67	0.60	0.48	0.40	0.30	**s/cm^3**
(1-E)/E		1.10						
Numerator (use slope of graph)		8.12						
K		7.40						

Summary of moment analysis for 40% Al_2O_3 in SnO_2 5% Propylene at 100 °C

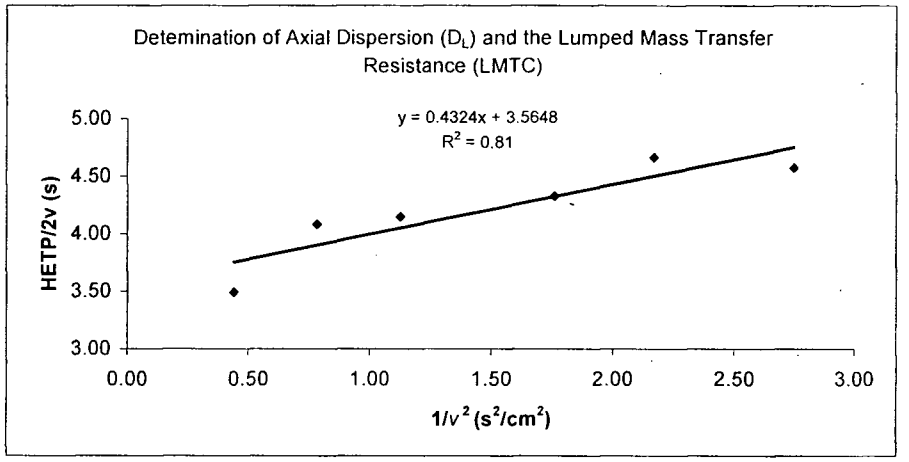

Correction for Dead Space in Reactor (carried out BT calculations with empty reactor (glass bead)								
Flow			80.00	90.00	100.00	125.00	150.00	200.00
residence time uncorrected		μ =	362.73	315.50	274.62	216.05	157.66	119.86
variance		σ^2	111261.67	92890.58	72711.22	52917.75	30984.53	20566.16
residence time dead space		μ_{soc}	63.39	60.08	51.98	42.43	35.57	26.66
variance dead space		σ^2_{soc}	1369.04	1070.50	803.07	546.20	385.96	232.86
residence corrected		μ_{soc}	299.33	255.42	222.64	173.62	122.09	93.20
variance corrected		σ^2_{soc}	109892.63	91820.07	71908.15	52371.55	30598.57	20333.29
HETP uncorrected		$(\sigma^2/\mu^2)L$	3.81	4.20	4.34	5.10	5.61	6.44
HETP corrected		$(\sigma^2/\mu^2)L$	5.52	6.33	6.53	7.82	9.24	10.53

Determination of Axial Dispersion Coefficient and Lumped Mass Transfer Coefficient:								
C_3H_6 over Alumina (24-42 mesh)		80.00	90.00	100.00	125.00	150.00	200.00	sccm
HETP (corrected)	$(\sigma^2/\mu^2)L$	5.52	6.33	6.53	7.82	9.24	10.53	cm
Interstitial Velocity	v	0.60	0.68	0.75	0.94	1.13	1.51	cm/s
x-axis	$1/v^2$	2.75	2.17	1.76	1.13	0.78	0.44	s^2/cm^2
y-axis	$(\sigma^2/\mu^2)L/(2v)$	4.57	4.67	4.33	4.15	4.08	3.49	s

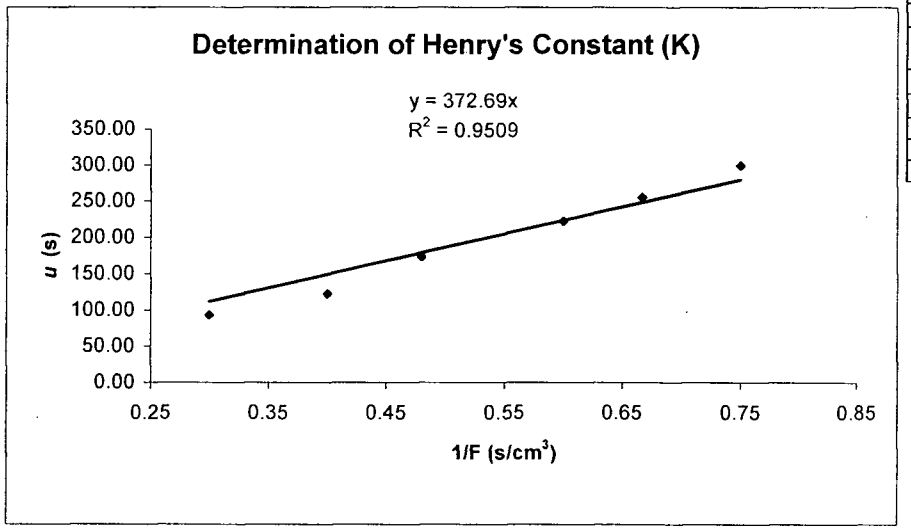

Determination of Henry's Constant								
C_3H_6 over Alumina (24-42 mesh)		80.00	90.00	100.00	125.00	150.00	200.00	sccm
Residence time	μ	299.33	255.42	222.64	173.62	122.09	93.20	s
F	sccs	1.33	1.50	1.67	2.08	2.50	3.33	
1/F	1/sccm	0.75	0.67	0.60	0.48	0.40	0.30	s/cm^3
(1-E)/E		1.00						
Numerator (use slope of graph)		36.48						
K		36.48						

Summary of moment analysis for 100% Al_2O_3 with 10% Propylene at 50 °C

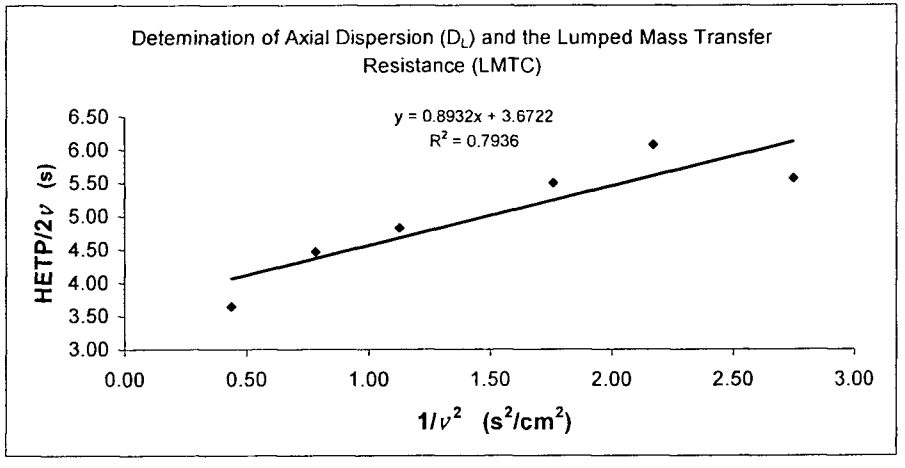

Correction for Dead Space in Reactor (carried out BT calculations with empty reactor (glass bead)								
Flow				80.00	90.00	100.00	125.00	150.00	200.00
residence time uncorrected			μ =	134.75	115.39	110.53	88.14	67.99	53.91
variance			σ^2	10480.63	8390.75	8326.91	5861.22	3471.04	2613.06
residence time dead space			μ_{100C}	55.20	51.20	45.93	36.26	30.41	22.25
variance dead space			σ^2_{100C}	1029.54	837.89	631.72	416.96	297.59	162.46
residence corrected			μ_{100C}	79.55	64.19	64.60	51.88	37.58	31.66
variance corrected			σ^2_{100C}	9451.09	7552.86	7695.20	5444.26	3173.44	2450.59
HETP uncorrected			$(\sigma^2/\mu^2)L$	2.60	2.84	3.07	3.39	3.38	4.05
HETP corrected			$(\sigma^2/\mu^2)L$	6.72	8.25	8.30	9.10	10.11	11.00

Determination of Axial Dispersion Coefficient and Lumped Mass Transfer Coefficient:								
C_3H_6 over Alumina (24-42 mesh)		80.00	90.00	100.00	125.00	150.00	200.00	sccm
HETP (corrected)	$(\sigma^2/\mu^2)L$	6.72	8.25	8.30	9.10	10.11	11.00	cm
Interstitial Velocity	v	0.60	0.68	0.75	0.94	1.13	1.51	cm/s
x-axis	$1/v^2$	2.75	2.17	1.76	1.13	0.78	0.44	s^2/cm^2
y-axis	$(\sigma^2/\mu^2)L/(2v)$	5.57	6.08	5.50	4.83	4.47	3.65	s

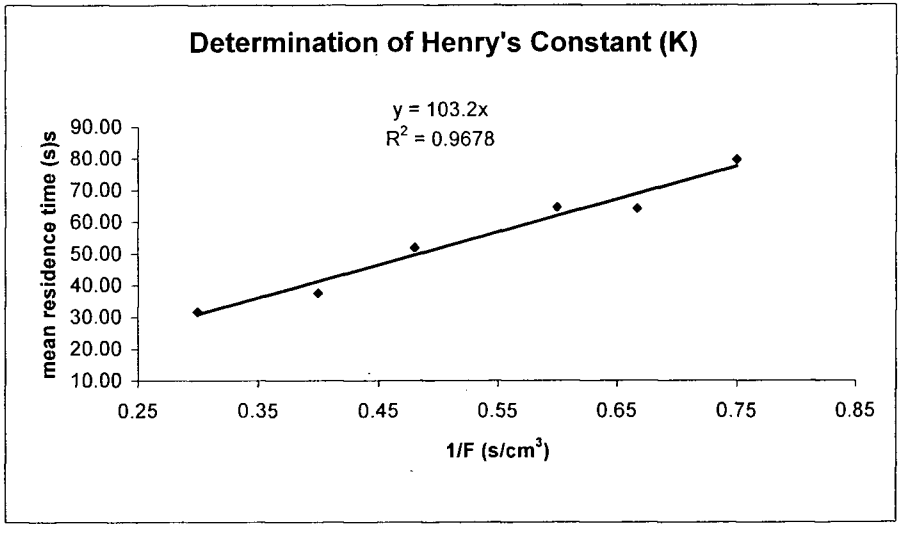

Determination of Henry's Constant								
C_3H_6 over Alumina (24-42 mesh)		80.00	90.00	100.00	125.00	150.00	200.00	sccm
Residence time	μ	79.55	64.19	64.60	51.88	37.58	31.66	s
F	sccs	1.33	1.50	1.67	2.08	2.50	3.33	
1/F	1/sccm	0.75	0.67	0.60	0.48	0.40	0.30	s/cm^3
(1-E)/E		1.00						
Numerator (use slope of graph)		9.38						
K		9.38						

Summary of moment analysis for 100% Al_2O_3 with 10% Propylene at 100 °C

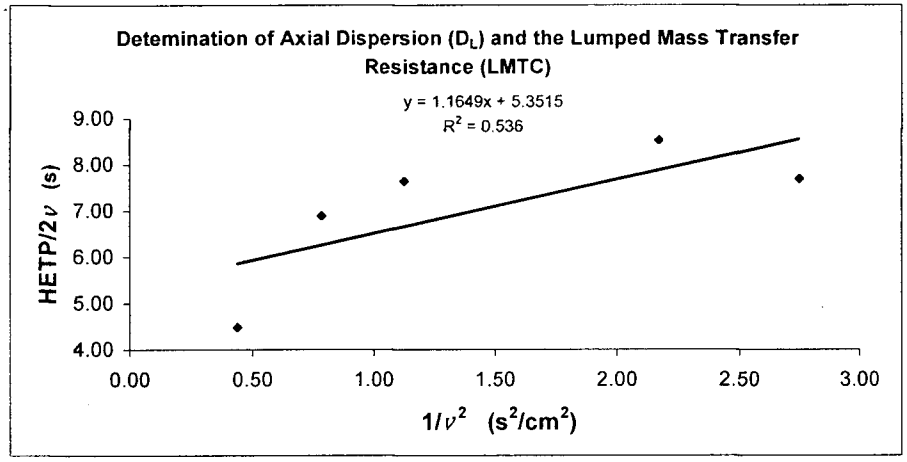

Correction for Dead Space in Reactor (carried out BT calculations with empty reactor (glass bead)								
Flow			80.00	90.00	100.00	125.00	150.00	200.00
residence time uncorrected		μ =	81.47	71.85	60.70	50.62	43.13	33.92
variance		σ^2	2697.81	2293.07	1770.29	1302.45	1049.48	693.80
residence time dead space		μ_{150C}	50.90	46.63	42.73	33.08	27.74	20.02
variance dead space		σ^2_{150C}	774.23	655.82	496.93	318.30	229.46	113.35
residence corrected		μ_{150C}	30.56	25.22	17.97	17.54	15.38	13.90
variance corrected		σ^2_{150C}	1923.58	1637.25	1273.36	984.16	820.02	580.46
HETP uncorrected		$(\sigma^2/\mu^2)L$	1.83	2.00	2.16	2.29	2.54	2.71
HETP corrected		$(\sigma^2/\mu^2)L$	9.27	11.58	17.75	14.39	15.59	13.52

Determination of Axial Dispersion Coefficient and Lumped Mass Transfer Coefficient:								
C_3H_6 over Alumina (24-42 mesh)		80.00	90.00	100.00	125.00	150.00	200.00	sccm
HETP (corrected)	$(\sigma^2/\mu^2)L$	9.27	11.58	17.75	14.39	15.59	13.52	cm
Interstitial Velocity	v	0.60	0.68	0.75	0.94	1.13	1.51	cm/s
x-axis	$1/v^2$	2.75	2.17	1.76	1.13	0.78	0.44	s^2/cm^2
y-axis	$(\sigma^2/\mu^2)L/(2v)$	7.68	8.53		7.63	6.89	4.48	s

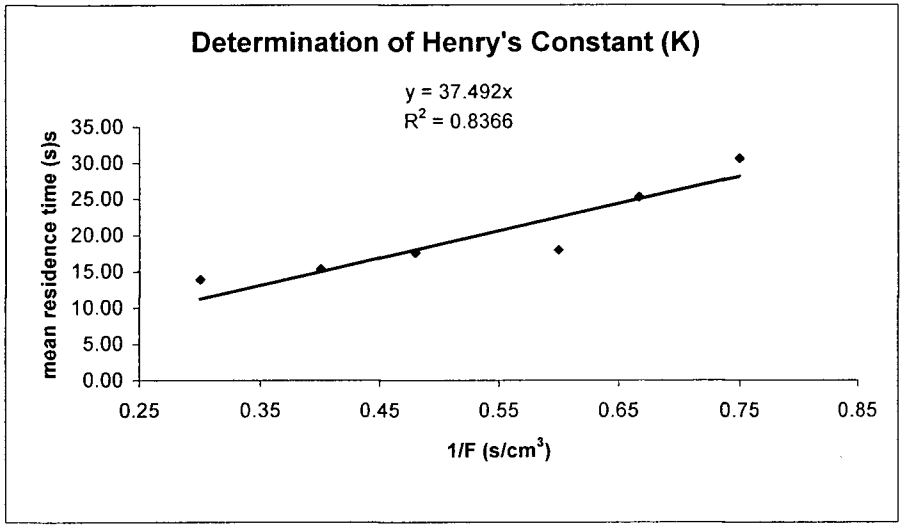

Determination of Henry's Constant								
C_3H_6 over Alumina (24-42 mesh)		80.00	90.00	100.00	125.00	150.00	200.00	sccm
Residence time	μ	30.56	25.22	17.97	17.54	15.38	13.90	s
F	sccs	1.33	1.50	1.67	2.08	2.50	3.33	
1/F	1/sccm	0.75	0.67	0.60	0.48	0.40	0.30	s/cm^3
(1-E)/E		1.00						
Numerator (use slope of graph)		2.77						
K		2.77						

Summary of moment analysis for 100% Al_2O_3 with 10% Propylene at 150 °C

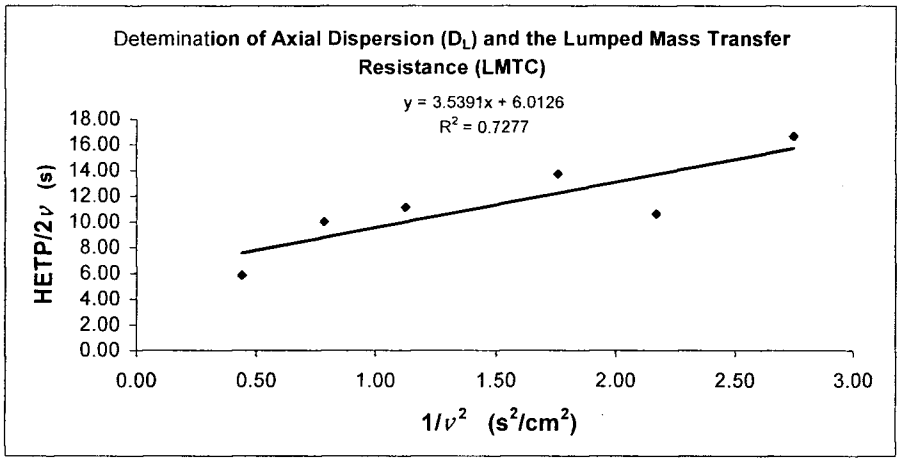

Correction for Dead Space in Reactor (carried out BT calculations with empty reactor (glass bead)								
Flow			80.00	90.00	100.00	125.00	150.00	200.00
residence time uncorrected	μ =		62.97	59.64	50.61	41.70	34.34	27.80
variance	σ^2		1576.30	1334.92	1026.51	777.14	526.67	414.23
residence time dead space	μ_{200C}		48.06	43.63	38.85	30.99	26.00	18.57
variance dead space	σ^2_{200C}		582.23	513.31	390.90	242.98	176.93	79.08
residence corrected	μ_{200C}		14.91	16.01	11.76	10.71	8.34	9.23
variance corrected	σ^2_{200C}		994.07	821.61	635.61	534.16	349.74	335.15
HETP uncorrected	$(\sigma^2/\mu^2)L$		1.79	1.69	1.80	2.01	2.01	2.41
HETP corrected	$(\sigma^2/\mu^2)L$		20.12	14.43	20.68	20.96	22.62	17.72

Determination of Axial Dispersion Coefficient and Lumped Mass Transfer Coefficient:								
C_3H_6 over Alumina (24-42 mesh)		**80.00**	**90.00**	**100.00**	**125.00**	**150.00**	**200.00**	sccm
HETP (corrected)	$(\sigma^2/\mu^2)L$	20.12	14.43	20.68	20.96	22.62	17.72	**cm**
Interstitial Velocity	v	0.60	0.68	0.75	0.94	1.13	1.51	**cm/s**
x-axis	$1/v^2$	2.75	2.17	1.76	1.13	0.78	0.44	**s^2/cm^2**
y-axis	$(\sigma^2/\mu^2)L/(2v)$	16.68	10.63	13.71	11.12	10.00	5.87	**s**

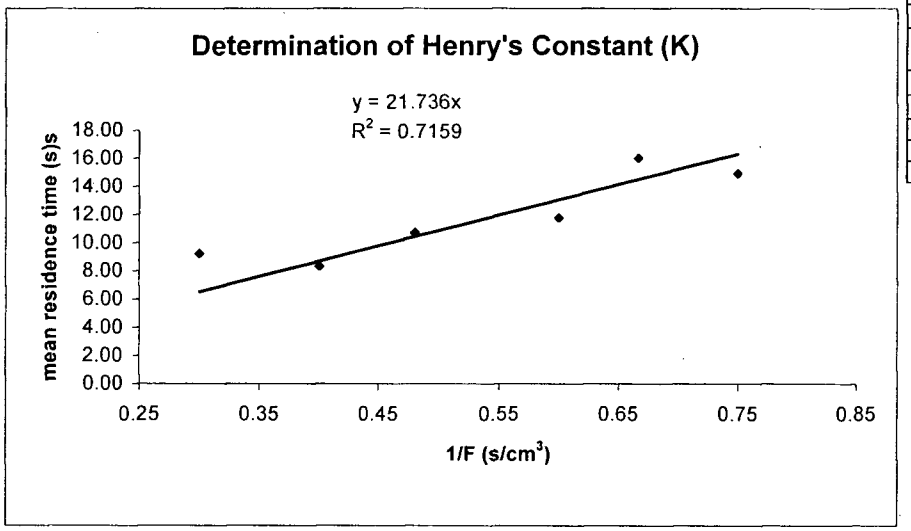

Determination of Henry's Constant								
C_3H_6 over Alumina (24-42 mesh)		**80.00**	**90.00**	**100.00**	**125.00**	**150.00**	**200.00**	sccm
Residence time	μ	14.91	16.01	11.76	10.71	8.34	9.23	**s**
F	sccs	1.33	1.50	1.67	2.08	2.50	3.33	
1/F	1/sccm	0.75	0.67	0.60	0.48	0.40	0.30	**s/cm^3**
(1-E)/E		1.00						
Numerator (use slope of graph)		1.19						
K		1.19						

Summary of moment analysis for 100% Al_2O_3 with 10% Propylene at 200 °C

Appendix D

Summary of Electrical Resistance Results

(10% C_3H_6 over 10 - 40% Al_2O_3 in SnO_2)

(1 - 10% C_3H_6 over 40% Al_2O_3 in SnO_2)

(Electrical Resistance Response Curves in order of increasing %Al_2O_3)

	1 hour oxydation data			1st 15 min oxydation data			2nd 15 min oxydation data		
Temp	Ra	Ra,He	Rg	Ra	Ra,He	Rg	Ra	Ra,He	Rg
oC	kΩ	kΩ	kΩ	kΩ	kΩ	kΩ	kΩ	kΩ	kΩ
10% Al_2O_3, 10% C_3H_6									
50	431.78	308.58	194.09	335.63	257.06	193.74	349.44	272.63	209.42
75	306.73	123.86	59.78	216.89	147.98	67.41	201.1	140.23	63.89
100	257.51	122.66	28.9	208.66	88.33	29.49	215.55	101.6	31.29
150	133.65	34.3	4.63	93.69	22.11	4.76	101.87	22.2	4.87
qVs (eV)	0.1672	0.2746	0.4654	0.1749	0.3206	0.4660	0.1659	0.3212	0.4680
90% conf.	0.2102	0.4050	0.5321	0.2521	0.4140	0.5275	0.2561	0.4413	0.5400
90% conf.	0.1241	0.1442	0.3987	0.0977	0.2272	0.4044	0.0757	0.2011	0.3961
G0	2.94E+02	2.10E+04	2.98E+07	5.03E+02	1.11E+05	2.90E+07	3.69E+02	1.08E+05	3.02E+07
R0	3.41E-03	4.76E-05	3.35E-08	1.99E-03	9.05E-06	3.44E-08	2.71E-03	9.22E-06	3.31E-08
20% Al_2O_3, 10% C_3H_6									
50	1309.04	888.6	366.4	829.82	653.59	358.12	855.26	590.56	343.16
75	1289.43	485.26	207.15	1023.57	494.56	129.46	1102.64	417.8	131.36
100	1145.49	252.13	55.59	639.14	187.11	54.28	603.91	203.41	56.11
150	626.27	112.28	18.14	407.69	81.09	17.93	378.9	71.73	18.39
qVs (eV)	0.1199	0.2780	0.4018	0.1277	0.2917	0.3846	0.1432	0.2878	0.3771
90% conf.	0.2062	0.3040	0.5232	0.2421	0.3985	0.4346	0.2776	0.3686	0.4159
90% conf.	0.0336	0.2521	0.2805	0.0133	0.1849	0.3347	0.0087	0.2070	0.3383
G0	1.61E+01	7.95E+03	1.48E+06	3.15E+01	1.54E+04	9.69E+05	5.19E+01	1.47E+04	7.57E+05
R0	6.22E-02	1.26E-04	6.78E-07	3.18E-02	6.49E-05	1.03E-06	1.93E-02	6.81E-05	1.32E-06
30% Al_2O_3, 10% C_3H_6									
oC	MΩ	MΩ	MΩ	MΩ	MΩ	MΩ	MΩ	MΩ	MΩ
50	4.8215	3.2735	1.522	2.6275	1.488	1.038	2.418	1.587	1.117
75	5.2696	1.8998	0.3492	2.5592	1.004	0.345	2.3369	0.9017	0.3464
100	5.296	1.4233	0.1882	2.6322	0.6689	0.188	2.4244	0.6579	0.1809
150	5.7246	1.2265	0.122	2.6883	0.4395	0.1085	2.7579	0.6105	0.1181
qVs (eV)	0.0130	0.1446	0.3179	0.0282	0.1769	0.2921	0.0152	0.1418	0.2907
90% conf.	0.0248	0.2284	0.5403	0.0352	0.2040	0.4286	0.0366	0.2417	0.4595
90% conf.	0.0012	0.0608	0.0956	0.0212	0.1499	0.1556	-0.0061	0.0419	0.1220
G0	1.05E+02	2.04E+04	2.84E+07	3.42E+02	1.28E+05	1.41E+07	2.40E+02	3.89E+04	1.31E+07
R0	9.53E-03	4.90E-05	3.52E-08	2.92E-03	7.81E-06	7.07E-08	4.17E-03	2.57E-05	7.62E-08
40% Al_2O_3, 10% C_3H_6									
50	25.6647	19.2938	7.261	13.3755	10.3587	6.2267			
100				6.1769	2.141	0.6758			
150	11.1095	5.0091	0.3068	6.2083	1.4426	0.2716			
qVs (eV)				0.1256	0.2686	0.4051			
90% conf. int.				0.4057	0.6523	0.7768			
90% conf. int.				-0.1546	-0.1152	0.0334			
G0				2.41E+03	5.50E+05	1.23E+08			
R0				4.14E-04	1.82E-06	8.13E-09			
(*Alternate Pretreatment*), 40% Al_2O_3, 10% C_3H_6									
50	900.04	672.05	345.1	586.18	411.65	292.7			
75	446.3	285.07	177.84	411.77	260.67	171.89	396.68	276.8	184.36
100	330.82	206.63	110.58	313.84	181.6	109.29	292.01	171.09	106.52
150	346.3	138.82	66.32	294.11	125.66	65.54	302.14	127.87	66.82
qVs (eV)	0.1395	0.2101	0.2246	0.1130	0.1712	0.2082			
90% conf.	0.2810	0.3185	0.2829	0.1762	0.2102	0.2436			
90% conf.	-0.0020	0.1018	0.1663	0.0497	0.1323	0.1728			
G0	6.80E+01	1.11E+03	3.28E+03	3.49E+01	3.90E+02	2.05E+03			
R0	1.47E-02	9.04E-04	3.05E-04	2.87E-02	2.56E-03	4.87E-04			

	1 hour oxydation data			15 min oxydation data			15 min oxydation data		
Temp	Ra	Ra,He	Rg	Ra	Ra,He	Rg	Ra	Ra,He	Rg
oC	MΩ	MΩ	MΩ	MΩ	MΩ	MΩ	MΩ	MΩ	MΩ
40% Al_2O_3, 10% C_3H_6									
50	25.6647	19.2938	7.261	13.3755	10.3587	6.2267			
100				6.1769	2.141	0.6758			
150	11.1095	5.0091	0.3068	6.2083	1.4426	0.2716			
qVs (eV)				0.1256	0.2686	0.4051			
90% conf. int.				0.4057	0.6523	0.7768			
90% conf. int.				-0.1546	-0.1152	0.0334			
G0				2.41E+03	5.50E+05	1.23E+08			
R0				4.14E-04	1.82E-06	8.13E-09			
40% Al_2O_3, 5% C_3H_6									
50	16.5895	14.0254	7.7426	13.0386	11.0968	7.1626			
100	14.9933	6.167	1.2948	10.5112	3.4156	0.9823	9.0534	3.0815	1.2436
150	9.3154	3.706	0.4414	6.3804	1.9079	0.4446			
qVs (eV)	0.0972	0.1890	0.3706	0.1138	0.2408	0.3632			
90% conf. i	0.2978	0.2385	0.5029	0.2834	0.3867	0.7059			
90% conf. i	-0.1033	0.1396	0.2382	-0.0558	0.0950	0.0248			
G0	5.99E+02	2.09E+04	2.65E+07	1.40E+03	1.75E+05	2.35E+07			
R0	1.67E-03	4.79E-05	3.78E-08	7.16E-04	5.71E-06	4.25E-08			
40% Al_2O_3, 1% C_3H_6									
50				15.8386	13.2589	8.8086			
100	18.4271	9.1168	1.545	11.6705	4.9009	1.514	11.2689	5.134	1.2609
150	16.8054	9.663	0.5172	10.9895	3.7868	0.5043	10.4645	4.1634	0.4933
qVs (eV)				0.0757	0.1822	0.3699			
90% conf. int.				0.1518	0.4174	0.4809			
90% conf. int.				-0.0003	-0.0530	0.2589			
G0				3.18E+02	1.84E+04	2.25E+07			
R0				3.15E-03	5.45E-05	4.45E-08			

Electrical Resistance (R/R_0) and TCD Response ($C/C_{0)}$ vs Time for uptake of 10% C_3H_6 over 10% Al_2O_3/SnO_2

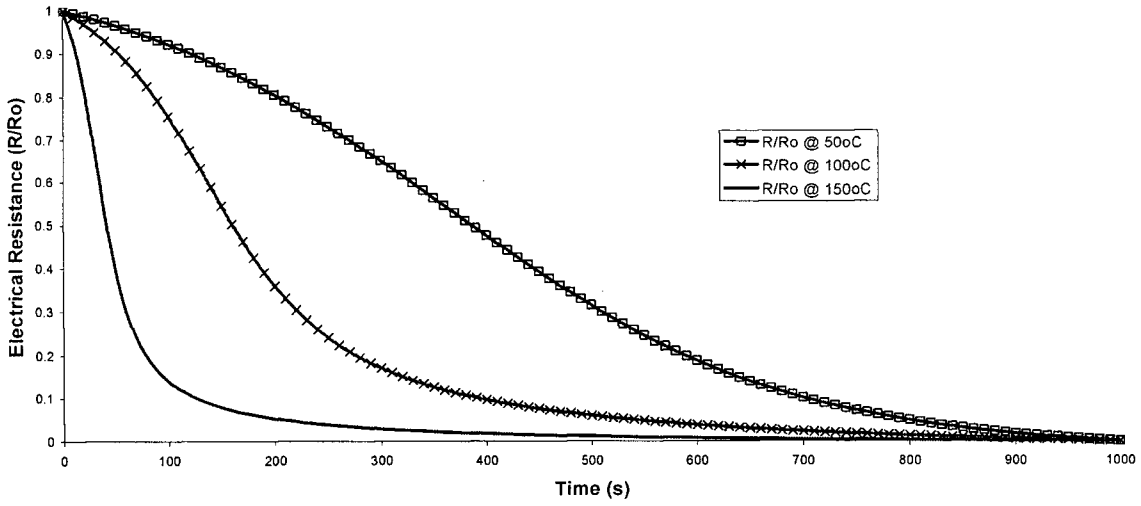

Electrical Resistance (R/R_0) and TCD Response ($C/C_{0)}$ vs Time for uptake of 10% C_3H_6 over 20% Al_2O_3/SnO_2

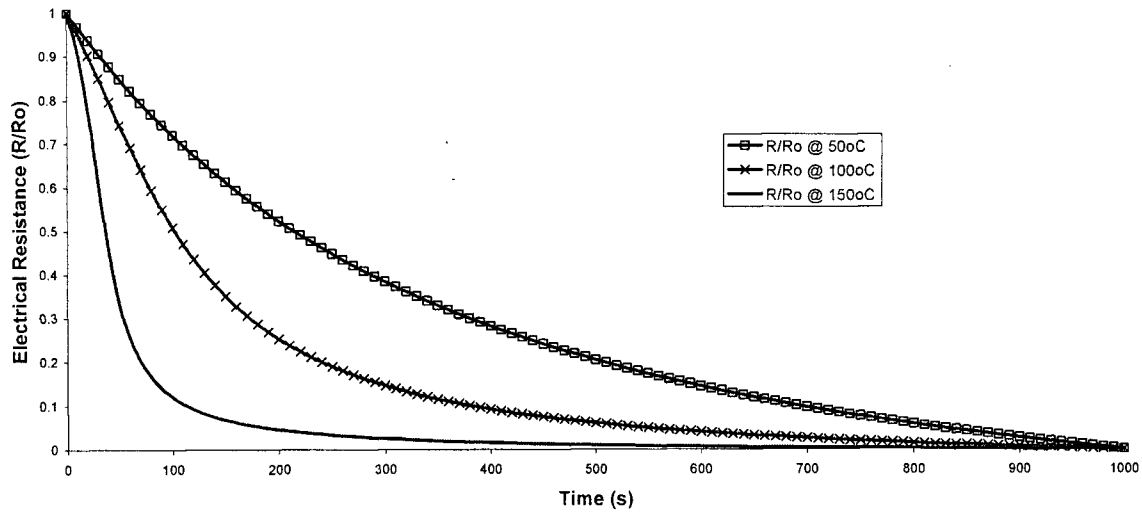

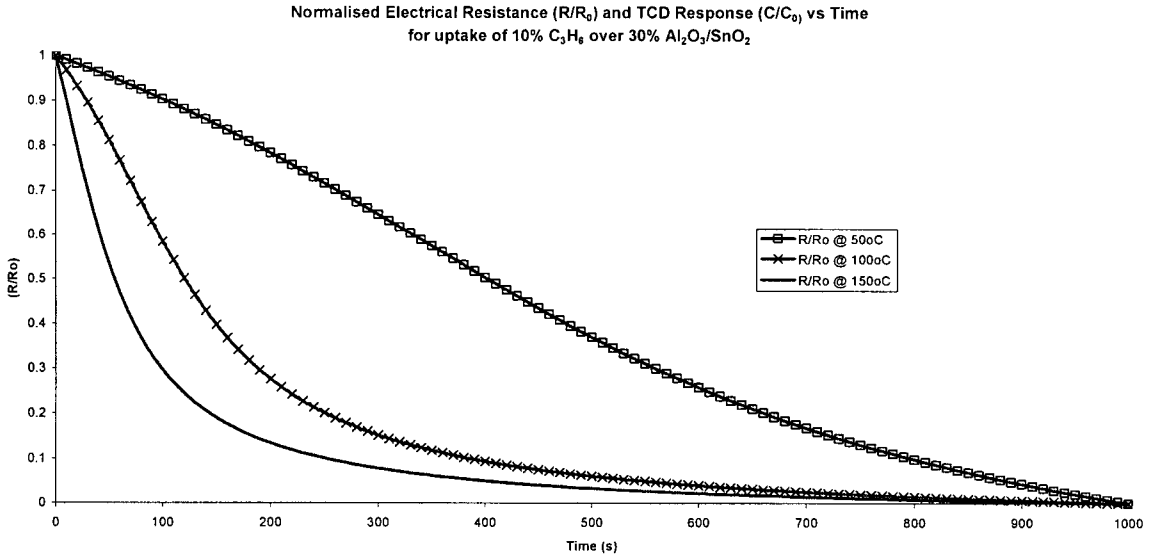
Normalised Electrical Resistance (R/R0) and TCD Response (C/C0) vs Time
for uptake of 10% C3H6 over 30% Al2O3/SnO2
(R/Ro)
Time (s)
R/Ro @ 50oC
R/Ro @ 100oC
R/Ro @ 150oC

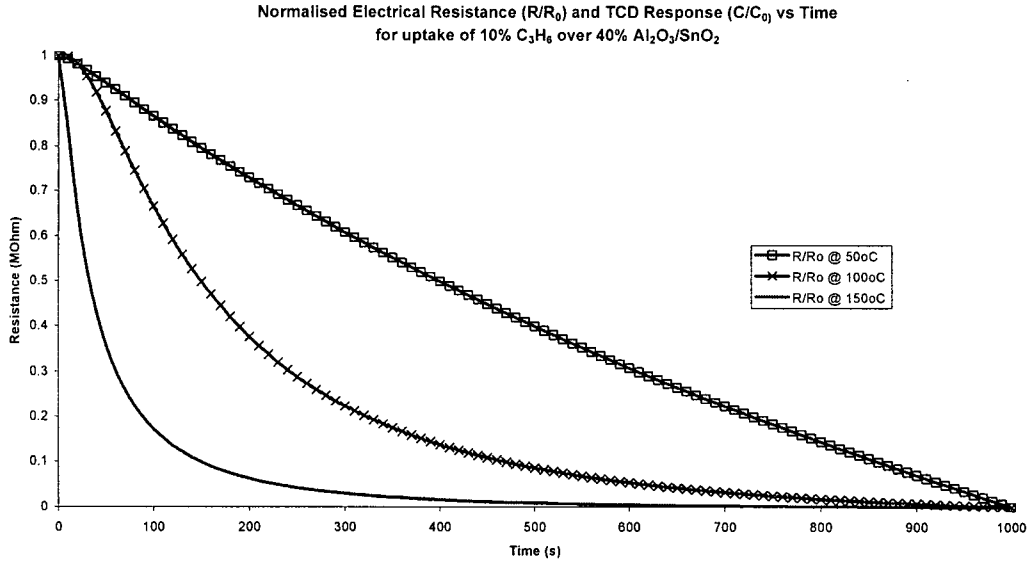
Normalised Electrical Resistance (R/R0) and TCD Response (C/C0) vs Time
for uptake of 10% C3H6 over 40% Al2O3/SnO2
Resistance (MOhm)
Time (s)
R/Ro @ 50oC
R/Ro @ 100oC
R/Ro @ 150oC

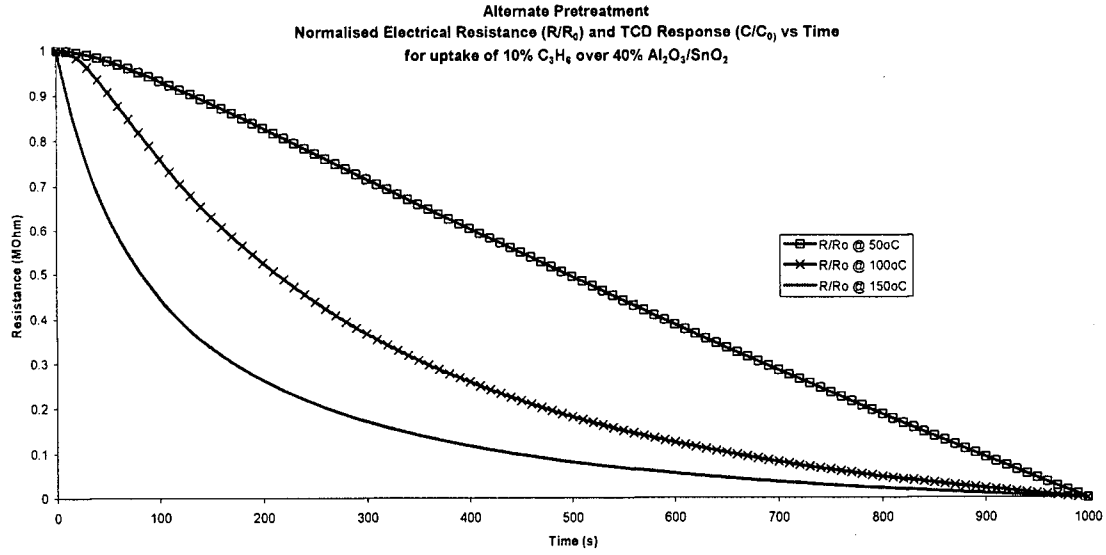
Alternate Pretreatment
Normalised Electrical Resistance (R/R0) and TCD Response (C/C0) vs Time
for uptake of 10% C3H6 over 40% Al2O3/SnO2
Resistance (MOhm)
Time (s)
R/Ro @ 50oC
R/Ro @ 100oC
R/Ro @ 150oC

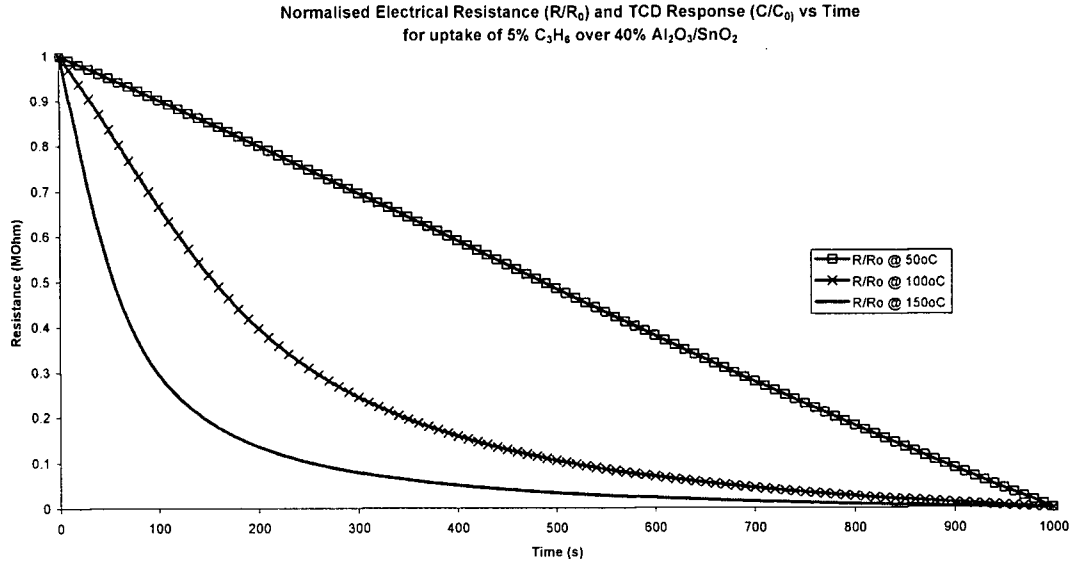
Normalised Electrical Resistance (R/R0) and TCD Response (C/C0) vs Time
for uptake of 5% C3H6 over 40% Al2O3/SnO2
Resistance (MOhm)
Time (s)
R/Ro @ 50oC
R/Ro @ 100oC
R/Ro @ 150oC

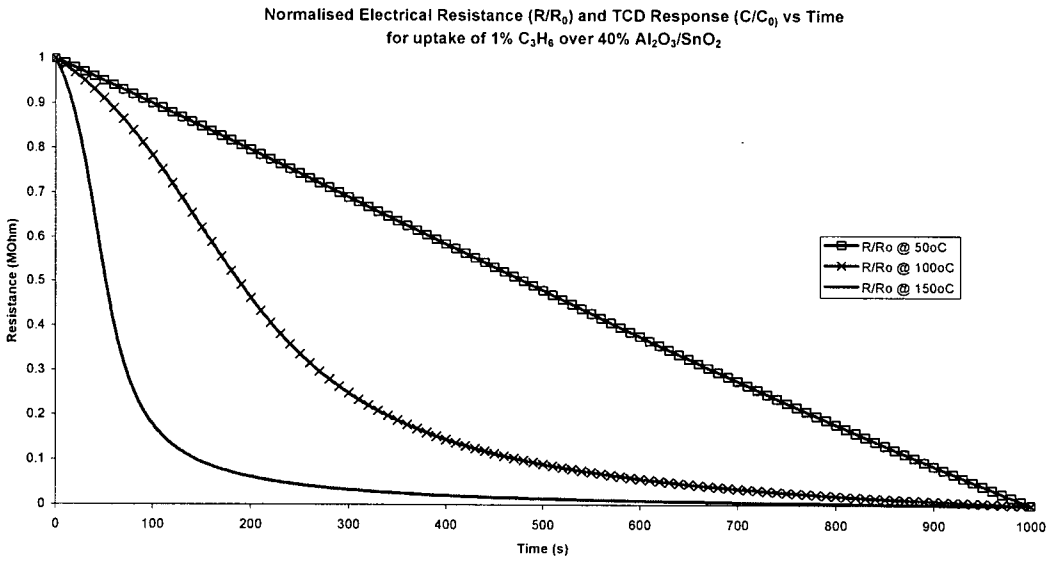
Normalised Electrical Resistance (R/R0) and TCD Response (C/C0) vs Time
for uptake of 1% C3H6 over 40% Al2O3/SnO2
Resistance (MOhm)
Time (s)
R/Ro @ 50oC
R/Ro @ 100oC
R/Ro @ 150oC
0
0.1
0.2
0.3
0.4
0.5
0.6
0.7
0.8
0.9
1
0
100
200
300
400
500
600
700
800
900
1000

Appendix E

Summary of Modeled Curves of

Resistance vs Breakthrough with Reaction Kinetics

from 50 – 100 °C

(10% C_3H_6 over 10 - 40% Al_2O_3 in SnO_2)

(*Alternate Pretreatment* - 10% C_3H_6 over 40% Al_2O_3 in SnO_2)

(1 - 10% C_3H_6 over 40% Al_2O_3 in SnO_2)

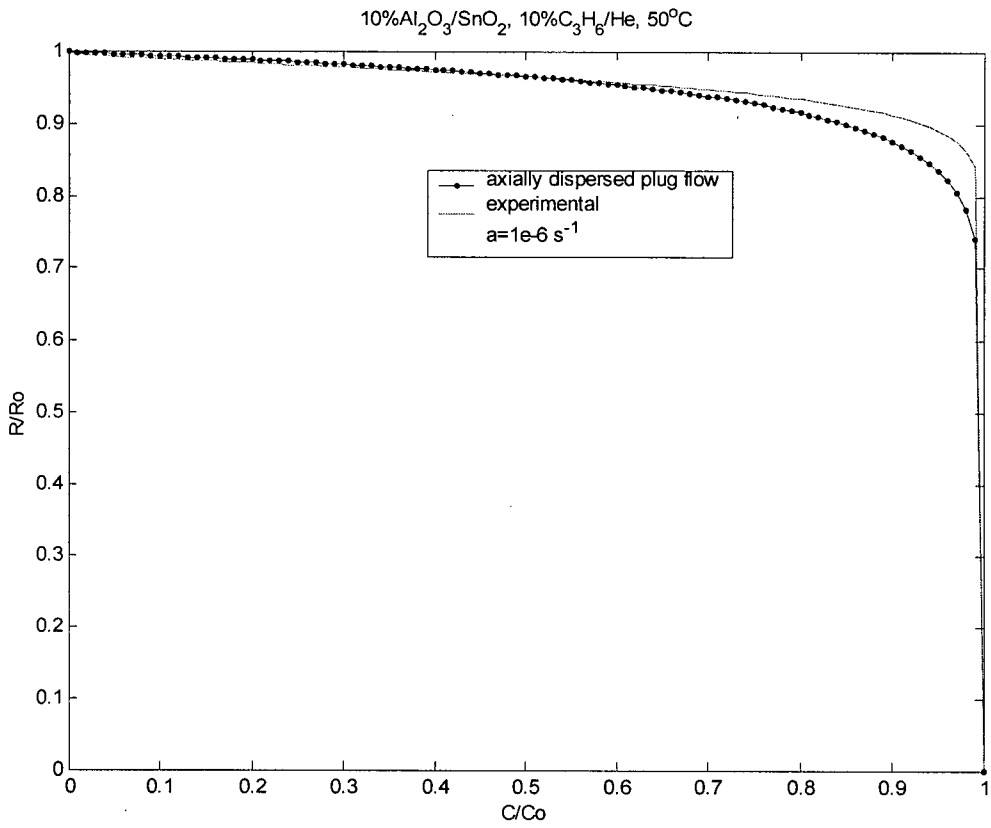
10%Al2O3/SnO2, 10%C3H6/He, 50°C
axially dispersed plug flow
experimental
a=1e-6 s-1
R/Ro
C/Co
0
0.1
0.2
0.3
0.4
0.5
0.6
0.7
0.8
0.9
1

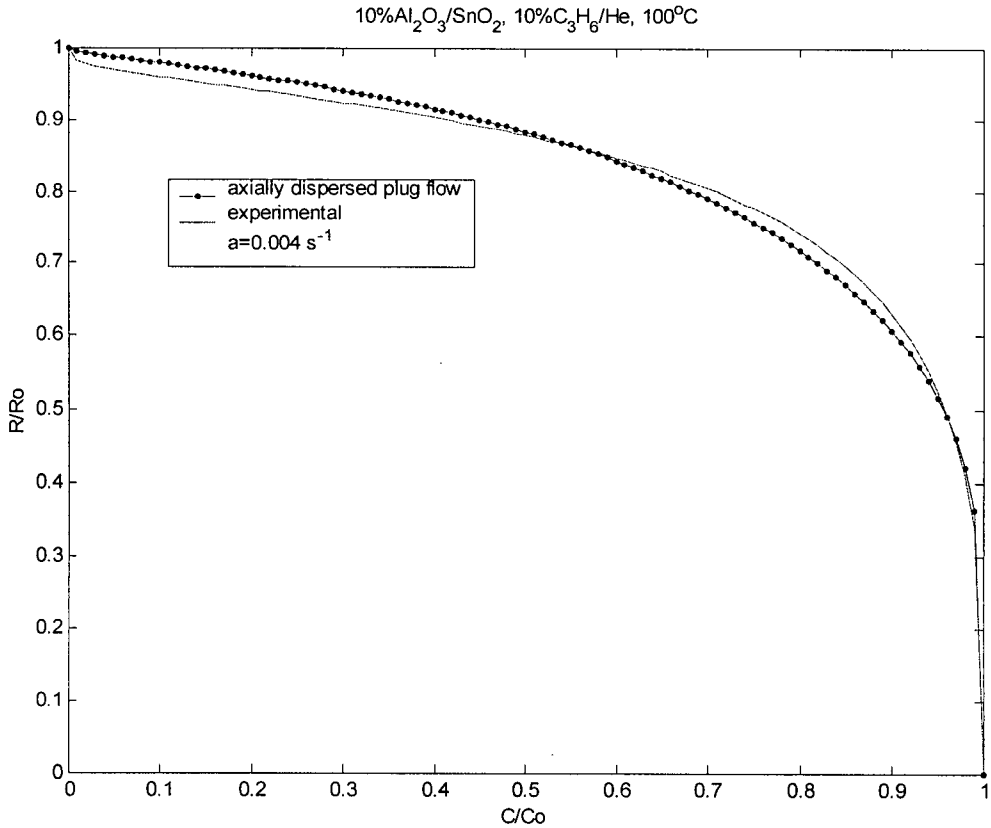
10%Al2O3/SnO2, 10%C3H6/He, 100°C
axially dispersed plug flow
experimental
a=0.004 s-1
R/Ro
C/Co
0
0.1
0.2
0.3
0.4
0.5
0.6
0.7
0.8
0.9
1

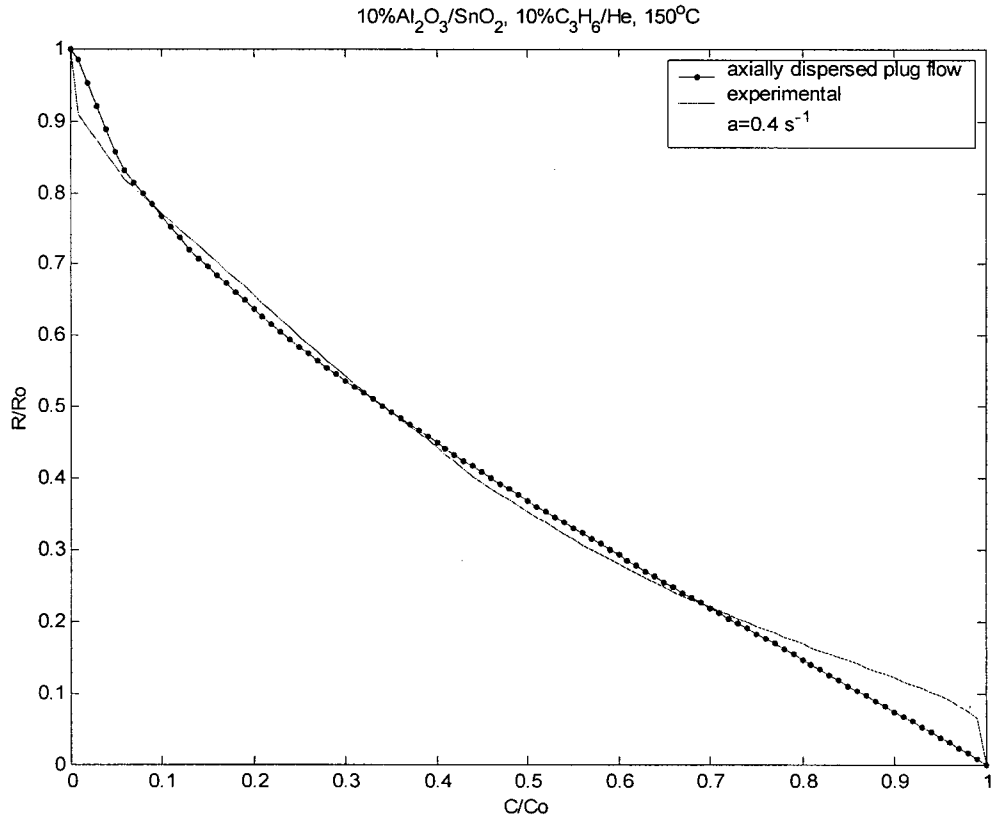
10%Al2O3/SnO2, 10%C3H6/He, 150°C
axially dispersed plug flow
experimental
a=0.4 s-1
R/Ro
C/Co
0
0.1
0.2
0.3
0.4
0.5
0.6
0.7
0.8
0.9
1

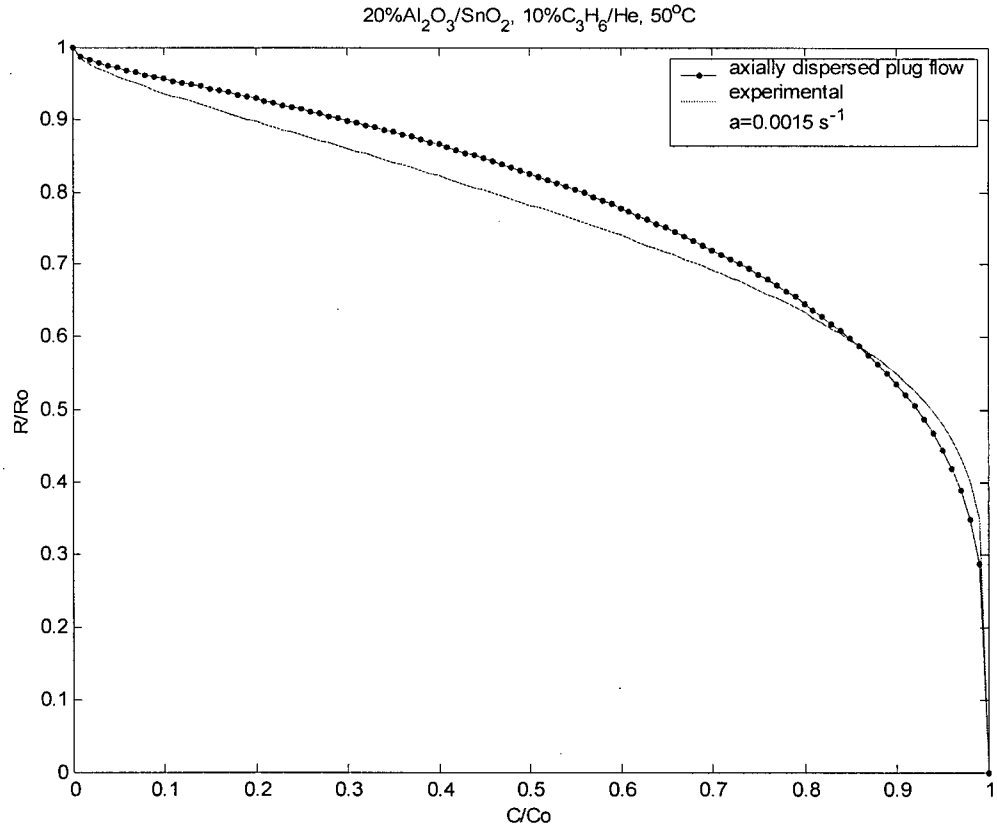
20%Al2O3/SnO2, 10%C3H6/He, 50°C
axially dispersed plug flow
experimental
a=0.0015 s-1
R/Ro
C/Co
0
0.1
0.2
0.3
0.4
0.5
0.6
0.7
0.8
0.9
1

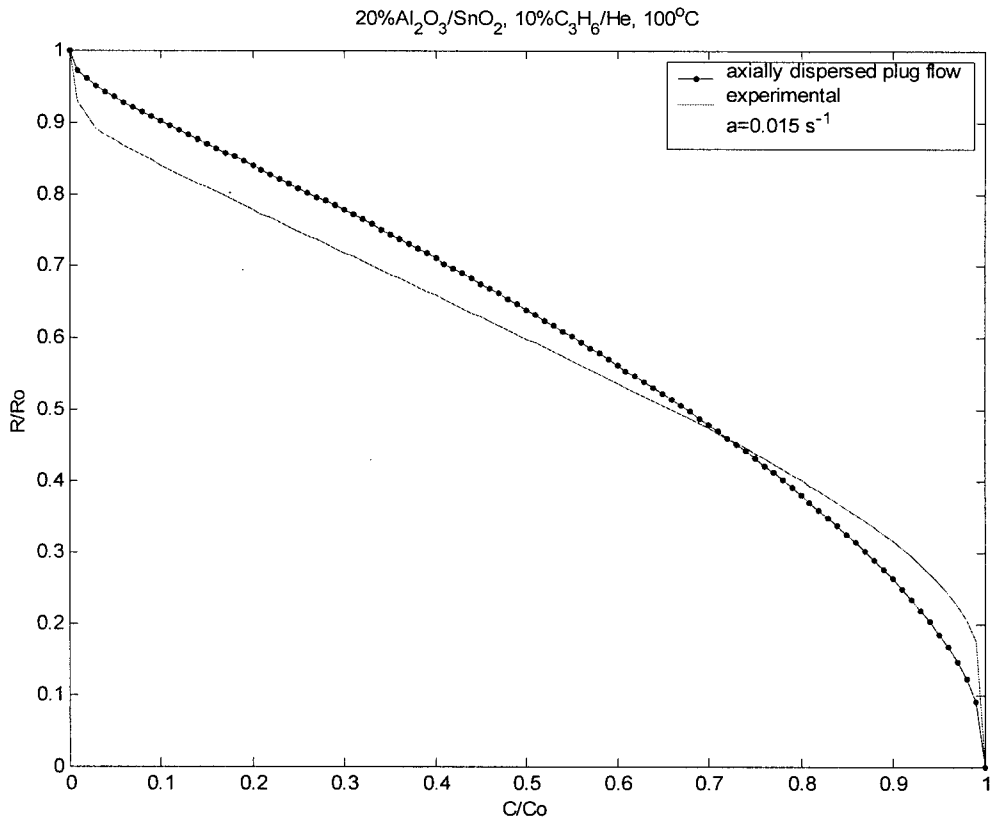
20%Al2O3/SnO2, 10%C3H6/He, 100°C
axially dispersed plug flow
experimental
a=0.015 s-1
R/Ro
C/Co
0
0.1
0.2
0.3
0.4
0.5
0.6
0.7
0.8
0.9
1

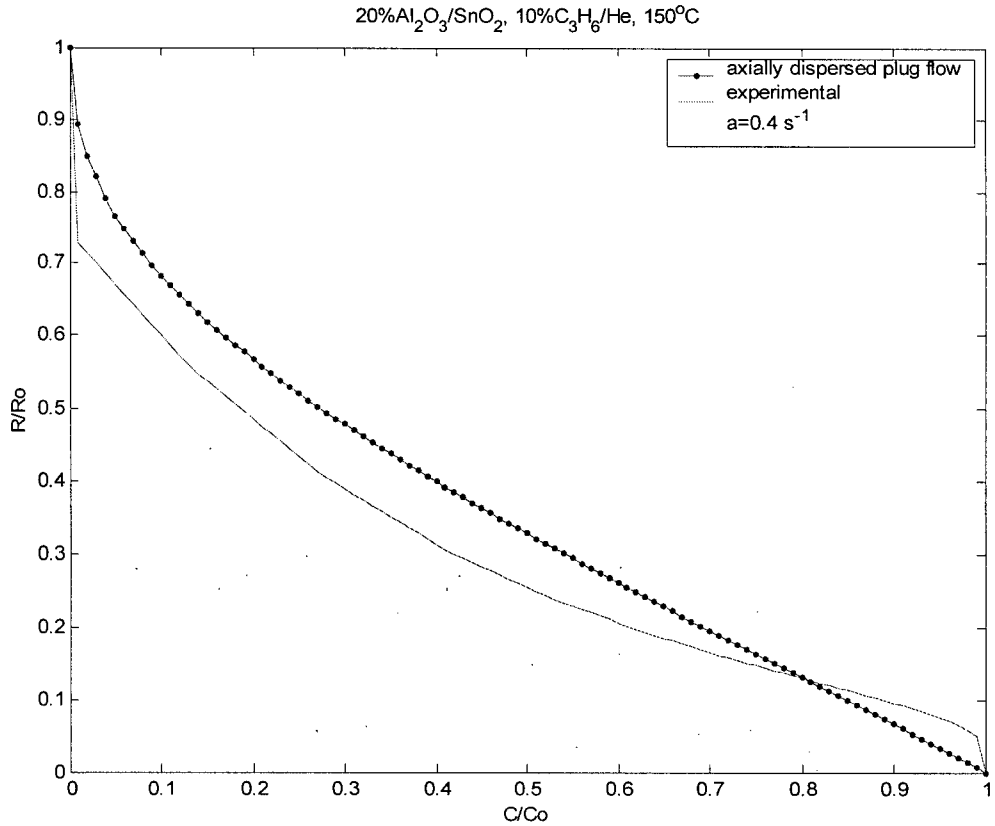
20%Al2O3/SnO2, 10%C3H6/He, 150°C
axially dispersed plug flow
experimental
a=0.4 s-1
R/Ro
C/Co
0
0.1
0.2
0.3
0.4
0.5
0.6
0.7
0.8
0.9
1

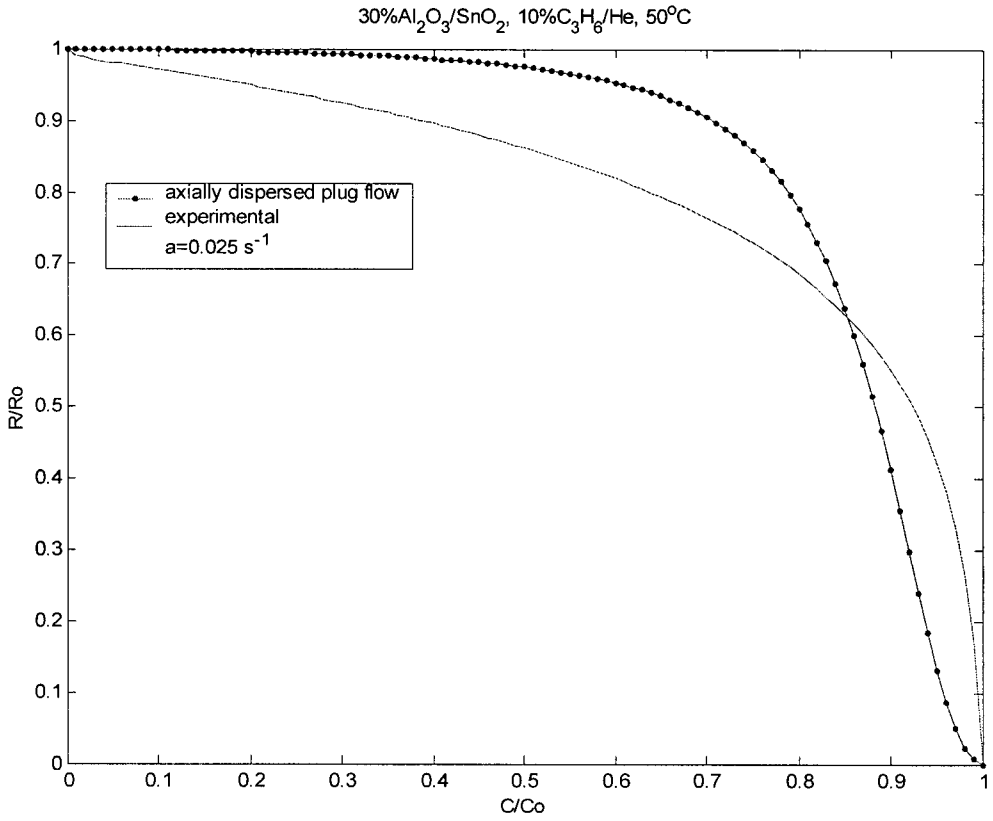
30%Al2O3/SnO2, 10%C3H6/He, 50°C
axially dispersed plug flow
experimental
a=0.025 s-1
R/Ro
C/Co
0
0.1
0.2
0.3
0.4
0.5
0.6
0.7
0.8
0.9
1

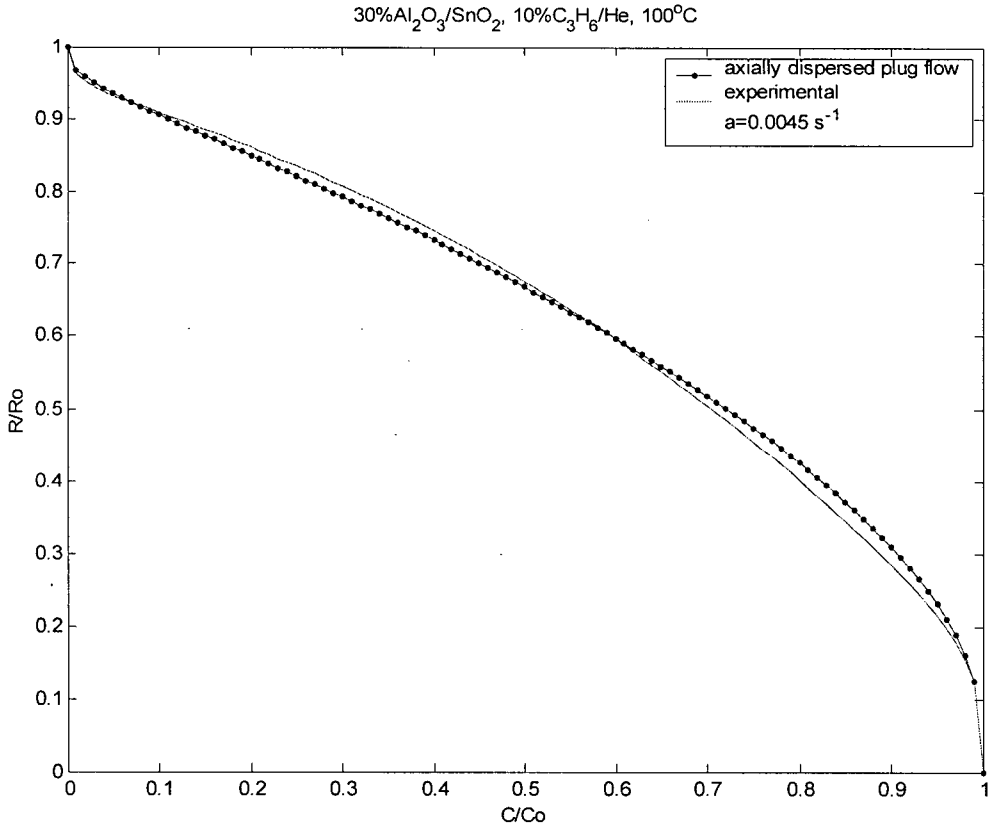
30%Al2O3/SnO2, 10%C3H6/He, 100°C
axially dispersed plug flow
experimental
a=0.0045 s-1
R/Ro
C/Co
0
0.1
0.2
0.3
0.4
0.5
0.6
0.7
0.8
0.9
1

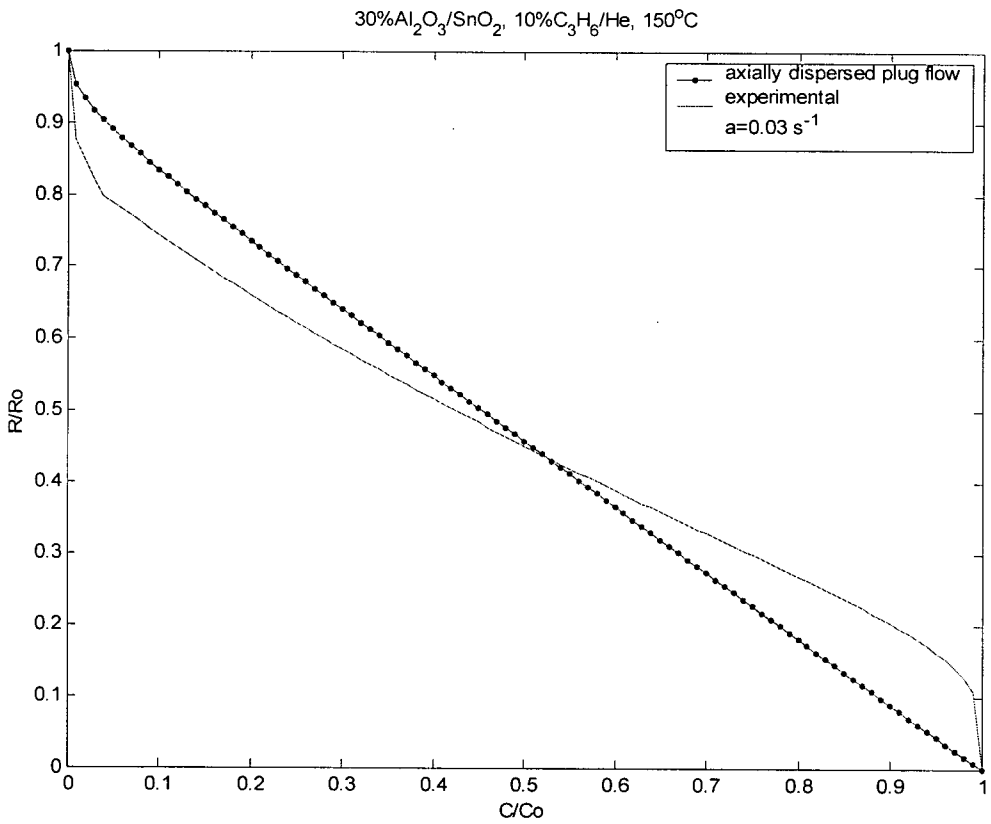
30%Al2O3/SnO2, 10%C3H6/He, 150°C
axially dispersed plug flow
experimental
a=0.03 s-1
R/Ro
C/Co
0
0.1
0.2
0.3
0.4
0.5
0.6
0.7
0.8
0.9
1

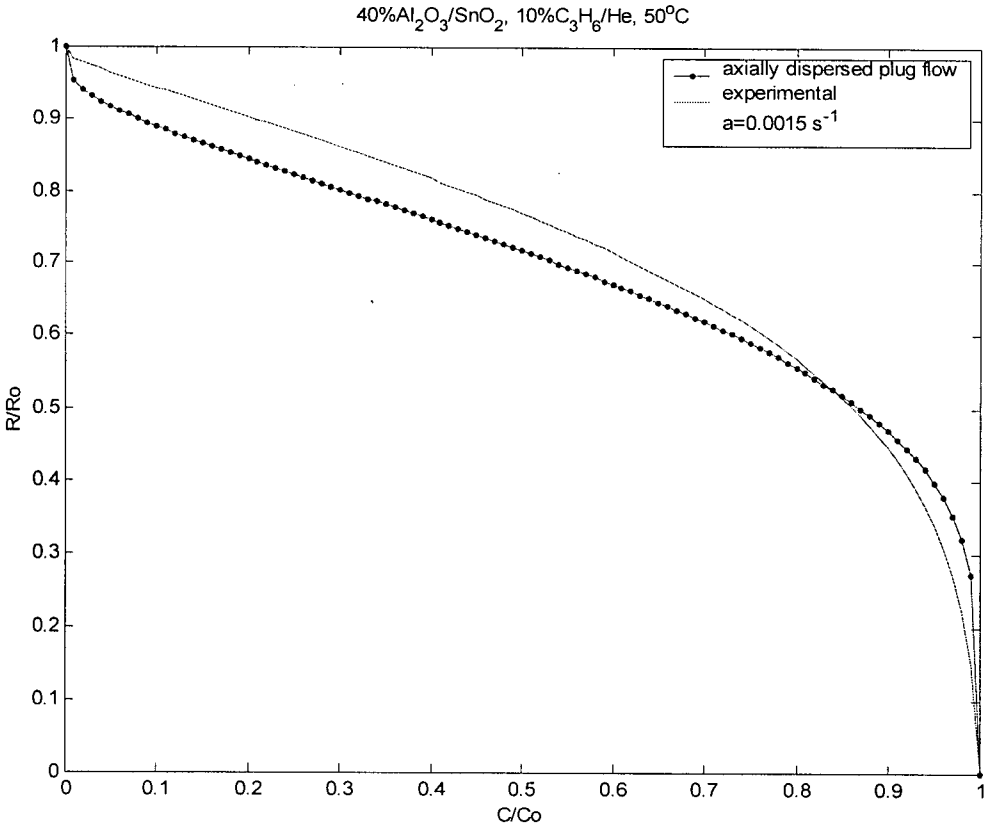
40%Al2O3/SnO2, 10%C3H6/He, 50°C
axially dispersed plug flow
experimental
a=0.0015 s-1
R/Ro
C/Co
0
0.1
0.2
0.3
0.4
0.5
0.6
0.7
0.8
0.9
1

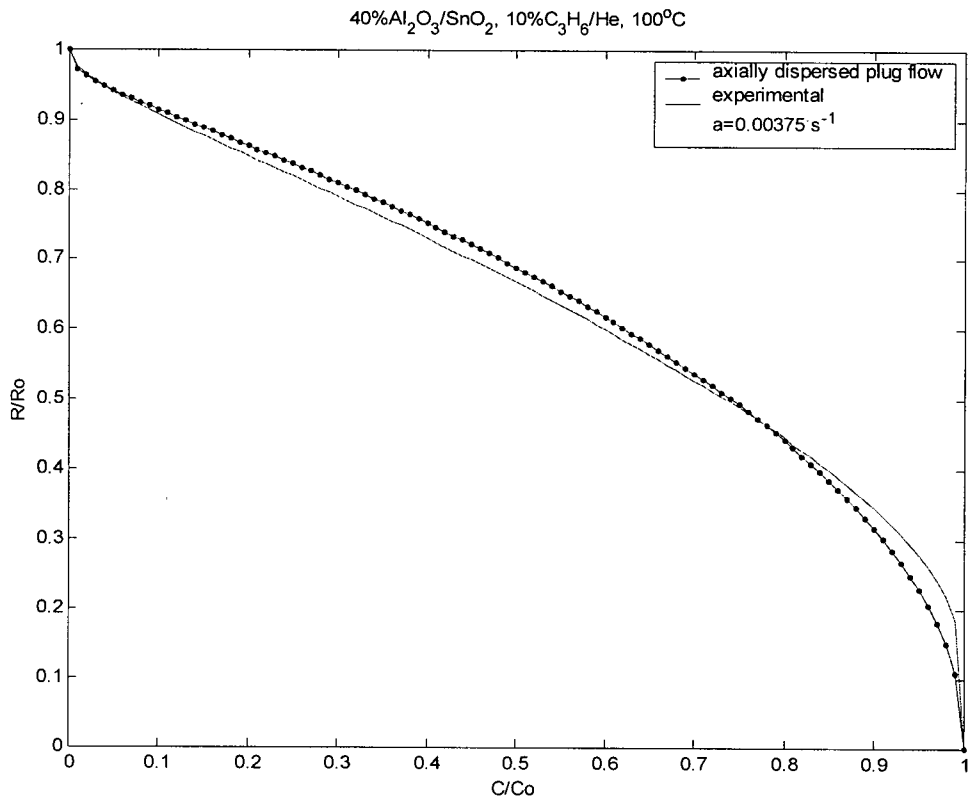
40%Al2O3/SnO2, 10%C3H6/He, 100°C
axially dispersed plug flow
experimental
a=0.00375 s-1
R/Ro
C/Co
0
0.1
0.2
0.3
0.4
0.5
0.6
0.7
0.8
0.9
1

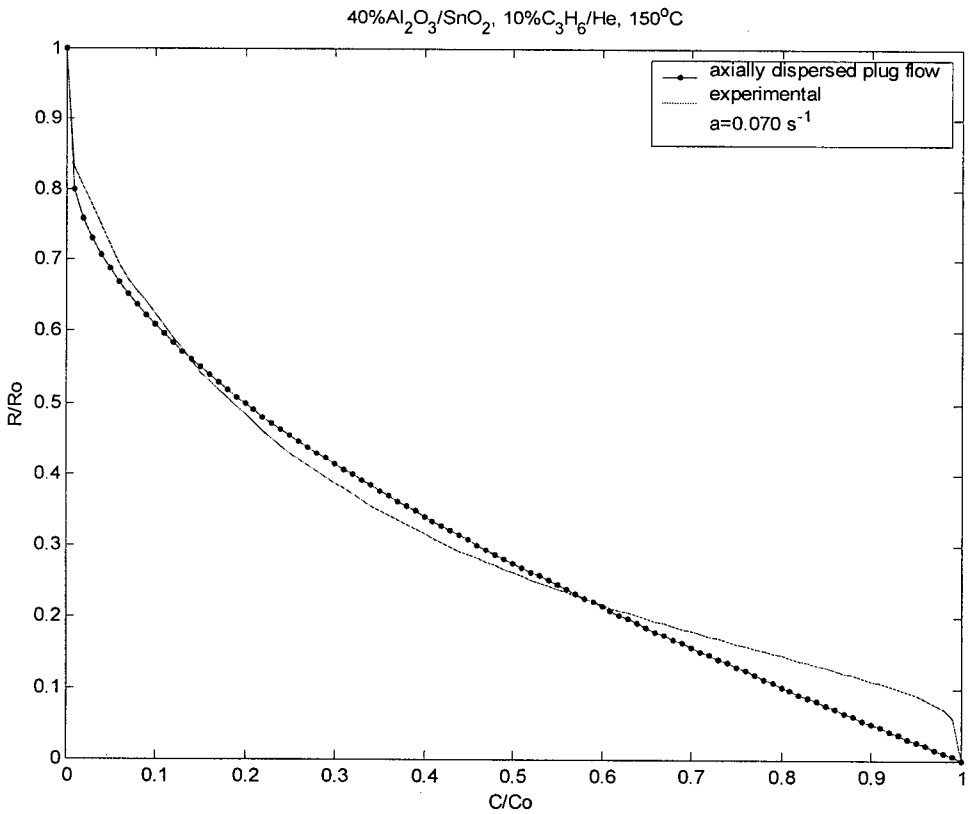
40%Al2O3/SnO2, 10%C3H6/He, 150°C
axially dispersed plug flow
experimental
a=0.070 s-1
R/Ro
C/Co
0
0.1
0.2
0.3
0.4
0.5
0.6
0.7
0.8
0.9
1

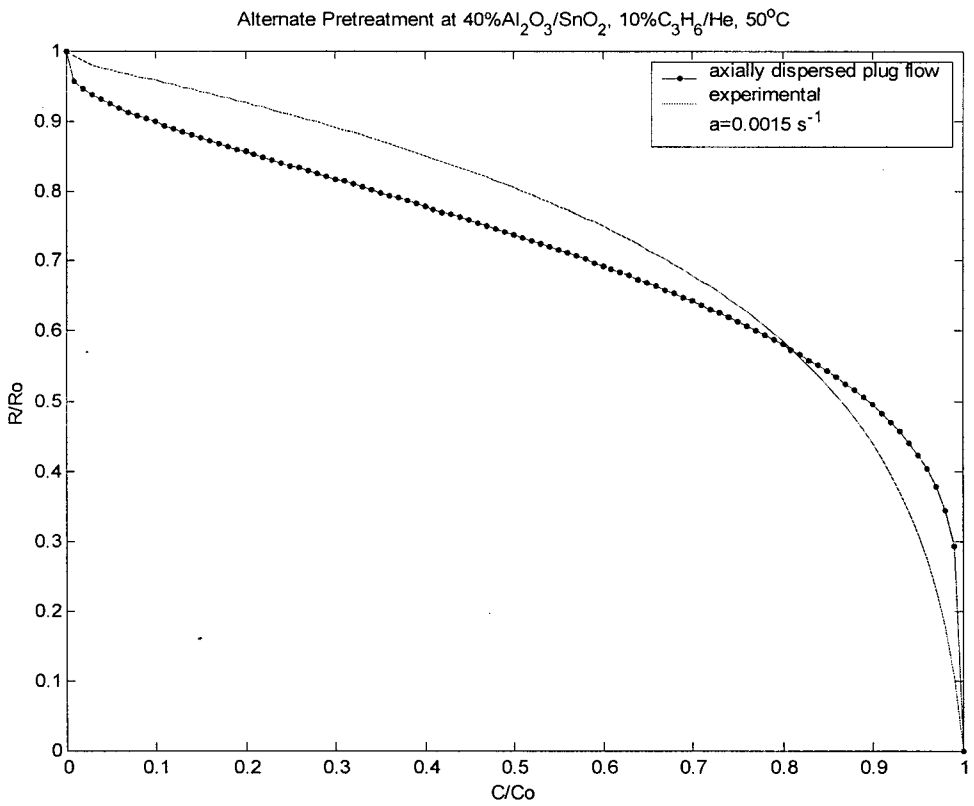
Alternate Pretreatment at 40%Al_2O_3/SnO_2, 10%C_3H_6/He, 50°C
axially dispersed plug flow
experimental
a=0.0015 s^{-1}
R/Ro
C/Co
0
0.1
0.2
0.3
0.4
0.5
0.6
0.7
0.8
0.9
1

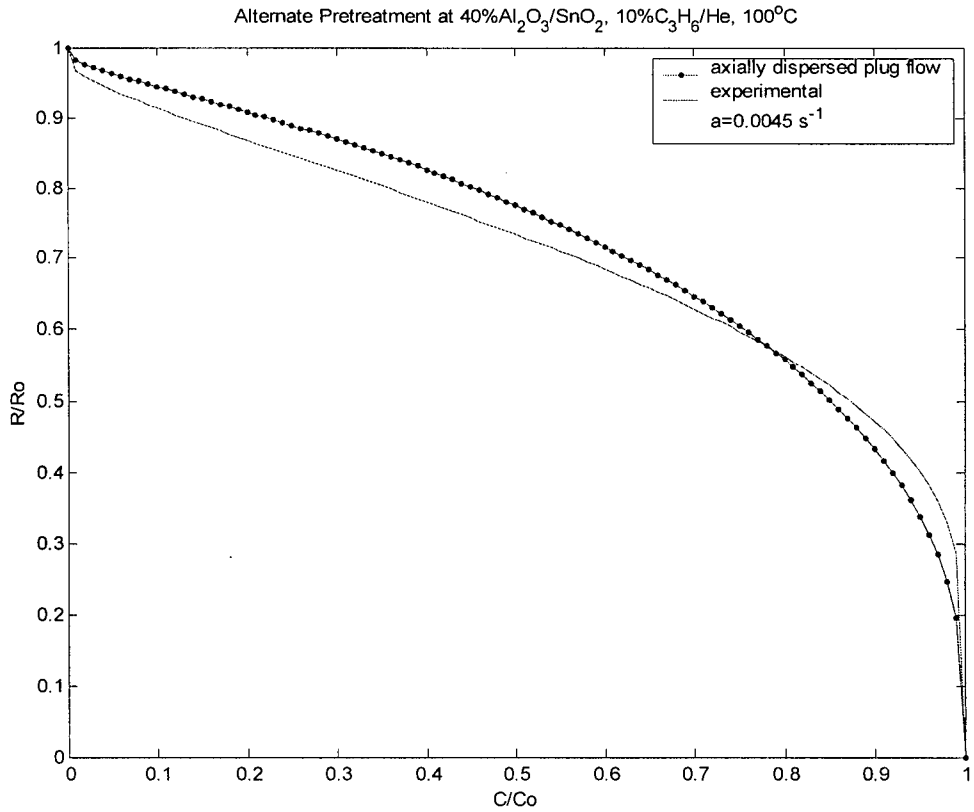
Alternate Pretreatment at 40%Al_2O_3/SnO_2, 10%C_3H_6/He, 100°C
axially dispersed plug flow
experimental
a=0.0045 s^{-1}
R/Ro
C/Co
0
0.1
0.2
0.3
0.4
0.5
0.6
0.7
0.8
0.9
1

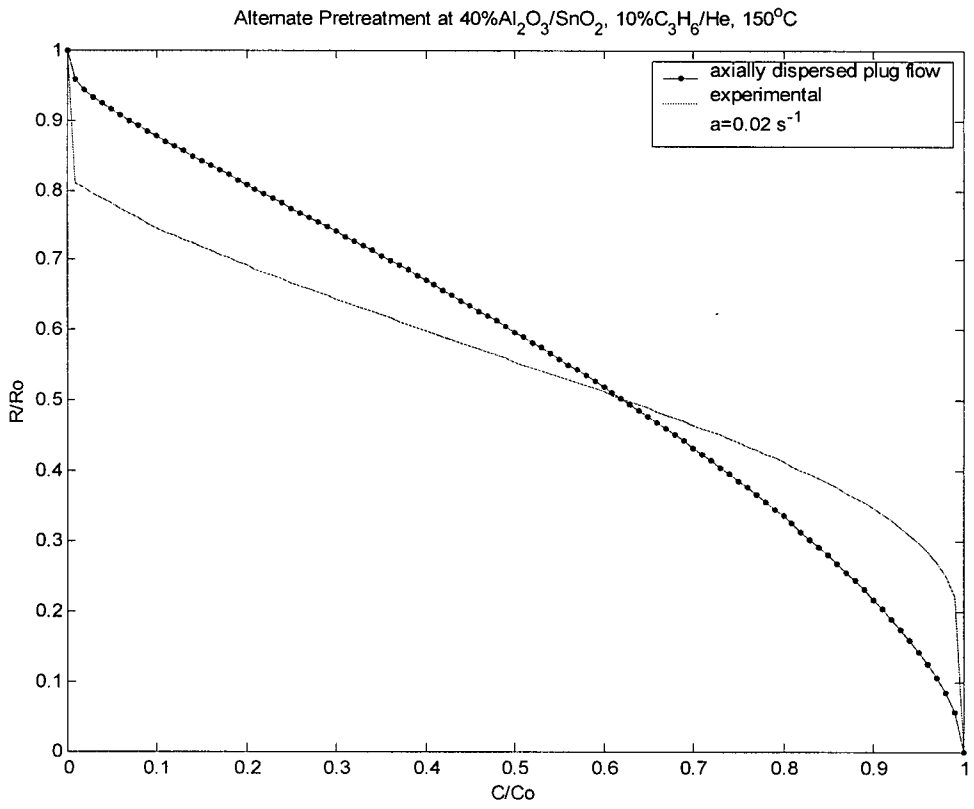
Alternate Pretreatment at 40%Al2O3/SnO2, 10%C3H6/He, 150°C
axially dispersed plug flow
experimental
a=0.02 s-1
R/Ro
C/Co
0
0.1
0.2
0.3
0.4
0.5
0.6
0.7
0.8
0.9
1

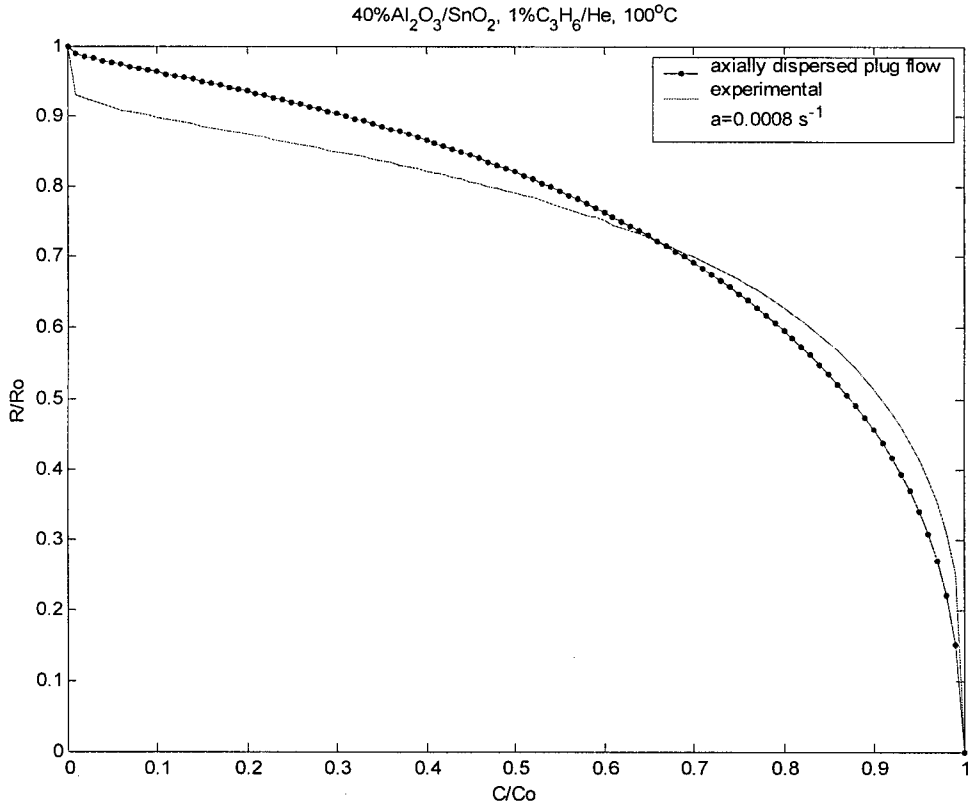
40%Al2O3/SnO2, 1%C3H6/He, 100°C
axially dispersed plug flow
experimental
a=0.0008 s-1
R/Ro
C/Co
0
0.1
0.2
0.3
0.4
0.5
0.6
0.7
0.8
0.9
1

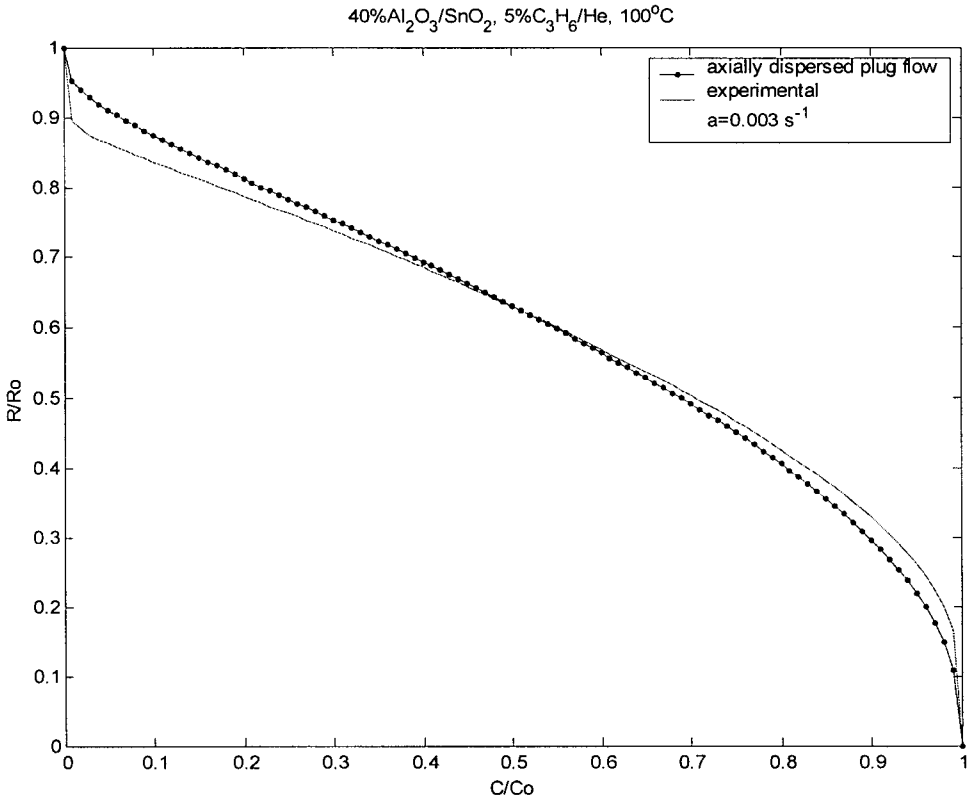
40%Al2O3/SnO2, 5%C3H6/He, 100°C
axially dispersed plug flow
experimental
a=0.003 s-1
R/Ro
C/Co
0
0.1
0.2
0.3
0.4
0.5
0.6
0.7
0.8
0.9
1

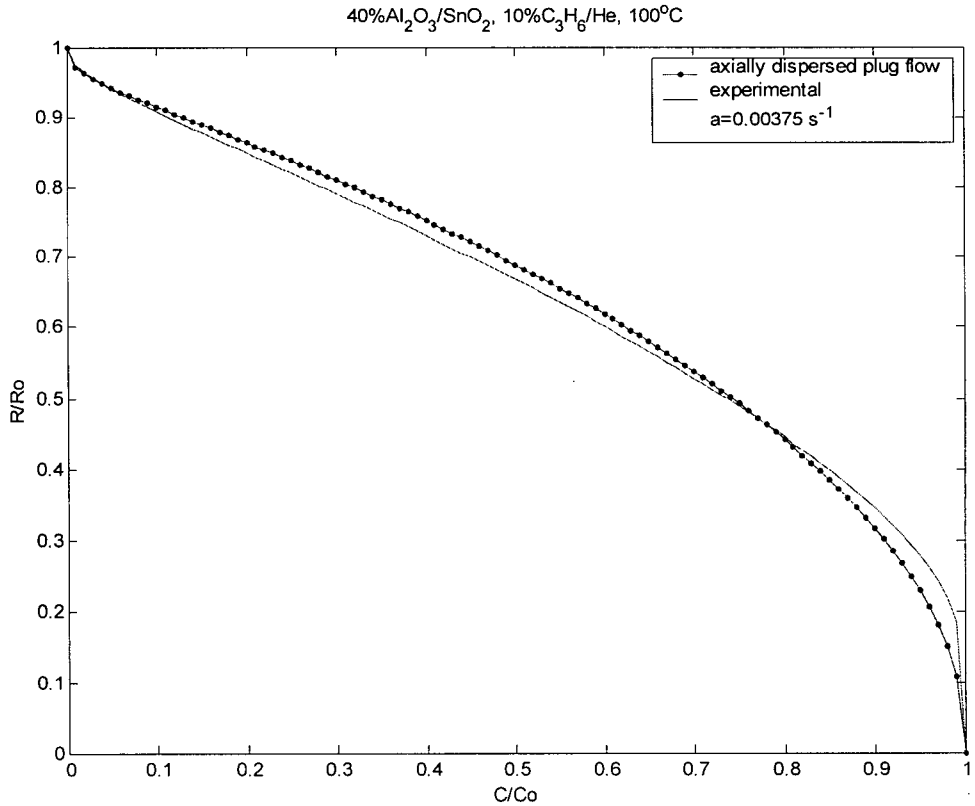
40%Al2O3/SnO2, 10%C3H6/He, 100°C
axially dispersed plug flow
experimental
a=0.00375 s-1
R/Ro
C/Co
0
0.1
0.2
0.3
0.4
0.5
0.6
0.7
0.8
0.9
1

Appendix F

Sample Matlab Program used to Perform Modeling Tasks

(This program utilizes imported data files, taken from *Excel*, that contain the raw data and then performs the modeling routines)

```
%bt100.m
%Matlab script program to predict the C/C0 and R/R0.
        %Axially dispersed plug flow; model 1b
        %Plug flow model, modified to include effects of DL and keff; model 1a

%Paramaters:

eps=.48;            %eps: bed voidage
v=.0063;            %v: interstitial velocity
K=5.24;             %K: Henry's constant
DL=9.76e-5;         %DL:  coefficient of axial dispersion
k=.044;             %effective mass transfer coefficient
mu=55.2;            %residence time of dead space in reactor at given conditions

ROi=2057;           %Total resistance in oxidised state (beginning of breakthru)
RRi=664;            %Total resistance in reduced state (end of breakthru)

z=0.001:.001:.05;   %z: distance down length of bed for which C/C0 is being predicted
t=.1:1:500;%-mu;
j=1:length(t);

%initial parallel resistances from ROi and RRi
ROT=length(z)*ROi;
RRT=length(z)*RRi;
a=.00375   %constant for 1st order kinetic reaction on the surface of metal oxide, model 1b
a1=0.003   %constant for 1st order kinetic reaction on the surface of metal oxide, model 1a

%Calculate additive effect of mass transfer and diffusion
kprime=1/((K*DL/v^2)*((1-eps)/eps)+1/k)  %model 1a

%Model
for i=1:length(z)
   tbar(i)=(z(i)/v)*(1+K*((1-eps)/eps));          %tbar: mean residence time, model 1b
   etaprime(i)=(kprime*K*z(i)/v)*((1-eps)/eps);   %model 1a

   for j=1:length(t)
      tauprime(i,j)=kprime*(t(j)-(z(i))/v);                %model 1a
      num(i,j)=(1-(t(j)/tbar(i)));                         %model 1b
      den(i,j)=2*(((DL/(v*z(i)))*(t(j)/tbar(i)))^(1/2));   %model 1b
      arg(i,j)=num(i,j)/den(i,j);  %arg: value of the argument to be calculated by erfc, model 1b
      if tauprime(i,j)<0
         if j==1
            tauprime(i,j)=1e-6;
         else
           tauprime(i,j)=tauprime(i,(j-1))+1e-6;
        end
      else
         tauprime(i,j)=tauprime(i,j);
      end
```

```
    argprime(i,j)=((etaprime(i)^0.5)-
(tauprime(i,j)^0.5)+(1/(8*etaprime(i)^0.5))+(1/(8*tauprime(i,j)^0.5)));  %model 1a

    bt(i,j)=erfc(arg(i,j));                          %model 1b
    btprime(i,j)=erfc(argprime(i,j));                %model 1a
    CoverC0(i,j)=0.5*bt(i,j);                        %model 1b
    CoverC0prime(i,j)=0.5*btprime(i,j);              %model 1a

    %Calculation of integrated resistance signal over length of bed, model 1b
    RO(i,j)=(1-CoverC0(i,j))*ROT;                    %oxidised state series resistance
    RR(i,j)=CoverC0(i,j)*(1/(((1/RRT)*(1-exp(-a*t(j))))+((1/ROT)*(exp(-a*t(j)))))); %reduced
series resistance
    RT(i,j)=RO(i,j)+RR(i,j);          %total resistance in each parallel circuit
    inverseRT(i,j)=1/RT(i,j);         %takes the inverse of each parallel resistance

    %Calculation of integrated resistance signal over length of bed, model 1a
    ROprime(i,j)=(1-CoverC0prime(i,j))*ROT;     %oxidised state series resistance
    RRprime(i,j)=CoverC0prime(i,j)*(1/(((1/RRT)*(1-exp(-a1*t(j))))+((1/ROT)*(exp(-
a1*t(j)))))); %reduced series resistance

    RTprime(i,j)=ROprime(i,j)+RRprime(i,j);      %total resistance in each parallel circuit
    inverseRTprime(i,j)=1/RTprime(i,j);          %inverse of each parallel resistance
  end
end

%"Integrated Resistance", model 1b
suminverseRT=sum(inverseRT);      %sums the inverse of each parallel resistance
Rint=1./suminverseRT;             % dot multiplication, the inverse of each element is taken

%"Integrated Resistance", model 1a
suminverseRTprime=sum(inverseRTprime);      %sums inverse of each parallel resistance
Rintprime=1./suminverseRTprime;             %dot multiplication, inverse of each element

%Normalised Resistance
for j=1:length(t)
  RoverR0(j)=1-(Rint(j)-Rint(1))/(Rint(length(t))-Rint(1));                    %model 1b
  RoverR0prime(j)=1-(Rintprime(j)-Rintprime(1))/(Rintprime(length(t))-Rintprime(1));
%model 1a
End

%OUTPUT
%Plot of c/c0 vs time
t=t+mu;    %shifts the modelled time axis by the dead space of the reator
figure(1)
plot(t,CoverC0(length(z),:),'.-',texp,CCOexp,'-');
title('40%Al_2O_3/SnO_2, 10%C_3H_6/He, 100^oC')
xlabel('time (s)')
ylabel('C/Co')
legend('C/Co axially dispersed plug flow','C/Co experimental')
```

```
%Plot the electrical response vs time
figure(2)
plot(t,RoverR0,':',texp,RROexp,'--');
title('40%Al_2O_3/SnO_2, 10%C_3H_6/He, 100^oC')
xlabel('time (s)')
ylabel('R/Ro')
legend('R/Ro axially dispersed plug flow','R/Ro experimental')

%Correlation of R/R0 vs C/C0 all models ("weighted data")
figure(3)
plot(CoverC0prime(length(z),:),RoverR0prime,'--',CoverC0(length(z),:),RoverR0,'.-
',CCOexp,RROexp,'-');
title('40%Al_{2}O_{3}/SnO_{2}, 10%C_{3}H_{6}/He, 100^{o}C')
xlabel('C/Co')
ylabel('R/Ro')
legend('plug flow','axially dispersed plug flow','experimental')

%Plot breakthrough; all models
figure(4)
plot(t,CoverC0prime(length(z),:),'--',t,CoverC0(length(z),:),'.-',texp,CCOexp,'-');
title('40%Al_2O_3/SnO_2, 10%C_3H_6/He, 100^oC')
xlabel('time (s)')
ylabel('C/Co')
legend('C/Co plug flow','C/Co axially dispersed plug flow','C/Co experimental')

%Interpolated Data Points (100 equally spaced points)to unweight the data from time axis
%Determination of sum of the squares:
for j=1:length(t)
   if CoverC0prime(length(z),j)==0
      n=0;
   else
      n=n+1;
      CoverC0prime(length(z),n)=CoverC0prime(length(z),j);
      RoverR0prime(n)=RoverR0prime(j);
   end
end

xexp=0:.01:1; xmod=0:.01:1;
yexp=interp1(CCOexp,RROexp,xexp);
ymod=interp1(CoverC0(length(z),:),RoverR0,xmod);
CoverC0prime=CoverC0prime(length(z),1:n);
RoverR0prime=RoverR0prime(1:n);
ymod1a=interp1(CoverC0prime,RoverR0prime,xmod);
ymod(1)=1; ymod1a(1)=1;
ymod(length(xmod))=0; ymod1a(length(xmod))=0;
```

```
for k=1:length(xmod)
   diff(k)=yexp(k)-ymod(k); diff1a(k)=yexp(k)-ymod1a(k);
end

diff(1)=0; diff1a(1)=0;
diff(length(xmod))=0; diff1a(length(xmod))=0;
sumsquare=sum((diff).^2)
sumsquare1a=sum((diff1a).^2)

%Plot Correlation of R/R0 vs C/C0; Model 1b
figure(5)
plot(xmod,ymod,'.-',xexp,yexp,'-');
title('40%Al_{2}O_{3}/SnO_{2}, 10%C_{3}H_{6}/He, 100^{o}C')
xlabel('C/Co')
ylabel('R/Ro')
legend('axially dispersed plug flow','experimental')

%Plot Correlation of R/R0 vs C/C0; all models
figure(6)
plot(xmod,ymod1a,'--',xmod,ymod,'.-',xexp,yexp,'-');
title('40%Al_{2}O_{3}/SnO_{2}, 10%C_{3}H_{6}/He, 100^{o}C')
xlabel('C/Co')
ylabel('R/Ro')
legend('plug flow','axially dispersed plug flow','experimental')
```